



A University of Sussex PhD thesis

Available online via Sussex Research Online:

<http://sro.sussex.ac.uk/>

This thesis is protected by copyright which belongs to the author.

This thesis cannot be reproduced or quoted extensively from without first obtaining permission in writing from the Author

The content must not be changed in any way or sold commercially in any format or medium without the formal permission of the Author

When referring to this work, full bibliographic details including the author, title, awarding institution and date of the thesis must be given

Please visit Sussex Research Online for more information and further details



University of Sussex

Non-adiabatic losses from radio frequency dressed cold atom traps

Kathryn Alice Burrows

Submitted in partial fulfilment for the degree of **Doctor of Philosophy**

University of Sussex

September 2015

UNIVERSITY OF SUSSEX

KATHRYN ALICE BURROWS, DOCTOR OF PHILOSOPHY

NON-ADIABATIC LOSSES FROM RADIO FREQUENCY DRESSED
COLD ATOM TRAPS

SUMMARY

Cold atom traps are a promising tool for investigating and manipulating atomic behaviour. Radio frequency (RF) dressed cold atom traps allow high versatility of trapping potentials, which is important for potential applications, particularly in atom interferometry. This thesis investigates non-adiabatic spin flip transitions which can lead to losses of atoms from RF-dressed cold atom traps. We develop two models for the adiabatic potentials associated with RF-dressed traps, for the cases in which gravity does and doesn't have a significant effect. Within these two models we use first order perturbation theory to calculate decay rates for the number of dressed spin flip transitions per unit time. Our obtained decay rates are dependent on the atomic energy. For RF-dressed cold atom traps in which spin flip transitions lead to losses of atoms from the trap, we are able to predict how non-adiabatic transitions decrease the trapped atom number. We achieve this by modelling the atomic distribution of energies for several different scenarios. The thesis concludes with a comparison to experimental data, including modelling how atomic energies are affected by noise in the currents generating the trapping magnetic fields.

Acknowledgements

By careful experimentation I have become aware of the fact that I can in no way be modelled as an isolated system. As a consequence there are many people who have contributed, directly or indirectly, to this work. Some of which like Gaston Leroux, Claude Debussy and Leonardo da Vinci I know the names of but have never met. Others like Janis Ian I have met only briefly and it is overwhelming to think of all those that I am simply unaware of. My thanks go to you all but here I must necessarily be brief.

The most direct contribution to this thesis is of course provided by my supervisor, Barry Garraway. I am in awe of your vast knowledge and amazed at the rapidity with which you can access it. I would like to thank you for all the time, effort and guidance you have given me over the last four years.

I also have to thank Germán Sinuco León. You have helped me grow as a scientist on many occasions, not to mention our very enjoyable office discussions and I am in your debt for the time and effort you have contributed thesis checking.

I would like to thank H  l  ne Perrin for her help during this project and to the whole group involved in collection of the data discussed.

I send my gratitude out to all of the attendees of theory club. Thanks to April, Frances, Niall, Sam, Jesús, John, Pedro, Jon, Germán, Graeme, Carlos and Sahar. In particular I would like to thank Pedro Nevado Serrano for organizing theory club. Theory club has been a source of enjoyment for me and helped my confidence as a researcher grow. I would also like to thank Samuel Fernández Lorenzo for all the help and advice he has given me. Me siento tan afortunada de haberte encontrado.

I would like to thank Bethany Logan and Richard Chambers, for answering so many of my thesis related queries so well, and Eduard Campillo Funollet for some very enjoyable discussions involving some miniature mathematics, which was helpful for work presented in this thesis.

My thanks also go to Tim Gadd, who has helped me more than I can express with words and who I personally feel does his job very well.

Thank you to everyone who ever turned up to one of my fortnightly science

socials. In particular I would like to thank my co-conspirator Ola, as well as Tom, Justyna/Tom, Eduard, Pedro, Graeme and Paul.

This leaves me with the people who I am lucky enough to share some DNA with. I carry an enormous amount of gratitude for my family. Your love is so enduring and unyielding that it makes a very potent force. I love you all very much and would like to make a special mention of my grandfather, who I cannot repay for all the inspiration and intelligence he has given me.

I would also like to thank Alice, Bella, Jellybean and Chanel; just for being who you are. You always cheer me up and you always give the best advice.

Post-viva acknowledgements

I must send my love and gratitude to Jesús Rubio Jiménez, who has helped and supported me greatly through these final few months.

Finally, I would also like to thank my examiners, José Verdú Galiana and Patrik Öhberg, for useful discussions and suggestions during the viva voce examination which have helped to greatly improve the published version of this work.

Contents

List of Tables	viii
List of Figures	ix
I Research outline	xiii
1 Introduction	1
II Background theory	3
2 Cold atom traps	4
2.1 Confining atoms with magnetic fields	4
2.2 Atom chips	6
2.3 RF-dressed cold atom traps	7
3 RF-dressed cold atom trap potentials	10
3.1 Hyperfine spin state basis	10
3.2 Rotating wave approximation	13
3.3 Dressing with the RF field	18
3.4 Examining the dressed trap Hamiltonian	21
4 Fermi's Golden Rule	25
4.1 Fermi's Golden Rule derivation	25
4.2 Using Fermi's Golden Rule to model spin state transitions	31
III Results and analysis	33
5 Rate of dressed spin state transitions	34
5.1 Minimal effect gravity model	35
5.1.1 Decay rate of the ground state	41

5.1.2	Pole approximation for higher atomic energies	46
5.1.3	Low decay limit	58
5.2	Full effect gravity model	63
5.3	Summary	80
6	Time evolution of trapped atom number	82
6.1	Maxwell-Boltzmann initial distribution	83
6.2	Squeezed thermal initial distribution	89
6.3	Bose-Einstein initial distribution	96
6.4	Dynamical distributions	107
6.4.1	Master equation model	108
6.4.2	Parametric heating model	116
6.5	Summary	128
7	Landau-Zener model for non-adiabatic losses	132
7.1	Landau-Zener model	132
7.2	Comparison of the quantum mechanical and semiclassical models . .	134
7.3	Summary	143
IV	Study of experimental data	144
8	Explaining atomic losses in experimental data by non-adiabatic transitions	145
8.1	CNRS Paris 13 experiment	145
8.2	Application of the presented models to experimental data	151
8.2.1	Minimal effect gravity model	152
8.2.2	Full effect gravity model	167
8.2.3	Master equation model	183
8.2.4	Parametric heating model	187
8.3	Summary	198
V	Conclusions	202
9	Summary, conclusion and outlook	203
	Bibliography	207

VI	Supporting material	214
A	Saddle point method	215
B	Double exponential fit	230
C	Asymmetric box example	235

List of Tables

5.1	Terms which contribute to the pole residue	50
5.2	Minimal effect gravity model versus full effect gravity model	80
6.1	Summary of chapter 6	130
6.2	Summary of trapped atom number graphs	131
8.1	Trap parameter values for the experimental data	151
8.2	Fitted Rabi frequency values for the minimal effect gravity model . .	162
8.3	Parametric heating model fitted parameters γ_a and Ω	195
8.4	Summary of experimental comparison graphs	200
8.5	Summary of experimental comparison results	201
B.1	Double exponential fit parameters	232

List of Figures

3.1	Hyperfine level Zeeman splitting	11
3.2	RF-dressed trap described with hyperfine spin levels	12
3.3	Linear cosine behaviour from two rotating motions	13
3.4	First reference frame transition in transforming to the adiabatic basis	15
3.5	Effect of the primary change of reference frame on the trap description	16
3.6	Second reference frame transition in transforming to the adiabatic basis	19
3.7	RF-dressed atom trap with adiabatic potentials	23
4.1	Behaviour of the function $\frac{\sin^2\left(\frac{\omega_{fi}t}{2}\right)}{\omega_{fi}^2}$	30
5.1	Adiabatic potentials	37
5.2	Hump height	38
5.3	Minimal effect gravity model potentials	39
5.4	Ground state decay rate as a function of Rabi frequency	44
5.5	Affect of the hump on the ground state decay rate	45
5.6	Pole approximation difference at high Rabi frequency	53
5.7	Pole approximation difference at low Rabi frequency	54
5.8	Affect of Rabi frequency and magnetic field gradient on the pole approximation	55
5.9	Pole approximation improves for low energy states	56
5.10	Pole approximation improves in the low decay regime	57
5.11	Low decay limit analytic formula	61
5.12	Fractional difference of low decay limit analytic formula	62
5.13	Magnitude of the gravitational sag	65
5.14	Full effect gravity model potentials	67
5.15	Full effect gravity and minimal effect gravity model potentials	68
5.16	Full effect gravity model decay rates variation with atom energy . . .	72
5.17	Decay rates variation with Rabi frequency	73
5.18	Decay rates variation with magnetic field gradient	74
5.19	Logarithm scale plot of decay rate oscillations	75

5.20	Full effect gravity model wavefunctions varying with atomic energy	77
5.21	Full effect gravity model wavefunctions varying with Rabi frequency	78
5.22	Behaviour of full effect gravity model integrands	79
6.1	Process to calculate the trapped atom number with a Maxwell-Boltzmann initial distribution	84
6.2	Maxwell-Boltzmann initial distribution affected by temperature and Rabi frequency	85
6.3	Trapped atom number prediction, with a Maxwell-Boltzmann initial distribution, affected by Rabi frequency or magnetic field gradient	86
6.4	Trapped atom number prediction, with a Maxwell-Boltzmann initial distribution, affected by temperature or initial atom number.	87
6.5	Trapped atom prediction for different decay rates	88
6.6	Squeezed thermal initial distribution	93
6.7	Process to calculate the trapped atom number with a squeezed ther- mal initial distribution	94
6.8	Trapped atom prediction with a squeezed thermal initial distribution	95
6.9	Process to calculate the trapped atom number with a Bose-Einstein initial distribution	99
6.10	Bose-Einstein distribution	100
6.11	Bose-Einstein distribution affected by Rabi frequency or temperature	101
6.12	Bose-Einstein distribution affected by RF frequency or initial atom number	102
6.13	Effect of different decay rates on trapped atom prediction	104
6.14	Affect of the initial distribution on trapped atom prediction	105
6.15	Affect of the hump on the trapped atom number prediction	106
6.16	Change of occupancy possibilities	107
6.17	Master equation model transitions	109
6.18	Master equation model with a variation in reservoir temperature	111
6.19	Master equation model with a variation in relaxation parameter	112
6.20	Parametric heating model transitions	120
6.21	Parametric heating model for various heating rates	122
6.22	Parametric heating model affected by initial distribution	123
6.23	Temperature variation for the parametric heating model	126
6.24	Components which lead to change in the average energy per atom for the parametric heating model	127
7.1	Landau-Zener variation with atom energy	137

7.2	Landau-Zener variation with Rabi frequency	138
7.3	Landau-Zener variation with magnetic field gradient	139
7.4	Landau-Zener trapped atom number prediction	141
7.5	Landau-Zener trapped atom number prediction with heating	142
8.1	Experimental setup	146
8.2	Atom cloud temperature contours	149
8.3	Atom cloud appearance	150
8.4	Minimal effect gravity model for the 5 kHz data set	153
8.5	Minimal effect gravity model for the 7 kHz data set	154
8.6	Minimal effect gravity model for the 8 kHz data set	155
8.7	Minimal effect gravity model for the 9 kHz data set	156
8.8	Minimal effect gravity model regression fitting for the 5 kHz data set .	158
8.9	Minimal effect gravity model regression fitting for the 7 kHz data set .	159
8.10	Minimal effect gravity model regression fitting for the 8 kHz data set .	160
8.11	Minimal effect gravity model regression fitting for the 9 kHz data set .	161
8.12	Comparison of fitted and experimentally determined Rabi frequencies for the minimal effect gravity model	164
8.13	Regression fitting parameter for the minimal effect gravity model . .	165
8.14	Full effect gravity model for the 5 kHz data set	167
8.15	Full effect gravity model for the 7 kHz data set	168
8.16	Full effect gravity model for the 8 kHz data set	169
8.17	Full effect gravity model for the 9 kHz data set	170
8.18	Regression fitting parameter for the full effect gravity model	171
8.19	Surface plot of the regression fitting parameter for the full effect grav- ity model	173
8.20	Maxwell-Boltzmann distribution, full effect gravity model, regression fitting for the 7 kHz data set	175
8.21	Bose-Einstein distribution, full effect gravity model, regression fitting for the 7 kHz data set	177
8.22	Difference between full and minimal effect gravity models for the vari- ation of trapped atom number with Rabi frequency	179
8.23	Dramatic Rabi frequency sensitivity in Maxwell-Boltzmann distribu- tion, full effect gravity model regression fitted results	180
8.24	Dramatic Rabi frequency sensitivity in Bose-Einstein distribution, full effect gravity model regression fitted results	182
8.25	Variation in recorded atom cloud temperature	184
8.26	Regression fitting difficulties with the master equation model	185

8.27	Parametric heating model regression fitting for the 5 kHz data set . . .	189
8.28	Parametric heating model regression fitting for the 7 kHz data set . . .	190
8.29	Parametric heating model regression fitting for the 8 kHz data set . . .	191
8.30	Parametric heating model regression fitting for the 9 kHz data set . . .	192
8.31	Comparison of fitted and experimentally determined Rabi frequencies for the parametric heating model	197
A.1	Location of the saddle point	218
A.2	Deformation of the integration path for the saddle point method . . .	220
A.3	Pole inclusion is necessary in the saddle point method	221
A.4	Pole inclusion remains necessary for a variety of magnetic field gradients	222
A.5	Different methods for calculating the desired integral	224
A.6	Fractional difference between the different methods for calculating the desired integral	225
A.7	Fractional difference between the pole approximation and the numer- ical determination of the desired integral	226
A.8	Fractional difference between the pole approximation and the numer- ical determination for the second desired integral	228
B.1	Double exponential regression fitting for the 5 kHz data set	231
B.2	Double exponential regression fitting for the 7 kHz data set	232
B.3	Double exponential regression fitting for the 8 kHz data set	233
B.4	Double exponential regression fitting for the 9 kHz data set	234
C.1	Asymmetric box model	235

Part I

Research outline

Chapter 1

Introduction

The existence and interactions of atoms constitute the majority of the physical world we see around us. Everyone can easily manipulate atoms on a macroscopic scale. For example, every time we move a finger we are forcing the vast number of atoms that form it to change their position and velocity. Yet the ability to control and model the behaviour of relatively small numbers of atoms properly, with quantum mechanics, is still a challenging task. Cold atom traps are one recent development that allow us to study the interactions of atoms, as well as allowing the manipulation of atoms for our own desires.

In this thesis a study into non-adiabatic losses from RF-dressed cold atom traps is performed. This spin dependent loss mechanism, that results from atoms making a transition to a dressed spin state in which they are no longer affected by the trapping magnetic field potentials, is well known amongst those working closely with RF-dressed cold atom traps. However, currently there are no quantum mechanical models to predict the rate of these non-adiabatic losses. Often an estimation for the rate of non-adiabatic losses is obtained from semiclassical Landau-Zener theory. There was comment on the need for a more detailed study of losses associated with dressed spin state transitions in the New Journal of Physics paper by Merloti *et al.* [1]. The need for further investigation, of non-adiabatic losses from RF-dressed cold atom traps, seemed to be strengthened when agreement between experimental results and Landau-Zener theory could not be found in the masters thesis of Matthieu Pierens from the same group [2]. My original contribution in this thesis is to use first order perturbation theory to model non-adiabatic losses from RF-dressed cold atom traps and to compare this theory to the semiclassical Landau-Zener model and experimental results.

This thesis begins in **chapter 2** with a discussion of the currently realisable experimental tool of cold atom traps. RF-dressed cold atom traps are qualitatively introduced, placing them in context of the wider research field. Aiming to highlight the promise for future applications of cold atom traps, atom chips are also discussed.

In **chapter 5** investigations into non-adiabatic losses are begun by establishing models which allow the use of Fermi's Golden Rule to determine decay rates, for the rate of non-adiabatic transitions for atoms of a specific energy. This is arguably the most important chapter, where quantum mechanical alternatives to the commonly used Landau-Zener decay rate are presented. For comparison with experimental results it is necessary to obtain a prediction for the time evolution of the number of trapped atoms. This is discussed in **chapter 6** considering Maxwell-Boltzmann, squeezed thermal and Bose-Einstein initial distributions of the atomic energy levels. Additionally we will examine how transitions between atomic energy levels, such as those caused by a heating process, would affect the predicted trapped atom lifetime.

Finally, **chapter 8** progresses through a series of comparisons between the theoretical results presented and experimental data recorded by the Villeteuse group led by H  l  ne Perrin. The experimental setup of the Paris 13 experiment is briefly reviewed, providing context to the experimental data considered. An investigation is then performed to determine if non-adiabatic losses, as predicted by the results presented in this thesis, can explain the experimental decline in trapped atom number observed.

Part II

Background theory

Chapter 2

Cold atom traps

This chapter gives a brief overview of the scientific field of cold atom traps, highlighting the importance of trapping and manipulating cold atoms. Atom chips are discussed due to their potential to be of great importance in future applications. Before beginning a mathematical treatment in chapter 3, RF-dressed cold atom traps are discussed here to express their current interest to the research community and hopes for future developments.

2.1 Confining atoms with magnetic fields

Cold atom traps has grown into an active and diverse field of investigation since its introduction in the late 1980s [3]. The first microscale atom traps (atom chips) were experimentally achieved in 1998 using static magnetic fields to confine their atoms [4]. The field developed even greater importance when it became clear that Bose-Einstein Condensates (BECs), the quantum state of matter in which the ground state of an integer spin system is macroscopically occupied, could be easily and reliably produced with cold atom traps [5, 6, 7, 8]. As BECs are a relatively new and active area of research, cold atom traps aid in the discovery of emerging phenomena associated with them, such as superfluidity. For example, the quantized vortices generated by disturbing a superfluid have been observed in BECs held in cold atom traps [9, 10, 11].

Cold atom traps have a diverse range of potential applications, particularly in the fields of metrology¹ and quantum information processing [12, 13]. There is particular interest in using cold atom traps as gravitational sensors; both for research purposes, such as accurately measuring the gravitational constant, or for applications in engineering or geophysics which require detecting small variations in

¹Metrology is the study of measurements and standards.

gravitational fields [14, 15]. Taking inspiration from the success of the laser, another promising application would be for coherent matter waves formed from cold atoms to create an ‘atom laser’ [16, 17].

As opposed to other basic constituents of matter such as ions or electrons, the overall neutral charge of atoms make electric fields unsuitable for use in their confinement. However, atoms do interact with magnetic fields, the strength of the interaction being characterized by the magnetic moment of the atom [18]. As the magnetic moment of an atom is dependent on the atoms spin, the force exerted on the atom is a spin dependent force. The interaction between the atomic spin and magnetic field is relatively weak, requiring that trapped atoms must be very cold. Cold atom traps typically require temperatures of milli-Kelvin (mK) and below; the sub-field of ultracold atom traps operate in the range of micro-Kelvin (μK) to nano-Kelvin (nK). If suitably cold the atoms within the trap move with a low velocity, such that the orientation of their magnetic moment is able to align with the local magnetic field direction. As the atoms have finite temperature they have non-zero velocity and move around confined within the volume of the trap. The collection of trapped atoms is often described as forming an ‘atom cloud’.

Even at such low temperatures atoms are rapidly lost from the trap, with typical experimental runs lasting no more than minutes. However, this is long enough for information to be extracted from the system, allowing experiments to be performed. Measurement of the atom cloud itself, for techniques such as absorption imaging [19], requires switching off the trap and destroying the trapped atom setup. This means that in contrast to experiments with trapped ions which can manipulate and observe the same ion for long time scales, such as days or even years for electrons. Atom based experiments have a much faster ‘load, manipulate, measure, repeat’ process due to the short longevity of the atom cloud in the trap and the destructive nature of measurement.

The spin dependence of the magnetic trapping force causes cold atom traps to be highly sensitive to the spin state of an atom. If the atom is in a spin state in which it no longer feels the trapping magnetic force, the atom can then travel out of the trapping region and be irreversibly lost from the trap. Cold atom traps thus suffer from spin dependent losses. One key disadvantage of early static magnetic field traps was the loss of atoms due to Majorana losses [20, 21]. In the presence of a magnetic field, Zeeman splitting of the atomic hyperfine spin states occurs [18]. The atoms response to the magnetic field is governed by its magnetic moment, dependent on its spin state. Low field seeking atoms feel a force directing them towards regions of low magnetic field value. High field seeking atoms are pushed towards regions

with high magnetic field value. Due to restrictions imposed by Earnshaw's theorem, which states that magnetic field maxima cannot exist, only low field seeking atoms can be trapped [22]. Majorana losses occur wherever the magnetic field value felt by the atoms is close to zero. The semiclassical interpretation of Majorana losses is as follows: without the presence of a magnetic field, no Zeeman splitting of the atomic hyperfine spin states occurs. Any time an atom traverses across a region in space in which the trapping magnetic field magnitude is suitably weak, it may lose alignment with the local magnetic field vector and can change from a low field seeking atom to a high field seeking atom. As only low field seeking atoms can be trapped, if an atom does make a transition to a high field seeking state it will subsequently be lost from the trap. There are now many different types of atom traps, such as QUIC² traps [23], TAAP³ traps [24], MOTs⁴ [25] and RF-dressed cold atom traps, partly as a response to overcome Majorana losses. Each of these has their advantages and disadvantages but for the purpose of this thesis RF-dressed cold atom traps are the central topic of investigation and will be discussed in greater detail later. First however, with a view to understanding further the importance of cold atom traps, we now discuss atom chips.

2.2 Atom chips

Atom chips have been in development since 1998 [4, 26]. Atom chips are not a new type of cold atom trap as different atom chips use different but existing theoretical models for describing the trap potentials. For example, there exist atom chips which trap atoms with static magnetic fields alone, use RF-dressed potentials or act as part of a MOT. Atom chips are instead defined by how the trapping magnetic fields are created. Atom chips generate magnetic fields by currents which flow in wires of micrometre width, mounted on a substrate that forms the chips surface [27].

The whole ensemble forms a chip in direct analogue to standard silicon computer chips. However, unlike in a computer chip, where information is carried by the presence of electrons flowing in the wires; here the information is contained within the atoms, that are trapped in the magnetic fields created by the flow of electrons in the wires. Atom chips can be produced by standard lithographic methods developed for computer chip technology [28]. They are also highly scalable and compact. These features make them favourable for applications which would allow cold atom traps to become an integral part of everyday practical devices.

²QUadrupole and Ioffe Configuration

³Time-Averaged Adiabatic Potential

⁴Magneto-Optical Traps

One of the most desired applications for atom chips is for small scale, on-chip atomic clocks [29, 30]. The weak interaction of atoms with the environment also makes them hopeful candidates for quantum information processing. Quantum gates, which perform logical operations on qubits, have been proposed and key requirements have been experimentally achieved [31, 32]. Atom chip trap geometries can be changed while atoms remain confined by changing the currents in the microwire conductors. This allows atoms to be transported and controlled dynamically while trapped. An ambitious use of this ability would be the realisation of quantum circuits, in which large networks of atom traps, waveguides and interferometers exist together on the surface of a single substrate. Taking inspiration from the similarities with electronics, the emerging field of atomtronics aims to enhance our information technology capabilities by making atom analogues of electrical circuits [33].

Currently cold atom traps is an active area of research producing experimental results which explore many quantum mechanical phenomena, particularly in the areas of degenerate quantum gases [34, 35] and condensed matter physics [36]. However, it is the future hope for cold atom traps, and in particular atom chips, which causes this research area to be so diverse and thriving.

2.3 RF-dressed cold atom traps

RF-dressed cold atom traps were suggested by Zobay and Garraway in 2001 [37] and their first experimental demonstration came in 2004 by the Paris 13 group led by Perrin [38]. Radio frequency (RF) dressed traps have two main components, a static magnetic field and a radio frequency oscillating magnetic field. These together form adiabatic⁵ potentials that act as a spin-dependent force on the atoms. RF fields are used as they are of an appropriate frequency to resonantly couple the Zeeman splitted levels of atomic hyperfine spin states. We shall see in chapter 3 that atoms are confined in a region of space around the location of resonant coupling between the hyperfine spin states and the RF magnetic field.

RF fields are used in all atom trap experiments for the technique of evaporative cooling which is necessary to cool the atoms to the low temperatures required for trapping. Evaporative cooling uses the RF field to couple the atomic states such that hot atoms leave the trap, with the remaining atoms respectively cooled [41]. Evaporative cooling is an important technique in its own right, especially in the process to achieve Bose-Einstein condensation. However, if the applied RF field

⁵The term adiabatic refers to the usage found in mechanics meaning a gradual change in external conditions [39], rather than the thermodynamics usage of a process with no change in heat [40].

is ramped sufficiently slowly to a desired magnitude an RF-dressed trap can be formed instead. In a semiclassical interpretation of an RF-dressed cold atom trap atoms follow adiabatic potentials, in which the atomic magnetic moment aligns with an apparent effective magnetic field. As this effective magnetic field is not a true magnetic field, it does not have to obey constraints imposed by Maxwell's equations. This allows RF-dressed cold atom traps to confine atoms within a very broad and diverse range of trapping potentials [42]. While not specific to them, RF-dressed cold atom traps can easily trap atoms in ring shaped potentials, which are of high interest for studying quantum mechanical systems with periodic boundary conditions [43, 44].

Additionally, RF-dressing allows trapping potentials to be changed easily by altering the magnitude or frequency of the RF field. The ability to move and manipulate atoms while trapped is of importance in experiments and potential applications for cold atom traps. RF-dressed traps in particular offer a high degree of control with relative ease for achieving this. It is for this reason, as well as the desire for on-chip interferometry, that RF-dressed cold atom traps are often found on atom chips. One of the main and early goals for cold atom traps was the desire for metrological standard atom interferometers [45, 46]. To form an atom interferometer it is necessary to split a trapped atom cloud into a minimum of two components, then recombine them to observe the resulting interference pattern. While there are several ways to achieve this with cold atom traps, the most promising is using RF-dressed atom traps, as these offer an easily achievable, phase-preserving and coherent splitting of the atom cloud [4]. Coherence of the splitting process is particularly important as it increases the precision of the atom interferometer. RF-dressed cold atom traps are therefore important to those working on the development of atom interferometry.

To create an RF-dressed trap on an atom chip usually two additional wires, with alternating current of radio frequency, are added to the chip either side of the main wire that creates the static magnetic trapping field [27]. Atom chip interferometers have been designed and implemented, making use of RF-dressing [45]. Such an interferometer could act as an important part of a 'phase gate', a device for quantum information processing [47]. As there are high hopes for the future importance of atom chips, understanding and exploiting RF-dressed cold atom traps is also of interest.

Whenever discussion of practical applications occurs, the robustness of the setup also has to be considered. While RF-dressed cold atom traps avoid Majorana losses by avoiding regions of low magnetic field value, they do suffer from a spin dependent loss mechanism. As the atoms are trapped by adiabatically following

the trap potentials formed by the effective magnetic field, this leads to a new loss mechanism specific to RF-dressed cold atom traps. If the atoms do not follow the effective potentials adiabatically, that is not sufficiently slowly, the atoms magnetic moment will no longer be orientated with the local magnetic field direction. This opens up the possibility for spin flip transitions, which can lead to losses of atoms from the trap as the trapping potential is dependent on the spin state of the atom. This loss mechanism is similar to Majorana losses, in that the atoms are lost by being in an inappropriate spin state. However, the key difference is that these non-adiabatic losses are not caused by regions of space in which the magnetic field vanishes but instead by atoms not keeping aligned with the local magnetic field direction. It is these non-adiabatic induced transitions that we will study in greater detail.

Knowing how RF-dressed cold atom traps are affected by non-adiabatic atomic losses can help to set limits on the suitable values for key variables such as the trap temperature or magnetic field gradient. The importance of RF-dressed traps is linked to the importance of atom chips. The desire of using RF-dressed atom chips to make reliable sensors or as a tool for quantum computing highlights why being able to model losses from the trap is important. We wish to see how far we can push the boundaries of the trap, to allow usage in a wide range of applications, while still retaining an appropriate trap lifetime; the length of time in which a significant number of the atoms remain trapped.

We will now proceed with a more rigorous mathematical treatment of the situation, with the aim of investigating the importance of non-adiabatic spin flips on RF-dressed cold atom traps.

Chapter 3

RF-dressed cold atom trap potentials

We will now derive the adiabatic potentials which lead to confinement of atoms in RF-dressed cold atom traps. We shall see the origin of coupling terms between the adiabatic potentials, which lead to the non-adiabatic losses from the trap. The derivation assumes a one dimensional¹ static magnetic field distribution, for a more general derivation of the trap Hamiltonian please refer to reference [42].

3.1 Hyperfine spin state basis

The Hamiltonian for a single non-relativistic atom with mass m_0 trapped in the z direction² is given by [18]

$$\hat{H} = \frac{\hat{p}_z^2}{2m_0} - \boldsymbol{\mu} \cdot \mathbf{B}. \quad (3.1)$$

The first term in the Hamiltonian is the atom's kinetic energy, where \hat{p}_z is the momentum operator in the z direction. The second term in the Hamiltonian describes how the atom responds to a magnetic field, due to the interaction between the atoms magnetic dipole moment $\boldsymbol{\mu}$ and a net magnetic field \mathbf{B} . The atomic magnetic dipole moment can more conveniently be written in terms of the atom's total angular momentum \mathbf{F} ³,

$$\hat{H} = \frac{\hat{p}_z^2}{2m_0} + g_F \frac{\mu_B}{\hbar} \mathbf{F} \cdot \mathbf{B}, \quad (3.2)$$

¹A one dimensional derivation is given to highlight the two key steps required in the process to obtain the dressed trap Hamiltonian. The one dimensional analysis presented in this thesis is suitable for anisotropic RF-dressed traps, like the one studied in chapter 8.

²The z direction in this derivation could be any one dimensional direction, however, later, after and including chapter 5, we will take the z direction to be the vertical direction to allow appropriate comparison with experiment in chapter 8.

³ \mathbf{F} is defined such that it has dimensions equivalent to those of \hbar .

with scaling factors \hbar, μ_B and g_F ; the reduced Planck constant, Bohr magneton and Landé g-factor for \mathbf{F} respectively. The total angular momentum of the atom is given by $\mathbf{F} = \mathbf{I} + \mathbf{L} + \mathbf{S}$, where \mathbf{I} is the nuclear spin operator and \mathbf{L}, \mathbf{S} are respectively the operators associated with the orbital angular momentum and spin of the electron cloud.

The presence of a magnetic field causes splitting of the atomic hyperfine energy levels, known as Zeeman splitting [39]. For the weak magnetic fields used in RF-dressed cold atom traps the Zeeman splitting is linear with respect to the magnetic field, as shown diagrammatically in figure 3.1.

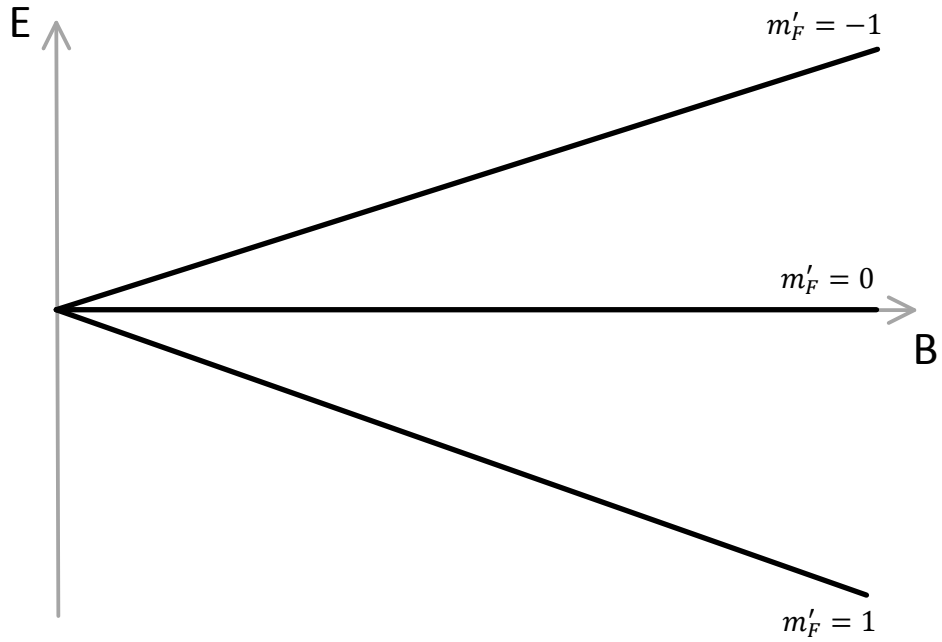


Figure 3.1: Zeeman splitting of hyperfine levels for a ^{87}Rb atom with $\mathbf{F} = 1$. m'_F is the hyperfine spin state, the projection of the total angular momentum in the z direction. For ^{87}Rb $F=1$, $g_F \approx -\frac{1}{2}$, such that $m'_F = -1$ is the low field seeking state and $m'_F = 1$ is the high field seeking state.

If a RF field is applied perpendicular to the static magnetic field this couples the hyperfine spin levels. In the absence of coupling an atom known to be in a particular hyperfine level at time t_0 , will be found in the same hyperfine level if measured at any later time. However, if the levels are coupled there will be a non-zero probability of finding the atom in a different hyperfine level, when a measurement is performed at a later time. We say that the coupling invokes transitions between hyperfine spin levels. Figure 3.2 aims to represent how the applied RF field couples the atoms. The coupling is strongest at the resonance location where the energy of

the applied RF field matches the Zeeman splitting of the energy levels.

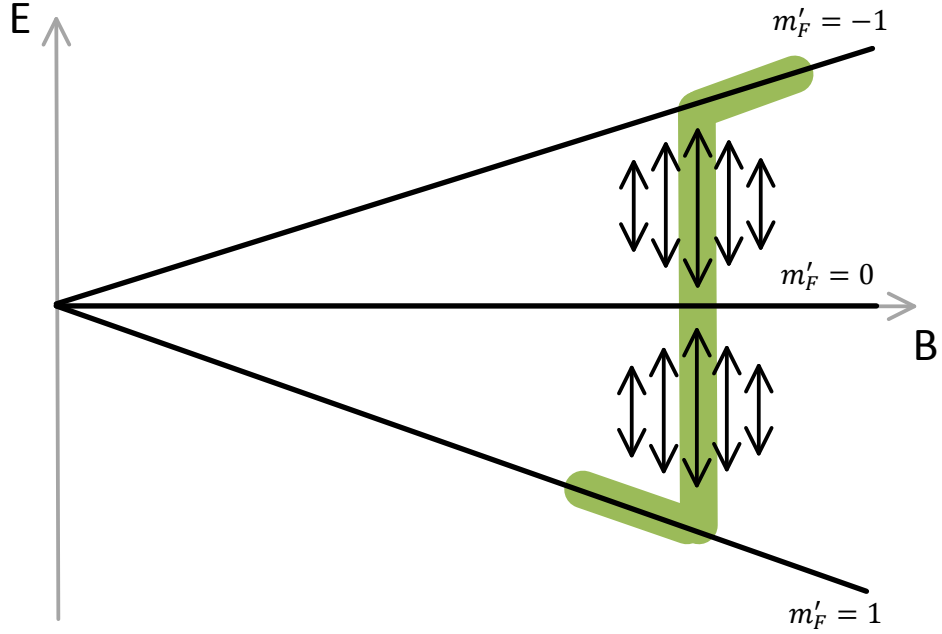


Figure 3.2: Zeeman splitting of hyperfine levels for a ^{87}Rb atom with $\mathbf{F} = 1$ in the presence of a perpendicular, oscillating RF frequency field. Arrows represent the possibility for transitions between the different hyperfine levels created by the presence of the RF magnetic field. The olive green path indicates the confinement of the atoms.

If a static magnetic field distribution is created with the strength of the magnetic field varying with position and a perpendicular RF frequency magnetic field is applied an RF-dressed cold atom trap is formed [37]. The applied RF field forces the atoms to make a transition between the different hyperfine spin levels so that the atoms are confined and forced to oscillate around the resonance location. A diagrammatic representation of their path is shown in olive green in figure 3.2.

To describe the trap a total magnetic field of the form

$$\mathbf{B} = \begin{pmatrix} B_{\text{rf}} \cos(\omega_{\text{rf}} t) \\ 0 \\ B_s(z) \end{pmatrix} \quad (3.3)$$

is considered, where $B_s(z)$ is the static position dependent magnetic field and $B_{\text{rf}} \cos(\omega_{\text{rf}} t)$ is the applied oscillating RF field. The RF field is assumed to have a large number of photons, such that any fluctuation in the number of RF photons is negligible, effectively taking a classical approximation of the RF field. B_{rf} is also

assumed to be position independent, which is reasonable for RF fields generated by macroscopic coils but is not suitable for atom chips. For a derivation appropriate for atom chips please see references [4, 42].

For the magnetic field configuration given in equation (3.3) the Hamiltonian becomes:

$$\hat{H} = \frac{\hat{p}_z^2}{2m_0} + g_F \frac{\mu_B}{\hbar} B_{\text{rf}} \cos(\omega_{\text{rf}} t) \hat{F}_x + g_F \frac{\mu_B}{\hbar} B(z) \hat{F}_z. \quad (3.4)$$

This Hamiltonian contains all the desired components to describe an RF-dressed cold atom trap. However, we shall continue our derivation until we are able to describe the trap in a more intuitive and useful form.

3.2 Rotating wave approximation

We will first transform to a new frame of reference and then take the rotating wave approximation to make our Hamiltonian time independent. We start by expressing our Hamiltonian as

$$\hat{H} = \frac{\hat{p}_z^2}{2m_0} + g_F \frac{\mu_B}{4\hbar} B_{\text{rf}} (e^{i\omega_{\text{rf}} t} + e^{-i\omega_{\text{rf}} t}) (\hat{F}_+ + \hat{F}_-) + g_F \frac{\mu_B}{\hbar} B(z) \hat{F}_z, \quad (3.5)$$

which is equivalent to equation (3.4), using the fact that

$$\cos(\omega_{\text{rf}} t) = \frac{e^{i\omega_{\text{rf}} t} + e^{-i\omega_{\text{rf}} t}}{2}. \quad (3.6)$$

Writing the RF oscillation in this way consists of decomposing it into two equal components, one rotating clockwise and one rotating anticlockwise, as illustrated in figure 3.3. The notation

$$\hat{F}_{\pm} = \hat{F}_x \pm i\hat{F}_y \quad (3.7)$$

is introduced for more aesthetically pleasing mathematics that will follow.

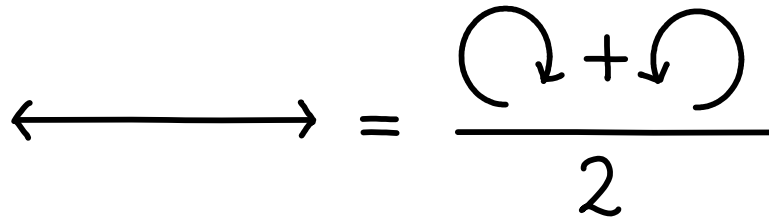


Figure 3.3: An interpretation of equation (3.6).

We now perform a unitary transformation,

$$\hat{U}_1 = e^{i \frac{g_F}{|g_F|} \frac{\omega_{\text{rf}}}{\hbar} t \hat{F}_z}, \quad (3.8)$$

to transfer us from the laboratory reference frame to a new frame of reference. It is beneficial to describe the interaction of the atom with the trapping magnetic fields from a new frame of reference, specified by equation (3.8), because with suitable approximations the dynamics of the system when observed from this new frame are stationary, which greatly simplifies the situation.

If viewed from the laboratory frame, the new frame appears to rotate around the z axis of the laboratory frame. The rotation frequency is chosen such that the frame rotates at the same rate as the oscillating RF magnetic field. The effect of the change in reference frame is shown schematically in figure 3.4. By transferring to a rotating frame of reference, the component of the magnetic field that rotates in the same direction as the transformation now appears stationary in the new reference frame (shown in purple in figure 3.4). In contrast, the component in the reverse direction now appears to be rotating twice as fast (shown in blue in figure 3.4).

We wish to express this change of reference frame mathematically. In the original reference frame the atom's time evolution is given by the Schrödinger equation:

$$i\hbar \frac{\partial \Psi}{\partial t} = \hat{H} \Psi. \quad (3.9)$$

In the new frame of reference the atom's wavefunction is given by,

$$\Psi_{\text{new}} = \hat{U} \Psi. \quad (3.10)$$

By applying our transformation operator \hat{U} to both sides of the Schrödinger equation (3.9) we see that [48]

$$i\hbar \hat{U} \frac{\partial \Psi}{\partial t} = \hat{U} \hat{H} \Psi. \quad (3.11)$$

To ensure that expectation values remain the same from any reference frame, transformations between reference frames must be described by a unitary operator satisfying $\hat{U} \hat{U}^\dagger = 1$. Therefore, we can equivalently express equation (3.11) as

$$i\hbar \hat{U} \frac{\partial \Psi}{\partial t} = \hat{U} \hat{H} \hat{U}^\dagger \hat{U} \Psi. \quad (3.12)$$

The chain rule of differential equations leads us to

$$i\hbar \left(\frac{\partial \hat{U} \Psi}{\partial t} - \frac{\partial \hat{U}}{\partial t} \Psi \right) = \hat{U} \hat{H} \hat{U}^\dagger \hat{U} \Psi \quad (3.13)$$

while rearranging and making use of $\hat{U} \hat{U}^\dagger = 1$ gives us

$$i\hbar \frac{\partial \hat{U} \Psi}{\partial t} = \hat{U} \hat{H} \hat{U}^\dagger \hat{U} \Psi + i\hbar \frac{\partial \hat{U}}{\partial t} \hat{U}^\dagger \hat{U} \Psi. \quad (3.14)$$

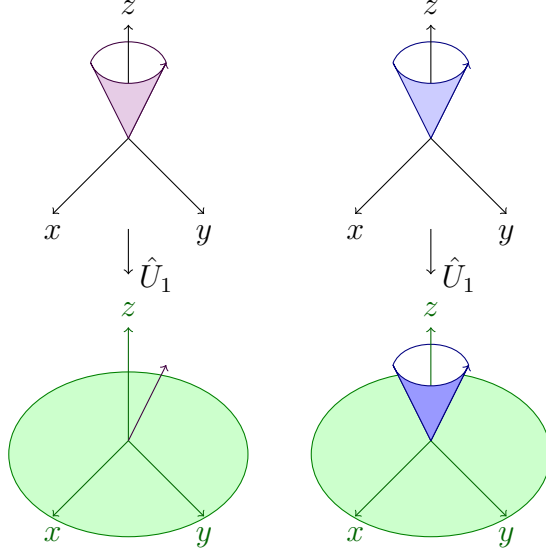


Figure 3.4: An interpretation of the effects of the unitary transform \hat{U}_1 . In the original frame of reference the total magnetic field vector for the two components rotates around the z axis, as represented by the coloured hollow cones. Different colours are used to signify that the two components are rotating in different directions as shown in figure 3.3. After the transformation to the new frame of reference has been made the co-ordinate axis can be considered to be rotating around the z axis, such that $x(t)$ and $y(t)$ sweep out the circular green path shown. The component which rotates in the same direction as the co-ordinate axis, shown by the purple spin vector, now appears stationary in the rotating frame. The other component which rotates in opposition to the co-ordinate axis, shown by the blue spin vector, now appears to rotate twice as fast.

We now have an expression for the time evolution in our new frame of reference,

$$i\hbar \frac{\partial \Psi_{\text{new}}}{\partial t} = \left(\hat{U} \hat{H} \hat{U}^\dagger + i\hbar \frac{\partial \hat{U}}{\partial t} \hat{U}^\dagger \right) \Psi_{\text{new}}. \quad (3.15)$$

As this must obey a Schrödinger equation of its own, we now have an expression to relate two Hamiltonians from different frames of reference [49]:

$$\hat{H}_{\text{new}} = \hat{U} \hat{H} \hat{U}^\dagger + i\hbar \frac{\partial \hat{U}}{\partial t} \hat{U}^\dagger. \quad (3.16)$$

The Hamiltonian of the trap in the new rotating frame of reference can be

obtained by combining equations (3.16), (3.8) and (3.5);

$$\begin{aligned}\hat{H} = & \frac{(\hat{U}_1 \hat{p}_z \hat{U}_1^\dagger)^2}{2m_0} + g_F \frac{\mu_B}{4\hbar} B_{\text{rf}} (e^{i\omega_{\text{rf}} t} + e^{-i\omega_{\text{rf}} t}) (\hat{U}_1 \hat{F}_+ \hat{U}_1^\dagger + \hat{U}_1 \hat{F}_- \hat{U}_1^\dagger) \\ & + g_F \frac{\mu_B}{\hbar} B(z) \hat{U}_1 \hat{F}_z \hat{U}_1^\dagger + i\hbar \frac{\partial \hat{U}_1}{\partial t} \hat{U}_1^\dagger.\end{aligned}\quad (3.17)$$

Differentiation of \hat{U}_1 gives the expression

$$\begin{aligned}\hat{H} = & \frac{(\hat{U}_1 \hat{p}_z \hat{U}_1^\dagger)^2}{2m_0} + g_F \frac{\mu_B}{4\hbar} B_{\text{rf}} (e^{i\omega_{\text{rf}} t} + e^{-i\omega_{\text{rf}} t}) (\hat{U}_1 \hat{F}_+ \hat{U}_1^\dagger + \hat{U}_1 \hat{F}_- \hat{U}_1^\dagger) \\ & + g_F \frac{\mu_B}{\hbar} B(z) \hat{U}_1 \hat{F}_z \hat{U}_1^\dagger - \frac{g_F}{|g_F|} \omega_{\text{rf}} \hat{F}_z.\end{aligned}\quad (3.18)$$

This spin dependent shift can be seen diagrammatically in figure 3.5, causing a crossing of the hyperfine spin levels at the resonance location.

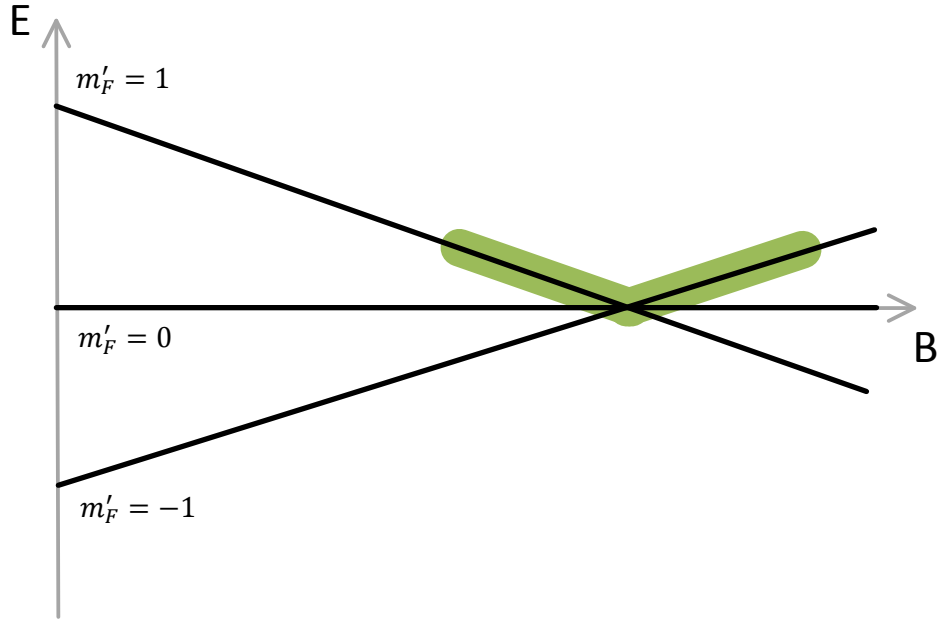


Figure 3.5: Zeeman splitting of hyperfine levels for a ^{87}Rb atom with $\mathbf{F} = 1$ shifted by a value $+m_F \hbar \omega_{\text{rf}}$. The olive green path indicates the confinement of the atoms.

As the rotation occurs about the z axis,

$$\hat{U}_1 \hat{p}_z \hat{U}_1^\dagger = \hat{p}_z \quad (3.19)$$

and

$$\hat{U}_1 \hat{F}_z \hat{U}_1^\dagger = \hat{F}_z, \quad (3.20)$$

this arises mathematically as \hat{p}_z and \hat{F}_z commute with the operator \hat{U}_1 . It makes sense intuitively as the z axis is equivalent in the two frames of reference such that quantities projected onto the z axis are unchanged switching between the two frames.

However,

$$\begin{aligned}\hat{U}_1 \hat{F}_+ \hat{U}_1^\dagger &= e^{i \frac{g_F}{|g_F|} \frac{\omega_{\text{rf}}}{\hbar} t \hat{F}_z} \hat{F}_+ e^{-i \frac{g_F}{|g_F|} \frac{\omega_{\text{rf}}}{\hbar} t \hat{F}_z} \\ &= \hat{F}_+ + i \frac{g_F}{|g_F|} \omega_{\text{rf}} t \hat{F}_+ + \frac{1}{2} \left(\frac{i \frac{g_F}{|g_F|} \omega_{\text{rf}} t}{\hbar} \right)^2 \hbar [\hat{F}_z, \hat{F}_+] + \dots \\ &= \hat{F}_+ e^{i \frac{g_F}{|g_F|} \omega_{\text{rf}} t}\end{aligned}\quad (3.21)$$

where we have used the expansion technique of

$$e^{\phi \hat{A}} \hat{B} e^{-\phi \hat{A}} = \hat{B} + \phi [\hat{A}, \hat{B}] + \frac{\phi^2}{2!} [\hat{A}, [\hat{A}, \hat{B}]] + \frac{\phi^3}{3!} [\hat{A}, [\hat{A}, [\hat{A}, \hat{B}]]] + \dots \quad (3.22)$$

[49] and the relation $[\hat{F}_z, \hat{F}_\pm] = [\hat{F}_z, \hat{F}_x] \pm i[\hat{F}_z, \hat{F}_y] = \pm \hbar \hat{F}_\pm$ [50]. Therefore,

$$\hat{U}_1 \hat{F}_- \hat{U}_1^\dagger = \left(\hat{U}_1 \hat{F}_+ \hat{U}_1^\dagger \right)^\dagger = \left(\hat{F}_+ e^{i \frac{g_F}{|g_F|} \omega_{\text{rf}} t} \right)^\dagger = \hat{F}_- e^{-i \frac{g_F}{|g_F|} \omega_{\text{rf}} t} \quad (3.23)$$

using the properties of complex conjugation.

The Hamiltonian for the atom trap, in the transformed frame of reference, is thus given by:

$$\begin{aligned}\hat{H} &= \frac{\hat{p}_z^2}{2m_0} + \left(g_F \frac{\mu_B}{\hbar} B(z) - \frac{g_F}{|g_F|} \omega_{\text{rf}} \right) \hat{F}_z \\ &\quad + g_F \frac{\mu_B}{4\hbar} B_{\text{rf}} (e^{i\omega_{\text{rf}} t} + e^{-i\omega_{\text{rf}} t}) \left(e^{i \frac{g_F}{|g_F|} \omega_{\text{rf}} t} \hat{F}_+ + e^{-i \frac{g_F}{|g_F|} \omega_{\text{rf}} t} \hat{F}_- \right).\end{aligned}\quad (3.24)$$

A change of notation now helps to simplify this expression. The Rabi frequency is used as a measure of the strength of the coupling between the RF field and the atom and is given by

$$\Omega = \left| g_F \frac{\mu_B}{2\hbar} B_{\text{rf}} \right|. \quad (3.25)$$

The notation:

$$\delta(z) = \left| g_F \frac{\mu_B}{\hbar} B(z) \right| - \omega_{\text{rf}} \quad (3.26)$$

shall be referred to as the ‘detuning’ [38]. The detuning is the frequency difference between the Zeeman splitted energy levels caused by the static magnetic field and the RF field frequency of oscillation. The detuning is zero at the resonance location.

In our new notation:

$$\hat{H} = \frac{\hat{p}_z^2}{2m_0} + \frac{g_F}{|g_F|} \delta(z) \hat{F}_z + \frac{g_F}{|g_F|} \Omega \hat{F}_x + \frac{\Omega}{2} \left(e^{2i \frac{g_F}{|g_F|} \omega_{\text{rf}} t} \hat{F}_+ + e^{-2i \frac{g_F}{|g_F|} \omega_{\text{rf}} t} \hat{F}_- \right). \quad (3.27)$$

We now apply the rotating wave approximation,

$$\hat{H} \approx \frac{\hat{p}_z^2}{2m_0} + \frac{g_F}{|g_F|} \delta(z) \hat{F}_z + \frac{g_F}{|g_F|} \Omega \hat{F}_x, \quad (3.28)$$

by neglecting the last two terms in equation (3.27). This is equivalent to retaining only the components of the RF field that rotate with the new frame of reference, while disregarding the components of the RF field that, in the laboratory frame, were rotating in the opposite direction. In the new frame of reference, these neglected terms are those that oscillate at twice the RF frequency shown in blue in figure 3.4. The argument for neglecting the counter rotating components is that they are off-resonant and as such have a negligible effect on the dynamics of the atom [51, 4]. The advantage of taking the rotating wave approximation is that our Hamiltonian becomes time independent.

3.3 Dressing with the RF field

We are now going to perform another change of reference frame, in an attempt to diagonalise our Hamiltonian, a technique referred to as ‘dressing’ [49]. We now align the resultant magnetic field vector with the z axis, as illustrated in figure 3.6. For our case dressing succeeds in diagonalising the Hamiltonian for regimes in which non-adiabatic effects are negligible. The dressing is achieved by a time independent change of reference frame, tilting the frame of reference about the y axis by an angle θ given by the unitary transformation

$$\hat{U}_2 = e^{i\frac{\theta(z)}{\hbar}\hat{F}_y}, \quad (3.29)$$

where the angle

$$\theta = \arctan \left[\frac{\Omega}{\delta(z)} \right]. \quad (3.30)$$

We reapply equation (3.16) so that the new Hamiltonian in the tilted reference frame is given by:

$$\hat{H} = \frac{\hat{U}_2 \hat{p}_z^2 \hat{U}_2^\dagger}{2m_0} + \frac{g_F}{|g_F|} \Omega \hat{U}_2 \hat{F}_x \hat{U}_2^\dagger + \frac{g_F}{|g_F|} \delta(z) \hat{U}_2 \hat{F}_z \hat{U}_2^\dagger. \quad (3.31)$$

Note that as the unitary transformation is time independent $\frac{\partial \hat{U}_2}{\partial t} = 0$. We shall make use of the commutation relation $[\hat{F}_x, \hat{F}_y] = i\hbar \hat{F}_z$ and its two other cyclic equivalents [50] to show that for the spin components

$$\begin{aligned} \hat{U}_2 \hat{F}_z \hat{U}_2^\dagger &= e^{i\frac{\theta}{\hbar}\hat{F}_y} \hat{F}_z e^{-i\frac{\theta}{\hbar}\hat{F}_y} \\ &= \hat{F}_z - \theta \hat{F}_x + \frac{1}{2} \left(\frac{i\theta}{\hbar} \right)^2 (i\hbar) [\hat{F}_y, \hat{F}_x] + \dots \\ &= \hat{F}_z \left(1 - \frac{\theta^2}{2} + \frac{\theta^4}{4!} + \dots \right) - \hat{F}_x \left(\theta - \frac{\theta^3}{3!} + \frac{\theta^5}{5!} + \dots \right) \\ &= \cos \theta \hat{F}_z - \sin \theta \hat{F}_x \end{aligned} \quad (3.32)$$

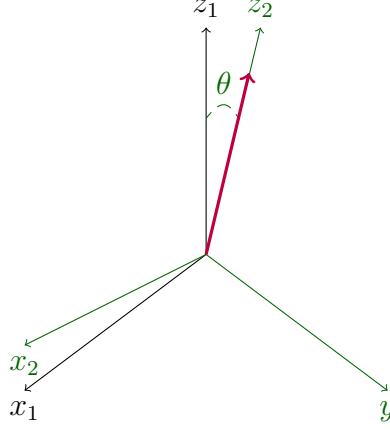


Figure 3.6: An interpretation of the unitary transformation \hat{U}_2 . The co-ordinate system experiences a rotation about the y axis of magnitude θ to align the z axis with the magnetic field orientation represented by the magenta arrow.

and

$$\begin{aligned}
 \hat{U}_2 \hat{F}_x \hat{U}_2^\dagger &= e^{i\frac{\theta}{\hbar} \hat{F}_y} \hat{F}_x e^{-i\frac{\theta}{\hbar} \hat{F}_y} \\
 &= \hat{F}_x + \theta \hat{F}_z + \frac{1}{2} \left(\frac{i\theta}{\hbar} \right)^2 (-i\hbar) [\hat{F}_y, \hat{F}_z] + \dots \\
 &= \hat{F}_x \left(1 - \frac{\theta^2}{2} + \frac{\theta^4}{4!} + \dots \right) + \hat{F}_z \left(\theta - \frac{\theta^3}{3!} + \frac{\theta^5}{5!} + \dots \right) \\
 &= \cos \theta \hat{F}_x + \sin \theta \hat{F}_z.
 \end{aligned} \tag{3.33}$$

Because of the definition of θ given in equation (3.30) the x component in the new frame of reference cancels as $\Omega \cos \theta - \delta \sin \theta = 0$, while for the z component $\delta \cos \theta + \Omega \sin \theta = \sqrt{\Omega^2 + \delta^2}$.

The position dependence of the angle θ prevents the unitary transformation \hat{U}_2 from commuting with the momentum operator and instead

$$\begin{aligned}
 \hat{U}_2 \hat{p}_z \hat{U}_2^\dagger &= e^{i\frac{\theta}{\hbar} \hat{F}_y} \hat{p}_z e^{-i\frac{\theta}{\hbar} \hat{F}_y} \\
 &= \hat{p}_z + \frac{i\hat{F}_y}{\hbar} [\theta, \hat{p}_z] + \dots \\
 &= \hat{p}_z - \frac{\partial \theta}{\partial z} \hat{F}_y,
 \end{aligned} \tag{3.34}$$

which gives,

$$\begin{aligned}
 \hat{U}_2 \hat{p}_z^2 \hat{U}_2^\dagger &= \hat{U}_2 \hat{p}_z \hat{U}_2^\dagger \hat{U}_2 \hat{p}_z \hat{U}_2^\dagger \\
 &= \left(\hat{p}_z - \frac{\partial \theta}{\partial z} \hat{F}_y \right) \left(\hat{p}_z - \frac{\partial \theta}{\partial z} \hat{F}_y \right) \\
 &= \hat{p}_z^2 + i\hbar \frac{\partial^2 \theta}{\partial z^2} \hat{F}_y - 2 \frac{\partial \theta}{\partial z} \hat{F}_y \hat{p}_z + \left(\frac{\partial \theta}{\partial z} \right)^2 \hat{F}_y^2.
 \end{aligned} \tag{3.35}$$

Trap Hamiltonian

The Hamiltonian for a single atom, already loaded into an RF-dressed cold atom trap, can therefore be expressed by

$$\hat{H} = \frac{\hat{p}_z^2}{2m_0} + \hat{V}_A \hat{F}_y + \hat{V}_B \hat{F}_y^2 + \frac{g_F}{|g_F|} \sqrt{\Omega^2 + \delta(z)^2} \hat{F}_z \quad (3.36)$$

where

$$\hat{V}_A = \frac{1}{2m_0} \left(i\hbar \frac{\partial^2 \theta}{\partial z^2} - 2 \frac{\partial \theta}{\partial z} \hat{p}_z \right) \quad (3.37)$$

and

$$\hat{V}_B = \frac{1}{2m_0} \left(\frac{\partial \theta}{\partial z} \right)^2. \quad (3.38)$$

As the components \hat{V}_A and \hat{V}_B are usually small, it is this Hamiltonian which we describe as the dressed trap Hamiltonian. When we talk of the atom being dressed by the RF photons, we mean that we examine the interaction of the atom and the RF frequency photons from a reference frame in which the Hamiltonian is diagonal and time independent. Here this is the case in a limit known as the adiabatic approximation. Our dressed Hamiltonian provides a very useful description for modelling the behaviour of an atom in an RF-dressed cold atom trap, as we shall see in the next section.

The Hamiltonian we have derived, given by equation (3.36), is already known within the scientific community expressed usually in the form [42, 21]:

$$\hat{H} = \frac{(\hat{\mathbf{p}} + \hat{\mathbf{A}})^2}{2m_0} + \sqrt{\Omega^2 + \delta(z)^2} \hat{F}_z. \quad (3.39)$$

$\hat{\mathbf{A}}(\mathbf{r}, t)$ is a gauge potential which emerges from the change in co-ordinate system [4] and relates to equation (3.36) through,

$$\hat{V}_A \hat{F}_y = \frac{\hat{p}_z \cdot \hat{A} + \hat{A} \cdot \hat{p}_z}{2m_0} \quad (3.40)$$

and

$$\hat{V}_B \hat{F}_y^2 = \frac{\hat{A}^2}{2m_0} \quad (3.41)$$

such that,

$$\hat{A}(\mathbf{r}, t) = -\frac{\partial \theta}{\partial z} \hat{F}_y \mathbf{e}_z. \quad (3.42)$$

The gauge potential term is often neglected to consider the Hamiltonian in the adiabatic approximation. Instead we will consider the full non-adiabatic Hamiltonian to model the losses from an RF-dressed trap caused by transitions between dressed spin states.

3.4 Examining the dressed trap Hamiltonian

The Hamiltonian given by equation (3.36) is our expression for the time evolution of an atom trapped in the z direction of an RF-dressed cold atom trap. We now examine this Hamiltonian to find out what it can tell us about the behaviour of the atom. For studying non-adiabatic losses we are particularly interested in spin flips, which constitute a change in the dressed spin state value. We begin by defining the following notation:

$$\Psi_i = |F, m_i\rangle \cdot \Psi_n^{(i)}(z) \quad (3.43)$$

for the wavefunction of an atom with initial dressed spin state $m_F = m_i$ and

$$\Psi_f = |F, m_f\rangle \cdot \Psi_{n_f}^{(f)}(z) \quad (3.44)$$

for the wavefunction of the final dressed spin state $m_F = m_f$ of the atom. Writing the atomic wavefunction in this way is equivalent to splitting the atom's wavefunction into separate spin dependent and position dependent components. F is the value of the total atomic angular momentum. m_F is the value obtained from the projection of \mathbf{F} onto the z direction in the dressed spin state basis which has to be an integer in the interval $[-F, F]$. n is the quantum number associated with the energy of the atom initially, while n_f is the quantum number associated with the energy of the atom after the spin flip has taken place.

The matrix elements for the spin components of our Hamiltonian (3.36) are:

$$\langle m_i, F | \hat{F}_z | F, m_f \rangle = \hbar \delta_{m_f}^{m_i}, \quad (3.45)$$

$$\begin{aligned} \langle m_i, F | \hat{F}_y | F, m_f \rangle &= \frac{\hbar}{2i} \left[\sqrt{(F + m_f + 1)(F - m_f)} \delta_{m_f+1}^{m_i} \right. \\ &\quad \left. - \sqrt{(F - m_f + 1)(F + m_f)} \delta_{m_f-1}^{m_i} \right] \end{aligned} \quad (3.46)$$

and

$$\begin{aligned} \langle m_i, F | \hat{F}_y^2 | F, m_f \rangle &= -\frac{\hbar^2}{4} \left\{ \sqrt{(F + m_f + 1)(F - m_f)} \right. \\ &\quad \sqrt{(F + m_f + 2)(F - m_f - 1)} \delta_{m_f+2}^{m_i} \\ &\quad - 2[F(F + 1) - m_f^2] \delta_{m_f}^{m_i} + \sqrt{(F - m_f + 1)(F + m_f)} \\ &\quad \left. \sqrt{(F - m_f + 2)(F + m_f - 1)} \delta_{m_f-2}^{m_i} \right\}. \end{aligned} \quad (3.47)$$

Our RF-dressed trap Hamiltonian, given by equation (3.36), therefore has four distinct components:

$$\hat{H} = \frac{\hat{p}_z^2}{2m_0} + V(z) + V_A + V_B \quad (3.48)$$

- Kinetic energy term given by $\frac{\hat{p}_z^2}{2m_0}$.
- Trap potentials given by $V(z)$.
- V_A a coupling between dressed spin states with $|\Delta m_F| = 1$.
- V_B a coupling between dressed spin states with $|\Delta m_F| = 2$.

Adiabatic potentials

The adiabatic potentials are given by terms in our Hamiltonian (3.36) that do not correspond to a change in the hyperfine spin state ($|\Delta m_F| = 0$). Therefore, the adiabatic potentials are given by the expression

$$V(z) = \hbar m_F \sqrt{\Omega^2 + \delta(z)^2} + \mathcal{H}(m_F) \left(\frac{\partial \theta}{\partial z} \right)^2. \quad (3.49)$$

Note that we have absorbed the term $\frac{g_F}{|g_F|}$ into m_F and we define dressed spin states which correspond to trapping potentials to have positive m_F values. We also introduce the notation:

$$\mathcal{H}(m_F) = \frac{\hbar^2 [F(F+1) - m_F^2]}{4m_0}, \quad (3.50)$$

which characterizes the scale of the contribution from $\hat{V}_B \hat{F}_y^2$ to the adiabatic potentials for a particular atomic species. The term that multiplies equation (3.50) in equation (3.49) adds a small positive contribution to all adiabatic potentials, regardless of dressed spin state, in the vicinity of the resonance location. For this reason we refer to it as the ‘hump’. In the scientific literature the hump is usually neglected from expressions for the adiabatic potentials, as it only arises when the non-adiabaticity is taken into account. Fortunately in limits associated with low rates of non-adiabatic decay, desirable for RF-dressed cold atom traps, the hump is negligible so that it can reasonably be ignored. We shall see this in subsequent chapters of this thesis.

Figure 3.7 shows the adiabatic potentials in the dressed atomic state basis. The dressed spin state levels are superpositions of the Zeeman splitted hyperfine levels. The fact that there is no longer any degeneracy in the energy at the resonance location, in the dressed state representation, is known as an ‘avoided crossing’, displayed in figure 3.7. In the absence of any non-adiabatic couplings between dressed spin states, an atom trapped in a positive m_F level should remain trapped indefinitely oscillating around the resonance position. These potentials are known as adiabatic potentials as they are the potentials seen by an atom that moves adiabatically, in other words, sufficiently slowly. By comparing figures 3.2 and 3.7 it can be seen how

the adiabatic potentials provide a much more intuitive and useful description of the atom trap. Rather than talking of atoms oscillating between the Zeeman m_F' spin states, we say the atoms are trapped by adiabatically following the energy levels associated with positive dressed m_F spin states.

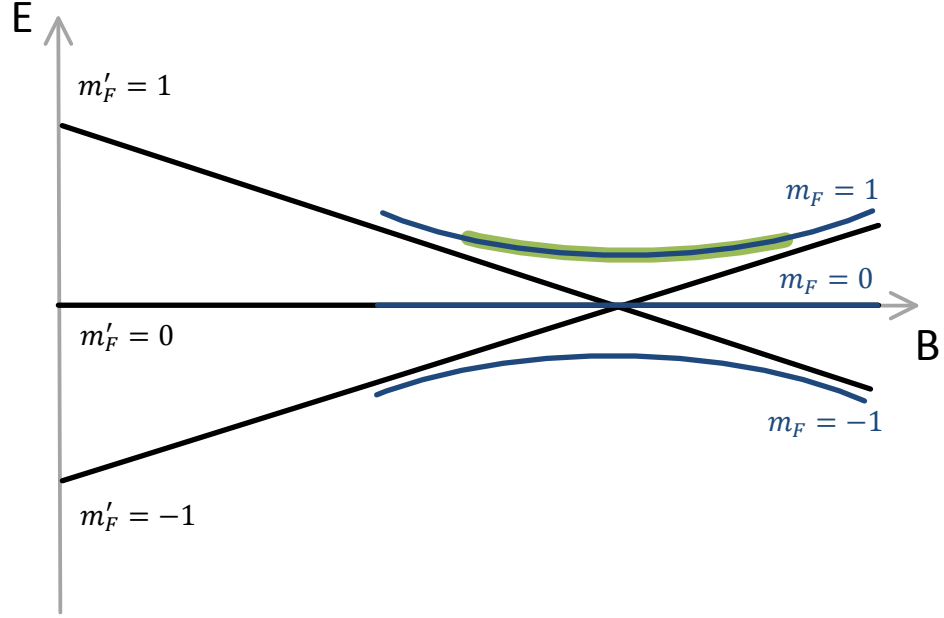


Figure 3.7: Adiabatic potentials for a ^{87}Rb atom with $\mathbf{F} = 1$ shown in dark blue in contrast to the hyperfine levels shown in black. The olive green path indicates the confinement of the atoms.

Non-adiabatic coupling terms

If the atoms move too fast, non-adiabatically, the terms V_A and V_B found in the trap Hamiltonian are no longer negligible. The terms V_A and V_B act as couplings between the different adiabatic potentials. This can lead to non-adiabatic losses from the trap if atoms make a transition to non-trapping dressed spin states. V_A gives the coupling between states with $|\Delta m_F| = 1$,

$$V_A = \frac{\hbar^2}{4m_0} \left(\frac{\partial^2 \theta}{\partial z^2} + 2 \frac{\partial \theta}{\partial z} \frac{\partial}{\partial z} \right) \left[\sqrt{(F + m_f + 1)(F - m_f)} \delta_{m_f+1}^{m_i} - \sqrt{(F - m_f + 1)(F + m_f)} \delta_{m_f-1}^{m_i} \right]. \quad (3.51)$$

While V_B gives the coupling between states with $|\Delta m_F| = 2$,

$$V_B = -\frac{\hbar^2}{8m_0} \left(\frac{\partial \theta}{\partial z} \right)^2 \left[\sqrt{(F + m_f + 1)(F - m_f)} \sqrt{(F + m_f + 2)(F - m_f - 1)} \delta_{m_f+2}^{m_i} + \sqrt{(F - m_f + 1)(F + m_f)} \sqrt{(F - m_f + 2)(F + m_f - 1)} \delta_{m_f-2}^{m_i} \right]. \quad (3.52)$$

It is the effect of these coupling terms which we shall study in this thesis, using Fermi's Golden Rule to find the rate of transitions induced by the non-adiabatic coupling in chapter 5.

It is more useful to express the non-adiabatic terms using the Rabi frequency and the detuning than it is the rotation parameter θ . Using equation (3.30) and a relation from reference [52] we can see that,

$$\theta = \frac{1}{2i} \ln \left| \frac{\delta(z) + i\Omega}{\delta(z) - i\Omega} \right|. \quad (3.53)$$

Differentiation of equation (3.53) gives

$$\frac{\partial \theta}{\partial z} = \frac{-\delta' \Omega}{\Omega^2 + \delta^2} \quad (3.54)$$

and

$$\frac{\partial^2 \theta}{\partial z^2} = \frac{2\delta\delta'^2\Omega}{(\Omega^2 + \delta^2)^2} - \frac{\delta''\Omega}{\Omega^2 + \delta^2}, \quad (3.55)$$

where a prime indicates differentiation by z i.e. $\delta' = \frac{\partial \delta}{\partial z}$.

We can therefore express the potential of the trap in terms of the Rabi frequency and detuning,

$$V(z) = \hbar m_F \sqrt{\Omega^2 + \delta^2} + \mathcal{H}(m_F) \frac{\Omega^2 \delta'^2}{(\Omega^2 + \delta^2)^2} \quad (3.56)$$

and the coupling terms as

$$\hat{V}_A = \frac{i\hbar}{2m_0} \left[\frac{2\delta\delta'^2\Omega}{(\Omega^2 + \delta^2)^2} - \frac{\delta''\Omega}{\Omega^2 + \delta^2} - \frac{2\delta'\Omega}{\Omega^2 + \delta^2} \frac{\partial}{\partial z} \right] \quad (3.57)$$

and

$$\hat{V}_B = \frac{1}{2m_0} \frac{\delta'^2 \Omega^2}{(\Omega^2 + \delta^2)^2}. \quad (3.58)$$

We shall make use of these expressions in the results and analysis section. However, we shall now continue with presentation of the relevant background theory by discussing Fermi's Golden Rule.

Chapter 4

Fermi's Golden Rule

Perturbation theory is a standard and highly useful technique for obtaining wavefunctions for Hamiltonian's which are challenging to solve (\hat{H}) but which do not vary significantly from a Hamiltonian with known eigenstates (\hat{H}_0). This is the case for our Hamiltonian, given by equation (3.36), which describes an atom initially confined in an RF-dressed trap in the dressed spin state basis. In this chapter we will use perturbation theory to derive Fermi's Golden Rule, before discussing how Fermi's Golden Rule can be used to determine the rate of transitions between dressed spin states.

4.1 Fermi's Golden Rule derivation

Fermi's Golden Rule is derived from first order, time dependent perturbation theory. It provides an expression for the transition rate between a single isolated energy level and a continuum.

A derivation of Fermi's Golden Rule can be found in many textbooks on quantum mechanics. We work through it briefly here drawing attention to the assumptions made in its derivation, which determine the suitability of its usage. This derivation is a combination of the derivations given in references [53, 54, 55] and [48].

Let us split the Hamiltonian for our system (\hat{H}) up into two components,

$$\hat{H} = \hat{H}_0 + \hat{V}, \quad (4.1)$$

an unperturbed Hamiltonian given here by \hat{H}_0 and a perturbing Hamiltonian given here by \hat{V} . For the moment this splitting is completely general. However, we shall later see that for Fermi's Golden Rule to be applicable, the perturbing Hamiltonian \hat{V} is required to have a less significant effect on the dynamics of the system in

comparison to the effect of the unperturbed Hamiltonian \hat{H}_0 . For our purposes of studying losses from the trap we assign specific meaning to the two distinct components. \hat{H}_0 is selected such that this component describes the evolution of an atom in a given dressed spin state and \hat{V} is chosen such that it describes the non-adiabatic couplings between different m_F states.

Knowledge of the eigenstates for the unperturbed Hamiltonian is assumed, such that

$$\hat{H}_0|\psi_n\rangle = E_n|\psi_n\rangle \quad (4.2)$$

with E_n , the energy of the n th state, and $|\psi_n\rangle$, the wavefunction of the n th state, being known quantities. In our model this requires knowledge of the energy and wavefunction associated with each of the $2F + 1$ adiabatic potentials (as there are $2F+1$ different m_F states). It is also assumed that the system is initially prepared in the eigenstate which corresponds to a single isolated energy level, represented by $|\psi_i\rangle$. For our model we select out the particular eigenstate that corresponds to an initially trapped atom.

The presence of the term \hat{V} in the total Hamiltonian \hat{H} means that $|\psi_n\rangle$ is not an eigenstate of the total Hamiltonian and therefore the system will have a non-trivial time evolution. We are no longer aware of the state of the system at any given moment. The new state of the system $|\Psi\rangle$ is a superposition of the unperturbed states,

$$|\Psi(t)\rangle = \sum_n a_n(t) e^{-\frac{iE_n t}{\hbar}} |\psi_n\rangle. \quad (4.3)$$

Here a_n are (currently unknown) co-efficients that weight the probability of the different available states of the system at any given time t . If we measure in the unperturbed basis by projecting on the state $\langle\psi_m|$ we now have a non-zero probability that the state will not be found in the state $|\psi_i\rangle$. If instead at the time of measurement we find the system to be in state $|\psi_f\rangle$ belonging to the continuum, we say that there has been a transition to the continuum. For our RF-dressed atom trap the \hat{H}_0 Hamiltonian has a mixture of trapped and untrapped atom eigenstates, determined by the value of the dressed spin state of the atom (m_F). Including \hat{V} thus allows the possibility for transitions from a trapped eigenstate to an untrapped eigenstate, which ultimately leads to losses of atoms from the trap.

The probability that an atom, initially in state $|\psi_i\rangle$ at $t = 0$ s, is found in a state belonging to the continuum at time t is given by

$$P_{i \rightarrow C}(t) = \sum_f |\langle\psi_f|\psi_i\rangle|^2 = \sum_f |a_f|^2, \quad (4.4)$$

where the summation is performed over all possible continuum states. We therefore wish to determine the co-efficients a_f .

The Schrödinger equation for the total Hamiltonian is

$$i\hbar \frac{\partial |\Psi\rangle}{\partial t} = \hat{H}_0 |\Psi\rangle + \hat{V} |\Psi\rangle. \quad (4.5)$$

Substitution of equation (4.3) into the Schrödinger equation gives,

$$\begin{aligned} & i\hbar \sum_n \dot{a}_n(t) e^{-\frac{iE_n t}{\hbar}} |\psi_n\rangle + \sum_n a_n(t) E_n e^{-\frac{iE_n t}{\hbar}} |\psi_n\rangle \\ &= \sum_n a_n(t) e^{-\frac{iE_n t}{\hbar}} \hat{H}_0 |\psi_n\rangle + \sum_n a_n(t) e^{-\frac{iE_n t}{\hbar}} \hat{V} |\psi_n\rangle. \end{aligned} \quad (4.6)$$

The notation \dot{a}_n represents a first order derivative in time $\frac{\partial a_n}{\partial t}$. It can be seen by use of equation (4.2) that the effect of the unperturbed Hamiltonian cancels, so the dynamics of the system are given by

$$i\hbar \sum_n \dot{a}_n(t) e^{-\frac{iE_n t}{\hbar}} |\psi_n\rangle = \sum_n a_n(t) e^{-\frac{iE_n t}{\hbar}} \hat{V} |\psi_n\rangle. \quad (4.7)$$

Now a measurement is performed to ascertain the state of the system at time t_m in the basis of the unperturbed Hamiltonian,

$$i\hbar \sum_n \dot{a}_n(t) e^{-\frac{iE_n t}{\hbar}} \langle \psi_m | \psi_n \rangle = \sum_n a_n(t) e^{-\frac{iE_n t}{\hbar}} \langle \psi_m | \hat{V} | \psi_n \rangle. \quad (4.8)$$

Simplification is possible using the orthogonality of the eigenstates of the unperturbed Hamiltonian,

$$\dot{a}_m(t) = -\frac{i}{\hbar} \sum_n a_n(t) e^{i\omega_{mn}t} V_{mn}(t), \quad (4.9)$$

this is a coupled set of differential equations where ω_{mn} is the Bohr frequency $\omega_{mn} = (E_m - E_n)/\hbar$ and where the interaction matrix element is given by

$$V_{mn}(t) = \langle \psi_m | \hat{V} | \psi_n \rangle. \quad (4.10)$$

Integration then gives

$$a_m(t_m) = \frac{1}{i\hbar} \int_0^{t_m} \sum_n a_n(t) e^{i\omega_{mn}t} V_{mn}(t) dt \quad (4.11)$$

which can be substituted into equation (4.4) to lead to the expression

$$P_{i \rightarrow c}(t_m) = \frac{1}{\hbar^2} \sum_f \left| \int_0^{t_m} \sum_n a_n(t) e^{i\omega_{fn}t} V_{fn}(t) dt \right|^2. \quad (4.12)$$

To solve equation (4.12) and gain the transition probability from the initial state to the continuum we resort to first order perturbation theory. \hat{V} is multiplied by a constant $0 \leq \lambda_s \leq 1$ and we expand the co-efficients in terms of λ_s , so that

$$a_n(t) = \sum_{k=0}^{\infty} \lambda_s^k a_{n,k}(t). \quad (4.13)$$

By substituting equation (4.13) into equation (4.9) we can obtain the perturbative expansion given by

$$\sum_{k=0}^{\infty} \lambda_s^k \dot{a}_{m,k}(t) = -\frac{i}{\hbar} \sum_n \sum_{k=0}^{\infty} \lambda_s^{k+1} a_{n,k}(t) e^{i\omega_{mn}t} V_{mn}(t). \quad (4.14)$$

To zeroth order in λ_s , we find $\dot{a}_{n,0}(t) = 0$. This can be expressed as $a_{m,0} = \delta_{mi}$. This result is appropriate as in the limit $\lambda_s \rightarrow 0$ only the zeroth order terms remain and we recover the unperturbed Hamiltonian. As expected, when there are no couplings to generate losses from the trap, the initial eigenstate remains unchanged.

To first order we obtain the expression

$$\dot{a}_{f,1}(t) = -\frac{i}{\hbar} \sum_n a_{n,0}(t) e^{i\omega_{fn}t} V_{fn}(t), \quad (4.15)$$

which describes processes in which the atom transitions directly to the state obtained by measurement $|\psi_f\rangle$ without passing through any intermediate states. $a_{m,0} = \delta_{mi}$ can be used to simplify this to

$$\dot{a}_{f,1}(t) = -\frac{i}{\hbar} e^{i\omega_{fi}t} V_{fi}(t), \quad (4.16)$$

so that we are only interested in the initial and final states of the transition. We now make our first approximation, by assuming that we can neglect the higher order terms,

$$P_{i \rightarrow C}(t_m) \approx \sum_f |a_{f,1}|^2. \quad (4.17)$$

We thus see that

$$P_{i \rightarrow C}(t_m) = \frac{1}{\hbar^2} \sum_f \left| \int_0^{t_m} e^{i\omega_{fi}t} V_{fi}(t) dt \right|^2. \quad (4.18)$$

We assume $V_{fi}(t) \approx V_{fi}(t = 0)$, which holds true if the interaction matrix element does not explicitly depend on time, giving

$$P_{i \rightarrow C}(t_m) = \sum_f \frac{|V_{fi}|^2}{\hbar^2} \left| \int_0^{t_m} e^{i\omega_{fi}t} dt \right|^2. \quad (4.19)$$

With this assumption equation (4.19) can be integrated to give

$$P_{i \rightarrow C}(t_m) = \sum_f \frac{4}{\hbar^2} |V_{fi}|^2 \frac{\sin^2\left(\frac{\omega_{fi}t_m}{2}\right)}{\omega_{fi}^2}. \quad (4.20)$$

Assuming $V_{fi}(t) \approx V_{fi}(t = 0)$ is reasonable as we are going to be calculating the interaction matrix element for V_A and V_B (as will be discussed in greater detail later). This means that our interaction matrix element depends on the magnitude

and frequency of the RF field and the magnitude of the static magnetic field. We have assumed already in our Hamiltonian derivation that these are constants in time. It should be noted that in a real trap noise may cause them to vary in time. However generally $V_{fi}(t) \approx V_{fi}(t=0)$ is a valid assumption as experimental sources are chosen carefully with the aim to minimise fluctuations in the generated magnetic fields [56].

Rather than summing final states we can rewrite equation (4.20) as a summation of final energies by introducing the density of states $D(E)$,

$$P_{i \rightarrow C}(t_m) = \frac{4}{\hbar^2} \sum_{E_f} |V_{fi}|^2 \frac{\sin^2\left(\frac{\omega_{fi} t_m}{2}\right)}{\omega_{fi}^2} D(E) \Delta E_f. \quad (4.21)$$

As the final states belong to a continuum, the difference in energies between final states will be very small and we can take the limit $\Delta E_f \rightarrow 0$ to give us an integral expression

$$P_{i \rightarrow C}(t_m) = \frac{4}{\hbar^2} \int |V_{fi}|^2 \frac{\sin^2\left(\frac{\omega_{fi} t_m}{2}\right)}{\omega_{fi}^2} D(E) dE_f. \quad (4.22)$$

In this limit the density of states, the number of states per unit of energy, becomes

$$D(E) = \frac{dn}{dE}. \quad (4.23)$$

Figure 4.1, on the next page, demonstrates graphically that the relation

$$\lim_{\epsilon \rightarrow 0} \delta^\epsilon(x) = \frac{\epsilon}{\pi} \frac{\sin^2(x/\epsilon)}{x^2} \quad (4.24)$$

holds true and that in the limit $t \rightarrow \infty$ the function $\frac{\sin^2\left(\frac{\omega_{fi} t_m}{2}\right)}{\omega_{fi}^2}$ will be a delta distribution function.

Figure 4.1 also shows that the transition probability displays an interference pattern. This is a characteristically quantum effect and can be thought of as arising due to interference of the wavefunctions for the different continuum final states. It is shown that the dominant transitions occur when energy conservation is maintained i.e. $E_f = E_i$ and that as the interaction time (the time until a transition occurs) increases, the greater the likelihood of resonant transitions.

Using equation (4.24) as well as the relation $\delta(bx) = \frac{1}{|b|} \delta(x)$ for delta functions (where b is a constant), it can be seen that as $t \rightarrow \infty$,

$$\frac{4}{\omega_{fi}^2} \sin^2\left(\frac{\omega_{fi} t}{2}\right) \rightarrow 2\pi \hbar t \delta(E_f - E_i). \quad (4.25)$$

In the long time limit we can therefore approximate the transition probability by considering only the resonant, energy matching case;

$$P_{i \rightarrow C}(t_m) \approx \frac{2\pi}{\hbar} t_m \int |V_{fi}|^2 D(E) \delta(E_f - E_i) dE_f. \quad (4.26)$$

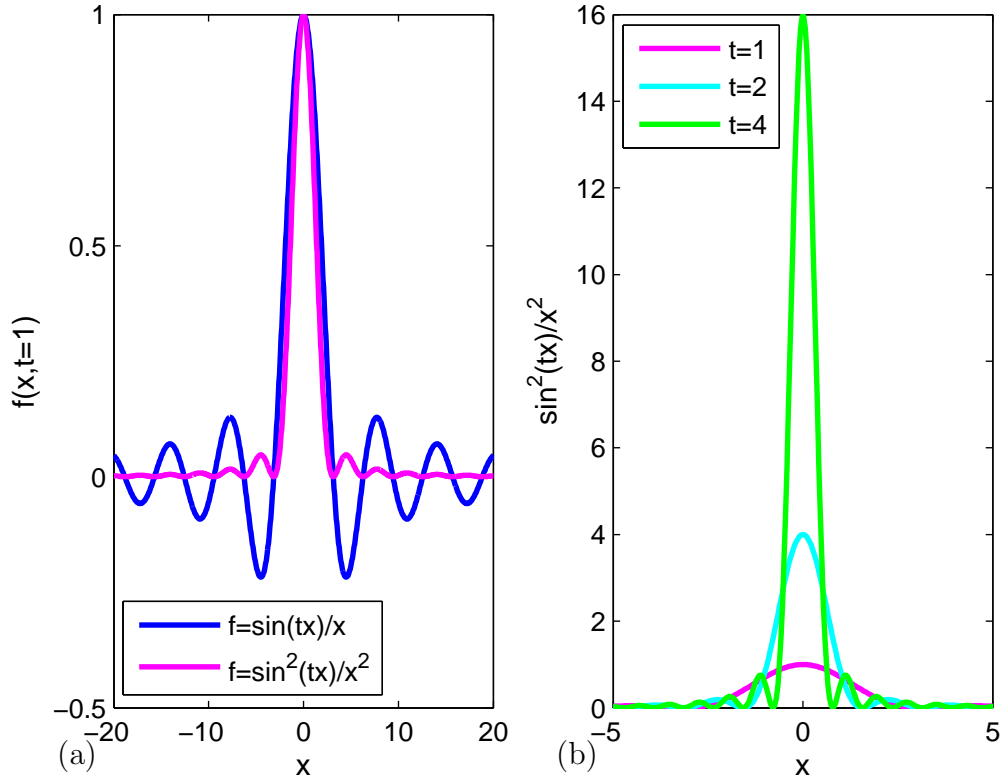


Figure 4.1: Demonstrating the behaviour of the function $\frac{\sin^2\left(\frac{\omega_{fi}t}{2}\right)}{\omega_{fi}^2}$ found within the transition probability given by equation (4.12). Plot (a) shows how the function displays an interference pattern with the dominant contribution at the resonant point, $\omega_{fi} = 0$. Plot (b) shows that as t increases, the energy conserving transitions become increasingly dominant.

Note that we actually have a conflicting limit occurring since we require

$$P_{i \rightarrow C}(t_m) \leq 1 \quad (4.27)$$

for $P_{i \rightarrow C}(t_m)$ to be considered as a probability. However, if the interaction time was truly infinite, to satisfy equation (4.25), $P_{i \rightarrow C}(t_m) \rightarrow \infty$ failing the condition given in equation (4.27). This is a consequence of our truncation to first order in equation (4.17). By assuming a weak perturbation, with V_{fi} sufficiently small, it is possible to find a region in which the interaction time is long enough to take the resonant energy assumption of equation (4.25), while not so large an interaction time so that equation (4.27) remains satisfied. As we are going to be using Fermi's Golden Rule for modelling non-adiabatic losses from cold atom traps, the couplings which lead to losses from the trap should desirably be low and thus should ensure the validity of

using Fermi's Golden Rule. However it is important to be aware that we are working with an approximate model for the losses and that accuracy in all cases cannot be guaranteed.

To progress from equation (4.26) to Fermi's Golden Rule we now only have to let the delta function select out the resonant energy transition,

$$\Gamma = \frac{P_{i \rightarrow C}}{t_m} = \frac{2\pi}{\hbar} |V_{fi}|^2 D(E_f = E_i). \quad (4.28)$$

This is Fermi's Golden Rule. The notation Γ is introduced, which gives the number of transitions per unit time and can be interpreted as a decay rate. Fermi's Golden Rule predicts a constant decay rate with respect to time, which implies that a single atom is equally likely to decay at any time. The knowledge of only two states, the initial state and the final state with matching energy, is necessary to determine the decay rate.

4.2 Using Fermi's Golden Rule to model spin state transitions

Fermi's Golden Rule states that the number of transitions per second (Γ) is proportional to the product of the density of final states ($D(E_f)$) and the interaction coupling ($|V_{if}|^2$). To calculate a decay rate we therefore need to calculate the appropriate interaction matrix element that gives the coupling between an initial state associated with a trapping potential to a final state associated with an untrapped potential. We also need to calculate the density of final states for the untrapped potential. For our model this can be expressed in terms of notation introduced in section 3.4. We wish to calculate the interaction matrix elements for the $\hat{V}_A \hat{F}_y$ and $\hat{V}_B \hat{F}_y^2$ Hamiltonian terms, as they couple different m_F states and jointly act as our perturbing \hat{V} Hamiltonian. The unperturbed Hamiltonian is given by $\frac{\hat{p}_z^2}{2m_0} + V(z)$, where we select $V(z)$ to be the potential for a trapped atom. For $\hat{V}_A \hat{F}_y$,

$$V_{iAf} = \langle m_i, F | \hat{F}_y | F, m_f \rangle \int_{-\infty}^{\infty} [\Psi_n^{(i)}(z)]^* \hat{V}_A \Psi_{n_f}^{(f)}(z) dz \quad (4.29)$$

and similarly for $\hat{V}_B \hat{F}_y^2$,

$$V_{iBf} = \langle m_i, F | \hat{F}_y^2 | F, m_f \rangle \int_{-\infty}^{\infty} [\Psi_n^{(i)}(z)]^* \hat{V}_B \Psi_{n_f}^{(f)}(z) dz. \quad (4.30)$$

We can simplify the spin components, given earlier by equations (3.46) and (3.47), by labelling the dressed spin states such that for our trapped state $m_i > 0$.

Therefore we are only interested in $m_i > m_f$, as we only wish to model the loss of atoms from the trap. We do not consider atoms re-entering the trap through the $m_i < m_f$ process. This limits our region of validity for modeling losses of atoms for traps with $F < 2$. For systems with $F < 2$ the V_A and V_B couplings cause the atoms to transition to untrapped continuum states, from which they are rapidly lost from the trapping region and therefore it is unlikely they would be able to re-enter the trap. However for $F > 2$ atoms may transition between different trapping potentials which leads to undesirable heating effects but not losses from the trap.

Taking $m_i > m_f$ in equation (3.46) gives equation (4.29) as

$$V_{iAf} = \frac{\hbar}{2i} \sqrt{(F + m_f + 1)(F - m_f)} \delta_{m_f+1}^{m_i} \int_{-\infty}^{\infty} \left[\Psi_n^{(i)}(z) \right]^* \hat{V}_A \Psi_{n_f}^{(f)}(z) dz. \quad (4.31)$$

Similarly use of $m_i > m_f$ in equation (3.47) gives equation (4.30) as

$$V_{iBf} = -\frac{\hbar^2}{4} \sqrt{(F + m_f + 1)(F - m_f)} \sqrt{(F + m_f + 2)(F - m_f - 1)} \delta_{m_f+2}^{m_i} \int_{-\infty}^{\infty} \left[\Psi_n^{(i)}(z) \right]^* \hat{V}_B \Psi_{n_f}^{(f)}(z) dz. \quad (4.32)$$

Wishing to express the coupling terms explicitly in terms of the Rabi frequency and detuning using equations (3.57) and (3.58), gives

$$\begin{aligned} V_{iAf} = & \frac{\hbar^2}{4m_0} \sqrt{(F + m_f + 1)(F - m_f)} \delta_{m_f+1}^{m_i} \\ & \times \left\{ \int_{-\infty}^{\infty} \left(\Psi_n^{(i)} \right)^* \left[\frac{2\delta\delta'^2\Omega}{(\Omega^2 + \delta^2)^2} - \frac{\delta''\Omega}{\Omega^2 + \delta^2} \right] \Psi_{n_f}^{(f)} dz \right. \\ & \left. - \int_{-\infty}^{\infty} \left(\Psi_n^{(i)} \right)^* \frac{2\delta'\Omega}{\Omega^2 + \delta^2} \frac{\partial \Psi_{n_f}^{(f)}}{\partial z} dz \right\} \end{aligned} \quad (4.33)$$

and

$$\begin{aligned} V_{iBf} = & -\frac{\hbar^2}{8m_0} \sqrt{(F + m_f + 1)(F - m_f)} \sqrt{(F + m_f + 2)(F - m_f - 1)} \delta_{m_f+2}^{m_i} \\ & \times \int_{-\infty}^{\infty} \left(\Psi_n^{(i)} \right)^* \frac{\delta'^2\Omega^2}{(\Omega^2 + \delta^2)^2} \Psi_{n_f}^{(f)} dz. \end{aligned} \quad (4.34)$$

Now all that is required to calculate decay rates using Fermi's Golden Rule is to know the wavefunctions that correspond to the initial and final states of the atom and to calculate the density of final states. To achieve this we shall now go on to develop our own models for the RF-dressed trap system and present the results obtained from them.

Part III

Results and analysis

Chapter 5

Rate of dressed spin state transitions

In this chapter we will derive and examine the rate of non-adiabatic spin flips out of an RF-dressed cold atom trap. To study non-adiabatic effects in detail a certain amount of generality has to be sacrificed, for example, we shall assume gravity is present in the trap. In a zero gravity environment a bubble trap would be formed (see reference [57]); we shall instead consider the case in which, due to the presence of the gravitational force, atoms collect around the resonance location with lowest height, to form an atom cloud (see figure 8.2). We shall determine the decay rate for a single atom, oscillating in the vertical direction within this atom cloud. The vertical direction is chosen as it is the dominant cause of non-adiabatic losses, which will be explained further in subsequent chapters. We do not consider any interactions between the atoms, which is reasonable for dilute clouds comprised of thermal atoms, however, it means the theory presented is not suitable for BECs without suitable extension.

We first introduce the minimal effect gravity model, in which we do not consider any change in the gravitational potential energy of the atom. This provides our most simplified description of the trap, for which we are able to determine analytic results for the decay rates obtained by use of Fermi's Golden Rule. We then improve our trap description to form the full effect gravity model, considering a change in gravitational potential energy of the atom and derive an integral expression for the rates of non-adiabatic transitions obtained in this case.

5.1 Minimal effect gravity model

The minimal effect gravity model is a simplified ‘box’ model of the trap, for which we approximate the adiabatic potential of the trapped m_i state by a harmonic oscillator and the adiabatic potential associated with the untrapped m_f state by an infinite well potential. Within this model it is possible to derive an exact analytic formula for the lowest atomic energy decay rate and an analytic ‘pole approximation’ for the higher atomic energies. We shall use the decay rate obtained by the pole approximation method to find an expression for the rate of non-adiabatic dressed spin state transitions in the limit of low decay.

We first consider the potential of an atom confined within an RF-dressed trap. To allow use of an analytic formula for the wavefunction of the trapped atoms we approximate the potential of the trap, given by a equation (3.56), by a harmonic oscillator. We achieve this by performing a Taylor expansion [58],

$$V(z) = V(z_0) + (z - z_0) \left. \frac{\partial V}{\partial z} \right|_{z_0} + \frac{(z - z_0)^2}{2} \left. \frac{\partial^2 V}{\partial z^2} \right|_{z_0} + \dots \quad (5.1)$$

where z_0 is selected to be the trap minimum in the z direction. For our trap potential, given by equation (3.56),

$$\begin{aligned} V(z) &= \hbar m_F \sqrt{\Omega^2 + \delta^2} + \mathcal{H} \frac{\Omega^2 \delta'^2}{(\Omega^2 + \delta^2)^2}, \\ \frac{\partial V}{\partial z} &= \hbar m_F \frac{\delta \delta'}{\sqrt{\Omega^2 + \delta^2}} + 2\mathcal{H} \Omega^2 \left[\frac{\delta' \delta''}{(\Omega^2 + \delta^2)^2} - \frac{2\delta \delta'^3}{(\Omega^2 + \delta^2)^3} \right], \\ \frac{\partial^2 V}{\partial z^2} &= \hbar m_F \left[\frac{\delta \delta''}{\sqrt{\Omega^2 + \delta^2}} + \frac{\Omega^2 \delta'^2}{(\Omega^2 + \delta^2)^{\frac{3}{2}}} \right] \\ &\quad + 2\mathcal{H} \Omega^2 \left[\frac{\delta''^2 + \delta' \delta'''}{(\Omega^2 + \delta^2)^2} - \frac{10\delta \delta'^2 \delta''}{(\Omega^2 + \delta^2)^3} + \frac{10\delta^2 \delta'^4 - 2\delta'^4 \Omega^2}{(\Omega^2 + \delta^2)^4} \right], \end{aligned} \quad (5.2)$$

where a prime indicates differentiation by z i.e. $\delta' = \frac{\partial \delta}{\partial z}$. We now make the simplifying assumption that for the trap $\delta' = -\lambda$, which will allow comparison with experimental results in chapter 8 and is appropriate for quadrupole fields typical of atom traps [27]. λ is a constant which can be defined as

$$\lambda = \left| g_F \frac{\mu_B}{\hbar} B' \right|, \quad (5.3)$$

where $B' = \frac{\partial B}{\partial z}$ is the magnetic field gradient in the z direction.

By assuming that the detuning is a linear function of z we are able to investigate our adiabatic potentials further. Figure 5.1 shows the three possible adiabatic potentials, dependent on the m_F state of the atom, for an atom with angular momentum of $F = 1$. Atoms with $m_F = 1$ would be trapped around the resonance

location, while atoms with $m_F = 0$ and $m_F = -1$ would accelerate away from the resonance location. In the limit in which the hump is negligible no acceleration would occur for the $m_F = 0$ eigenstate, however, there is also no confining potential to prevent the atoms leaving. The \hat{V}_A coupling causes trapped atoms with $m_i = 1$ to make a transition to the $m_f = 0$ eigenstate. The \hat{V}_B coupling causes trapped atoms to make a transition to the $m_f = -1$ state. Once in the $m_f = 0$ and $m_f = -1$ states the atoms will almost certainly be lost forever from the trap.

For figure 5.1 the values of Ω and B' were chosen to demonstrate the hump. Even for these values the affect of the hump is very small, showing up most clearly for the $m_F = 0$ state. The hump also causes a raising of the $m_F = 1$ and $m_F = -1$ adiabatic potentials around $z = 0$, which is barely noticeable by eye. Figure 5.2 shows that the height of the hump is only a few nano-Kelvin and that its small effect on the adiabatic trap potentials decreases further in the high Rabi frequency and low magnetic field gradient limits. Note that the transformation $z \rightarrow z + \frac{\omega_{rf}}{\lambda}$ has been performed so that the origin of the z axis is now the resonance location. Unless explicitly stated otherwise, whenever z is referred to from this point onwards it will be referring to this axis with $\delta(z = 0) = 0$.

Using $\delta' = -\lambda$ we are able to remove the higher order δ differentials from our expansion, so that equation (5.2) is simplified to

$$\begin{aligned} V(z) &= \hbar m_F \sqrt{\Omega^2 + \delta^2} + \mathcal{H} \Omega^2 \lambda^2 \frac{1}{(\Omega^2 + \delta^2)^2}, \\ \frac{\partial V}{\partial z} &= -\hbar m_F \lambda \frac{\delta}{\sqrt{\Omega^2 + \delta^2}} + 4\mathcal{H} \Omega^2 \lambda^3 \frac{\delta}{(\Omega^2 + \delta^2)^3}, \\ \frac{\partial^2 V}{\partial z^2} &= \hbar m_F \Omega^2 \lambda^2 \frac{1}{(\Omega^2 + \delta^2)^{\frac{3}{2}}} + 4\mathcal{H} \Omega^2 \lambda^4 \frac{(5\delta^2 - \Omega^2)}{(\Omega^2 + \delta^2)^4}. \end{aligned} \quad (5.4)$$

It is aesthetically pleasing to introduce the variable,

$$\Delta S = \left| \frac{\Omega}{\lambda} \right| \quad (5.5)$$

which gives the ratio of the magnitude of the applied RF field and the static magnetic field gradient. ΔS is a length scale associated with the couplings introduced by the RF field. We perform an expansion about the resonance location, the point where the detuning is zero so that $\delta(z_0) = 0$ and consequently

$$\begin{aligned} V(z_0) &= \hbar m_F \Omega + \frac{\mathcal{H}}{\Delta S^2}, \\ \left. \frac{\partial V}{\partial z} \right|_{z_0} &= 0, \\ \left. \frac{\partial^2 V}{\partial z^2} \right|_{z_0} &= \frac{\hbar m_F \Omega}{\Delta S^2} - \frac{4\mathcal{H}}{\Delta S^4}. \end{aligned} \quad (5.6)$$

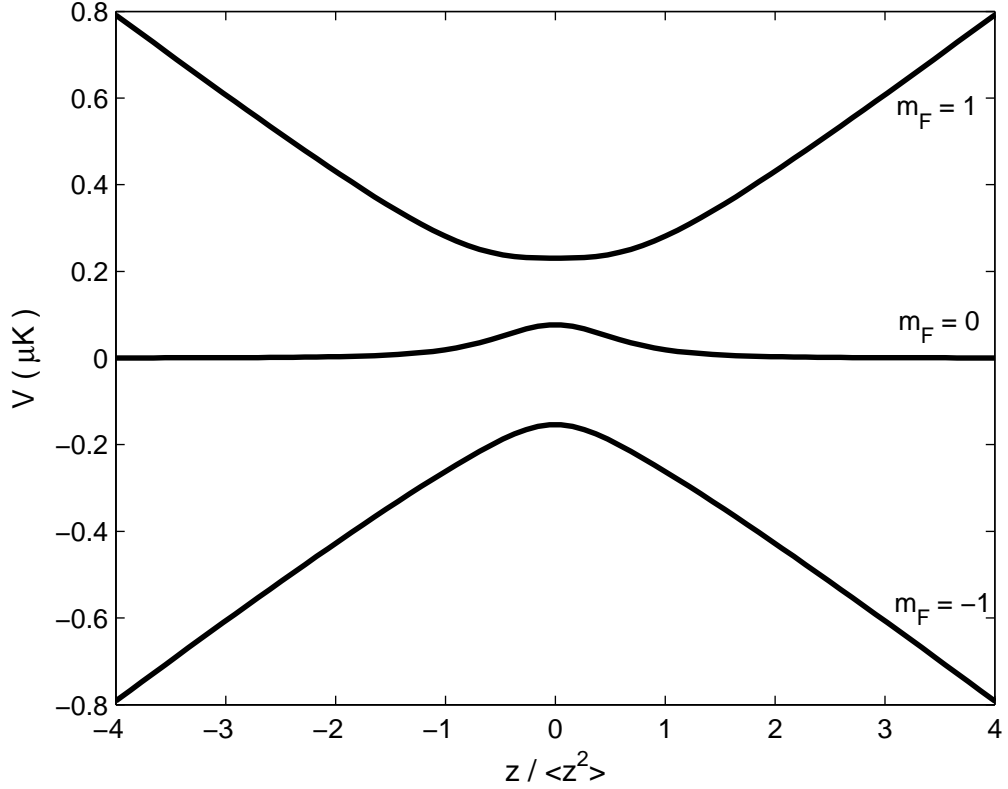


Figure 5.1: Adiabatic potentials given by equation (3.56) with $\delta' = -\lambda$. ^{87}Rb atoms with $F = 1$ with trap parameters: $\Omega/2\pi = 4\text{ kHz}$ and $B' = 3\text{ T/m}$.

A harmonic approximation of the potential for the trapped $m_F = m_i$ state can then be obtained using equation (5.1),

$$V_i(z) = \hbar m_i \Omega + \frac{\mathcal{H}(m_i)}{\Delta S^2} + \frac{z^2}{2\Delta S^2} \left[\hbar m_i \Omega - \frac{4\mathcal{H}(m_i)}{\Delta S^2} \right]. \quad (5.7)$$

The harmonic oscillator potential is valid in the region $z \ll \Delta S$ for positive m_F states. The contribution of the hump threatens to turn the curvature of the harmonic oscillator potential negative. To prevent this, from equation (5.6), we can set the condition

$$\hbar m_i \Omega - \frac{4\mathcal{H}(m_i)\lambda^2}{\Omega^2} > 0 \quad (5.8)$$

which can be transformed into a lower limit for acceptable Rabi frequencies in our model:

$$\Omega > \left[\frac{4\lambda^2 \mathcal{H}(m_i)}{\hbar m_i} \right]^{\frac{1}{3}}. \quad (5.9)$$

Now we have to choose our model potential for the untrapped state. We focus our attention on the \hat{V}_A decay process, given by equation (4.33). Crude numeri-

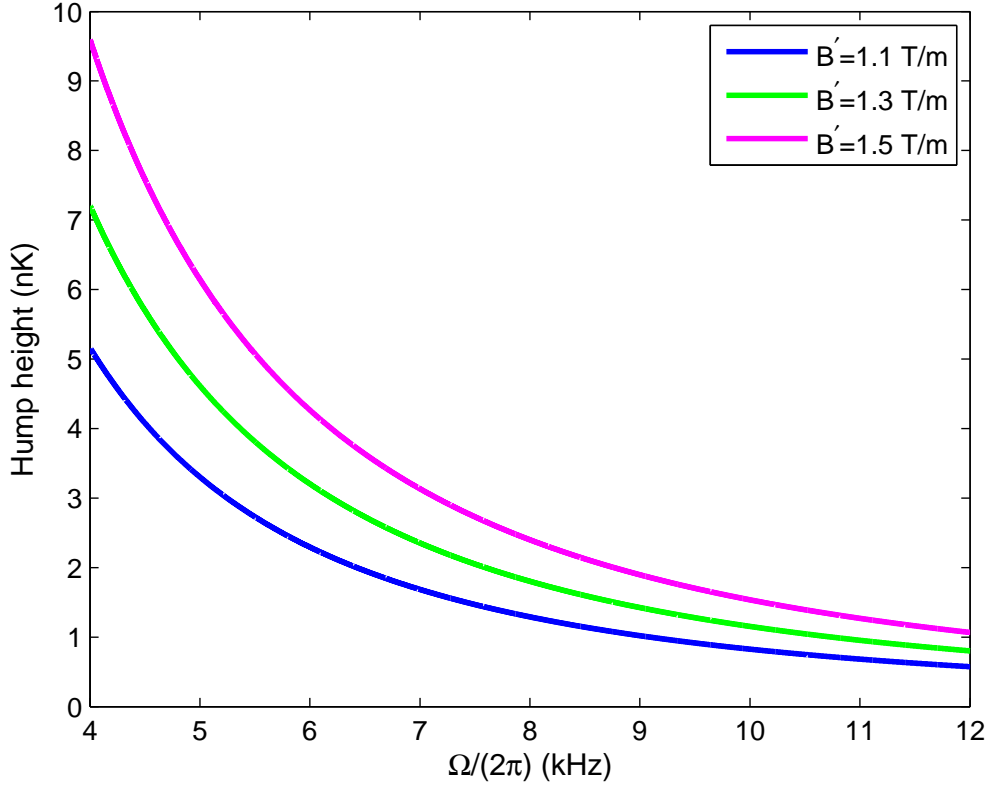


Figure 5.2: Height of the hump variation with Rabi frequency for different magnetic field gradients. Hump height is defined to be the difference in the potential, given by equation (3.56), with $\mathcal{H} \neq 0$ and $\mathcal{H} = 0$ at the resonance location, given by $\mathcal{H}_{\Omega^2}^{\lambda^2}$. The atomic species of ^{87}Rb with a dressed spin state $|1, 1\rangle$. The hump height for the dressed spin state $|1, -1\rangle$ is identical to that plotted. For $|1, 0\rangle$ the hump height is twice the plotted values.

cal investigations, modelling the \hat{V}_B decay process (equation (4.34)) with either a constant or sloping untrapped state potential, have shown to be several orders of magnitude smaller. We also assume $F = 1$, as will be required in comparison to experimental data given in section 8. This limits the region of validity of the results we obtain for the rate of non-adiabatic transitions to $F = 1$ spin systems. The process can be extended to other spin systems by substitution of an alternative final state wavefunction. However, for $F > 1$ Fermi's Golden Rule would not be appropriate for determining decay rates for atoms trapped in $m_i \geq 2$ as the final untrapped state is no longer a continuum.

For our untrapped $m_F = m_f$ state, we approximate the potential felt by the

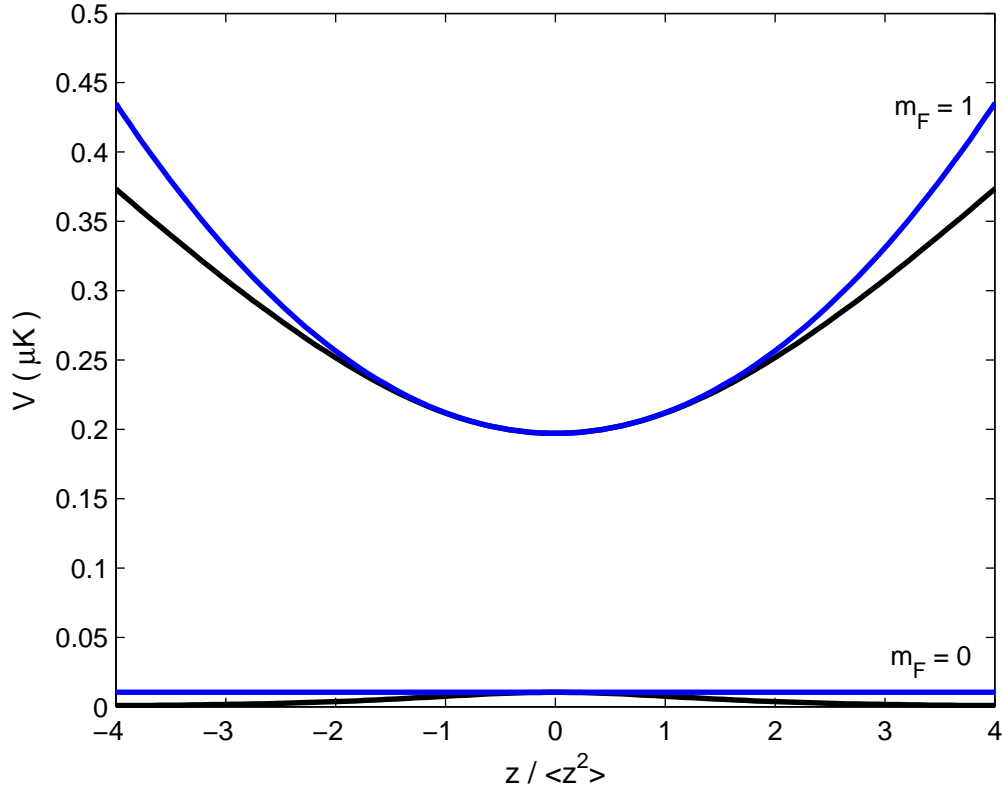


Figure 5.3: Comparing the potential of the trap (black) with the minimal effect gravity model (blue). The plot was created using a magnetic field gradient $B' = 1.1 \text{ T/m}$ and $\Omega/2\pi = 4 \text{ kHz}$ for ^{87}Rb atom $F = 1$ hyperfine splitting and with $L > 1 \mu\text{m}$.

atoms by an infinite square well,

$$V_f(z) = \begin{cases} \infty, & z \leq -\frac{L}{2}, \\ \hbar m_f \Omega + \frac{\mathcal{H}(m_f)}{\Delta S^2}, & -\frac{L}{2} \ll z \ll \frac{L}{2}, \\ \infty, & z \geq \frac{L}{2}. \end{cases}$$

The contribution to the potential from the hump has been included as a position independent energy shift. Removing the position dependence is largely for convenience, although it does model the $m_F = 0$ potential in the highly reasonable limit in which the hump is negligible. Figure 5.3 demonstrates how our simplified minimal effect gravity model matches well to the potential landscape of the trap as given by equation (3.56). As the Rabi frequency is increased or the magnetic field gradient is lowered, the trapping potential becomes more harmonic leading to greater agreement for $m_F = 1$. Additionally, as seen from figure 5.2, the height of the hump decreases so that the $m_F = 0$ potential model improves as well.

Our choice of simplification for the trap potentials allows us to use exact analytic expressions for the wavefunctions of an atom in each required m_F state. The wavefunction for an atom in the initial trapped m_i state is the well known harmonic oscillator wavefunction [59],

$$\Psi_n(z) = \frac{H_n\left(\frac{z}{\sigma}\right)e^{-\frac{z^2}{2\sigma^2}}}{\sqrt{n!2^n\sigma\sqrt{\pi}}}, \quad (5.10)$$

where n is a positive integer ($n \in \mathbb{N}$) which selects the energy of the trapped atom from the allowed discrete harmonic oscillator energy levels given by

$$E_n = \left(n + \frac{1}{2}\right) \hbar\omega + \hbar m_i \Omega + \frac{\mathcal{H}(m_i)}{\Delta S^2}. \quad (5.11)$$

The variable

$$\sigma = \sqrt{\frac{\hbar}{m_0\omega}} \quad (5.12)$$

is a length scale associated with the size of the ground state wave packet, dependent on the trap frequency given by

$$\omega = +\sqrt{\frac{\hbar m_i \lambda^2}{m_0 \Omega} - \frac{4\mathcal{H}(m_i)}{m_0 \Delta S^4}}. \quad (5.13)$$

The hump appears in our model as a modification to the oscillation frequency ω and a shift in the energy levels.

The final state is taken to be a state in the infinite square well, denoted by the positive integer n_f , which satisfies the condition $E_{n_f} = E_n$. This ensures energy conservation in the transition, necessary for Fermi's Golden Rule (as discussed in chapter 4). To allow calculation of the density of states (also necessary for use of Fermi's Golden Rule) we consider a square well with finite boundaries at $z = \pm \frac{L}{2}$; however, we later extend the box to infinity ($L \rightarrow \infty$) to provide us with a continuum of final states and allow an exact match of energies to occur. For a more general derivation using an asymmetric box and discussion of the validity of this process please refer to appendix C. The wavefunction of the final state n_f is given by

$$\Psi_{n_f}(z) = \frac{1}{\sqrt{2L}} [e^{ikz} + (-1)^{n_f+1} e^{-ikz}] \quad (5.14)$$

with discrete energy levels

$$E_{n_f} = \frac{k^2 \hbar^2}{2m_0} + \hbar m_f \Omega + \frac{\mathcal{H}(m_f)}{\Delta S^2}. \quad (5.15)$$

The wave number is determined by

$$k = \frac{n_f \pi}{L} \quad (5.16)$$

$$= \sqrt{\frac{2n+1}{\sigma^2} + \frac{2m_0\Omega}{\hbar}(m_i - m_f) + \frac{m_f^2 - m_i^2}{2\Delta S^2}} \quad (5.17)$$

from setting the relation $E_{n_f} = E_n$. k is dependent on the harmonic oscillator state n and shall often be written as k_n to make this clear. The hump creates a shift in the energy levels of the infinite well potential and adds a term to the wave number expression.

We now examine the leakage from this model caused by the term $\hat{V}_A \hat{F}_y$. The relevant interaction matrix element necessary for Fermi's Golden Rule is calculated, by substitution into equation (4.33), giving

$$\begin{aligned}
 V_{iAf} = & -\frac{\hbar^2}{2m_0} \frac{\Delta S}{\sqrt{2^{n+1}n!L\sigma\sqrt{\pi}}} \sqrt{(F+m_f+1)(F-m_f)} \delta_{m_f+1}^{m_i} \\
 & \times \left\{ \int_{-\frac{L}{2}}^{\frac{L}{2}} \frac{z H_{n_i}(\frac{z}{\sigma}) e^{-\frac{z^2}{2\sigma^2}}}{(z^2 + \Delta S^2)^2} \left[e^{ik_n z} + (-1)^{n_f+1} e^{-ik_n z} \right] dz \right. \\
 & \left. - ik_n \int_{-\frac{L}{2}}^{\frac{L}{2}} \frac{H_{n_i}(\frac{z}{\sigma}) e^{-\frac{z^2}{2\sigma^2}}}{z^2 + \Delta S^2} \left[e^{ik_n z} + (-1)^{n_f} e^{-ik_n z} \right] dz \right\}. \quad (5.18)
 \end{aligned}$$

These are the integrals we are required to solve, to get an expression for the transition rate from the n th harmonic oscillator state to the infinite square well state with matching energy denoted by n_f .

5.1.1 Decay rate of the ground state

We are able to continue with an analytic exact solution by setting $n = 0$, taking the harmonic oscillator ground state. As $H_0(\frac{z}{\sigma}) = 1$ [52] this considerably simplifies the integrals so that

$$\begin{aligned}
 V_{iAf} = & -\frac{\hbar^2}{2m_0} \frac{\Delta S}{\sqrt{2L\sigma\sqrt{\pi}}} \sqrt{(F+m_f+1)(F-m_f)} \delta_{m_f+1}^{m_i} \\
 & \times \left\{ \int_{-\frac{L}{2}}^{\frac{L}{2}} \frac{z e^{-\frac{z^2}{2\sigma^2}}}{(z^2 + \Delta S^2)^2} \left[e^{ikz} + (-1)^{n_f+1} e^{-ikz} \right] dz \right. \\
 & \left. - ik_n \int_{-\frac{L}{2}}^{\frac{L}{2}} \frac{e^{-\frac{z^2}{2\sigma^2}}}{z^2 + \Delta S^2} \left[e^{ikz} + (-1)^{n_f} e^{-ikz} \right] dz \right\}. \quad (5.19)
 \end{aligned}$$

As we are integrating over an even interval only even n_f states will contribute, which means

$$\begin{aligned}
 V_{iAf} = & -\frac{i\hbar^2}{m_0} \frac{\Delta S}{\sqrt{2L\sigma\sqrt{\pi}}} \sqrt{(F+m_f+1)(F-m_f)} \delta_{m_f+1}^{m_i} \\
 & \times \left[\int_{-\frac{L}{2}}^{\frac{L}{2}} \frac{z e^{-\frac{z^2}{2\sigma^2}}}{(z^2 + \Delta S^2)^2} \sin(kz) dz \right. \\
 & \left. - k \int_{-\frac{L}{2}}^{\frac{L}{2}} \frac{e^{-\frac{z^2}{2\sigma^2}}}{z^2 + \Delta S^2} \cos(kz) dz \right]. \quad (5.20)
 \end{aligned}$$

Integration by parts gives us the expression

$$V_{iAf} = \frac{i\hbar^2}{m_0} \frac{\Delta S}{\sqrt{2L\sigma}\sqrt{\pi}} \sqrt{(F+m_f+1)(F-m_f)} \delta_{m_f+1}^{m_i} \left[\frac{e^{-\frac{L^2}{8\sigma^2}}}{\frac{L^2}{4} + \Delta S^2} + \frac{1}{2\sigma^2} \int_{-\frac{L}{2}}^{\frac{L}{2}} \frac{ze^{-\frac{z^2}{2\sigma^2}}}{z^2 + \Delta S^2} \sin(kz) dz + \frac{k}{2} \int_{-\frac{L}{2}}^{\frac{L}{2}} \frac{e^{-\frac{z^2}{2\sigma^2}}}{z^2 + \Delta S^2} \cos(kz) dz \right]. \quad (5.21)$$

If we now take $L \rightarrow \infty$ limit,

$$V_{iAf} = \frac{i\hbar^2}{m_0} \frac{\Delta S}{\sqrt{2L\sigma}\sqrt{\pi}} \sqrt{(F+m_f+1)(F-m_f)} \delta_{m_f+1}^{m_i} \times \left[\frac{1}{\sigma^2} \int_0^\infty \frac{ze^{-\frac{z^2}{2\sigma^2}}}{z^2 + \Delta S^2} \sin(kz) dz + k \int_0^\infty \frac{e^{-\frac{z^2}{2\sigma^2}}}{z^2 + \Delta S^2} \cos(kz) dz \right], \quad (5.22)$$

integrals 3.954.1 and 3.954.2 from Gradshteyn and Ryzhik [52] can be used to give us an expression for the interaction matrix element,

$$V_{iAf} = \frac{\pi i \hbar^2 \Delta S}{4m_0 \sigma^2} \frac{e^{\frac{\Delta S^2}{2\sigma^2}}}{\sqrt{2L\sigma}\sqrt{\pi}} \sqrt{(F+m_f+1)(F-m_f)} \delta_{m_f+1}^{m_i} \times \left[\frac{2k\sigma^2}{\Delta S} \cosh(k\Delta S) - 2 \sinh(k\Delta S) - e^{-k\Delta S} \left(1 + \frac{k\sigma^2}{\Delta S} \right) \times \operatorname{erf} \left(\frac{\Delta S}{\sqrt{2}\sigma} - \frac{k\sigma}{\sqrt{2}} \right) + e^{k\Delta S} \left(1 - \frac{k\sigma^2}{\Delta S} \right) \times \operatorname{erf} \left(\frac{\Delta S}{\sqrt{2}\sigma} + \frac{k\sigma}{\sqrt{2}} \right) \right] \quad (5.23)$$

where erf is the error function [52] defined as

$$\operatorname{erf}(\phi) = \frac{2}{\sqrt{\pi}} \int_0^\phi e^{-x^2} dx. \quad (5.24)$$

The final requirement for application of Fermi's Golden Rule is the 'density of final states' which is defined by

$$D(E) = \frac{1}{2} \frac{\partial n_f}{\partial E}. \quad (5.25)$$

The density of states is halved, compared to its definition in equation (4.23), as only half the states (those with even n_f) contribute. For further details please refer to appendix C. For the energy of infinite well states given by equation (5.15) differentiation gives

$$D(E) = \frac{m_0 L}{2\pi k_n \hbar^2}. \quad (5.26)$$

Note that, $|\Psi_{n_f}|^2$ scales with a factor $1/L$ (see equation (5.14)) such that there are no issues with taking the $L \rightarrow \infty$ limit when using Fermi's Golden Rule.

We now have knowledge of all the necessary components required for use of Fermi's Golden Rule. Substitution of the density of states and the interaction matrix element into equation (4.28), gives the rate of dressed spin state transitions for an atom in the harmonic oscillator ground state as

$$\Gamma_0 = \frac{\pi^2 \hbar \Delta S^2}{32 m_0 k_0 \sigma^5 \sqrt{\pi}} e^{\frac{\Delta S^2}{\sigma^2}} (F + m_f + 1)(F - m_f) \delta_{m_f+1}^{m_i} \times \left\{ e^{-k_0 \Delta S} \left(\frac{k_0 \sigma^2}{\Delta S} + 1 \right) \times \operatorname{erfc} \left[\frac{\Delta S}{\sqrt{2} \sigma} \left(1 - \frac{k_0 \sigma^2}{\Delta S} \right) \right] + e^{k_0 \Delta S} \left(\frac{k_0 \sigma^2}{\Delta S} - 1 \right) \times \operatorname{erfc} \left[\frac{\Delta S}{\sqrt{2} \sigma} \left(1 + \frac{k_0 \sigma^2}{\Delta S} \right) \right] \right\}^2, \quad (5.27)$$

expressed in terms of the complementary error function [60]

$$\operatorname{erfc}(\phi) = 1 - \operatorname{erf}(\phi) = \frac{2}{\sqrt{\pi}} \int_{\phi}^{\infty} e^{-x^2} dx. \quad (5.28)$$

A further change of notation to

$$\frac{2\pi}{\omega} \Gamma_0 = \frac{\pi^3 \alpha^2}{16 \beta_h \sqrt{\pi}} e^{\alpha^2} (F + m_f + 1)(F - m_f) \delta_{m_f+1}^{m_i} \times \left\{ e^{-\alpha \beta_h} \left(\frac{\beta_h}{\alpha} + 1 \right) \times \operatorname{erfc} \left[\frac{\alpha}{\sqrt{2}} \left(1 - \frac{\beta_h}{\alpha} \right) \right] + e^{\alpha \beta_h} \left(\frac{\beta_h}{\alpha} - 1 \right) \times \operatorname{erfc} \left[\frac{\alpha}{\sqrt{2}} \left(1 + \frac{\beta_h}{\alpha} \right) \right] \right\}^2 \quad (5.29)$$

shows that in fact only two dimensionless parameters,

$$\alpha = \frac{\Delta S}{\sigma} \quad (5.30)$$

and

$$\beta_h = k_n \sigma, \quad (5.31)$$

are required to express the trap leakage in terms of transitions per harmonic oscillator period. The variable

$$\alpha = \left\{ \frac{m_0 m_i \Omega^3}{\hbar \lambda^2} - [F(F+1) - m_i^2] \right\}^{\frac{1}{4}} \quad (5.32)$$

is the ratio of the length scale associated with the non-adiabatic coupling compared to the length scale associated with the trapped atom wavepacket size. The variable

$$\beta_h = \sqrt{1 + 2n + 2(m_i - m_f) \frac{\Omega}{\omega} + \frac{m_f^2 - m_i^2}{2\alpha^2}} \quad (5.33)$$

compares the scale of the trapped atom wavepacket size to the wavelength of the untrapped free particle, where

$$\frac{\Omega}{\omega} = \left[\frac{\hbar m_i \lambda^2}{m_0 \Omega^3} - \frac{4\mathcal{H}(m_i)}{m_0 \Omega^2 \Delta S^4} \right]^{-\frac{1}{2}}. \quad (5.34)$$

Therefore, equation (5.27) provides an expression for the rate at which atoms initially in the harmonic oscillator ground state, transition due to non-adiabatic effects determined by the $\hat{V}_A \hat{F}_y$ coupling to the infinite well state of matching energy from which they will be lost from the trap. Figure 5.4 shows that to minimise losses due to the coupling, high Rabi frequencies (Ω) and low magnetic field gradients (B') are favourable. (As only the $n = 0$ harmonic oscillator ground state is considered, equation (5.27) and figure 5.4 are only representative for very low temperatures, when the majority of the atom cloud is in the ground state.) Figure 5.5 shows

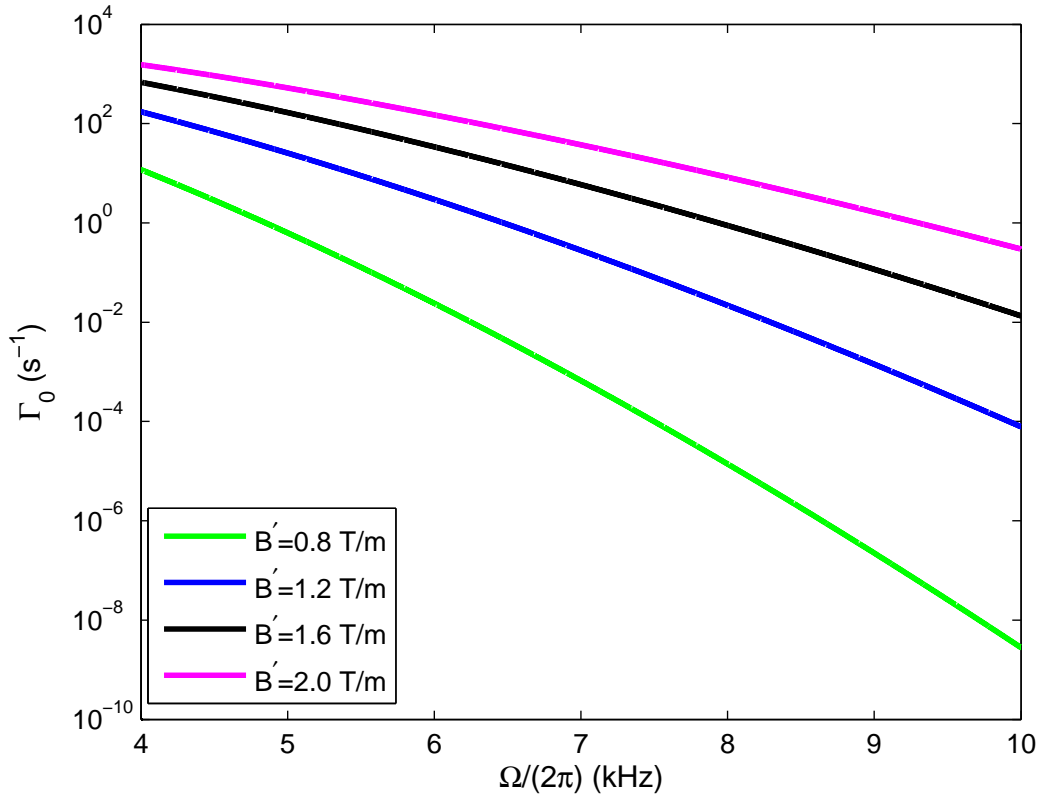


Figure 5.4: Ground state decay rate variation with Rabi Frequency (Ω) and magnetic field gradient (B'). The atomic species is taken to be ^{87}Rb with a dressed spin state transition $|1, 1\rangle \rightarrow |1, 0\rangle$.

how by including the hump contribution in our model, slightly lower decay rates are predicted than if the hump had been ignored. The difference in decay rate caused by

the hump is small and as would be expected decreases, as Rabi frequency increases, when non-adiabatic effects become less significant.

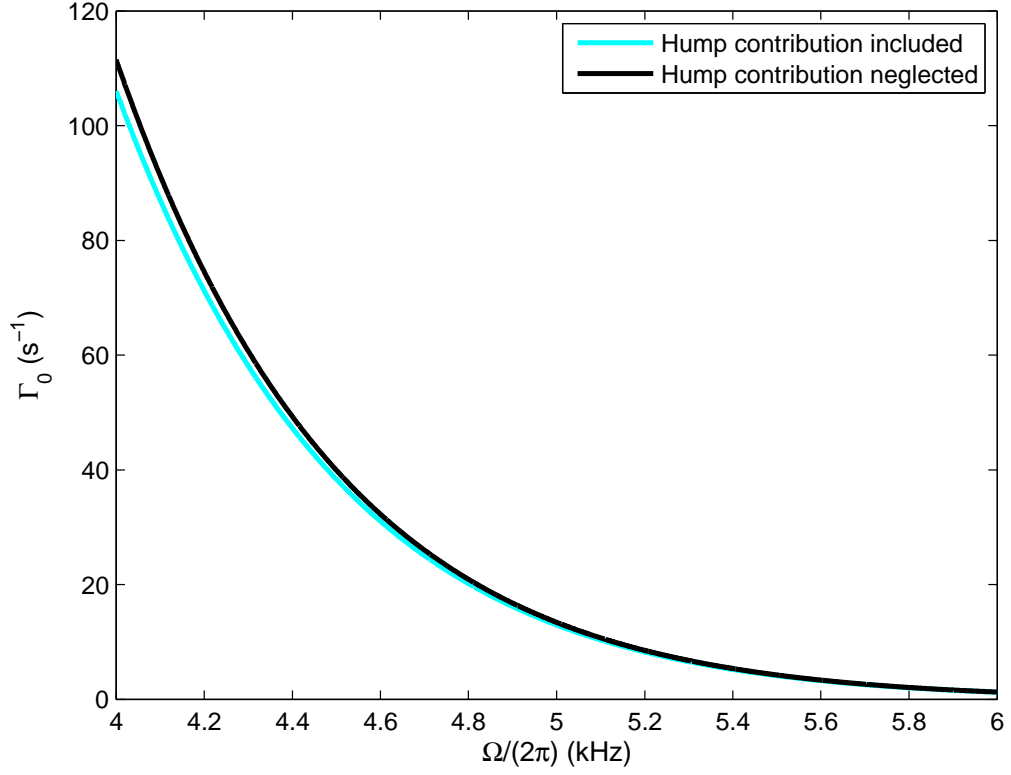


Figure 5.5: Affect of the hump on the ground state decay rate variation with Rabi frequency. The atomic species is taken to be ^{87}Rb with a dressed spin state transition $|1,1\rangle \rightarrow |1,0\rangle$. A magnetic field gradient of $B' = 1.1 \text{ T/m}$ was used to produce this graph.

5.1.2 Pole approximation for higher atomic energies

Let us return to equation (5.18) and try to find a transition rate for higher energy trapped atoms with $n > 0$, as at temperatures in which RF-dressed cold atom traps generally operate there is a significant probability of a trapped atom being in one of the harmonic oscillator's excited states. Equation (5.18) can be combined with the density of states given by equation (5.26) to use Fermi's Golden Rule to give an integral expression for the decay rate for any allowed trapped atom energy, given by

$$\Gamma_n = \frac{\hbar \Delta S^2}{2^{n+3} m_0 n! k_n \sigma \sqrt{\pi}} (F + m_f + 1)(F - m_f) \delta_{m_f+1}^{m_i} \times \left| \left\{ \int_{-\frac{L}{2}}^{\frac{L}{2}} \frac{z H_n(\frac{z}{\sigma}) e^{-\frac{z^2}{2\sigma^2}}}{(z^2 + \Delta S^2)^2} \left[e^{ik_n z} + (-1)^{n_f+1} e^{-ik_n z} \right] dz - ik_n \int_{-\frac{L}{2}}^{\frac{L}{2}} \frac{H_n(\frac{z}{\sigma}) e^{-\frac{z^2}{2\sigma^2}}}{z^2 + \Delta S^2} \left[e^{ik_n z} + (-1)^{n_f} e^{-ik_n z} \right] dz \right\} \right|^2. \quad (5.35)$$

Unfortunately the integrals contained within equation (5.35) are difficult to solve, as they are highly oscillatory and become very large as n increases. The integrals can be calculated numerically¹, which was done using two methods: an in-built quadrature integrator 'quadgk', designed for integrating oscillatory functions and a differential solver 'ode45', both used in Mathworks software, Matlab [61]. It is always useful to have an analytic formula for the decay rate if possible and while the integrals in equation (5.35) cannot be solved, they can be approximated.

To obtain analytic expressions for the minimal effect gravity model decay rates, given by equation (5.35), the saddle point approximation method was applied. Fortunately the saddle point approximation can be simplified dramatically as the contribution from the residue of the pole dominates and has a much simpler formula. While the saddle point method was used to justify our approximation, it is no longer necessary in our derivation of an analytic formula for the decay rate from any initial harmonic oscillator state. Details of the saddle point method approximation can be found in appendix A. We will now calculate the residue of the pole and use it as an approximation to the integrals contained within equation (5.35), this will lead us to our pole approximation decay rates which provide an analytic expression for the decay rates provided by Fermi's Golden Rule for any n state.

The integrals we are trying to solve are:

$$I_1 = \int_{-\frac{L}{2\sigma}}^{\frac{L}{2\sigma}} \frac{H_n(z) e^{-\frac{z^2}{2}}}{z^2 + \alpha^2} e^{i\beta_n z} dz = \int_{-\frac{L}{2\sigma}}^{\frac{L}{2\sigma}} J_1(z) dz \quad (5.36)$$

¹Dramatic improvement is seen with the numeric integration if the Hermite polynomial functions are scaled by the factor of $1/(2^{n/2}\sqrt{n!})$. See equation (5.77).

and

$$I_2 = \int_{-\frac{L}{2\sigma}}^{\frac{L}{2\sigma}} \frac{z H_n(z) e^{-\frac{z^2}{2}}}{(z^2 + \alpha^2)^2} e^{i\beta_h z} dz = \int_{-\frac{L}{2\sigma}}^{\frac{L}{2\sigma}} J_2(z) dz \quad (5.37)$$

along with their complex conjugates, I_1^* and I_2^* . The variable α is defined in equation (5.32) and β_h is given in equation (5.33).

The residue of the pole is found by multiplying the Laurent series co-efficient for the term $(z - z_p)^{-1}$ by $2\pi i$, where z_p is the location of the pole [62]. We begin with the integrand

$$J_1 = \frac{H_n(z) e^{-\frac{z^2}{2}} e^{i\beta_h z}}{(z + i\alpha)(z - i\alpha)}. \quad (5.38)$$

A change of variable, $y = z - i\alpha$, is then helpful so that we can calculate the residue for the pole at $i\alpha$,

$$J_1 = \frac{H_n(y + i\alpha) e^{-\frac{(y+i\alpha)^2}{2}} e^{i\beta_h(y+i\alpha)}}{(y + 2i\alpha)y}. \quad (5.39)$$

We now begin to expand the integrand in terms of powers of y . Rearrangement gives

$$J_1 = \frac{e^{\frac{\alpha^2}{2} - \alpha\beta_h} H_n(y + i\alpha) e^{-\frac{y^2}{2}} e^{i(\beta_h - \alpha)y}}{2i\alpha \left(1 - \frac{iy}{2\alpha}\right) y}. \quad (5.40)$$

Use of

$$e^x = \sum_{n=0}^{\infty} \frac{x^n}{n!} \quad (5.41)$$

allows us to expand the exponentials, giving

$$J_1 = \frac{e^{\frac{\alpha^2}{2} - \alpha\beta_h}}{2i\alpha} \sum_{p=0}^{\infty} \sum_{q=0}^{\infty} \frac{\left(-\frac{1}{2}\right)^p}{p!} \frac{[i(\beta_h - \alpha)]^q}{q!} \frac{H_n(y + i\alpha)}{\left(1 - \frac{iy}{2\alpha}\right)} y^{2p+q-1}. \quad (5.42)$$

Another expansion can be obtained by

$$\frac{1}{1-x} = \sum_{n=0}^{\infty} x^n \quad \text{where } |x| < 1, \quad (5.43)$$

the use of this formula can be justified from the assumption $z \ll \Delta S$ that has already been made for the harmonic oscillator validity, using the fact that $z \approx \sigma$, $|y/\alpha| < \sqrt{2}$. This leads to the expression

$$J_1 = \frac{e^{\frac{\alpha^2}{2} - \alpha\beta_h}}{2i\alpha} \sum_{p=0}^{\infty} \sum_{q=0}^{\infty} \sum_{m=0}^{\infty} \frac{\left(-\frac{1}{2}\right)^p}{p!} \frac{[i(\beta_h - \alpha)]^q}{q!} \left(\frac{i}{2\alpha}\right)^m H_n(y + i\alpha) y^{2p+q+m-1}. \quad (5.44)$$

A series expansion for the Hermite polynomials can be determined from the series given in reference [52],

$$H_n(x) = \sum_{r=0}^R (-1)^r 2^{n-r} (2r-1)!! \binom{n}{2r} x^{n-2r} = \sum_{r=0}^R h_n(r) x^{n-2r} \quad (5.45)$$

where $R = n/2$ for even n and $R = (n - 1)/2$ for odd n . Expanding out the Hermite polynomials gives

$$J_1 = \frac{e^{\frac{\alpha^2}{2} - \alpha\beta_h}}{2i\alpha} \sum_{p=0}^{\infty} \sum_{q=0}^{\infty} \sum_{m=0}^{\infty} \sum_{r=0}^R \frac{(-\frac{1}{2})^p}{p!} \frac{[i(\beta_h - \alpha)]^q}{q!} \left(\frac{i}{2\alpha}\right)^m \times h_n(r) (y + i\alpha)^{n-2r} y^{2p+q+m-1}. \quad (5.46)$$

Finally a binomial expansion,

$$(x + a)^\nu = \sum_{k=0}^{\infty} \binom{\nu}{k} x^k a^{\nu-k} \quad \text{where} \quad \left|\frac{x}{a}\right| < 1, \quad (5.47)$$

leads us to

$$J_1 = \frac{e^{\frac{\alpha^2}{2} - \alpha\beta_h}}{2i\alpha} \sum_{p=0}^{\infty} \sum_{q=0}^{\infty} \sum_{m=0}^{\infty} \sum_{r=0}^R \sum_{k=0}^{\infty} \frac{(-\frac{1}{2})^p}{p!} \frac{[i(\beta_h - \alpha)]^q}{q!} \left(\frac{i}{2\alpha}\right)^m \times h_n(r) \binom{n-2r}{k} (i\alpha)^{n-2r-k} y^{2p+q+m+k-1}. \quad (5.48)$$

This is the Laurent series expansion for the integrand J_1 . For the residue of the pole we want to select the y^{-1} co-efficient. As p, q, m and k are positive integers, this means $p = q = m = k = 0$ for the y^{-1} co-efficient. The y^{-1} co-efficient is therefore

$$j_1 = \frac{e^{\frac{\alpha^2}{2} - \alpha\beta_h}}{2i\alpha} \sum_{r=0}^R h_n(r) (i\alpha)^{n-2r} = \frac{e^{\frac{\alpha^2}{2} - \alpha\beta_h}}{2i\alpha} H_n(i\alpha), \quad (5.49)$$

where equation (5.45) has been used to reintroduce a Hermite polynomial. The integral contribution for the pole is given by

$$I_1 \approx 2\pi i j_1, \quad (5.50)$$

which gives

$$I_1 = \frac{\pi}{\alpha} e^{\frac{\alpha^2}{2} - \alpha\beta_h} H_n(i\alpha) \quad (5.51)$$

and

$$I_1^* = \frac{\pi}{\alpha} e^{\frac{\alpha^2}{2} - \alpha\beta_h} H_n(-i\alpha) = (-1)^n I_1. \quad (5.52)$$

For the last equality in equation (5.52) the fact that

$$H_n(-a) = (-1)^n H_n(a) \quad (5.53)$$

has been used which can be deduced from examination of equation (5.45). The integral given in equation (5.18) is thus given in our pole approximation by,

$$I_1 + (-1)^{n_f} I_1^* = I_1 [1 + (-1)^{n+n_f}] = 2I_1 \quad (5.54)$$

where we use the fact that $n + n_f$ is always even, as we are integrating over an even interval, we require the integrands to be even.

We next repeat the process with the integral I_2 given by equation (5.37), with integrand

$$J_2 = \frac{z H_n(z) e^{-\frac{z^2}{2}} e^{i\beta_h z}}{(z + i\alpha)^2 (z - i\alpha)^2}. \quad (5.55)$$

As before we perform a change of variable,

$$J_2 = \frac{(y + i\alpha) H_n(y + i\alpha) e^{-\frac{(y+i\alpha)^2}{2}} e^{i\beta_h(y+i\alpha)}}{(y + 2i\alpha)^2 y^2}, \quad (5.56)$$

to $y = z - i\alpha$, to allow calculation of the residue for the pole at $i\alpha$. We now begin to expand the integrand in terms of y . Rearrangement gives

$$J_2 = e^{\frac{\alpha^2}{2} - \alpha\beta_h} e^{-\frac{y^2}{2}} e^{i(\beta_h - \alpha)y} \cdot \frac{(y + i\alpha) H_n(y + i\alpha)}{(y + 2i\alpha)^2 y^2} \quad (5.57)$$

and equation (5.41) allows us to expand the exponentials so that

$$J_2 = \frac{e^{\frac{\alpha^2}{2} - \alpha\beta_h}}{(2i\alpha)^2} \sum_{p=0}^{\infty} \sum_{q=0}^{\infty} \frac{\left(-\frac{1}{2}\right)^p}{p!} \frac{[i(\beta_h - \alpha)]^q}{q!} \frac{(y + i\alpha) H_n(y + i\alpha)}{\left(1 - \frac{iy}{2\alpha}\right)^2} y^{2p+q-2}. \quad (5.58)$$

Use of the relation

$$\frac{1}{(1-x)^2} = \sum_{n=0}^{\infty} (n+1) x^n \quad \text{where } |x| < 1, \quad (5.59)$$

with the same justification as for equation (5.43), leads to

$$\begin{aligned} J_2 &= \frac{e^{\frac{\alpha^2}{2} - \alpha\beta_h}}{(2i\alpha)^2} \sum_{p=0}^{\infty} \sum_{q=0}^{\infty} \sum_{m=0}^{\infty} \frac{\left(-\frac{1}{2}\right)^p}{p!} \frac{[i(\beta_h - \alpha)]^q}{q!} (m+1) \left(\frac{i}{2\alpha}\right)^m (y + i\alpha) \\ &\quad \times H_n(y + i\alpha) y^{2p+q+m-2}. \end{aligned} \quad (5.60)$$

Expanding out the Hermite polynomials, using equation (5.45), gives

$$\begin{aligned} J_2 &= \frac{e^{\frac{\alpha^2}{2} - \alpha\beta_h}}{(2i\alpha)^2} \sum_{p=0}^{\infty} \sum_{q=0}^{\infty} \sum_{m=0}^{\infty} \sum_{r=0}^R \frac{\left(-\frac{1}{2}\right)^p}{p!} \frac{[i(\beta_h - \alpha)]^q}{q!} (m+1) \left(\frac{i}{2\alpha}\right)^m (y + i\alpha) \\ &\quad \times h_n(r) (y + i\alpha)^{n-2r} y^{2p+q+m-2}. \end{aligned} \quad (5.61)$$

Finally, a binomial expansion is performed using equation (5.47) so that

$$\begin{aligned} J_2 &= \frac{e^{\frac{\alpha^2}{2} - \alpha\beta_h}}{(2i\alpha)^2} \sum_{p=0}^{\infty} \sum_{q=0}^{\infty} \sum_{m=0}^{\infty} \sum_{r=0}^R \sum_{k=0}^{\infty} \frac{\left(-\frac{1}{2}\right)^p}{p!} \frac{[i(\beta_h - \alpha)]^q}{q!} (m+1) \left(\frac{i}{2\alpha}\right)^m \\ &\quad \times h_n(r) \binom{n-2r}{k} (i\alpha)^{n-2r-k} (y + i\alpha) y^{2p+q+m+k-2}, \end{aligned} \quad (5.62)$$

which is equivalent to

$$J_2 = \frac{e^{\frac{\alpha^2}{2} - \alpha\beta_h}}{(2i\alpha)^2} \sum_{p=0}^{\infty} \sum_{q=0}^{\infty} \sum_{m=0}^{\infty} \sum_{r=0}^R \sum_{k=0}^{\infty} \frac{(-\frac{1}{2})^p}{p!} \frac{[i(\beta_h - \alpha)]^q}{q!} (m+1) \left(\frac{i}{2\alpha}\right)^m \\ \times h_n(r) \binom{n-2r}{k} (i\alpha)^{n-2r-k} (y^{2p+q+m+k-1} + i\alpha y^{2p+q+m+k-2}). \quad (5.63)$$

This is the Laurent series expansion for the integrand J_2 . For calculating the residue of the pole we want to select the y^{-1} co-efficient. As p, q, m and k are positive integers, this means $p = 0$ for the y^{-1} co-efficient. This gives the y^{-1} co-efficient as

$$j_2 = \frac{e^{\frac{\alpha^2}{2} - \alpha\beta_h}}{(2i\alpha)^2} \sum_{q=0}^{\infty} \sum_{m=0}^{\infty} \sum_{r=0}^R \sum_{k=0}^{\infty} \frac{[i(\beta_h - \alpha)]^q}{q!} (m+1) \left(\frac{i}{2\alpha}\right)^m \\ \times h_n(r) \binom{n-2r}{k} (i\alpha)^{n-2r-k} (y^{q+m+k-1} + i\alpha y^{q+m+k-2}). \quad (5.64)$$

For $y^{q+m+k-1}$ the y^{-1} co-efficient is given by $q = m = k = 0$. For $y^{q+m+k-2}$ there are three terms which contribute to the integral detailed in table 5.1.

q	m	k
1	0	0
0	1	0
0	0	1

Table 5.1: Possible configurations of q, m and k that lead to y^{-1} in equation (5.64).

Therefore j_2 is given by

$$j_2 = \frac{e^{\frac{\alpha^2}{2} - \alpha\beta_h}}{(2i\alpha)^2} \sum_{r=0}^R h_n(r) \left[(i\alpha)^{n-2r} + i(\beta_h - \alpha) (i\alpha)^{n-2r+1} \right. \\ \left. + 2 \left(\frac{i}{2\alpha}\right) (i\alpha)^{n-2r+1} + \binom{n-2r}{1} (i\alpha)^{n-2r} \right], \quad (5.65)$$

which simplifies to

$$j_2 = \frac{e^{\frac{\alpha^2}{2} - \alpha\beta_h}}{(2i\alpha)^2} \sum_{r=0}^R h_n(r) (i\alpha)^{n-2r} [\alpha^2 - \alpha\beta_h + (n-2r)]. \quad (5.66)$$

Further simplification seems possible by re-expressing j_2 in terms of Hermite polynomials. Two clear terms are seen

$$j_2 = \frac{e^{\frac{\alpha^2}{2} - \alpha\beta_h}}{(2i\alpha)^2} \left[(\alpha^2 - \alpha\beta_h) \sum_{r=0}^R h_n(r) (i\alpha)^{n-2r} + \sum_{r=0}^R h_n(r) (i\alpha)^{n-2r} (n-2r) \right]. \quad (5.67)$$

Use of equation (5.45) gives

$$j_2 = \frac{e^{\frac{\alpha^2}{2} - \alpha\beta_h}}{(2i\alpha)^2} \left[(\alpha^2 - \alpha\beta_h) H_n(i\alpha) + \sum_{r=0}^R (-1)^r 2^{n-r} (2r-1)!! \binom{n}{2r} (n-2r)(i\alpha)^{n-2r} \right] \quad (5.68)$$

which can equivalently be written as

$$j_2 = \frac{e^{\frac{\alpha^2}{2} - \alpha\beta_h}}{(2i\alpha)^2} \left[(\alpha^2 - \alpha\beta_h) H_n(i\alpha) + 2ni\alpha \sum_{r=0}^R (-1)^r 2^{n-1-r} (2r-1)!! \binom{n-1}{2r} (i\alpha)^{n-1-2r} \right]. \quad (5.69)$$

The last term is a Hermite polynomial with order one less than n , such that

$$j_2 = \frac{e^{\frac{\alpha^2}{2} - \alpha\beta_h}}{(2i\alpha)^2} [(\alpha^2 - \alpha\beta_h) H_n(i\alpha) + 2ni\alpha H_{n-1}(i\alpha)]. \quad (5.70)$$

The integral contribution for the pole is given by $2\pi i \cdot j_2$, which gives

$$I_2 = \frac{\pi}{2\alpha} e^{\frac{\alpha^2}{2} - \alpha\beta_h} [2nH_{n-1}(i\alpha) + i(\beta_h - \alpha) H_n(i\alpha)] \quad (5.71)$$

and

$$\begin{aligned} I_2^* &= \frac{\pi}{2\alpha} e^{\frac{\alpha^2}{2} - \alpha\beta_h} [2nH_{n-1}(-i\alpha) - i(\beta_h - \alpha) H_n(-i\alpha)] \\ &= (-1)^{n-1} I_2 \end{aligned} \quad (5.72)$$

The integral given in equation (5.18) is thus given in our pole approximation by

$$I_2 + (-1)^{n_f+1} I_2^* = I_2 [1 + (-1)^{n+n_f}] = 2I_2, \quad (5.73)$$

where as before we have used the fact that $n + n_f$ is always even.

We therefore have an analytic approximation to the integrals in equation (5.18),

$$\int_{\frac{-L}{2\sigma}}^{\frac{L}{2\sigma}} \frac{H_n(z) e^{-\frac{z^2}{2}}}{z^2 + \frac{\Delta S^2}{\sigma^2}} [e^{ik_n \sigma z} + (-1)^{n_f} e^{-ik_n \sigma z}] dz \approx 2\pi \frac{\sigma}{\Delta S} e^{\frac{\Delta S^2}{2\sigma^2} - k_n \Delta S} H_n\left(i \frac{\Delta S}{\sigma}\right)$$

and

$$\begin{aligned} &\int_{\frac{-L}{2\sigma}}^{\frac{L}{2\sigma}} \frac{H_n(z) z e^{-\frac{z^2}{2}}}{\left(z^2 + \frac{\Delta S^2}{\sigma^2}\right)^2} [e^{ik_n \sigma z} + (-1)^{n_f+1} e^{-ik_n \sigma z}] dz \\ &\approx \pi \frac{\sigma}{\Delta S} e^{\frac{\Delta S^2}{2\sigma^2} - k \Delta S} \left[2n H_{n-1}\left(i \frac{\Delta S}{\sigma}\right) + i \left(k\sigma - \frac{\Delta S}{\sigma}\right) H_n\left(i \frac{\Delta S}{\sigma}\right) \right]. \end{aligned}$$

By substituting the integral expressions into equation (5.35) we can obtain an analytic expression for the rate of non-adiabatic transitions from any initial atomic energy level, given by

$$\Gamma_n = \frac{\pi^{\frac{3}{2}} \hbar}{2^{n+3} n! m_0 k_n \sigma^3} (F + m_f + 1)(F - m_f) \delta_{m_f+1}^{m_i} e^{\frac{\Delta S^2}{\sigma^2} - 2k_n \Delta S} \times \left| \left[2n H_{n-1} \left(i \frac{\Delta S}{\sigma} \right) - i \left(k_n \sigma + \frac{\Delta S}{\sigma} \right) H_n \left(i \frac{\Delta S}{\sigma} \right) \right] \right|^2. \quad (5.74)$$

Equation (5.74) can be expressed as the number of decays per harmonic oscillator period, using the dimensionless variables α and β to be

$$\frac{2\pi}{\omega} \Gamma_n = \frac{\pi^{\frac{5}{2}}}{2^{n+2} n! \beta_h} (F + m_f + 1)(F - m_f) \delta_{m_f+1}^{m_i} e^{\alpha^2 - 2\alpha\beta_h} \times \left| [2n H_{n-1}(i\alpha) - i(\beta_h + \alpha) H_n(i\alpha)] \right|^2. \quad (5.75)$$

For accurate quantitative results at high n it is advisable to scale the Hermite factorial by the factor of $1/2^{\frac{n}{2}} \sqrt{n!}$ such that:

$$\frac{2\pi}{\omega} \Gamma_n = \frac{\pi^{\frac{5}{2}}}{4\beta_h} (F + m_f + 1)(F - m_f) \delta_{m_f+1}^{m_i} e^{\alpha^2 - 2\alpha\beta_h} \times \left| \left[\sqrt{2n} \tilde{H}_{n-1}(i\alpha) - i(\beta_h + \alpha) \tilde{H}_n(i\alpha) \right] \right|^2 \quad (5.76)$$

where

$$\tilde{H}_n(x) = \frac{H_n(x)}{2^{\frac{n}{2}} \sqrt{n!}}. \quad (5.77)$$

It is also beneficial to use the recursion relation 8.952.2 from reference [52] to calculate equation (5.77).

The decay rate obtained by the pole approximation, given in equation (5.74), is shown in figures 5.6 and 5.7. The decay rate is seen to increase with increasing n , which agrees with the semiclassical interpretation of the trapping force. The higher the energy of the trapped atom the faster it moves, so the greater the likelihood the atom will be unable to adiabatically follow the local magnetic field spin direction. This means the higher energy, the greater the probability that the atom will transition to an untrapped state and be lost from the trap. Figure 5.6 shows how for sufficiently high Rabi frequency the pole approximation is a very good approximation for the non-adiabatic decay rates. Figure 5.7 shows that at lower Rabi frequency, the pole approximation is a reasonable approximation for the non-adiabatic decay rates but there is a clear difference from equation (5.35) which calculates the decay rate using numerical integration.

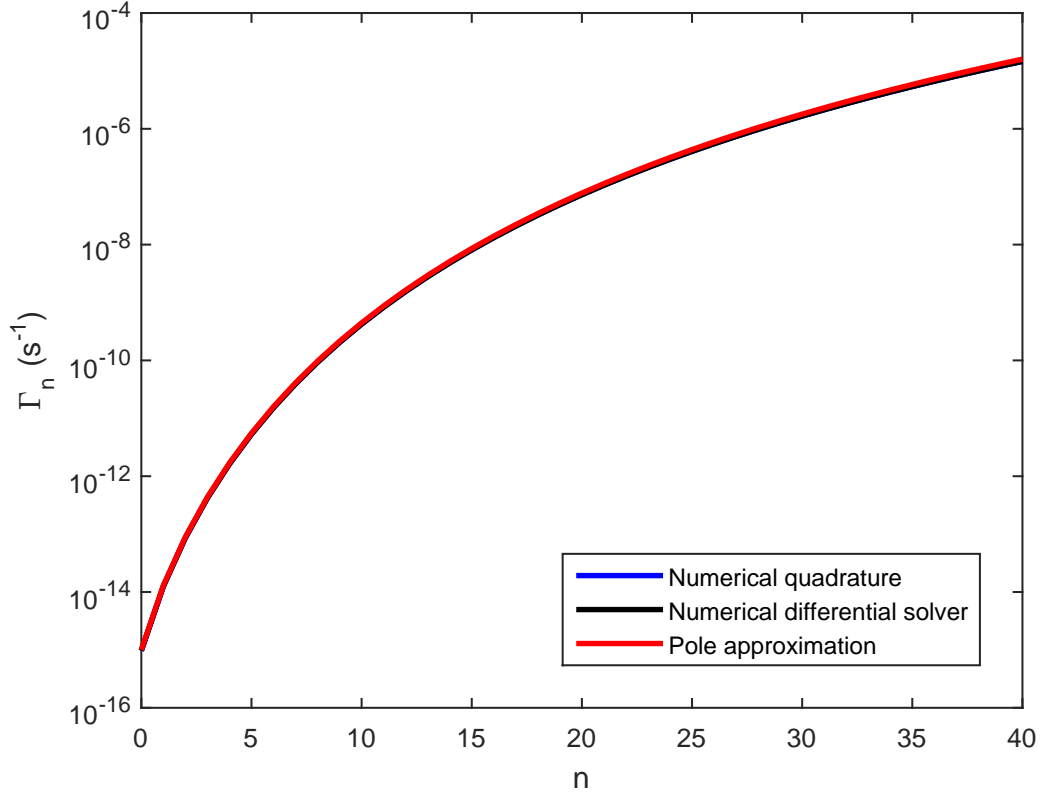


Figure 5.6: Comparing the pole approximation (red line) with decay rates obtained by numerical integration (blue and black lines) at high Rabi frequency. Continuous lines are plotted for clarity, however, n the quantum number which specifies the atomic energy E_n can only take integer values. A magnetic field gradient of $B' = 1.5 \text{ T/m}$ and Rabi Frequency $\Omega/2\pi = 20 \text{ kHz}$ was used to produce this graph. ^{87}Rb data was used for the following transition $|1, 1\rangle \rightarrow |1, 0\rangle$ that leads to losses of atoms from the trap. The two numerical methods are in agreement such that the blue line is underneath the black line. The black line is itself almost completely covered by the red line.

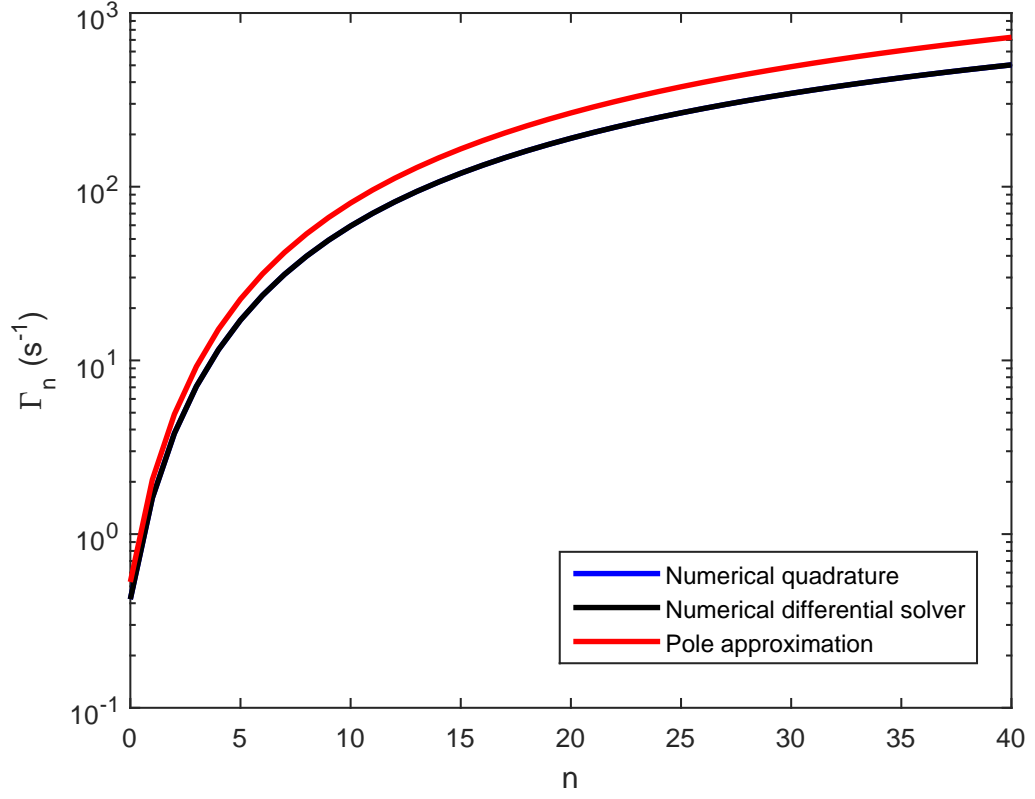


Figure 5.7: Comparing the pole approximation (red line) with decay rates obtained by numerical integration (blue and black lines) at low Rabi frequency. Continuous lines are plotted for clarity, however, n the quantum number which specifies the atomic energy E_n can only take integer values. A magnetic field gradient of $B' = 1.5 \text{ T/m}$ and Rabi Frequency $\Omega/2\pi = 8 \text{ kHz}$ was used to produce this graph. ^{87}Rb data was used for the following dressed spin state transition $|1, 1\rangle \rightarrow |1, 0\rangle$ that leads to losses of atoms from the trap. The blue line is under the black line such that as desired the two different numerical methods are in agreement.

Increasing the Rabi frequency or decreasing the magnetic field gradient decreases the decay due to non-adiabatic losses, as shown in figure 5.8. The pole approximation is a good approximation although there is deviation at low Rabi frequencies which (though somewhat hidden by the logarithmic scale plotted) does lead to significant differences.

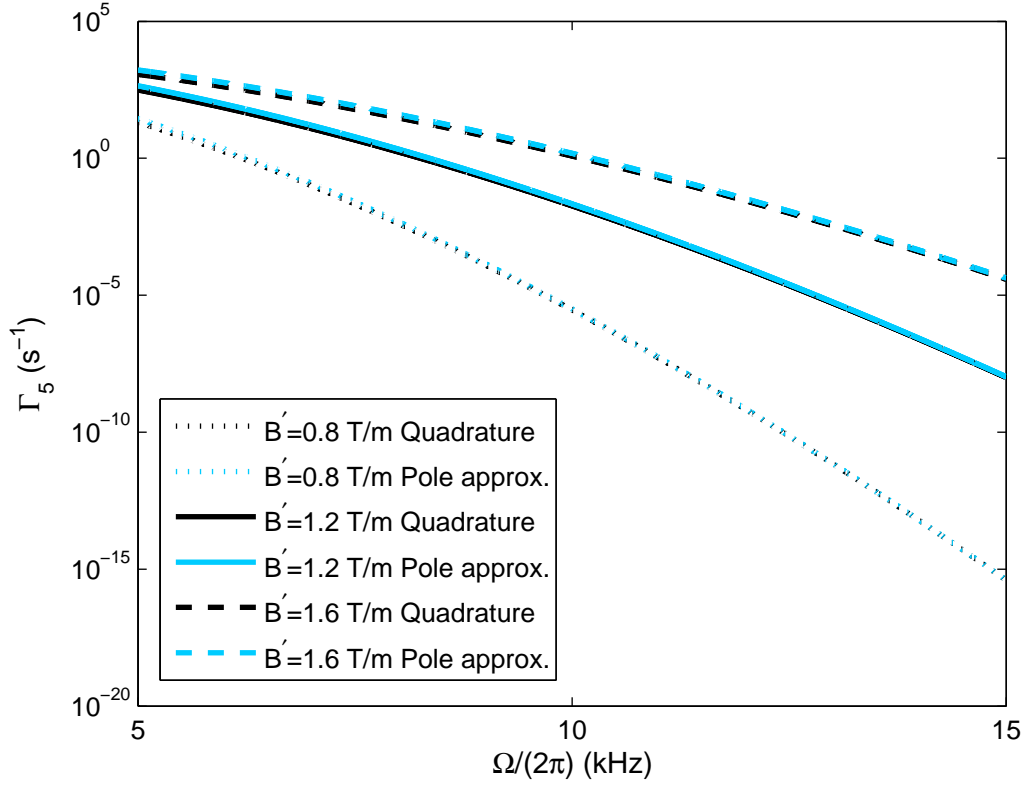


Figure 5.8: Affect of Rabi frequency and magnetic field gradient on the pole approximation decay rate and its agreement with the decay rate predicted by numerical quadrature integration. For ^{87}Rb , in the $n = 5$ level with dressed spin flip transition $|1, 1\rangle \rightarrow |1, 0\rangle$.

Figure 5.9 details how the pole approximation improves for high Rabi Frequencies which could be limiting for its usefulness in this study as non-adiabatic losses are dominant at low Rabi frequency. However, high Rabi frequency is the favourable region for RF-dressed trap operation, due to reduced non-adiabatic losses there, such that the pole approximation should be reliable for the majority of RF-dressed cold atom trap setups². Figure 5.9 also shows that the pole approximation provides a better model for the rate of non-adiabatic transitions from low energy harmonic

²Provided the minimal effect gravity model is itself appropriate for use, which shall be discussed in greater detail later.

oscillator states, this should not be a significant limitation as the low energy states are the most highly populated for the temperatures associated with cold atom traps.

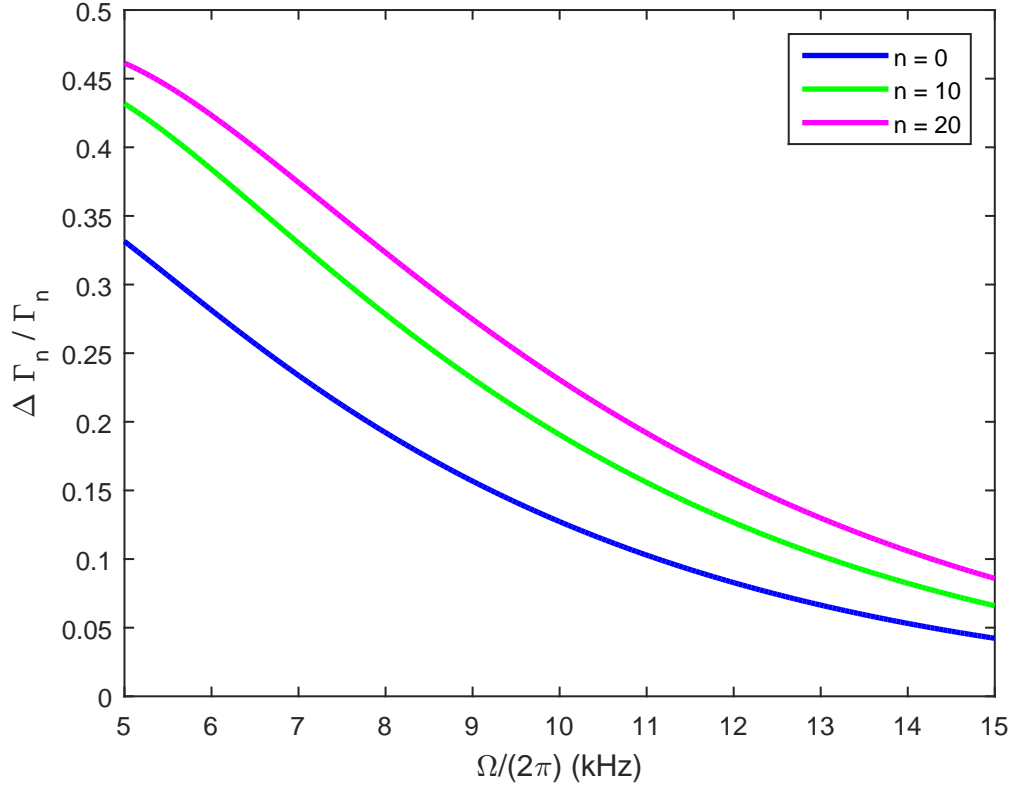


Figure 5.9: Error in the pole approximation variation with Rabi frequency for three different harmonic oscillator states. The error in the pole approximation is given by the difference between the decay rate given by the pole approximation and from equation (5.35) numerically integrated using quadrature analysis, divided by the quadrature decay rate. A magnetic field gradient of $B' = 1.1$ T/m was used. The atomic species being ^{87}Rb with the loss channel being $|1, 1\rangle \rightarrow |1, 0\rangle$ in the creation of this graph.

Figure 5.10 reconfirms that the pole approximation is a better approximation at high Rabi frequency values and additionally shows that the pole approximation is better at a lower magnetic field gradient. Low magnetic field gradients lead to less confinement in the trapping potentials and also lead to low rates associated with non-adiabatic decay, as seen in figure 5.8.

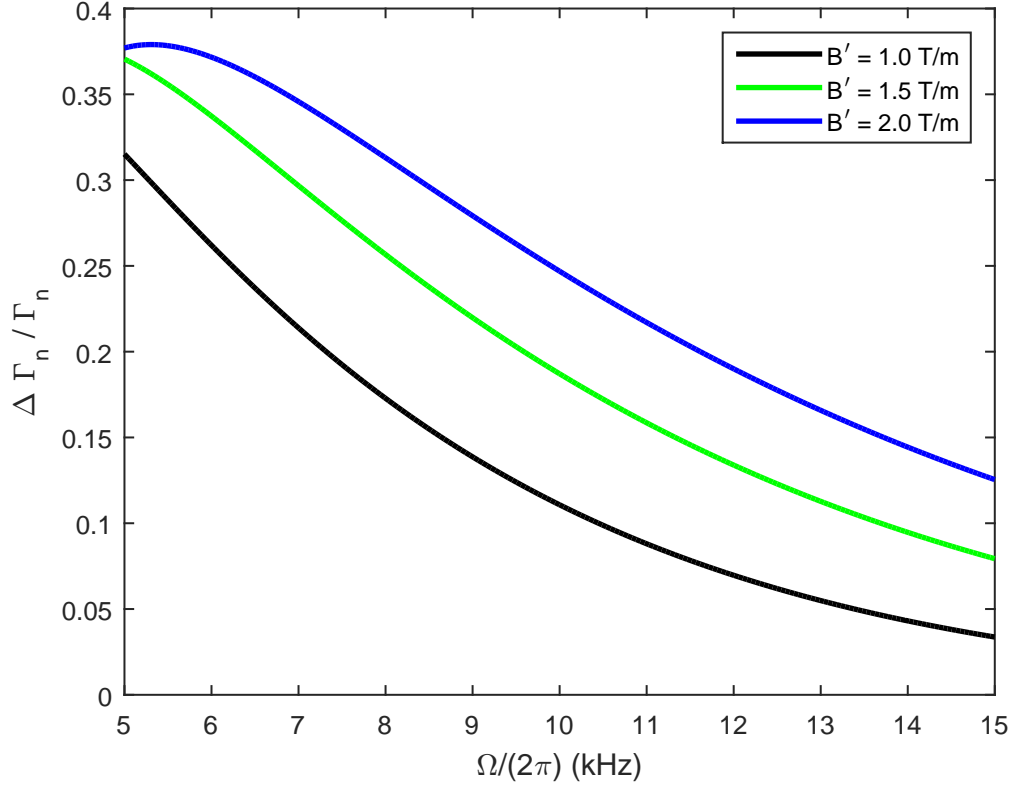


Figure 5.10: Error in the pole approximation variation with Rabi frequency for different magnetic field gradient values. The error in the pole approximation is given by the difference between the decay rate given by the pole approximation and from equation (5.35) numerically integrated using quadrature analysis divided by the quadrature obtained decay rate. The atomic species is ^{87}Rb , with dressed spin flip transition $|1, 1\rangle \rightarrow |1, 0\rangle$. The atom was assumed to be in the harmonic oscillator ground state.

5.1.3 Low decay limit

In this section we will simplify our analytic expression for the pole approximation, to see the dominant underlying behaviour. If the large α limit is taken, we are simultaneously finding the $\Omega \rightarrow \infty$ and $\lambda \rightarrow 0$ limits. These limits, in which decay due to non-adiabatic spin flips are low, are the regions in which cold atom traps favourably operate.

Equation (5.75) gives us the pole approximation expression for the decay rate from any initial harmonic oscillator n state. To begin in taking the $\alpha \rightarrow \infty$ limit we approximate the Hermite polynomials by their largest term using $H_n(x) \approx 2^n x^n$,

$$\begin{aligned} \frac{2\pi}{\omega} \Gamma_n &\approx \frac{\pi^2 \sqrt{\pi}}{2^{n+2} n! \beta_h} (F + m_f + 1)(F - m_f) \delta_{m_f+1}^{m_i} e^{\alpha^2 - 2\alpha\beta_h} \\ &\times \left| \left[2^n n (i\alpha)^{n-1} - 2^n i (\beta_h + \alpha) (i\alpha)^n \right] \right|^2. \end{aligned} \quad (5.78)$$

Common factors can be pulled out of the bracketed expression,

$$\begin{aligned} \frac{2\pi}{\omega} \Gamma_n &= \frac{2^n \pi^2 \sqrt{\pi}}{4n! \beta_h} (F + m_f + 1)(F - m_f) \delta_{m_f+1}^{m_i} \alpha^{2n} e^{\alpha^2 - 2\alpha\beta_h} \\ &\times \left| \left[n (i\alpha)^{-1} - i (\beta_h + \alpha) \right] \right|^2, \end{aligned} \quad (5.79)$$

to see that in the high α limit the dominant term is

$$\frac{2\pi}{\omega} \Gamma_n \approx \frac{2^n \pi^2 \sqrt{\pi}}{4n! \beta_h} (F + m_f + 1)(F - m_f) \delta_{m_f+1}^{m_i} (\beta_h + \alpha)^2 \alpha^{2n} e^{\alpha^2 - 2\alpha\beta_h}. \quad (5.80)$$

It is now instructive to return to equations (5.32) and (5.33) to consider the relative magnitudes of α and β_h . In the high α limit we can ignore the contributions from the ‘hump’ to give,

$$\alpha_{nh} = \left(\frac{m_0 m_i \Omega^3}{\hbar \lambda^2} \right)^{\frac{1}{4}} \quad (5.81)$$

and

$$\beta_{nh} = \sqrt{1 + 2n + 2(m_i - m_f) \frac{\Omega}{\omega}}. \quad (5.82)$$

In the no hump limit, β_h can be written equivalently as,

$$\beta_{nh} = \sqrt{1 + 2n + 2 \left(1 - \frac{m_f}{m_i} \right) \alpha_{nh}^2}, \quad (5.83)$$

due to

$$\omega = \frac{\Omega m_i}{\alpha_{nh}^2}. \quad (5.84)$$

It can be seen that in the $\alpha \rightarrow \infty$ limit, the ratio of β_h over α tends to a constant,

$$\frac{\beta_h}{\alpha} \rightarrow \sqrt{2 \left(1 - \frac{m_f}{m_i} \right)}. \quad (5.85)$$

It is therefore useful to rewrite equation (5.80) in the equivalent form

$$\frac{2\pi}{\omega}\Gamma_n \approx \frac{2^n \pi^2 \sqrt{\pi}}{4n!} (F + m_f + 1)(F - m_f) \delta_{m_f+1}^{m_i} \frac{\alpha}{\beta_h} \left(1 + \frac{\beta_h}{\alpha}\right)^2 \alpha^{2n+1} e^{\alpha^2 - 2\alpha\beta_h} \quad (5.86)$$

such that it is easier to see which terms will grow with an increase in α .

We can also study the value of the exponent, which will have the dominant influence on the limiting behaviour. The exponent is given by

$$\alpha^2 - 2\alpha\beta_h = \alpha^2 \left[1 - 2\sqrt{2\left(1 - \frac{m_f}{m_i}\right)} \sqrt{1 + \frac{1+2n}{2\left(1 - \frac{m_f}{m_i}\right)\alpha^2}} \right]. \quad (5.87)$$

A binomial expansion of this expression leads us to

$$\alpha^2 - 2\alpha\beta_h \approx \alpha^2 \left\{ 1 - 2\sqrt{2\left(1 - \frac{m_f}{m_i}\right)} \left[1 + \frac{1+2n}{4\left(1 - \frac{m_f}{m_i}\right)\alpha^2} \right] \right\} \quad (5.88)$$

such that in the high α limit there are two key contributing terms to the exponent,

$$\left[1 - 2\sqrt{2\left(1 - \frac{m_f}{m_i}\right)} \right] \alpha^2 \quad (5.89)$$

and

$$- \frac{1+2n}{\sqrt{2\left(1 - \frac{m_f}{m_i}\right)}}. \quad (5.90)$$

This allows us to express the high α limit of the pole approximation analytic expression for the rate of non-adiabatic transitions, expressed per harmonic oscillator period, as

$$\begin{aligned} \frac{2\pi}{\omega}\Gamma_n \approx & \frac{2^n \pi^2 \sqrt{\pi}}{4n!} (F + m_f + 1)(F - m_f) \frac{\delta_{m_f+1}^{m_i}}{\sqrt{2\left(1 - \frac{m_f}{m_i}\right)}} \left[1 + \sqrt{2\left(1 - \frac{m_f}{m_i}\right)} \right]^2 \\ & \cdot \alpha^{2n+1} \cdot e^{\left[1 - 2\sqrt{2\left(1 - \frac{m_f}{m_i}\right)}\right] \alpha^2} \cdot e^{-(1+2n)\left[2\left(1 - \frac{m_f}{m_i}\right)\right]^{-\frac{1}{2}}}. \end{aligned} \quad (5.91)$$

Use of equation (5.84) allows us to find the expression for the number of dressed spin flip transitions per second, as

$$\begin{aligned} \Gamma_n = & \frac{2^n \pi \sqrt{\pi} m_i}{8n!} (F + m_f + 1)(F - m_f) \frac{\delta_{m_f+1}^{m_i}}{\sqrt{2\left(1 - \frac{m_f}{m_i}\right)}} \left[1 + \sqrt{2\left(1 - \frac{m_f}{m_i}\right)} \right]^2 \\ & \cdot \Omega \alpha^{2n-1} \cdot e^{\left[1 - 2\sqrt{2\left(1 - \frac{m_f}{m_i}\right)}\right] \alpha^2} \cdot e^{-(1+2n)\left[2\left(1 - \frac{m_f}{m_i}\right)\right]^{-\frac{1}{2}}}. \end{aligned} \quad (5.92)$$

Therefore, the limiting behaviour for high Rabi frequency is

$$\Gamma_n \propto \Omega^{\frac{6n+1}{4}} e^{-\kappa \Omega^{\frac{3}{2}}}, \quad (5.93)$$

where κ is the appropriate constant when only Ω is allowed to vary and the limiting behaviour for low magnetic field gradient is

$$\Gamma_n \propto \frac{e^{-\frac{\kappa'}{\lambda}}}{\lambda^{\frac{2n-1}{2}}}, \quad (5.94)$$

where κ' is the appropriate constant when only λ is allowed to vary.

If we were to select the $F = 1$ transition from $m_i = 1$ to $m_f = 0$, we would obtain the high α limit decay rate of non-adiabatic transitions for an atom with energy associated with the n th harmonic oscillator level as

$$\Gamma_n \rightarrow \frac{2^n \pi \sqrt{2\pi}}{8n!} (1 + \sqrt{2})^2 \left(\frac{m_0^{2n-1} \Omega^{6n+1}}{\hbar^{2n-1} \lambda^{4n-2}} \right)^{\frac{1}{4}} e^{-\frac{1+2n}{\sqrt{2}}} e^{(1-2\sqrt{2})\sqrt{\frac{m_0 \Omega^3}{\hbar \lambda^2}}}. \quad (5.95)$$

It is clearer to see in this limiting formula, as opposed to equation (5.74), that the key trap parameters which affect non-adiabatic transitions are Ω and λ . The Rabi frequency, given by equation (3.25), is directly proportional to the magnitude of the RF magnetic field, while λ (see equation (5.3)) is directly proportional to the static magnetic field gradient (B'). Examining the exponents of equations (5.93) and (5.94) it is clear to see that the rate of non-adiabatic transitions decrease with an increase in Rabi frequency or a decrease in magnetic field gradient. This was shown earlier in figures 5.4 and 5.8 and is already known within the scientific community [1, 57].

This behaviour makes sense from our semiclassical interpretation. The trap frequency is increased for high magnetic field gradient or low Rabi frequency, which could be determined from equation (5.13). In these limits the atoms can be thought of as travelling faster, with a greater velocity. Additionally tighter trapping potentials leads to the orientation of the local magnetic field direction changing more rapidly over a given distance. Both of these factors result in a greater probability for an atom to become misaligned from the local magnetic field vector, leading to greater non-adiabatic losses as $\Omega \rightarrow 0$ or $B' \rightarrow \infty$. Equations (5.93) and (5.94) are useful for specifying the main dependence of non-adiabatic decay rates on Ω and λ , additionally indicating that the process is more sensitive to Rabi frequency than magnetic field gradient.

Figure 5.11 displays a comparison of the limiting formulae given by equation (5.92) with the decay rate for the pole approximation from which it is derived. Apart from at the lowest Rabi frequency values plotted, the limiting formula does appear

to agree with the pole approximation. This is useful, as the limiting formula given by equation (5.95) has a much simpler form than the pole approximation formula given by equation (5.74). However, figure 5.12 issues a word of caution in relying on the limiting formula for more than an order of magnitude estimation. It can be seen that the limiting formula given by equation (5.95) is not particularly reliable, especially with an increase in atomic energy. It is also worth remembering that the pole approximation from which we have derived the limiting formula is itself an approximation.

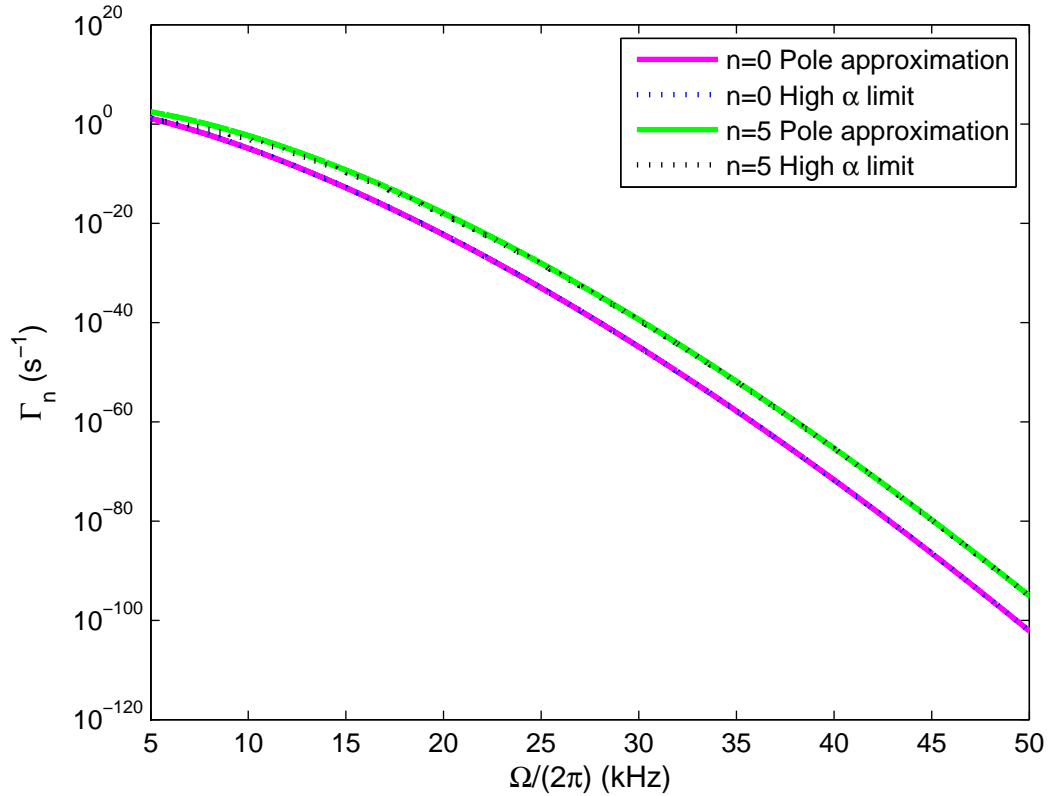


Figure 5.11: Comparing the limiting formula given by equation (5.95) with the exact analytical result given by equation (5.74) for the $n = 0$ and $n = 5$ levels. A magnetic field gradient of $B' = 1.1$ T/m was used for ^{87}Rb atoms.

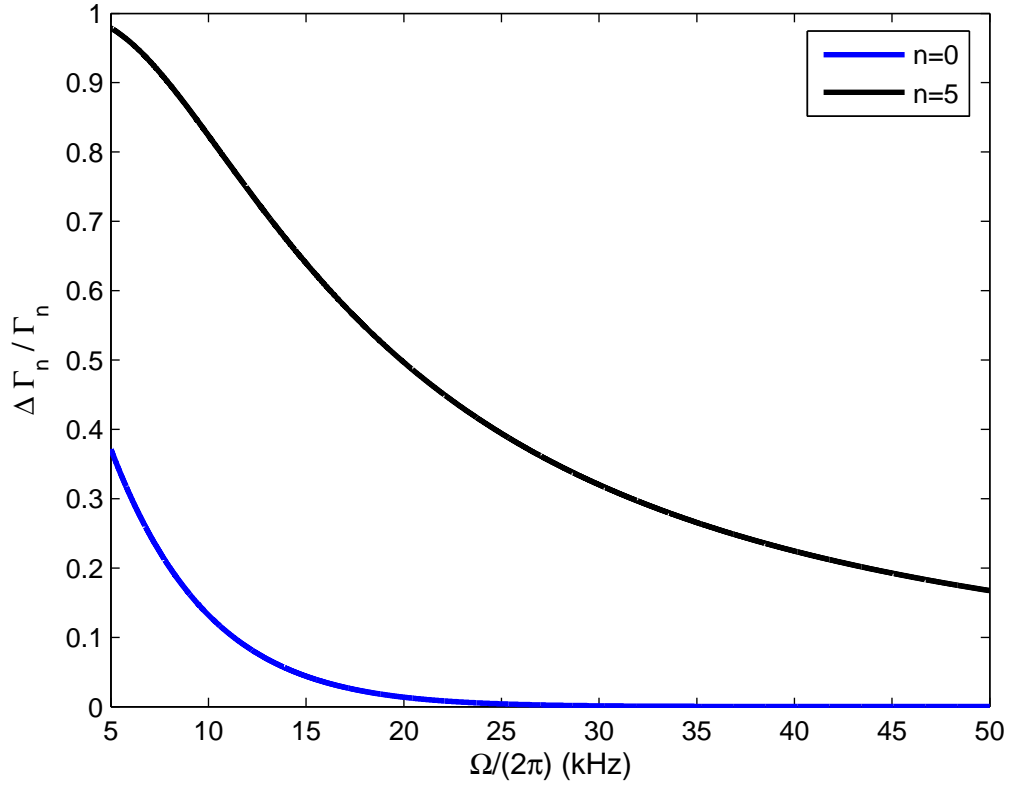


Figure 5.12: Fractional difference between the limiting formula given by equation (5.95) with the pole approximation decay rate given by equation (5.74) for the $n = 0$ and $n = 5$ levels. A magnetic field gradient of $B' = 1.1$ T/m was used for ^{87}Rb atoms.

We have now used Fermi's Golden Rule to derive several decay rates associated with the minimal effect gravity model. We have equation (5.74) which provides an analytic pole approximation for the rate of dressed spin state transitions and its limiting formula, given by equation (5.92), studied here. We have an exact result for the decay rate for an atom trapped with ground state energy, given by equation (5.27), and we are able to find non-approximate decay rate values to a given accuracy from numerical integration of equation (5.35). This concludes our development of the minimal effect gravity model. From this point onwards our analytic results for the minimal effect gravity model shall be grouped together. When the pole approximation is referred to from now on, this denotes using equation (5.74) for $n > 0$ and the ground state decay rate given by equation (5.27) for the $n = 0$ case.

5.2 Full effect gravity model

We now develop the full effect gravity model by including the contribution of the gravitational potential in our trapped atom Hamiltonian. For comparison with experimental results which we shall undertake in chapter 8, the z axis, the one dimensional direction of interest, is the vertical direction (see figure 8.1) meaning that a trapped atom feels the full force of gravity. Inclusion of gravity in the model alters the adiabatic potentials and thus the atom's wavefunction and subsequently its decay rate. To include gravity in our model we add a term of m_0gz onto our minimal effect gravity Hamiltonian given by equation (3.36), so that

$$V(z) = \hbar m_F \sqrt{\Omega^2 + \delta^2} + \mathcal{H} \frac{\Omega^2 \delta'^2}{(\Omega^2 + \delta^2)^2} + m_0 g z \quad (5.96)$$

where g is the gravitational acceleration. The zero line of gravitational potential energy is defined to coincide with the origin of the z axis, where the detuning is zero.

As performed at the start of section 5.1 we Taylor expand our trap potential to approximate the confinement of the atom in the vertical direction by a harmonic oscillator. Differentiation of equation (5.96) gives

$$\begin{aligned} V(z) &= \hbar m_F \sqrt{\Omega^2 + \delta^2} + \mathcal{H} \frac{\Omega^2 \lambda^2}{(\Omega^2 + \delta^2)^2} + m_0 g z, \\ \frac{\partial V}{\partial z} &= -\hbar m_F \lambda \frac{\delta}{\sqrt{\Omega^2 + \delta^2}} + 4\mathcal{H} \Omega^2 \lambda^3 \frac{\delta}{(\Omega^2 + \delta^2)^3} + m_0 g, \\ \frac{\partial^2 V}{\partial z^2} &= \hbar m_F \Omega^2 \lambda^2 \frac{1}{(\Omega^2 + \delta^2)^{\frac{3}{2}}} - 4\mathcal{H} \Omega^2 \lambda^4 \frac{(\Omega^2 - 5\delta^2)}{(\Omega^2 + \delta^2)^4}. \end{aligned} \quad (5.97)$$

The atoms are located at the minimum point of the potential where $\frac{\partial V}{\partial z} \big|_{z_0} = 0$, leading us to the expression

$$0 = m_F \frac{\delta_0}{\sqrt{\Omega^2 + \delta_0^2}} - \frac{4\mathcal{H}}{\hbar} \Omega^2 \lambda^2 \frac{\delta_0}{(\Omega^2 + \delta_0^2)^3} - \epsilon. \quad (5.98)$$

$\delta_0 = \delta(z_0)$ is the detuning at the centre of the atom cloud and the variable

$$\epsilon = \frac{m_0 g}{\hbar \lambda} \quad (5.99)$$

is introduced as the ratio of the gravitational force to the force applied by the magnetic field gradient. Equation (5.98) can be numerically evaluated to find δ_0 . For an analytic expression for δ_0 we can take the limit in which the hump is negligible,

giving us

$$0 \approx m_F \frac{\delta_0}{\sqrt{\Omega^2 + \delta_0^2}} - \epsilon, \quad (5.100)$$

$$\epsilon^2 = \frac{m_F^2 \delta_0^2}{\Omega^2 + \delta_0^2}, \quad (5.101)$$

$$\delta_0^2 = \frac{\epsilon^2 \Omega^2}{m_F^2 - \epsilon^2}, \quad (5.102)$$

$$\delta_0 = \frac{\epsilon \Omega}{\sqrt{m_F^2 - \epsilon^2}}. \quad (5.103)$$

This gives the displacement from the resonant detuning position as

$$z_0 = -\frac{\epsilon \Delta S}{\sqrt{m_F^2 - \epsilon^2}}. \quad (5.104)$$

This shows the first effect of gravity: the centre of the harmonic potential is not on the resonant ellipsoid but below it. As the variable ϵ is small the centre of the trap is still located close to the resonant ellipsoid. However, this shift away from the resonance location will have a significant influence on non-adiabatic effects. The magnitude of this shift is shown in figure 5.13, while the effect on our models is shown later in figures 5.14 and 5.15.

Substitution of equation (5.104) into equation (5.97) gives

$$\begin{aligned} V(z_0) &= \frac{\hbar \Omega}{\sqrt{m_F^2 - \epsilon^2}} (m_F |m_F| - \epsilon^2) + \frac{\mathcal{H}}{\Delta S^2} \frac{(m_F^2 - \epsilon^2)^2}{m_F^4}, \\ \left. \frac{\partial V}{\partial z} \right|_{z_0} &= \frac{\hbar \Omega \epsilon}{\Delta S} \left(1 - \frac{m_F}{|m_F|} \right) + \frac{4\mathcal{H}\epsilon}{\Delta S^3} \frac{(m_F^2 - \epsilon^2)^{\frac{5}{2}}}{m_F^6}, \\ \left. \frac{\partial^2 V}{\partial z^2} \right|_{z_0} &= \frac{\hbar m_F \Omega}{\Delta S^2} \frac{(m_F^2 - \epsilon^2)^{\frac{3}{2}}}{|m_F|^3} + \frac{4\mathcal{H}}{\Delta S^4} (6\epsilon^2 - m_F^2) \frac{(m_F^2 - \epsilon^2)^3}{m_F^8}. \end{aligned} \quad (5.105)$$

If instead δ_0 is calculated numerically³ with the hump included,

$$\begin{aligned} V(z_0) &= \hbar m_F \sqrt{\Omega^2 + \delta_0^2} + \mathcal{H} \Omega^2 \lambda^2 \frac{1}{(\Omega^2 + \delta_0^2)^2} + m_0 g z_0, \\ \left. \frac{\partial V}{\partial z} \right|_{z_0} &= 0, \\ \left. \frac{\partial^2 V}{\partial z^2} \right|_{z_0} &= \hbar m_F \Omega^2 \lambda^2 \frac{1}{(\Omega^2 + \delta_0^2)^{\frac{3}{2}}} - 4\mathcal{H} \Omega^2 \lambda^4 \frac{(\Omega^2 - 5\delta_0^2)}{(\Omega^2 + \delta_0^2)^4}. \end{aligned} \quad (5.106)$$

In either case the trap potential is approximated by a harmonic potential

$$V_i(z') = V_0 + \frac{1}{2} m_0 \omega_g^2 z'^2, \quad (5.107)$$

³Use equation (5.103) as the starting value for determining δ_0 numerically with equation (5.98). Matlab function ‘fzero’ was the solver used in the results presented here [61].

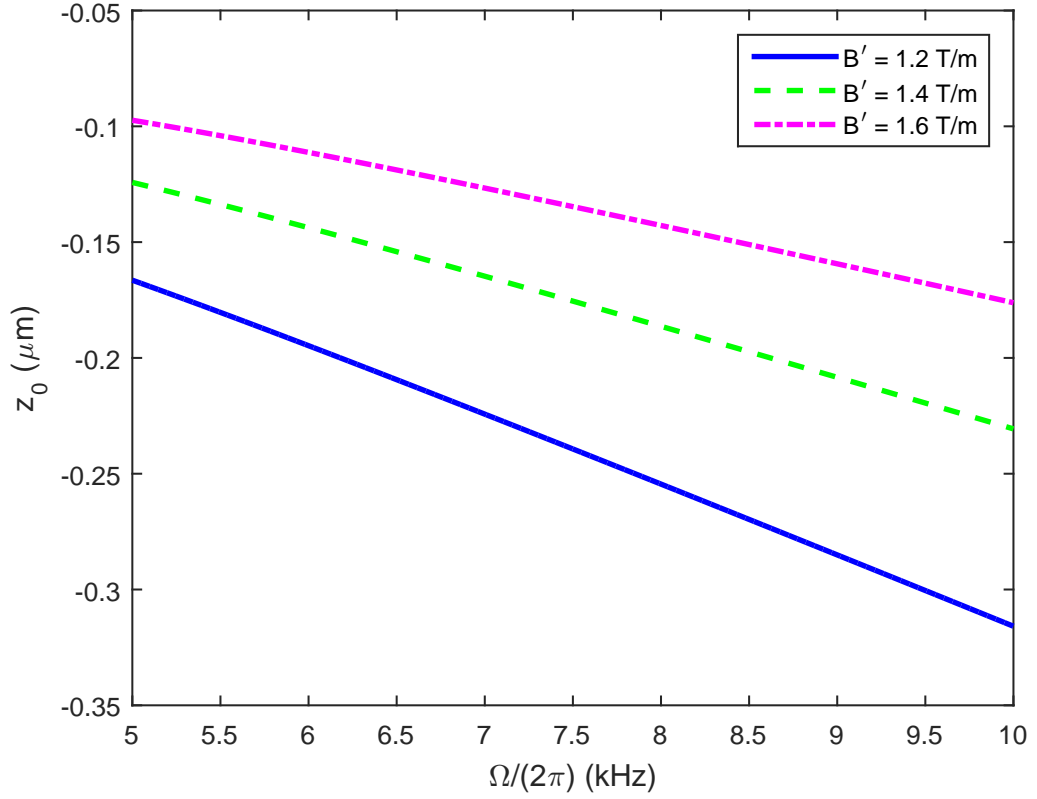


Figure 5.13: The magnitude of the shift below resonance in the full effect gravity model given by $z_0 = \delta_0/\lambda$. δ_0 is calculated by numerically solving equation (5.98) using Matlab in-built function ‘fzero’ [61].

where

$$z' = z + \frac{\delta_0}{\lambda} \quad (5.108)$$

is a new co-ordinate system defined such that the origin coincides with the minima of the harmonic potential, which should be the centre of the atomic cloud. The harmonic potential has energy offset

$$V_0 = \hbar m_i \sqrt{\Omega^2 + \delta_0^2} + \frac{\mathcal{H}\Omega^4}{\Delta S^2} \frac{1}{(\Omega^2 + \delta_0^2)^2} - \hbar \epsilon \delta_0 \quad (5.109)$$

and trap frequency

$$\omega_g = \sqrt{\frac{\Omega^4}{m_0 \Delta S^2} \left[\frac{\hbar m_i}{(\Omega^2 + \delta_0^2)^{\frac{3}{2}}} + \frac{4\mathcal{H}\Omega^2}{\Delta S^2} \frac{(5\delta_0^2 - \Omega^2)}{(\Omega^2 + \delta_0^2)^4} \right]} \quad (5.110)$$

in the general case. Alternatively in the $\mathcal{H} \rightarrow 0$ limit, the energy offset is given by

$$V_0 = \hbar \Omega \sqrt{m_i^2 - \epsilon^2}, \quad (5.111)$$

with trap frequency

$$\omega_g = \sqrt{\frac{\hbar\Omega}{m_0\Delta S^2} \frac{(m_i^2 - \epsilon^2)^{\frac{3}{2}}}{m_i^2}}. \quad (5.112)$$

The wavefunction for the harmonic potential $V_i(z')$ is

$$\Psi_n(z') = \frac{H_n\left(\frac{z'}{\sigma}\right)e^{-\frac{z'^2}{2\sigma^2}}}{\sqrt{n!2^n\sigma\sqrt{\pi}}} \quad (5.113)$$

for atoms with corresponding energy

$$E_n = \left(n + \frac{1}{2}\right) \hbar\omega_g + V_0. \quad (5.114)$$

For the untrapped state the potential has now acquired a position dependence,

$$V_f(z) = \begin{cases} \infty, & z \leq -\frac{L}{2}, \\ \hbar m_f \Omega + \frac{\mathcal{H}(m_f)}{\Delta S^2} + m_0 g z, & z > -\frac{L}{2}, \end{cases}$$

which will have a significant effect on the results obtained. The stationary Schrödinger equation for the untrapped state is

$$\Delta E \Psi_{n_f} = -\frac{\hbar^2}{2m_0} \frac{\partial^2 \Psi_{n_f}}{\partial z^2} + m_0 g z \Psi_{n_f} \quad (5.115)$$

where the value

$$\Delta E = E_n - \left[\hbar m_f \Omega + \frac{\mathcal{H}(m_f)}{\Delta S^2} \right] \quad (5.116)$$

is shown in figure 5.14. Equation (5.115) can be written as a second order partial differential equation,

$$0 = \frac{\partial^2 \Psi_{n_f}}{\partial \zeta^2} - \zeta \Psi_{n_f} \quad (5.117)$$

where

$$\zeta(z) = \left(\frac{2m_0^2 g}{\hbar^2} \right)^{\frac{1}{3}} \left(z - \frac{\Delta E}{m_0 g} \right). \quad (5.118)$$

The solution of equation (5.117) can be obtained from reference [60] and tells us that the wavefunction for the untrapped state is

$$\Psi_{n_f}(z) = a \text{Ai}(\zeta) = a \text{Ai}[G(z - z_t)] \quad (5.119)$$

[60] where a is a normalisation constant and $\text{Ai}(\zeta)$ is the Airy function of the first kind. The $\text{Bi}(\zeta)$ component of the solution to equation (5.117) is not present as its normalisation co-efficient is zero to allow Ψ_{n_f} to be normalisable. The variable

$$G = \left(\frac{2m_0^2 g}{\hbar^2} \right)^{\frac{1}{3}} \quad (5.120)$$

is a inverse length which relates a unit change in z to a unit change in the standardized Airy function. The variable

$$z_t = \frac{\Delta E}{m_0 g} \quad (5.121)$$

determines the location of the largest peak for the untrapped state wavefunction which is set to select out the untrapped state with energy equivalent to the trapped state, shown in figure 5.14.

Figure 5.14 shows the full effect gravity model, with the new z' axis which is shifted by z_0 from the z axis. The z axis aligns with the origin at the resonance location. The z' axis is instead defined, as shown in figure 5.14, from the centre of the shifted harmonic oscillator.

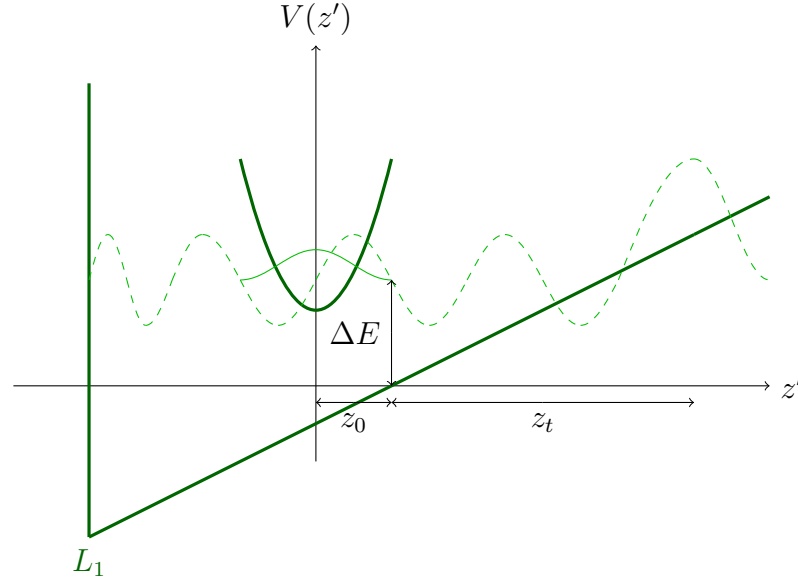


Figure 5.14: Schematic diagram showing the full effect gravity model. The ground state wavefunction of the harmonic oscillator is shown setting the Airy wavefunction energy and the value of ΔE . z_t and ΔE would increase for a higher n state.

Figure 5.15 compares the full effect gravity and minimal effect gravity models. The harmonic oscillator minimum has shifted away from its previous position where the detuning is zero. For low energy eigenstates of the harmonic oscillator this should lower the decay rate of the atoms as they are now more likely to be found in regions away from resonance. However, some higher energy eigenstates may have an increased decay rate as with the shifting of the harmonic oscillator potential, they may now overlap with the resonance position when they did not previously.

The interaction matrix element will also be significantly affected by the fact that potential of the final state now slopes.

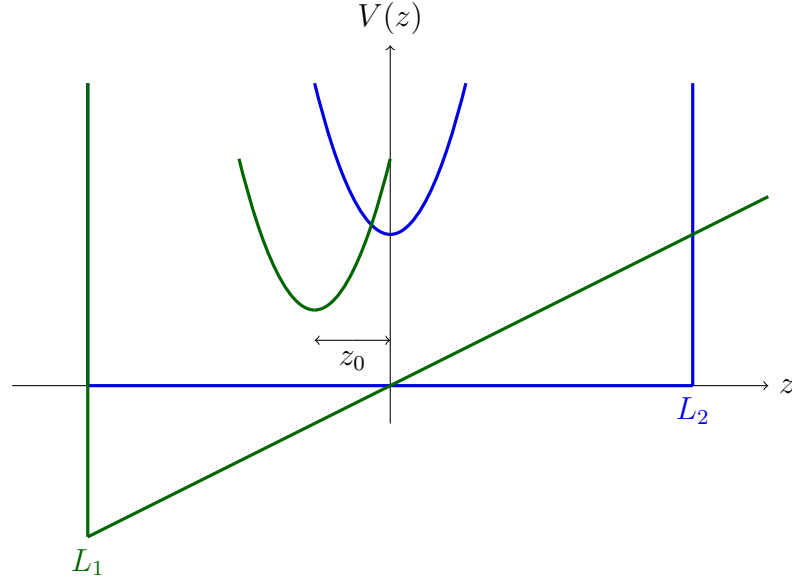


Figure 5.15: Schematic diagram comparing the minimal effect gravity model, shown in blue, and the full effect gravity model, shown in green. The vertical axis marks the resonance location.

The normalisation constant a for the untrapped state wavefunction can be determined from the condition that

$$1 = |a|^2 \int_{-\frac{L}{2}}^{\infty} |\text{Ai}[\zeta(z)]|^2 dz, \quad (5.122)$$

which can be written more conveniently as

$$1 = \frac{|a|^2}{G} \int_{\zeta(-\frac{L}{2})}^{\zeta(\infty)} |\text{Ai}(\zeta)|^2 d\zeta. \quad (5.123)$$

The Airy function can be approximated in the small ζ limit [39] by

$$\text{Ai}(\zeta) \approx \frac{\sin \left[\frac{2}{3}(-\zeta)^{\frac{3}{2}} + \frac{\pi}{4} \right]}{\sqrt{\pi}(-\zeta)^{\frac{1}{4}}}. \quad (5.124)$$

Use of the asymptotic form of the Airy function allows equation (5.123) to be expressed as

$$1 = \frac{|a|^2}{G} \left\{ \int_{\zeta(-\frac{L}{2})}^w \frac{\sin^2 \left[\frac{2}{3}(-\zeta)^{\frac{3}{2}} + \frac{\pi}{4} \right]}{\pi \sqrt{(-\zeta)}} d\zeta + \int_w^{\zeta(\infty)} |\text{Ai}(\zeta)|^2 d\zeta \right\} \quad (5.125)$$

where w is a negative constant. This is equivalent to

$$1 = \frac{|a|^2}{G} \left\{ \int_{\zeta(-\frac{L}{2})}^w \frac{1 - \cos \left[\frac{4}{3}(-\zeta)^{\frac{3}{2}} + \frac{\pi}{2} \right]}{2\pi \sqrt{(-\zeta)}} d\zeta + \int_w^{\zeta(\infty)} |\text{Ai}(\zeta)|^2 d\zeta \right\}. \quad (5.126)$$

Due to the fact that $L \rightarrow \infty$, the dominant term of this expression is

$$1 = \frac{|a|^2}{2\pi G} \int_{\zeta(-\frac{L}{2})}^w \frac{1}{\sqrt{-\zeta}} d\zeta, \quad (5.127)$$

this is a solvable integral giving the expression

$$1 \approx \frac{|a|^2}{\pi G} \sqrt{-\zeta \left(-\frac{L}{2} \right)}, \quad (5.128)$$

Therefore, an approximate normalisation constant for the untrapped state wavefunction is given by

$$|a|^2 \approx \frac{\pi G}{\sqrt{-\zeta \left(-\frac{L}{2} \right)}}. \quad (5.129)$$

To obtain an expression for the density of states, necessary for use of Fermi's Golden Rule, we consider the boundary condition for the wavefunction:

$$\Psi_{n_f} \left(-\frac{L}{2} \right) = 0 = \text{Ai} \left[\zeta \left(-\frac{L}{2} \right) \right]. \quad (5.130)$$

The asymptotic form of the Airy function, given by equation (5.124), can be used to express this condition as

$$0 \approx \sin \left\{ \frac{2}{3} \left[-\zeta \left(-\frac{L}{2} \right) \right]^{\frac{3}{2}} + \frac{\pi}{4} \right\}, \quad (5.131)$$

which signifies a quantization condition for the allowed n_f states associated with the untrapped potential, given by

$$n_f \pi = \frac{2}{3} \left[-\zeta \left(-\frac{L}{2} \right) \right]^{\frac{3}{2}} + \frac{\pi}{4}. \quad (5.132)$$

Differentiation of the quantization condition leads to our expression for the density of the states,

$$D(E_{n_f}) = \frac{\partial n_f}{\partial E_{n_f}} = \frac{\partial n_f}{\partial \zeta} \frac{\partial \zeta}{\partial E_{n_f}} = \frac{G}{\pi m_0 g} \sqrt{-\zeta \left(-\frac{L}{2} \right)}. \quad (5.133)$$

It is noteworthy that the L dependence cancels in the product

$$|a|^2 \cdot D(E_{n_f}) = \frac{G^2}{m_0 g} \quad (5.134)$$

such that we will have no issues when taking the $L \rightarrow \infty$ limit.

The interaction matrix element, required for Fermi's Golden Rule, is calculated using equation (4.33),

$$V_{iAf} = \frac{\hbar}{2i} \sqrt{(F + m_f + 1)(F - m_f)} \delta_{m_f+1}^{m_i} \int_{-\infty}^{\infty} \Psi_n^{*(i)}(z) \hat{V}_A \Psi_{n_f}^{(f)}(z) dz$$

in which we shall use the new wavefunctions given by equations (5.113) and (5.119). For more accurate numerical integration it is better to integrate over an even interval in z' , as the Gaussian associated with the harmonic oscillator wavefunction creates an envelope for the integrand. The interaction matrix element, expressed in terms of the z' co-ordinate system, is

$$\begin{aligned} V_{iAf} = & -\frac{\hbar^2 \Delta S a}{2m_0} \sqrt{\frac{(F + m_f + 1)(F - m_f)}{n! 2^n \sigma \sqrt{\pi}}} \delta_{m_f+1}^{m_i} \\ & \times \left\{ \int_{-\infty}^{\infty} H_n \left(\frac{z'}{\sigma} \right) e^{-\frac{z'^2}{2\sigma^2}} \frac{\left(z' - \frac{\delta_0}{\lambda} \right)}{\left[\left(z' - \frac{\delta_0}{\lambda} \right)^2 + \Delta S^2 \right]^2} \text{Ai}(\zeta) dz' \right. \\ & \left. - G \int_{-\infty}^{\infty} \frac{H_n \left(\frac{z'}{\sigma} \right) e^{-\frac{z'^2}{2\sigma^2}}}{\left(z' - \frac{\delta_0}{\lambda} \right)^2 + \Delta S^2} \frac{\partial \text{Ai}(\zeta)}{\partial \zeta} dz' \right\} \end{aligned} \quad (5.135)$$

where ζ , given by equation (5.118), is a function of z' , defined in equation (5.108). By substituting the density of states, square of the interaction matrix element and approximation for the normalisation constant into Fermi's Golden Rule (4.28), the expression for the rate of dressed spin state transitions in the full effect gravity model is given by

$$\begin{aligned} \Gamma_n = & \frac{\sqrt{\pi} \hbar \Delta S^2}{m_0 G \sigma} \frac{(F + m_f + 1)(F - m_f)}{n! 2^n} \delta_{m_f+1}^{m_i} \\ & \times \left| \left\{ \int_{-\infty}^{\infty} H_n \left(\frac{z'}{\sigma} \right) e^{-\frac{z'^2}{2\sigma^2}} \frac{\left(z' - \frac{\delta_0}{\lambda} \right)}{\left[\left(z' - \frac{\delta_0}{\lambda} \right)^2 + \Delta S^2 \right]^2} \text{Ai}(\zeta) dz' \right. \right. \\ & \left. \left. - G \int_{-\infty}^{\infty} \frac{H_n \left(\frac{z'}{\sigma} \right) e^{-\frac{z'^2}{2\sigma^2}}}{\left(z' - \frac{\delta_0}{\lambda} \right)^2 + \Delta S^2} \frac{\partial \text{Ai}(\zeta)}{\partial \zeta} dz' \right\} \right|^2. \end{aligned} \quad (5.136)$$

This shall be left as an integral expression, as the integrals contained within equation (5.136) are not readily solvable. Instead numerical integration techniques can be used to find the full effect gravity model decay rates. For the results presented here in-built Matlab functions 'airy' and numerical integrator 'quadgk' were used [61].

There is a dramatic change in the decay rate obtained when the full effects of gravity are brought into consideration, as can be seen from figure 5.16. There are two key differences between the minimal effect gravity and full effect gravity

models; the shift of the harmonic oscillator centre away from the resonant detuning location and the change in the wavefunction for the untrapped state. The change to an Airy function for the untrapped state wavefunction significantly affects the obtained decay rates. Unlike in the minimal effect gravity model, the amplitude and frequency of oscillations in the final state wavefunction now vary with position. This leads to oscillatory behaviour in the interaction matrix elements.

The shift in the centre of the harmonic oscillator also has significant effects. For states which have a high probability to be found in the centre of the harmonic oscillator (the most important of these being the ground state) gravity suppresses decay as it shifts the atoms away from the resonant detuning location, where losses are most likely to occur. However, for some harmonic oscillator n states the shift can increase losses, as peaks in the harmonic oscillator wavefunction that were previously above the resonant detuning location now get shifted into resonance.

The result of the combination of these effects is seen in figure 5.16. Most strikingly, it is now possible that atoms with higher energy can, in some instances, be sheltered from non-adiabatic effects. The lower predicted transition rate that may occur for higher energy atoms is counter to classical intuition and is not found in the minimal effect gravity model.

Figures 5.17 to 5.19 further highlight the difference in the obtained decay rates once gravitational effects have been fully considered. The oscillatory nature of the full effect gravity model decay rate values, with both Rabi frequency and magnetic field gradient, is due to the Airy function untrapped state wavefunction⁴. Overall the decay rate is reduced compared to the minimal effect gravity model due to the shifting of the harmonic oscillator. For the full effect gravity model there is no longer a smooth dependence on n, Ω or B' ; we shall see later that the loss of a 1 – 1 mapping between the decay rate values and the value of the Rabi frequency will have a significant effect on results discussed in chapter 8.

⁴This can be seen most clearly numerically by removing the Airy function from equation (5.136) and noticing that the oscillatory behaviour has now vanished.

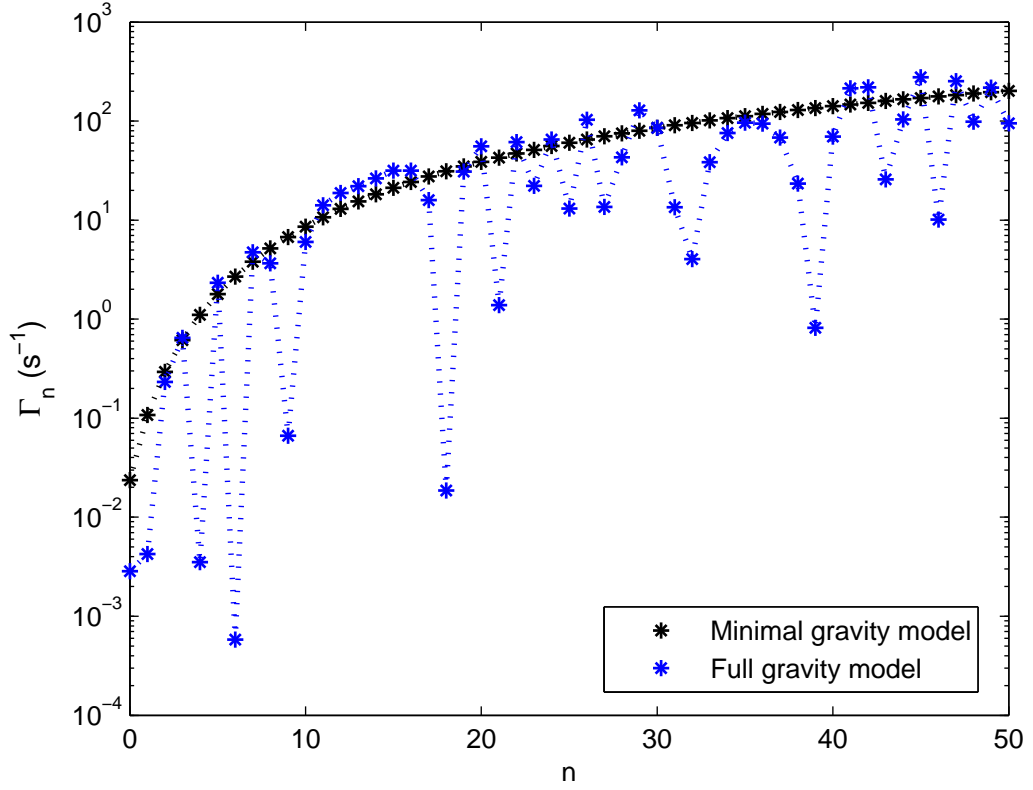


Figure 5.16: Full effect gravity model decay rates as given by equation (5.136) dependence on the harmonic oscillator energy level (n). Plotted for comparison are the minimal effect gravity model decay rates as given by equation (5.35). Dotted lines are added to guide the eye. A magnetic field gradient of $B' = 1.1 \text{ T/m}$ and a Rabi frequency of $\Omega/2\pi = 7.5 \text{ kHz}$ were used for ^{87}Rb atoms with dressed spin flip transition $|1, 1\rangle \rightarrow |1, 0\rangle$.

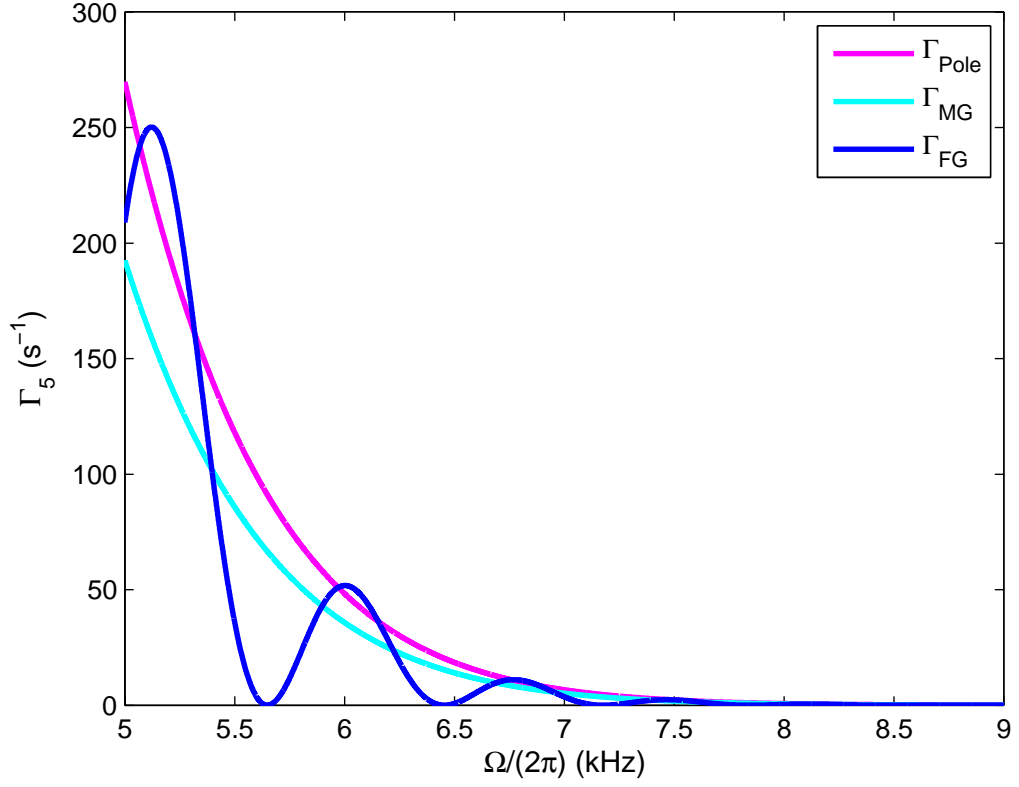


Figure 5.17: Different decay rates variation with Rabi frequency. Γ_{FG} signifies the decay rate obtained for the full effect gravity model, given by equation (5.136). Γ_{MG} signifies the decay rate obtained for the minimal effect gravity model, given by equation (5.35). For the minimal effect gravity model there is also the decay rates obtained by the pole approximation, represented by Γ_{Pole} . The $n = 5$ state of ^{87}Rb , $B' = 1.1 \text{ T/m}$ with dressed spin flip transition $|1, 1\rangle \rightarrow |1, 0\rangle$ was used.

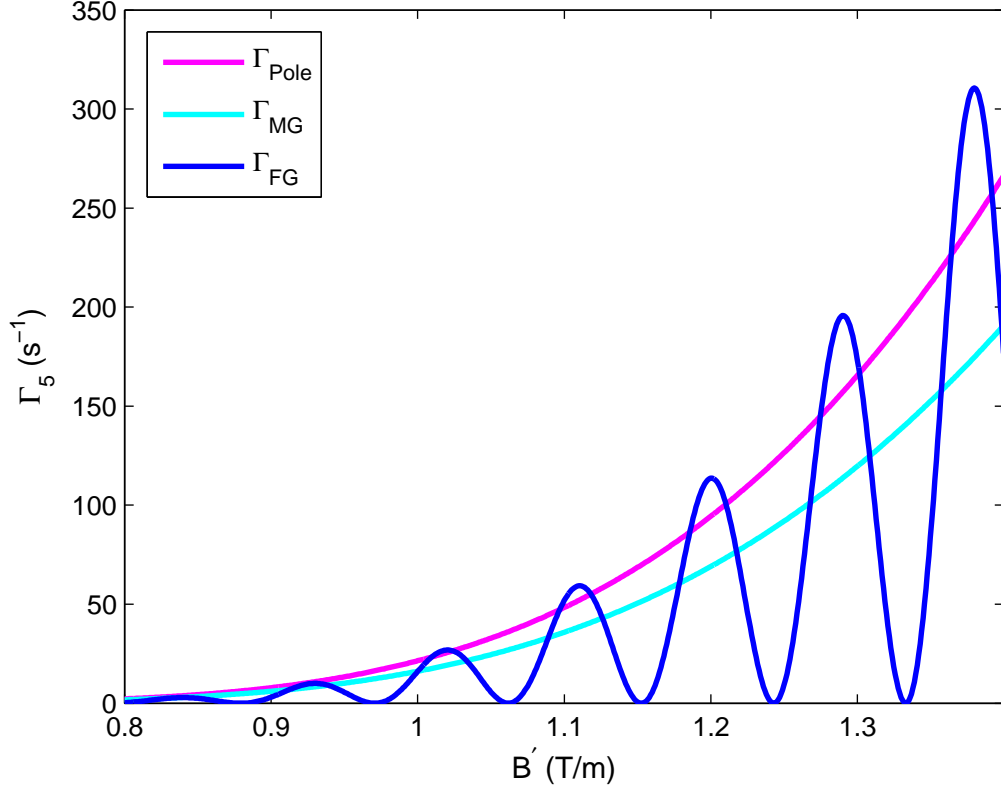


Figure 5.18: Different decay rates variation with magnetic field gradient. Γ_{FG} signifies the decay rate obtained for the full effect gravity model, given by equation (5.136). Γ_{MG} signifies the decay rate obtained for the minimal effect gravity model, given by equation (5.35). For the minimal effect gravity model there is also the decay rates obtained by the pole approximation, represented by Γ_{Pole} . The $n = 5$ state of ^{87}Rb , $\Omega/(2\pi) = 6$ kHz with dressed spin flip transition $|1, 1\rangle \rightarrow |1, 0\rangle$ was used.

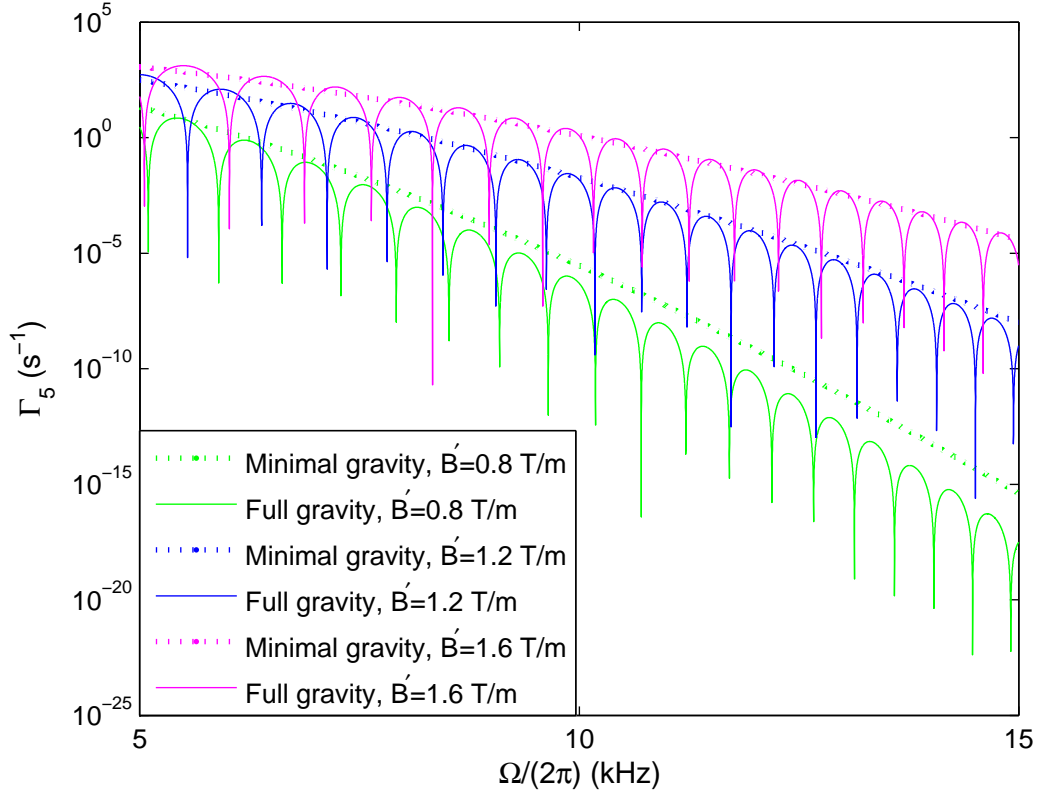


Figure 5.19: Examining how the full effect gravity decay rates, as given by equation (5.136), vary with Rabi frequency and magnetic field gradient for the $n = 5$ state. Plotted for guidance are the minimal effect gravity decay rates, as given by equation (5.35). The Rabi frequencies were sampled at a spacing of 1 Hz. ^{87}Rb , with dressed spin flip transition $|1, 1\rangle \rightarrow |1, 0\rangle$ was used.

To understand the origin of the oscillatory behaviour exhibited by the decay rates obtained, displayed in figures 5.16 to 5.19, it is necessary to examine the full effect gravity model in greater detail. First we consider the results displayed in figure 5.16. Figure 5.20 shows how the atom's two possible wavefunctions, for the trapped and untrapped states, are affected by a change in atom energy. The trapped atom wavefunction changes dramatically with a change in harmonic oscillator level. It can be seen for the $n = 1$ case (dashed light blue) that the value of the wavefunction at $z = 0$, the resonant detuning location, is now non-zero. This indicates that it would increase the decay rate for this $n = 1$ case (this is only an indication as the couplings do not only occur at the resonant detuning location). However, for many harmonic oscillator n states such as the ground state (dashed green) the shifting of the trap centre now moves peaks of the trapped atom wavefunctions away from the resonance location. This explains why in general the full effect gravity model leads to a lower rate of non-adiabatic transitions than the minimal effect gravity model, as seen in figure 5.19. It can also be seen from figure 5.20 that as the energy of the untrapped state is set to match that of the trapped atom, necessary to satisfy Fermi's Golden Rule, changing the harmonic oscillator energy level affects the Airy wavefunction. The shifts which occur for the trapped and untrapped state wavefunctions for increasing E_n combine together to lead to the behaviour observed in figure 5.16.

Now we consider, using figures 5.21 and 5.22, the results displayed in figure 5.17. Figure 5.21 shows the behaviour of the trapped and untrapped state wavefunctions with a change in Rabi frequency. From the vertical dotted line, acting as a guide to the centre of the ground state wavefunction, it can be seen that the highest probability point has been shifted away from the resonant detuning location at $z = 0$. However, the shift in the z' axis does not change significantly with a change in Rabi frequency when compared to the shift of z_t for the Airy function. As Ω is increased the Airy function value at the centre of the z' axis progresses between peaks and troughs.

Figure 5.22 shows that peaks in the decay rate oscillations correspond to the centre of integration slicing through an oscillation in the integrand value, while troughs in the decay rate values correspond to the integrand being approximately zero at the centre of integration. This is not too dissimilar to behaviour found for even and odd functions such that as Rabi frequency is increased decay rate values pass from integrand structures like (a) with maximal integral value to structures like (b) with zero integral value. In this way the Airy function oscillations, which shift with Rabi frequency, can alter our integrands such that our integrals and the

decay rates obtained from them also exhibit oscillatory behaviour.

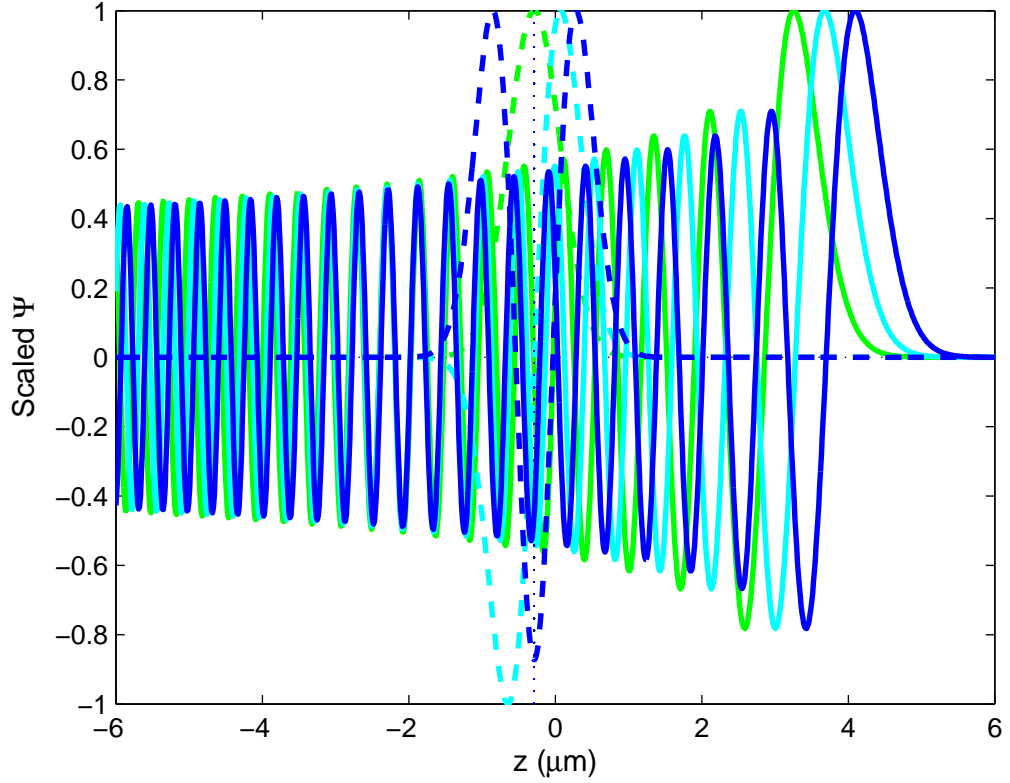


Figure 5.20: Examining the wavefunctions for the full effect gravity model. Three different harmonic oscillator energy levels values are plotted: $n = 0$ displayed in green, $n = 1$ displayed in light blue and $n = 2$ displayed in dark blue. The trapped harmonic oscillator ground state is displayed with dashed lines, while the Airy function untrapped state is displayed with solid lines. The wavefunctions have been scaled so that they reach a value of one at the maximum height. Data for ^{87}Rb , a Rabi frequency of $\Omega/2\pi = 7.5\text{ kHz}$ and a magnetic field gradient $B' = 1.1\text{ T/m}$ were used.

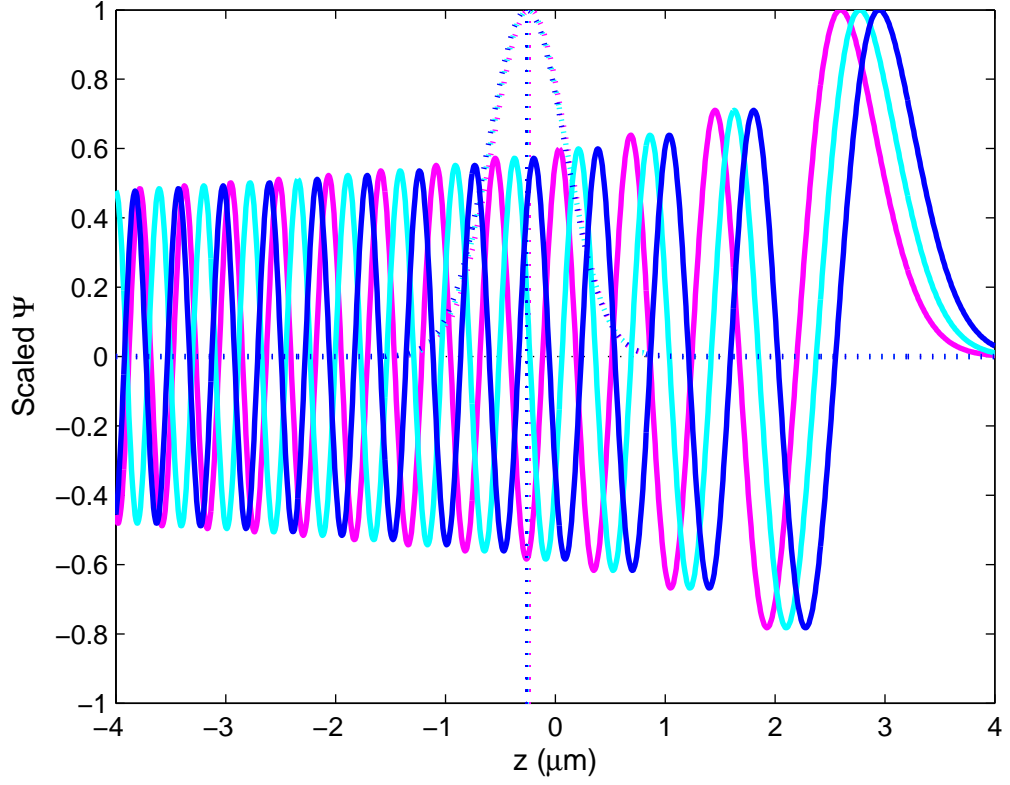


Figure 5.21: Examining the wavefunctions for the full effect gravity model. Three different Rabi frequency values are plotted: $\Omega/2\pi = 6.0$ kHz displayed in pink, $\Omega/2\pi = 6.4$ kHz displayed in light blue and $\Omega/2\pi = 6.8$ kHz displayed in dark blue. The trapped harmonic oscillator ground state is displayed with dotted lines, while the Airy function untrapped state is displayed with solid lines. The wavefunctions have been scaled so that they reach a value of one at the maximum height. Data for ^{87}Rb and a magnetic field gradient $B' = 1.1$ T/m were used to produce this graph.

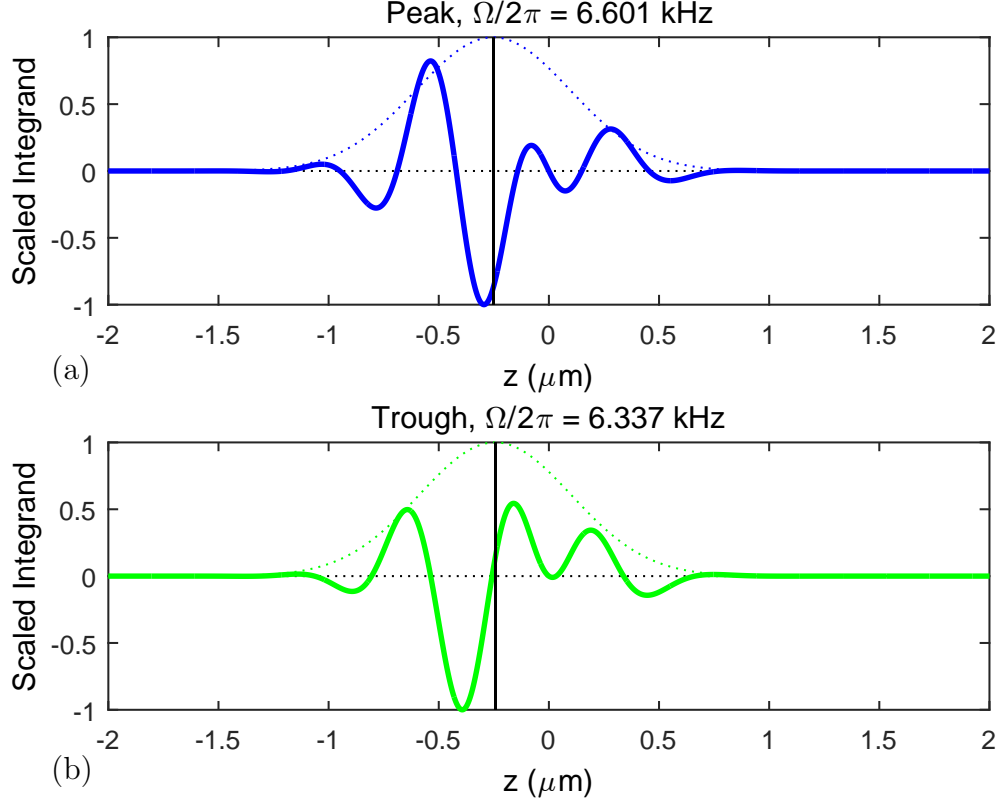


Figure 5.22: Two integrands which lead to (a) a peak or (b) a trough in the full effect gravity model decay rate. The integrand plotted is for the first integral in equation (5.136). The trapped harmonic oscillator ground state is displayed for guidance with dotted lines. The vertical black line indicates the centre of integration given by $z' = 0$. The wavefunction and integrand have been scaled so that they reach a value of one at the maximum height. Data for ^{87}Rb with $n = 0$ and a magnetic field gradient $B' = 1.1$ T/m were used.

5.3 Summary

In this section we have created models and derived corresponding decay rates, using Fermi's Golden Rule, that enable us to predict the rate of dressed spin state transitions for RF-dressed cold atom traps.

Two models have been presented, summarised in table 5.2. We first developed the minimal effect gravity model, in which the trap potential is approximated by a harmonic oscillator and the untrapped state potential by an infinite square well. As would intuitively be expected, we find rates of transitions increase with higher initial atom energy. One of the benefits of having analytic approximations is that we are able to derive a simplified limiting formula for the high Rabi frequency or low magnetic field gradient limits for the decay rates obtained by the pole approximation.

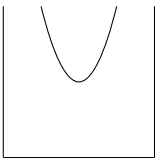
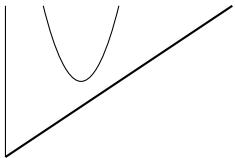
Model	Minimal effect gravity	Full effect gravity
Schematic trap potentials		
Trapped Ψ_n	Equation (5.10)	Equation (5.113)
Untrapped Ψ_{n_f}	Equation (5.14)	Equation (5.119)
Numerical decay rates	Equation (5.35)	Equation (5.136)
Analytic decay rates	Equation (5.27) for $n = 0$; equation (5.74) for $n > 0$	-
Gravity collects atoms at the lowest bubble height	✓	✓
Gravity alters Ψ and Γ_n	×	✓

Table 5.2: Summary of the two models presented in this chapter

We then derived the full effect gravity model, which improves upon the simple box model by considering the effect of the gravitational force on the atom. It can be seen from figure 5.19 that the minimal effect gravity model gives a crude approximation, following the general trend of the full effect gravity decay rates. For quantitative analysis or to obtain the quantum mechanical oscillatory behaviour of the non-adiabatic decay rates, it is necessary to use the full effect gravity model. In the full effect gravity model the trap potential is given by a harmonic oscillator, with gravity shifting the centre of the symmetry axis of the parabola below resonant

detuning, which was its location in the minimal effect gravity model. The untrapped atom state is now modelled by a sloping potential, due directly to the effects of gravity, with state described mathematically by an Airy function of the first kind. This has surprising quantum mechanical effects on the predicted decay rates, as there is now high sensitivity in the system both to the atomic energy and the trap Rabi frequency and magnetic field gradient. It is now possible for an atom to have a greater energy but lower decay probability, which is counter to classical intuition.

Chapter 6

Time evolution of trapped atom number

We now use the decay rates obtained in the previous chapter to find a formula for the number of atoms remaining in the trap as a function of time. This is necessary as experiments with cold atom traps can deduce the atomic population using imaging techniques but they cannot determine the decay rate directly. We will examine the different predictions of trapped atom number obtained for Maxwell-Boltzmann, squeezed thermal and Bose-Einstein initial distributions. We will also consider how time dependent transitions between atomic energy levels affect the trapped atom number prediction, by examining master equation and parametric heating models.

Trapped atom number decline

If it is assumed that each non-adiabatic transition leads to the loss of an atom from the trap, we can use our obtained decay rates to model how the number of trapped atoms decreases due to changes of dressed spin state. Assuming that each atom of a given energy has the same probability to decay as any other and that each atom is equally likely to decay at any given time then

$$-\frac{1}{N_n} \frac{\partial N_n}{\partial t} = \Gamma_n, \quad (6.1)$$

or equivalently one unit of atoms in state n decays at a rate given by Γ_n . The notation N_n , indicates the number of trapped atoms with energy E_n at any given time, t . The relation can equivalently be expressed as $-\int \frac{1}{N_n} dN_n = \Gamma_n \int dt$, then integrated to show that the number of atoms in state n evolves in time according to

$$N_n(t) = N_n(t_0)e^{-\Gamma_n t}. \quad (6.2)$$

The total number of trapped atoms, N , must be equal to the sum of the

number of trapped atoms with all allowed energies, so that

$$N(t) = \sum_n N_n(t). \quad (6.3)$$

Therefore the total number of trapped atoms varies with time as

$$N(t) = \sum_n N_n(t_0) e^{-\Gamma_n t}. \quad (6.4)$$

We define

$$P_n(t) = \frac{N_n(t)}{N(t)} \quad (6.5)$$

as the probability of finding a trapped atom with energy E_n at time t .

This means equation (6.4) can alternatively be written as

$$N(t) = N(t_0) \sum_{n=0}^{\infty} P_n(t_0) e^{-\Gamma_n t}. \quad (6.6)$$

Assuming that non-adiabatic spin flip transitions are the dominant cause of losses from the trap, Γ_n should be given by the expressions obtained in the previous chapter. To be able to determine how the total number of trapped atoms varies with time we therefore need to know the initial distribution of atomic energies.

6.1 Maxwell-Boltzmann initial distribution

For a thermal cloud of atoms there will be a certain probability of being in the n th harmonic oscillator state, given by Maxwell-Boltzmann statistics. The occupation probability (P_n) depends on the initial temperature of the atomic cloud according to

$$P_n = \frac{e^{-\beta E_n}}{Z} = \frac{e^{-\beta E_n}}{\sum_{n=0}^{\infty} e^{-\beta E_n}} \quad (6.7)$$

where Z is the partition function and

$$\beta = \frac{1}{k_B T}, \quad (6.8)$$

with k_B retaining its usual meaning as the Boltzmann constant. For a harmonic oscillator system

$$P_n = \frac{e^{-\beta \hbar \omega n}}{\sum_{n=0}^{\infty} e^{-\beta \hbar \omega n}}. \quad (6.9)$$

The relation

$$\sum_{r=0}^{\infty} a^r = \frac{1}{1-a} \quad (6.10)$$

[52] can be used to express the denominator of equation (6.9) as the infinite summation of a geometric series,

$$P_n = e^{-\beta\hbar\omega n} (1 - e^{-\beta\hbar\omega}) \quad (6.11)$$

or equivalently

$$P_n = 2 \sinh\left(\frac{\beta\hbar\omega}{2}\right) e^{-\beta\hbar\omega(n+\frac{1}{2})}. \quad (6.12)$$

The process for calculating the number of trapped atoms from an initial Maxwell-Boltzmann distribution as a function of time is shown in figure 6.1. There are four main input variables; the Rabi frequency Ω , the magnetic field gradient B' , the temperature T and the initial total number of trapped atoms $N(t_0)$. The initial atom probability distribution P_n and the decay rate for a given harmonic oscillator energy level Γ_n have to be calculated to gain an expression for the number of trapped atoms as a function of time.

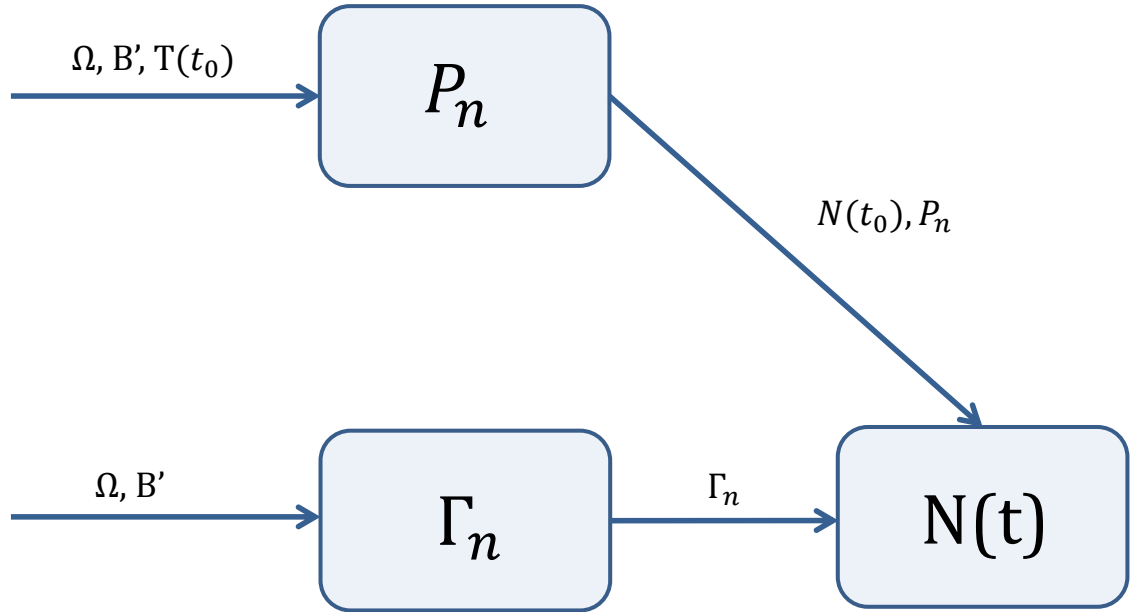


Figure 6.1: Flow diagram showing the process to calculate the number of trapped atoms at any given time with a Maxwell-Boltzmann initial distribution. The variables that need to be calculated are shown in boxes, with the required input variables show on the arrows preceding them.

Changes in Rabi frequency and temperature of the atomic cloud affect the initial energy distribution, as shown in figure 6.2. A change in temperature has the most dramatic effect in the allocation of atomic energies. For any temperature increase there are a greater number of atoms in higher energy harmonic oscillator

levels. We therefore expect atoms to be lost faster at higher temperatures as in general decay rates increase for higher n states. Changes in Rabi frequency result in a less dramatic variation in the distribution of atomic energies. However, the percentage of atoms in the harmonic ground state does appear to be sensitive to the Rabi frequency of the trap. This suggests that the Rabi frequency will be important in determining the long time behaviour of the trap, as the low value of Γ_0 causes the ground state to dominate in the long time limit. It is also noteworthy that the lower the Rabi frequency the higher the occupation of low n states. This should counteract slightly the general trend of increasing losses for lower Rabi frequency decay rates.

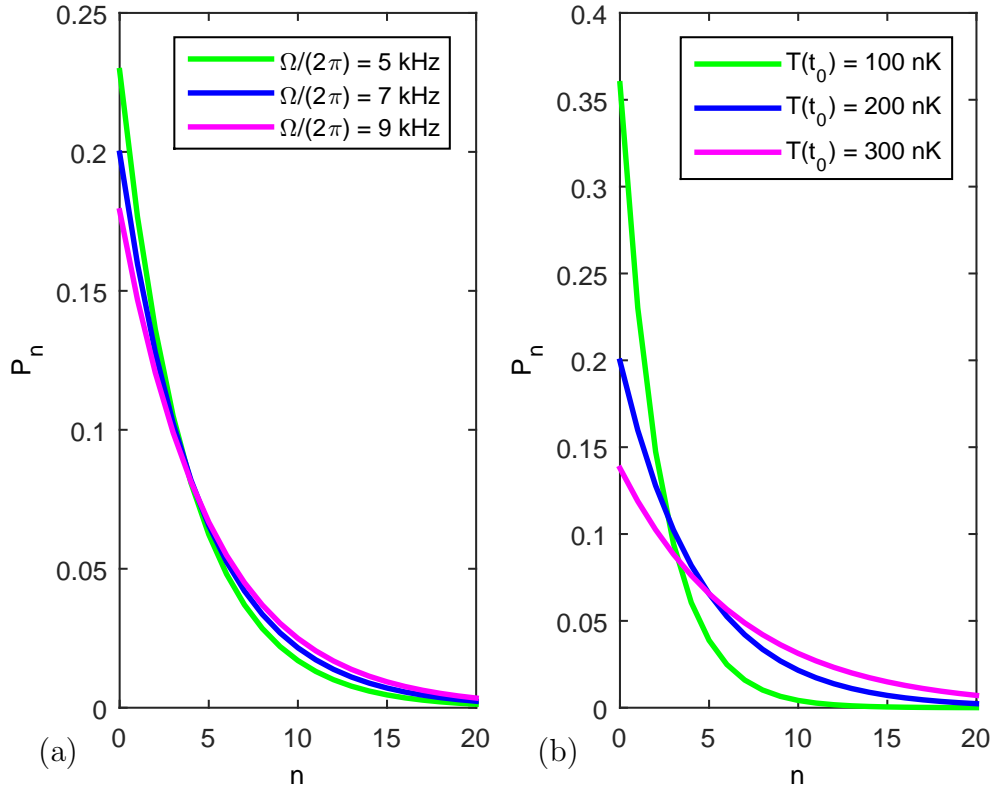


Figure 6.2: Maxwell-Boltzmann probability distribution, given by equation (6.12), for a variety of: (a) Rabi frequencies at a temperature of 200 nK. (b) temperatures with a Rabi frequency of 7 kHz. Solid lines are drawn to aid the eye, however, n can only have integer values. Both plots use an atomic species of ^{87}Rb and a magnetic field gradient of 1.1 T/m.

Figures 6.3 and 6.4 demonstrate how the number of trapped atoms is affected by changes in the key variables of Rabi frequency, magnetic field gradient, initial atom number and temperature. Rabi frequency and the magnetic field gradient

have similar effects altering the curvature of the decline in trapped atom number. To maximise trap lifetimes a high Rabi frequency or low magnetic field gradient are desired. This follows directly from what was found for the non-adiabatic decay rates. Initial atom number and temperature affect the probability distribution P_n without affecting the decay rates. Rather than affecting the curvature of the atomic loss, they lead to a vertical shift of the curve. To maximise trap lifetimes a high initial atom number or a low temperature is desired.

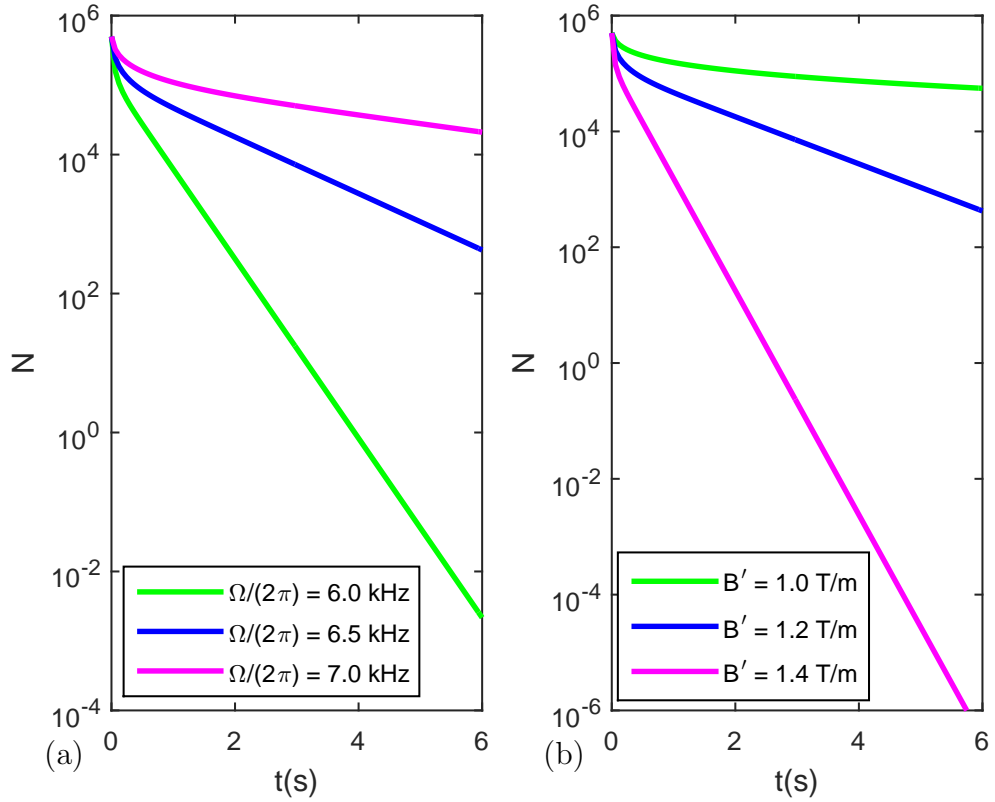


Figure 6.3: Effect of (a) Rabi frequency and (b) magnetic field gradient on the predicted trapped atom number N variation with time t given in seconds. Pole approximation decay rates and a Maxwell-Boltzmann initial distribution of atoms were used in equation (6.4). An initial temperature $T(t_0) = 200$ nK and an initial atom number $N(t_0) = 5 \times 10^5$ were used to produce these graphs. Plot (a) used a magnetic field gradient of $B' = 1.2$ T/m; while plot (b) used a Rabi frequency of $\Omega/2\pi = 6.5$ kHz.

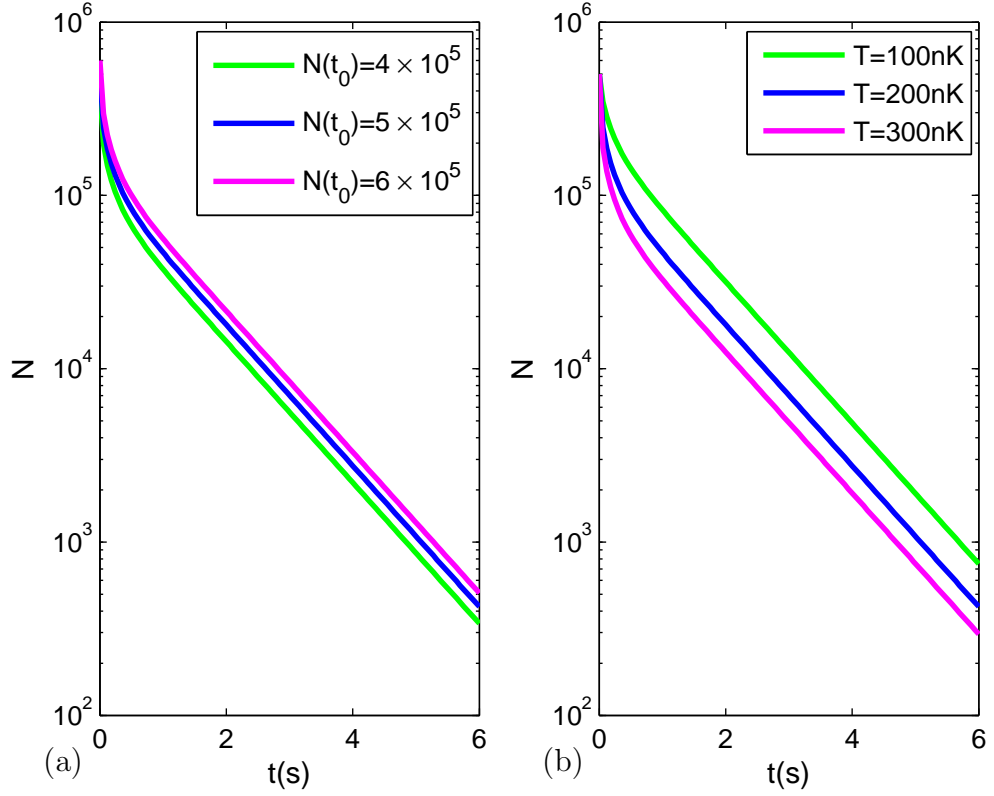


Figure 6.4: Effect of (a) initial atom number and (b) initial temperature on the predicted trapped atom number N variation with time t given in seconds. Pole approximation decay rates and a Maxwell-Boltzmann initial distribution of atoms were used in equation (6.4). A Rabi frequency of 6.5 kHz and a magnetic field gradient of 1.2 T/m were used to produce these graphs. Plot (a) used an initial atom cloud temperature of 200 nK; while plot (b) used an initial atom number of $N(t_0) = 5 \times 10^5$.

Figure 6.5 illustrates the importance of using an appropriate model for the non-adiabatic decay rates, as is shown by the sensitivity of the time evolution to the decay rate model used. Differences obtained in the light and dark blue lines indicate that the pole approximation leads to small but noticeable errors in the time evolution prediction for the trap parameters used in figure 6.5. The predicted number of trapped atoms for the full effect gravity model is seen to be much greater than that predicted by the simpler minimal effect gravity model, showing that the full effect gravity model is necessary for quantitative predictions.

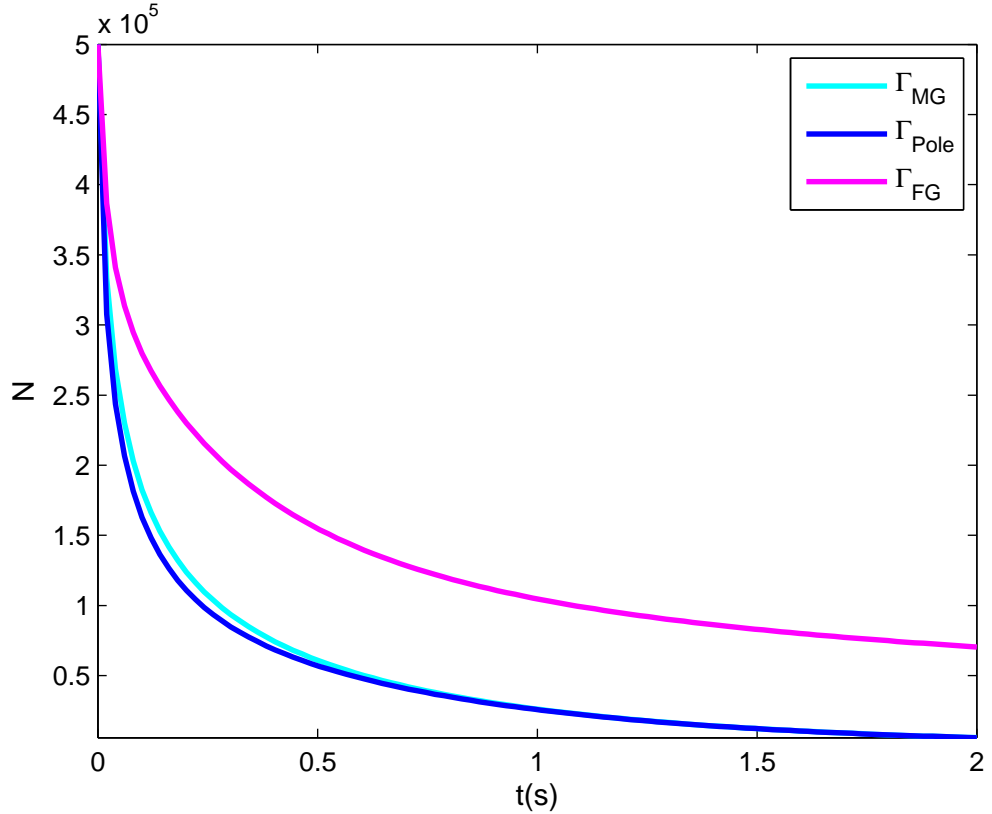


Figure 6.5: Comparison of the time evolution obtained for three different decay rates. The predicted trapped atom number, N , variation with time t was calculated from equation (6.4). The three decay rates used were: Γ_{MG} for the minimal effect gravity model given by equation (5.35), Γ_{Pole} given by the analytic pole approximation equations (5.27) and (5.74) and Γ_{FG} for the full effect gravity model given by equation (5.136). A Maxwell-Boltzmann initial distribution was used with $\Omega/2\pi = 6$ kHz and $B' = 1.12$ T/m. The atom cloud contained 5×10^5 atoms ^{87}Rb atoms at an initial temperature of $T(t_0) = 200$ nK.

6.2 Squeezed thermal initial distribution

In this section we consider an alternative model for the initial distribution of atomic energies given by a squeezed thermal distribution. To minimise the loss of trapped atoms due to non-adiabatic effects, cold atom traps can be loaded using a much higher, low leakage, Rabi frequency then dropped to the lower, desired Rabi frequency when the experiment commences. If the change in Rabi frequency is relatively sudden, this would mean the distribution of atoms does not have a chance to re-thermalise. As the mapping between two harmonic oscillators with different frequencies is the squeeze transformation (as will be discussed), the probability distribution of our atoms at the initial time would be a squeezed thermal distribution of atoms.

Let us demonstrate the mapping between the initial harmonic oscillator with frequency ω_1 and the final harmonic oscillator with frequency ω_2 . The stationary Schrödinger equation for the n th level of the initial harmonic oscillator is

$$E_1(n)\Psi_1(n) = \left[\hbar\omega_1 \left(\hat{a}_1^\dagger \hat{a}_1 + \frac{1}{2} \right) + V_1 \right] \Psi_1(n). \quad (6.13)$$

where E_1 is the harmonic oscillator energy given by

$$E_1(n) = \hbar\omega_1 \left(n + \frac{1}{2} \right) + V_1, \quad (6.14)$$

$\Psi_1(n)$ is the time independent wavefunction of a harmonic oscillator with frequency ω_1 ; \hat{a}_1 and \hat{a}_1^\dagger are the annihilation and creation operators defined (with the appropriate frequency) as

$$\hat{a} = \frac{1}{\sqrt{2\hbar}} \left(\sqrt{m_0\omega} \hat{z} + \frac{i\hat{p}}{\sqrt{m_0\omega}} \right), \quad (6.15)$$

$$\hat{a}^\dagger = \frac{1}{\sqrt{2\hbar}} \left(\sqrt{m_0\omega} \hat{z} - \frac{i\hat{p}}{\sqrt{m_0\omega}} \right), \quad (6.16)$$

while V_i denotes the energy of the turning point of the harmonic oscillator. If we squeeze equation (6.13) with the squeeze operator given by [49]

$$\hat{S} = \exp \left(-\frac{re^{i\phi}}{2} \hat{a}_1^{\dagger 2} + \frac{re^{-i\phi}}{2} \hat{a}_1^2 \right) \quad (6.17)$$

where r and ϕ are squeeze parameters to be determined; we get

$$E_1(n)\hat{S}\Psi_1(n) = \left[\hbar\omega_1 \left(\hat{S}\hat{a}_1^\dagger\hat{S}^\dagger\hat{S}\hat{a}_1\hat{S}^\dagger + \frac{1}{2} \right) + V_1 \right] \hat{S}\Psi_1(n) \quad (6.18)$$

where the unitarity $\hat{S}\hat{S}^\dagger = 1$ has been used repeatedly. If we now define $\Psi_2(n) = \hat{S}\Psi_1(n)$, $\hat{a}_2^\dagger = \hat{S}\hat{a}_1^\dagger\hat{S}^\dagger$, $\hat{a}_2 = \hat{S}\hat{a}_1\hat{S}^\dagger$ and use the relation for E_1 given by equation

(6.14); it can be seen that

$$\left[\hbar\omega_1 \left(n + \frac{1}{2} \right) + V_1 \right] \Psi_2(n) = \left[\hbar\omega_1 \left(\hat{a}_2^\dagger \hat{a}_2 + \frac{1}{2} \right) + V_1 \right] \Psi_2(n) \quad (6.19)$$

which is equivalent to

$$\left[\hbar\omega_2 \left(n + \frac{1}{2} \right) + \frac{\omega_2}{\omega_1} V_1 \right] \Psi_2(n) = \left[\hbar\omega_2 \left(\hat{a}_2^\dagger \hat{a}_2 + \frac{1}{2} \right) + \frac{\omega_2}{\omega_1} V_1 \right] \Psi_2(n). \quad (6.20)$$

This is the stationary Schrödinger equation for a harmonic oscillator with frequency ω_2 and energy

$$E_2(n) = \hbar\omega_2 \left(n + \frac{1}{2} \right) + \frac{\omega_2}{\omega_1} V_1, \quad (6.21)$$

indicating that the squeezing transformation correctly transforms between two harmonic oscillators of differing frequencies.

To find the exact squeezing transformation necessary to transform between a specific ω_1 and ω_2 , we need to know r and ϕ for the squeezing operator given by equation (6.17). We begin by looking at the relations,

$$\hat{a}_2 = \hat{S} \hat{a}_1 \hat{S}^\dagger, \quad (6.22)$$

$$\hat{a}_2^\dagger = \hat{S} \hat{a}_1^\dagger \hat{S}^\dagger. \quad (6.23)$$

It can be found by direct calculation or using relations given in reference [49] that this corresponds to

$$\hat{a}_2 = \hat{a}_1 \cosh r + \hat{a}_1^\dagger e^{i\phi} \sinh r, \quad (6.24)$$

$$\hat{a}_2^\dagger = \hat{a}_1^\dagger \cosh r + \hat{a}_1 e^{-i\phi} \sinh r, \quad (6.25)$$

which can be expressed in terms of the operators \hat{x} and \hat{p} as

$$\begin{aligned} \sqrt{m_0\omega_2} \hat{x} \pm \frac{i\hat{p}}{\sqrt{m_0\omega_2}} &= \left(\sqrt{m_0\omega_1} \hat{x} \pm \frac{i\hat{p}}{\sqrt{m_0\omega_1}} \right) \cosh r \\ &+ \left(\sqrt{m_0\omega_1} \hat{x} \mp \frac{i\hat{p}}{\sqrt{m_0\omega_1}} \right) e^{\pm i\phi} \sinh r. \end{aligned} \quad (6.26)$$

Equating \hat{x} and \hat{p} components for each equation, leads to four relations;

$$\begin{aligned} \sqrt{m_0\omega_2} &= \sqrt{m_0\omega_1} (\cosh r + e^{i\phi} \sinh r), \\ \sqrt{m_0\omega_2} &= \sqrt{m_0\omega_1} (\cosh r + e^{-i\phi} \sinh r), \\ \frac{1}{\sqrt{m_0\omega_2}} &= \frac{1}{\sqrt{m_0\omega_1}} (\cosh r - e^{i\phi} \sinh r), \\ \frac{-1}{\sqrt{m_0\omega_2}} &= \frac{-1}{\sqrt{m_0\omega_1}} (\cosh r - e^{-i\phi} \sinh r). \end{aligned}$$

This indicates that $e^{i\phi} = e^{-i\phi} = \pm 1$, with the squeeze parameter ϕ being an integer multiple of π . Substituting in for ϕ gives

$$\begin{aligned}\sqrt{m_0\omega_2} &= \sqrt{m_0\omega_1} (\cosh r \pm \sinh r), \\ \frac{1}{\sqrt{m_0\omega_2}} &= \frac{1}{\sqrt{m_0\omega_1}} (\cosh r \mp \sinh r),\end{aligned}\tag{6.27}$$

which can be expressed as a single equation,

$$\sqrt{\frac{\omega_2}{\omega_1}} = \frac{e^r}{2} (1 \pm 1) + \frac{e^{-r}}{2} (1 \mp 1).\tag{6.28}$$

We can condense this expression to state that

$$e^{2r} = \begin{cases} \frac{\omega_2}{\omega_1}, & \omega_2 > \omega_1, \\ \frac{\omega_1}{\omega_2}, & \omega_1 > \omega_2. \end{cases}$$

In our case we are increasing the trap frequency when ramping from a low leakage to high leakage trap, so we shall use the squeeze parameter r defined by

$$r = \frac{1}{2} \ln \left(\frac{\omega_2}{\omega_1} \right).\tag{6.29}$$

The values for ω_1 and ω_2 can be found by substituting the appropriate Rabi frequency values into equation (5.13) for the minimal effect gravity model or into equation (5.110) for the full effect gravity model.

The probability distribution of a squeezed thermal distribution can be taken directly from reference [63]:

$$P_{ST}(n_2) = \frac{1}{1 + \bar{n}_1} \sum_{n_1} P_{SN}(n_2, n_1) \left(\frac{\bar{n}_1}{1 + \bar{n}_1} \right)^{n_1},\tag{6.30}$$

where n_1 is the state of the initial high Rabi frequency preparation and n_2 is the state of the lower Rabi Frequency experimental setup. The notation \bar{n} donates the average value of n for our system of trapped atoms as given by

$$\bar{n}(t) = \sum_{n=0}^{\infty} n P_n(t).\tag{6.31}$$

To apply equation (6.30) we are interested in the initial distribution so we need to calculate $\bar{n}(t_0)$. For a harmonic oscillator we can use equation (6.11) to give

$$\bar{n}(t_0) = (1 - e^{-\beta\hbar\omega}) \sum_{n=0}^{\infty} n e^{-\beta\hbar\omega n},\tag{6.32}$$

this can be rewritten as

$$\bar{n}(t_0) = (1 - e^{-\beta\hbar\omega}) \sum_{n=0}^{\infty} e^{-\beta\hbar\omega n} \left(\sum_{m=0}^{\infty} e^{-\beta\hbar\omega m} - 1 \right)\tag{6.33}$$

and equation (6.10) can be used to give the average occupation number for a harmonic oscillator with frequency ω as

$$\bar{n}(t_0) = \frac{1}{e^{\beta\hbar\omega} - 1}. \quad (6.34)$$

The squeezed number distribution (also taken from reference [63]) is given by:

$$P_{SN}(n_2, n_1) = \frac{n_1!n_2!}{[\cosh(r)]^{(2n_2+1)}} \left[\frac{\tanh(r)}{2} \right]^{(n_1-n_2)} S_q \cos^2 \left[\frac{\pi}{2} (n_1 - n_2) \right] \quad (6.35)$$

where

$$S_q = \left| \sum_m \frac{(-1)^m \sinh^{2m}(r)}{2^{2m} m! (n_2 - 2m)! [m + (n_1 - n_2)/2]!} \right|^2 \quad (6.36)$$

with the condition that $\frac{n_2-n_1}{2} \leq m \leq \frac{n_2}{2}$.

Figure 6.6 shows how squeezing the thermal distribution pushes more atoms into higher energy n harmonic oscillator states.

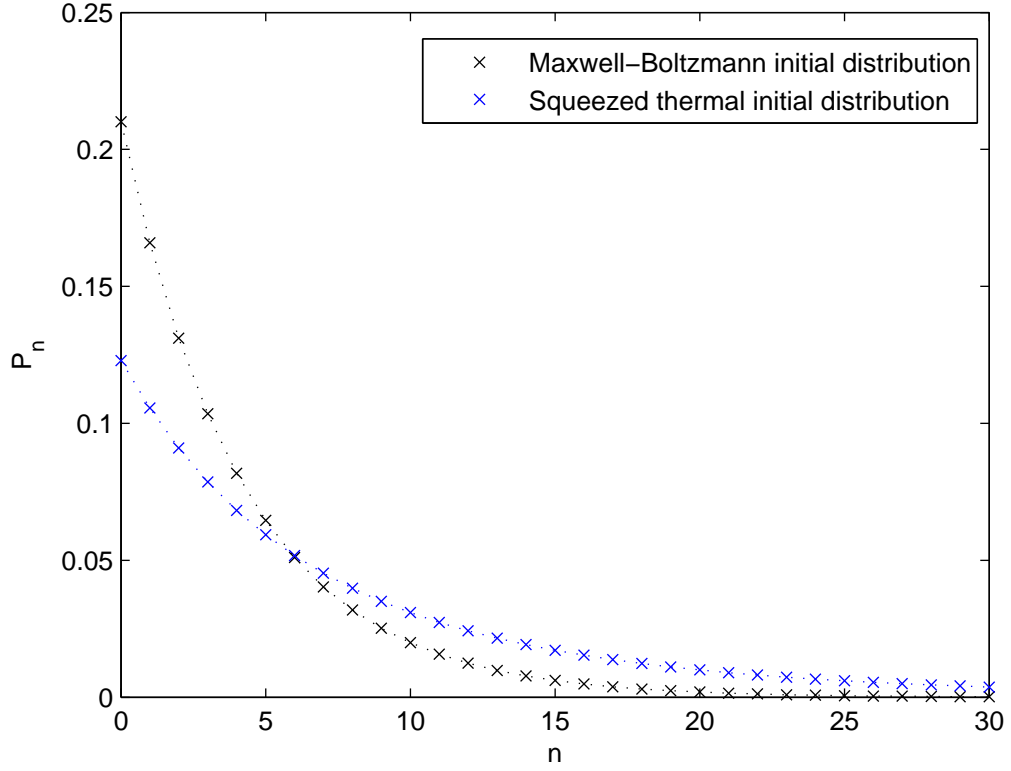


Figure 6.6: Squeezed thermal initial distribution, given by equation (6.30), plotted in comparison with a Maxwell-Boltzmann initial distribution, as given by equation (6.12). A Rabi frequency $\Omega/2\pi = 6.2$ kHz, magnetic field gradient $B' = 1.1$ T/m and an initial temperature $T(t_0) = 200$ nK were used. The initial high Rabi frequency value was chosen to be $\Omega_i/2\pi = 20$ kHz. The squeeze parameter was calculated to be $r = 0.288$ (3sf). Dotted lines are added to guide the eye.

The squeezed distribution can be used as the initial distribution of atomic energies to calculate the number of trapped atoms as a function of time. The process for achieving this is shown in figure 6.7. In comparison to the Maxwell-Boltzmann distribution, as was detailed in figure 6.1, the squeezed thermal distribution requires an additional calculation step to evaluate the squeeze parameter r and an additional input variable Ω_i , the initial high loading Rabi frequency. It is assumed that other input variables remain constant during the squeezing process.

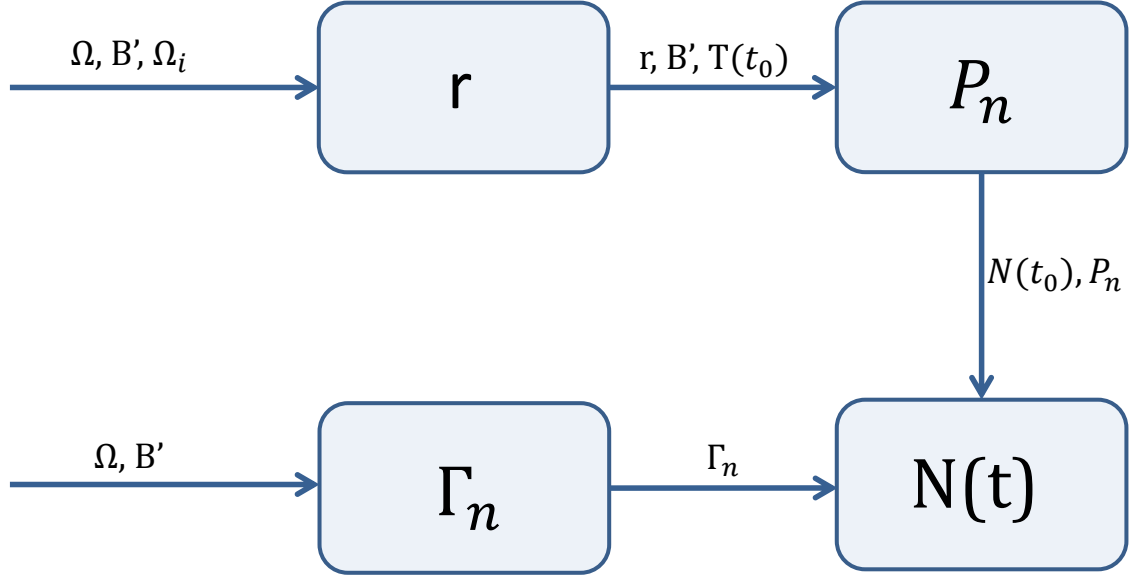


Figure 6.7: Flow diagram showing the process to calculate the number of trapped atoms at any given time with a squeezed thermal initial distribution. The variables that need to be calculated are shown in boxes, with the required input variables shown on the arrows preceding them.

Figure 6.8 shows how squeezing the initial distribution of atoms affects the time evolution of the number of trapped atoms. As shown in figure 6.6 when the thermal distribution is squeezed, there are more atoms in higher energy harmonic oscillator states, which in general have a greater decay rate compared to low energy n states. This means a squeezed thermal distribution leads to less atoms in the trap at any given time, which is a significant effect for the values used in figure 6.8. Figure 6.8 also highlights the importance of the initial distribution of atoms in affecting how quickly atoms are lost from the trap.

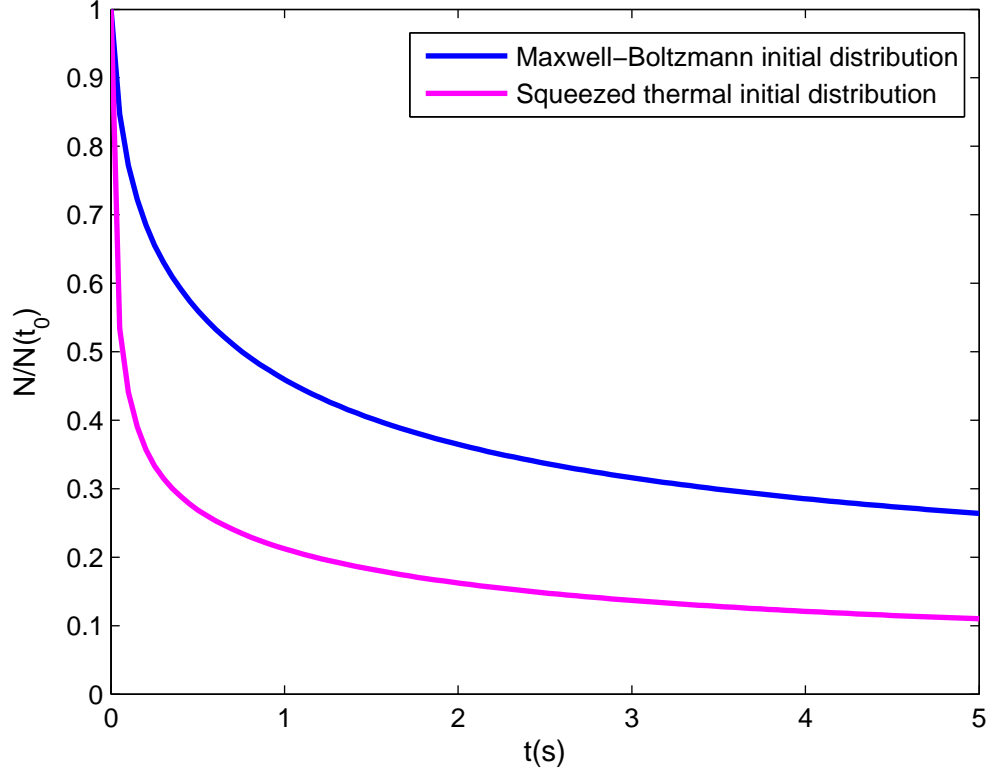


Figure 6.8: Number of atoms remaining in the trap as a function of time calculated using full effect gravity model decay rates given by equation (5.136). This graph compares using a Maxwell-Boltzmann initial distribution as given by equation (6.12), with a squeezed thermal distribution as given by equation (6.30). A magnetic field gradient $B' = 1.1 \text{ T/m}$ and a temperature $T = 200 \text{ nK}$ were used to produce this graph. The initial high Rabi frequency value was chosen to be $\Omega_i/2\pi = 52 \text{ kHz}$ and the squeeze parameter was $r = 0.498$ (3sf) for $\Omega/2\pi = 7 \text{ kHz}$. ^{87}Rb atoms were chosen with $|1, 1\rangle \rightarrow |1, 0\rangle$ transition for the decay rates.

6.3 Bose-Einstein initial distribution

The Maxwell-Boltzmann distribution gives the equilibrium distribution of atomic energies for a classical ideal gas. However, if the temperature of the gas is reduced close to absolute zero (0 K) two distinct equilibrium distributions are observed, dependent on whether the particle involved is a fermion¹ or boson², neither of which being modelled appropriately by the Maxwell-Boltzmann distribution. The behaviour observed depends on the spin of the particle as the spin dictates how the particles can be arranged into the different states available [64]. Atoms held in cold atom traps are commonly bosons, as is the case for the experimental data studied in chapter 8. For low temperatures the initial distribution is then more appropriately given by a Bose-Einstein distribution:

$$N_n = \frac{1}{e^{\beta(\mathcal{E}_n - \mu)} - 1} \quad (6.37)$$

where $\beta = \frac{1}{k_B T}$, \mathcal{E}_n is the energy of the n th state and μ is the chemical potential of the system [39]. As we are considering a single atomic species the chemical potential is the Gibb's free energy per atom, where the Gibb's free energy is the amount of work required to create a system [40]. The chemical potential μ can be determined numerically³ by solving the condition $N(t_0) = \sum_{n=0}^{\infty} N_n$ from equation (6.3).

While continuing to study non-adiabatic losses in one dimension, the z direction, it is now necessary to take into account that atom traps are three dimensional, as the total energy \mathcal{E}_n depends on all three spacial degrees of freedom. To find an expression for \mathcal{E}_n we can assume that the trap is given by three orthogonal harmonic oscillators. We retain the notation ω for the trap frequency in the z direction and introduce ω_x for the trap frequency in the x direction and ω_y for the trap frequency in the y direction. The initial distribution of atoms is therefore given by

$$N_n = \sum_{n_x=0}^{\infty} \sum_{n_y=0}^{\infty} [e^{\hbar\beta(n_x\omega_x + n_y\omega_y + n\omega) - \beta\mu} - 1]^{-1} \quad (6.38)$$

where any offset of the energy of the harmonic oscillators is absorbed into the chemical potential. We require $\omega \gg \omega_{x,y}$ to ensure that it is appropriate to consider non-adiabatic losses in the z direction alone. This occurs as in general the rate of non-adiabatic losses increases with the energy of the trapped atoms, which is directly proportional to the frequency of the trap (see figure 5.16 and equation (5.114)).

¹Particles with half-integer spin value

²Particles with integer spin value

³Determining the value of μ accurately requires some careful attention, the process can be slow or prone to converging incorrectly if not set up correctly. Matlab function 'fzero' was used in the results presented here [61], with different starting values depending on the initial temperature.

The Bose-Einstein distribution thus requires us to have knowledge of the trap frequencies in the x and y directions. However, these frequencies are specific to the static magnetic field configuration. The trap frequencies could be determined experimentally for use in equation (6.38), alternatively we shall now derive an expression for the horizontal trap frequencies ω_x, ω_y . If we assume the static magnetic field configuration of the atom trap is a quadrupole field, typical for atom traps and necessary for experimental comparison in chapter 8, the iso-magnetic field lines are ellipsoids given by the formula

$$|\mathbf{B}| = \frac{B'}{2} \sqrt{x^2 + y^2 + 4\tilde{z}^2}. \quad (6.39)$$

The magnetic field gradient in the z direction is twice the magnetic field gradient in the ρ direction. As a higher magnetic field gradient generally leads to a higher rate of non-adiabatic transitions, in this configuration, the z direction is the dominant direction for non-adiabatic losses. The atoms will be trapped in the vicinity of the resonant ellipsoid [24], which selects out the iso- \mathbf{B} ellipsoid for which the static magnetic field strength is such that the hyperfine splitting caused is resonant with the RF field. The resonant ellipsoid is given by

$$x^2 + y^2 + 4\tilde{z}^2 = \rho^2 + 4\tilde{z}^2 = r_0^2 \quad (6.40)$$

[1] where

$$r_0 = \frac{2\omega_{\text{rf}}}{\lambda}, \quad (6.41)$$

with ω_{rf} the RF frequency of oscillation. For a quadrupole field $\omega_x = \omega_y = \omega_\rho$. Note that \tilde{z} is defined from the centre of the ellipsoid, such that

$$\tilde{z} = z - \frac{\omega_{\text{rf}}}{\lambda}. \quad (6.42)$$

If we define ϕ as the deviation from the vertical \tilde{z} axis and r as the length of the circle that matches the curvature of ellipsoid, the motion of the atoms can be modelled as simple harmonic, using

$$m_0 r \frac{\partial^2 \phi}{\partial t^2} = -m_0 g \sin \phi, \quad (6.43)$$

$$\frac{\partial^2 \phi}{\partial t^2} \approx -\frac{g}{r} \phi, \quad (6.44)$$

which leads us to an expression for the horizontal trap frequency

$$\omega_\rho = \sqrt{\frac{g}{r}}. \quad (6.45)$$

To find r we must match the curvature of the circle $\rho^2 + (\tilde{z} - r + \frac{r_0}{2})^2 = r^2$ to that of the ellipsoid $\rho^2 + 4\tilde{z}^2 = r_0^2$ around the location of the atoms at $(\rho = 0, \tilde{z} = -\frac{r_0}{2})$.

This ignores the slight gravitational sag in the centre of the atom cloud below the resonance location for the full effect gravity model but is exact for the minimal effect gravity model.

Substitution of $\rho = 0 + \delta\rho$ and $\tilde{z} = -\frac{r_0}{2} + \delta\tilde{z}$ into the circle and ellipsoid equations gives:

$$\begin{aligned} \text{Ellipse} \quad \delta\rho^2 &= 4r_0\delta\tilde{z} - 4\delta\tilde{z}^2, \\ \text{Circle} \quad \delta\rho^2 &= 2r\delta\tilde{z} - \delta\tilde{z}^2. \end{aligned}$$

For small angles ($\delta\tilde{z}^2 \approx 0$) the circle and ellipse formulae agree when $r = 2r_0$, so that the horizontal trap frequency is given by⁴

$$\omega_\rho = \sqrt{\frac{g}{2r_0}} = \sqrt{\frac{\lambda g}{4\omega_{\text{rf}}}}. \quad (6.46)$$

For the quadrupole distribution considered here, with $\omega_x = \omega_y$, the initial Bose-Einstein distribution is given by

$$N_n = \sum_{n'=0}^{\infty} \frac{n' + 1}{e^{\beta[h(n'\omega_\rho + n\omega) - \mu]} - 1} \quad (6.47)$$

where n' is a summation index⁵. Equation (6.47) only requires knowledge of ω_{rf} , by use of equation (6.46), which is preferable to ω_x and ω_y as it is easier to determine.

The Bose-Einstein distribution can be used for the initial distribution of atoms, to enable us to calculate the number of trapped atoms as a function of time. At low temperatures the Bose-Einstein distribution is more accurate than the Maxwell-Boltzmann distribution although, as shown in figure 6.9, it comes at a cost of a greater requirement for assumed knowledge. In comparison to the Maxwell-Boltzmann distribution, which was summarised in figure 6.1, the Bose-Einstein distribution requires one additional calculation step of the chemical potential μ . For a quadrupole field distribution one additional input variable ω_{rf} , the RF field oscillation frequency, is also required and in the general case ω_x and ω_y would be required instead of ω_{rf} .

There is a dramatic difference between the Maxwell-Boltzmann and Bose-Einstein distributions for low n states, as is seen in figure 6.10. The high occupancy of the ground state level is a key feature of the Bose-Einstein distribution and is present in figure 6.10 at a temperature of 200 nK, a reasonable temperature for a cold atom trap.

⁴The ω_{rf} dependence arises (due to equation 6.41) as the frequency of the RF field determines the position of the resonance location, see reference [1].

⁵Replacing the two summations of n_x and n_y with a single summation over n' is preferable as it speeds up the numerical determination of μ .

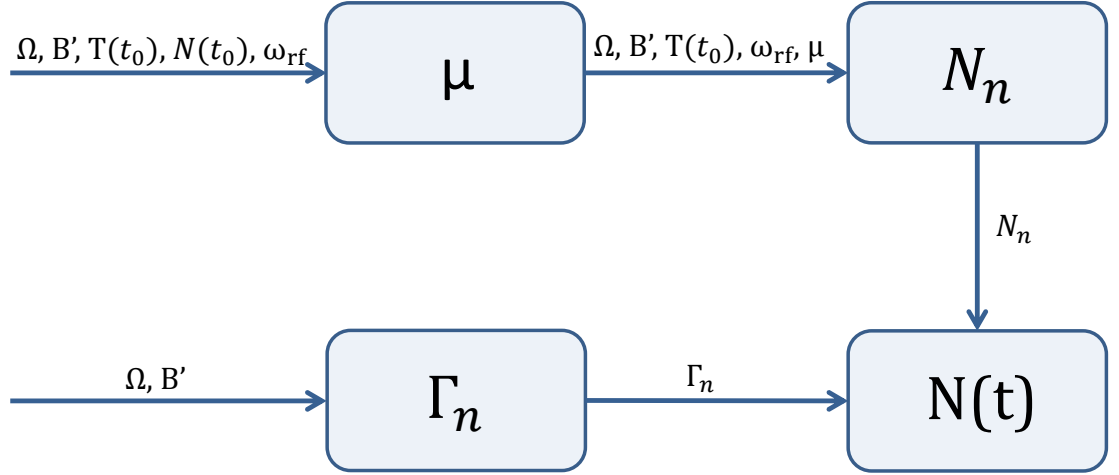


Figure 6.9: Flow diagram showing the process to calculate the number of trapped atoms at any given time with a Bose-Einstein initial distribution. The variables that need to be calculated are shown in boxes, with the required input variables shown on the arrows preceding them.

Figures 6.11 and 6.12 demonstrate how the Bose-Einstein distribution changes for key trap parameters. By contrasting with figure 6.2, the high occupation of the ground state indicative of Bose-Einstein condensation can be seen. Figure 6.11 (b) shows that this does not occur at high temperatures or as shown in figure 6.12 (b) for low atom numbers. As the ground state is typically a state with a very low decay rate, it would be expected that using a Bose-Einstein initial distribution would increase the overall trap lifetime.

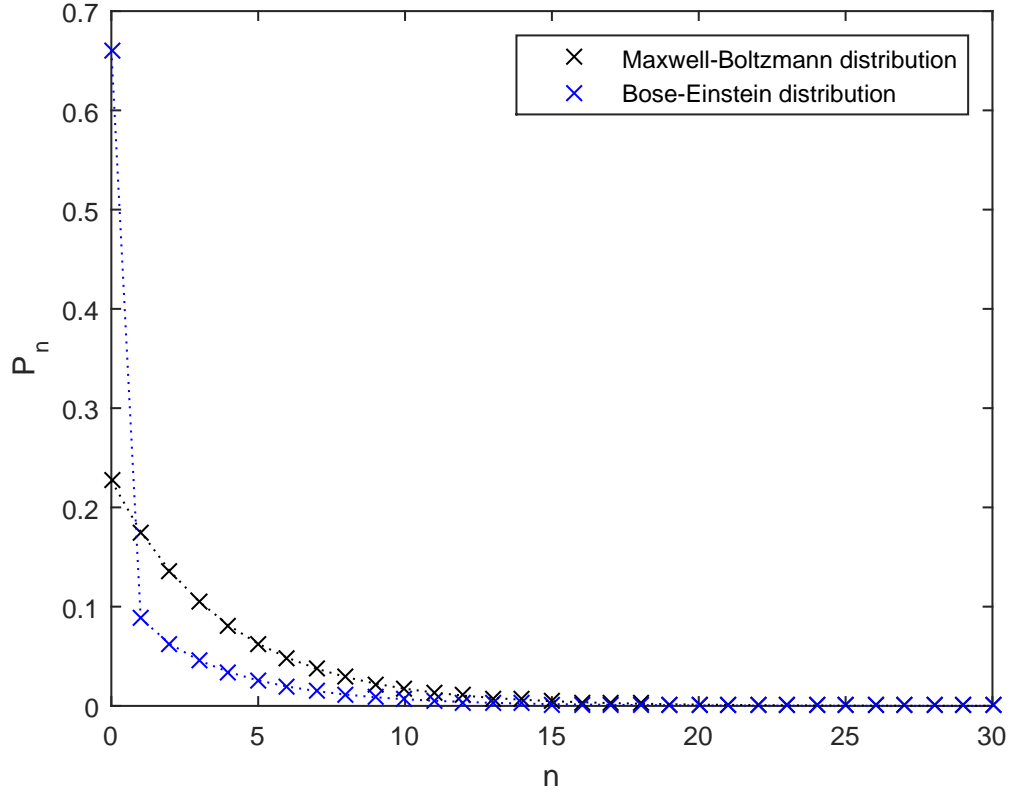


Figure 6.10: Bose-Einstein distribution for atomic energies. The Maxwell-Boltzmann distribution is also plotted for comparison. This graph uses a vertical trap frequency of $\omega/(2\pi) = 1.0$ kHz (2sf) and a radial trap frequency $\omega_\rho/(2\pi) = 21$ Hz (2sf) as calculated from equations (5.13) and (6.46) for ^{87}Rb atoms with $\Omega/2\pi = 6$ kHz, $B' = 1.1$ T/m and $\omega_{\text{rf}}/2\pi = 1.2$ MHz. The atom cloud contained 5×10^5 atoms and has a temperature of $T = 200$ nK. Dotted lines are added to guide the eye.

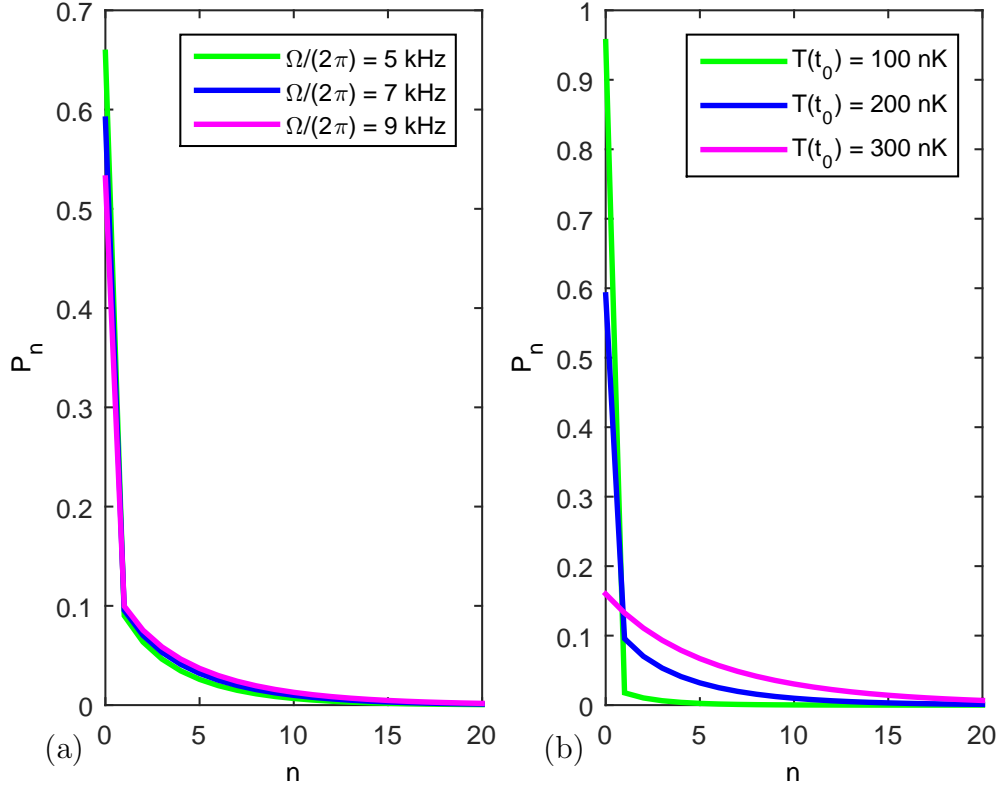


Figure 6.11: Bose-Einstein probability distribution affected by changes in: (a) Rabi frequency at a temperature of 200 nK. (b) temperature at a Rabi frequency of 7 kHz. For both panels 5×10^5 ^{87}Rb atoms initially occupy the trap with $B' = 1.1$ T/m and $\omega_{\text{rf}}/2\pi = 1.2$ MHz. Solid lines are drawn to aid the eye but n can only exist in integer values.

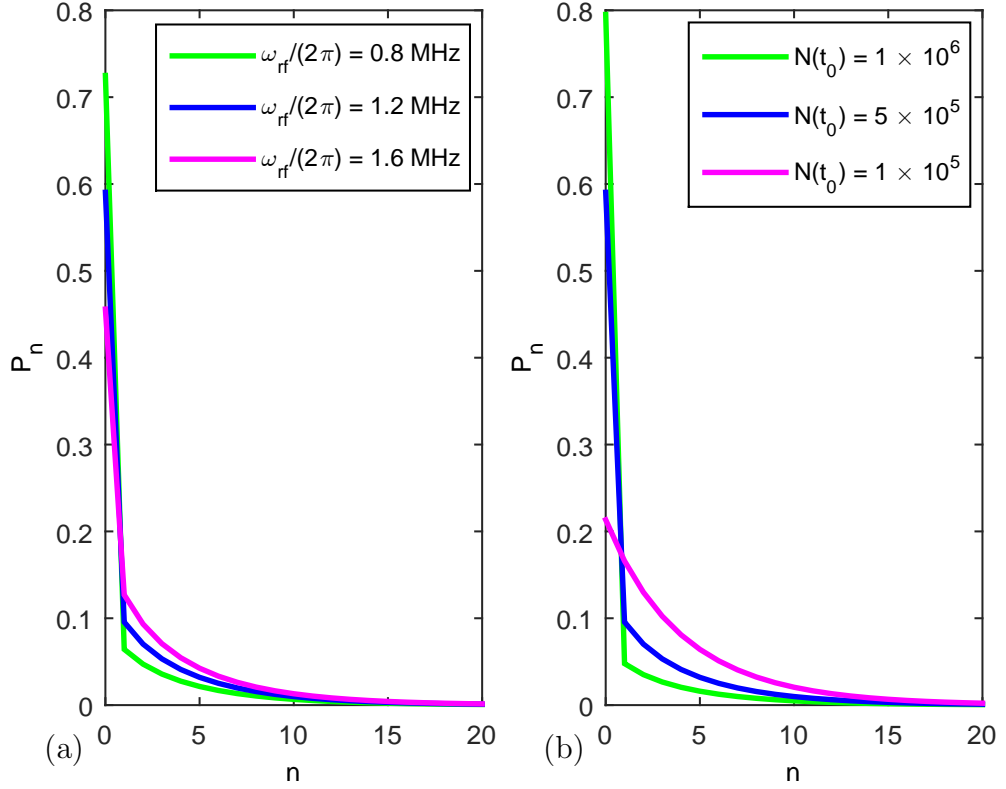


Figure 6.12: Bose-Einstein probability distribution affected by changes in: (a) RF frequency with an initial atom number of 5×10^5 atoms. (b) initial atom number at a RF frequency of $\omega_{\text{rf}}/2\pi = 1.2 \text{ MHz}$. Both graphs use atomic species ^{87}Rb atoms with $\Omega/2\pi = 7 \text{ kHz}$, $B' = 1.1 \text{ T/m}$ and $T(t_0) = 200 \text{ nK}$. Solid lines are drawn to aid the eye but n can only exist in integer values.

Figure 6.13 demonstrates how the different decay rates obtained in chapter 5 affect the trapped atom number evolution with a Bose-Einstein initial distribution. The analytic decay rates (Γ_{Pole}) lead to a prediction of trapped atom number that agrees closely with the minimal effect gravity model numerically integrated decay rates. This is helped significantly for a Bose-Einstein distribution by the use of our exact result for the ground state given by equation (5.27). At the temperature of 200 nK plotted in figure 6.13, there is a large occupation of the ground state, as can be seen by figure 6.10.

Figure 6.13 also shows a diminished difference between the minimal effect gravity and full effect gravity models, in comparison to figure 6.5. Indicating the importance of modelling both the non-adiabatic decay rates and the initial distribution appropriately for a quantitative prediction of the time evolution of trapped atom number. As was seen in figure 6.5 gravity has the effect of increasing trap lifetime.

Figure 6.14 shows how changing the initial distribution of energies has a greater effect than changing the non-adiabatic decay rate model used. The squeezed thermal distribution has the greatest rate of the decay having the greatest number of atoms in high n states. The Bose-Einstein distribution, with the greatest occupation of the ground state out of the three distributions considered, leads to the slowest decrease in trapped atom number.

Finally we conclude by examining the affect of the hump, the non-adiabatic contribution to the trapping potentials introduced in section 3.4. We saw from figure 5.5 that the hump does alter the non-adiabatic decay rates obtained. Figure 6.15 shows that the change in predicted trapped atom number, that occurs by including the hump in our model, is very slight and only noticeable in the long time limit. This makes the usual negligence of the hump highly reasonable.

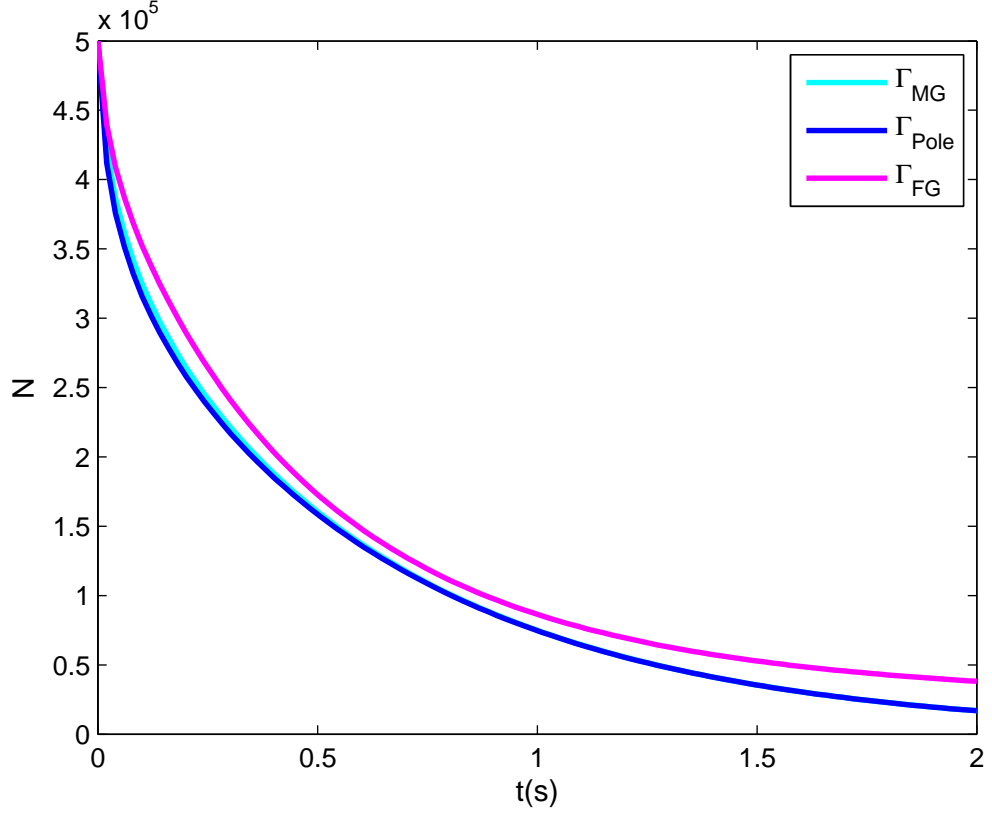


Figure 6.13: Trapped atom number (N) variation with time (t) given in seconds for a Bose-Einstein initial distribution, calculated from equation (6.4). The three decay rates used were: Γ_{MG} for the minimal effect gravity model given by equation (5.35), Γ_{Pole} given by the analytic pole approximation equations (5.27) and (5.74) and Γ_{FG} for the full effect gravity model given by equation (5.136). The atom cloud contained 5×10^5 ^{87}Rb atoms initially and had an initial temperature of $T(t_0) = 200 \text{ nK}$. $\Omega/2\pi = 6 \text{ kHz}$, $B' = 1.12 \text{ T/m}$ and $\omega_{rf}/2\pi = 1.2 \text{ MHz}$.

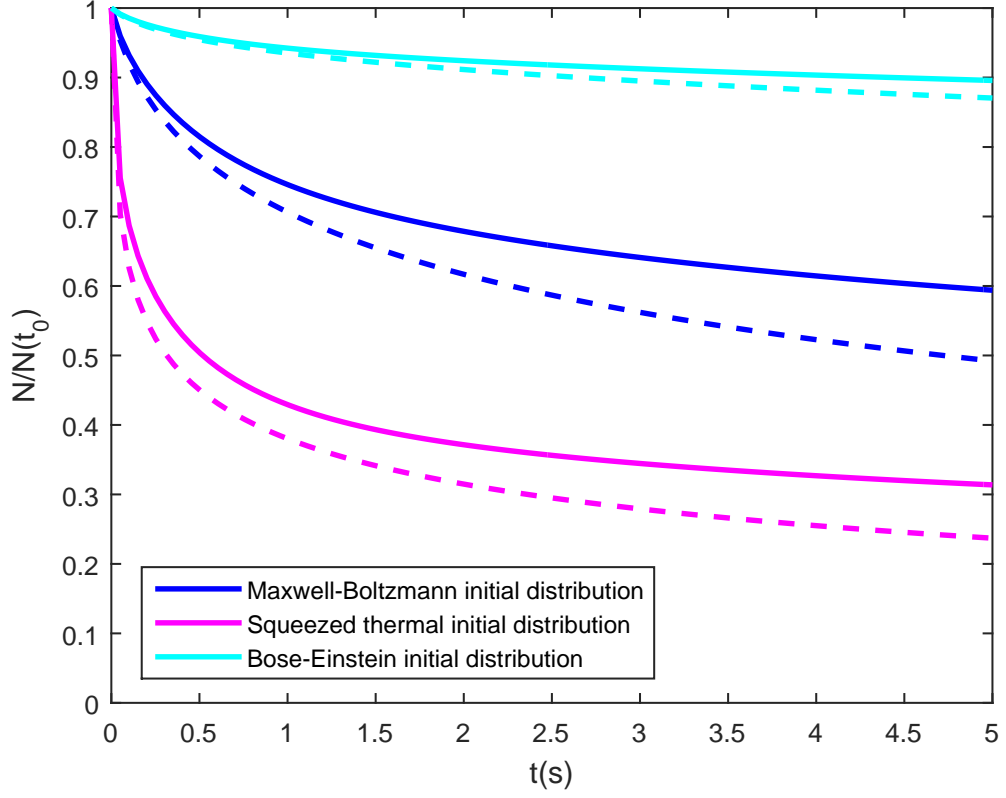


Figure 6.14: Comparing the different initial distributions effect on trapped atom number. The solid lines were calculated using the full effect gravity model decay rates, the dashed lines were calculated using the minimal effect gravity model decay rates. In both instances the decay rates were calculated by numerical integration. ^{87}Rb atoms with $\Omega/2\pi = 8.5\text{ kHz}$, $B' = 1.2\text{ T/m}$ and $\omega_{\text{rf}}/2\pi = 1.2\text{ MHz}$. The atom cloud contained 1×10^6 atoms initially and had an initial temperature of $T(t_0) = 200\text{ nK}$. The squeezing parameter was calculated to be 0.45 (2sf) for both models.

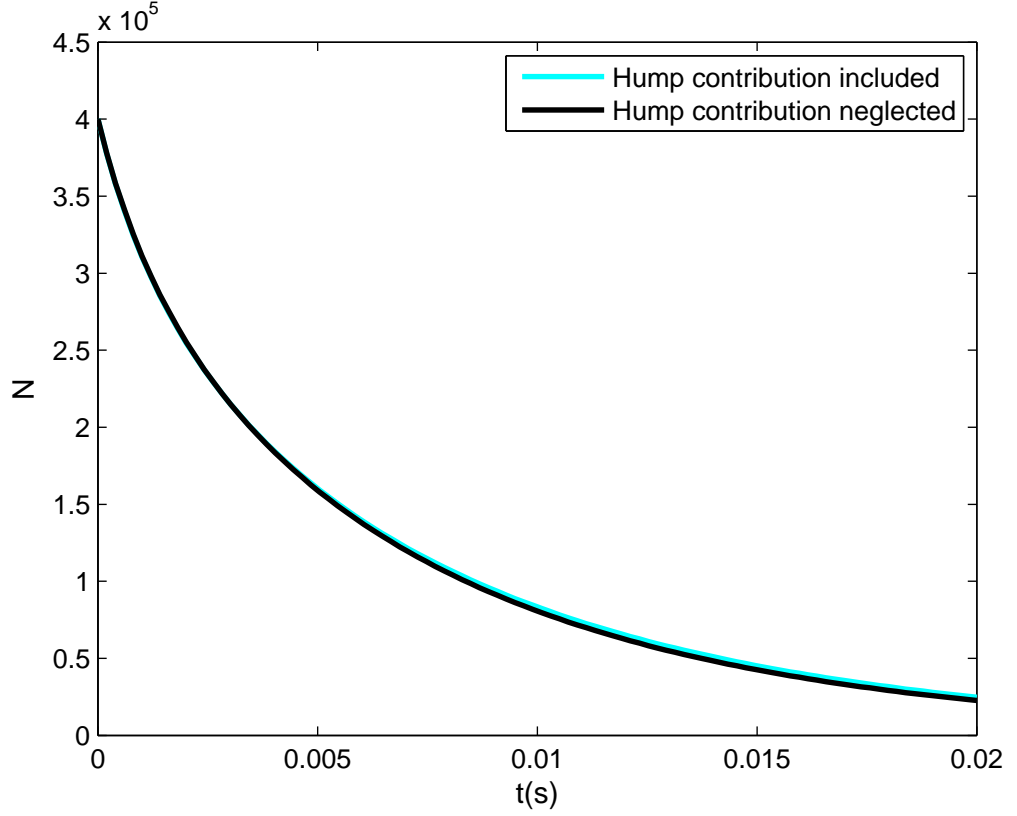


Figure 6.15: Hump contribution affect on the predicted trapped atom number time evolution. The decay rates were calculated using equation (5.35) for the minimal effect gravity model. A Bose-Einstein initial distribution was used with ^{87}Rb atoms with $\Omega/2\pi = 4\text{ kHz}$, $B' = 1.12\text{ T/m}$ and $\omega_{\text{rf}}/2\pi = 1.2\text{ MHz}$. The atom cloud contained 4×10^5 atoms initially and had an initial temperature of $T(t_0) = 200\text{ nK}$.

6.4 Dynamical distributions

We saw in chapter 5 that the probability of decay of an atom, at any given time, is dependent on the energy that would be obtained from a measurement performed at that time. In our trap there are multiple possible atomic energies. To predict the time evolution of an ensemble of atoms (an atom cloud) requires taking into account the complete set of possible atomic energies, with their respective likelihoods. Any process that affects the probability that an atom has a specific energy will, due to the energy dependence of our decay rates, affect the loss of atoms from the trap.

Previously in this chapter, we have set an initial distribution of atomic energies, then calculated the decrease in atom number from decay due to non-adiabatic losses. However, the real situation is more complex, there may be noise in the trap potential, collisions between trapped atoms, collisions between trapped and untrapped atoms and stray electromagnetic fields which may all induce atoms to transition between energy levels or become lost from the trap. Here we shall derive more sophisticated models to dynamically predict how the number of trapped atoms in a given harmonic oscillator state varies in time.

Technically, we do not know what the atom is doing in between measurements. However, by keeping track of the predicted possibility for measuring a particular energy at a given time, we are able to predict the trapped atom number time evolution.

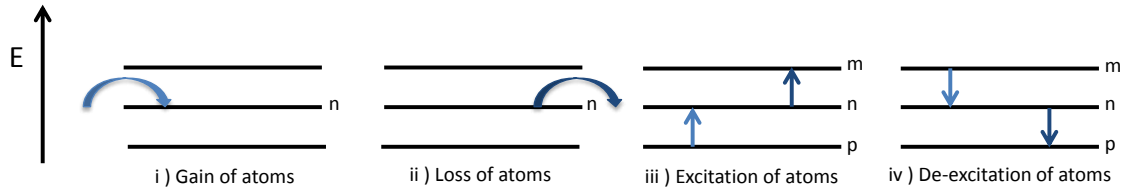


Figure 6.16: Diagram to represent the different possible processes that may change the occupancy of the n th energy level.

Figure 6.16 highlights the four possible processes that can change the number of trapped atoms occupying a particular harmonic oscillator energy level. We assume process i) gain of atoms into the trap is negligible as, due to an interference effect, couplings between a discrete state and a continuum leads to exponential decay with no repopulation of the discrete state [65]. This ensures that once an atom makes a transition to the continuum associated with the untrapped adiabatic potential, it is highly unlikely to make a transition back to a state associated with the trapping harmonic oscillator potential.

Process ii) loss of atoms from the trap is the only process we have considered

so far. We shall continue to assume losses from the trap can be modelled dominantly by our non-adiabatic spin flip decay rates (Γ_n). However, in reality there will always be other processes that induce losses from the trap and in some regimes these may become dominant. The term Γ_{bl} will be included in our model to account for any background losses which affect all harmonic oscillator levels equally, these energy independent losses will be specific to a given experimental setup.

Processes iii) and iv) the possibility for transitions between energy levels, have so far not been considered in our determination of the number of trapped atoms. Due to the decay rates varying dramatically for different harmonic oscillator energy levels, these processes can have a significant effect. In this section models to account for the relative rates of excitation and de-excitation between energy levels are considered.

6.4.1 Master equation model

To obtain a dynamical model for the atomic population we first consider an open quantum systems master equation approach. The harmonic oscillator of our trap is the system of interest which we now couple to an unknown reservoir. The interaction between the reservoir and the atomic system leads to the occupancy of the different harmonic oscillator energy levels varying with time. By taking into consideration any coupling to the reservoir, the system is no longer in an eigenstate of the total Hamiltonian. Therefore the state of the system will have a non-trivial time evolution. If we were to measure the state of the system, we would find that the coupling to the reservoir has meant that there is now a non-zero probability for the system to be found in a different eigenstate then it was in originally. We say that the reservoir causes the system to transition between eigenstates of the non-coupled Hamiltonian.

This is the process of adding a small perturbation onto a Hamiltonian, as discussed in section 4, except now the perturbation is coupling to an unknown reservoir not between different known spin states. Fermi's Golden Rule cannot be applied in this case, as that requires knowledge of the unknown reservoir we do not have access to. Instead the Schrödinger equation can be used to find a master equation to model the evolution of the system. The unknown reservoir can be modelled as an infinite collection of harmonic oscillators with varying frequency. If the rotating-wave approximation and the weak Born approximation are taken then the interaction picture master equation given in terms of the reduced density matrix of the system of interest ($\hat{\rho}_S$) is:

$$\frac{\partial \rho_S}{\partial t} = \frac{\gamma}{2} \bar{n}_f (2\hat{a}^\dagger \hat{\rho}_S \hat{a} - \hat{a} \hat{a}^\dagger \hat{\rho}_S - \hat{\rho}_S \hat{a} \hat{a}^\dagger) + \frac{\gamma}{2} (\bar{n}_f + 1) (2\hat{a} \hat{\rho}_S \hat{a}^\dagger - \hat{a}^\dagger \hat{a} \hat{\rho}_S - \hat{\rho}_S \hat{a}^\dagger \hat{a}) \quad (6.48)$$

For a derivation please see reference [66]. This master equation is usually given the physical meaning of an atom interacting with a radiation field in which case the physical interpretation of γ and \bar{n}_f can be inferred from Einstein AB theory [67]. γ can be interpreted as the rate of spontaneous emission. The product $\gamma\bar{n}_f$ gives the rate of stimulated emission and absorption. However, our analysis is more general, as there may be many different processes that contribute to the possibility for atomic transitions and losses from the trap. γ shall be called the relaxation parameter, used to determine how quickly the system thermalises to a steady state. The steady state is characterized by \bar{n}_f , which is the average occupation number in the long time limit.

As the reduced density matrix of the system is given by $\rho_S = \rho_{nm}|n\rangle\langle m|$ and the atomic population is given by $P_n = \rho_{nn}$ [68] we can derive an expression for the time evolution of the probability of occupation of the n th harmonic oscillator state,

$$\frac{\partial P_n}{\partial t} = \gamma\bar{n}_f [nP_{n-1} - (n+1)P_n] + \gamma(\bar{n}_f + 1) [(n+1)P_{n+1} - nP_n] \quad (6.49)$$

Figure 6.17 shows diagrammatically equation (6.49).

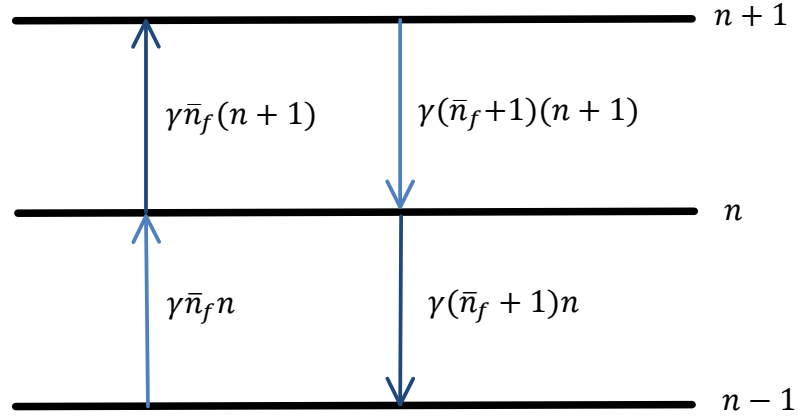


Figure 6.17: Transitions into and out of the n th energy level considered in the master equation model.

Equation (6.49) assumes the number of atoms remains constant while there are (as we wish to model) losses from the trap. Therefore an extra term is added to equation (6.49), to include the decay rates associated with loss of atoms from the trap, giving

$$\begin{aligned} \frac{\partial N_n}{\partial t} = & \gamma\bar{n}_f [nN_{n-1} - (n+1)N_n] + \gamma(\bar{n}_f + 1) [(n+1)N_{n+1} - nN_n] \\ & - (\Gamma_n + \Gamma_{bl}) N_n. \end{aligned} \quad (6.50)$$

The notation N_n , the number of trapped atoms with energy E_n is used in equation (6.50) rather than P_n , the probability for a single trapped atom to have energy E_n used in equation (6.49). Equation (6.50) provides a more complete expression to model the number of trapped atoms. Note that if $\gamma = 0$ we recover our previous model given by equation (6.2). Equation (6.50) forms an infinite chain of coupled differential equations, which for a given initial condition of $N_n(t_0)$ can be solved to give $N_n(t)$ for any desired time. Matlab differential solver ‘ode45’ was used in the results presented here [61].

The greater sophistication of equation (6.50) comes at the cost of an increase in unknown variables. There are now two extra unknowns γ and \bar{n}_f to determine or (as it is easier experimentally and intuitively to work with temperatures) γ and T_f , where T_f is the temperature of the reservoir or equivalently the final thermodynamical equilibrium temperature of the system. The unknown T_f can replace the unknown \bar{n}_f if it is assumed that the reservoir is in thermal equilibrium, so that we can adapt equation (6.34) to use

$$\bar{n}_f = \frac{1}{e^{\frac{\hbar\omega}{k_B T_f}} - 1}. \quad (6.51)$$

Equation (6.31) can be used to track how \bar{n} varies with time. If we assume the distribution of atoms is given by a Maxwell-Boltzmann distribution then we can calculate a temperature for the atomic cloud from

$$T = \frac{\hbar\omega}{k_B} \frac{1}{\ln\left(\frac{1+\bar{n}}{\bar{n}}\right)}, \quad (6.52)$$

which is a rearrangement of equation (6.34).

Figures 6.18 and 6.19 show how the master equation model is affected by changes in γ and T_f . The blue curve in both plots corresponds with the previously obtained results for the case in which there is no coupling to the reservoir. You can see that in this case the temperature of the atom cloud cools as hot atoms are more likely to be lost from the trap due to non-adiabatic transitions. Now for non-zero relaxation parameter the atom number is seen to decrease significantly with increasing reservoir temperature or relaxation parameter. The temperature of the atom cloud is also highly affected, being heated or cooled depending on the values of γ and T_f . Interaction with an external reservoir could clearly have a dramatic effect on the observed lifetime of the trap.

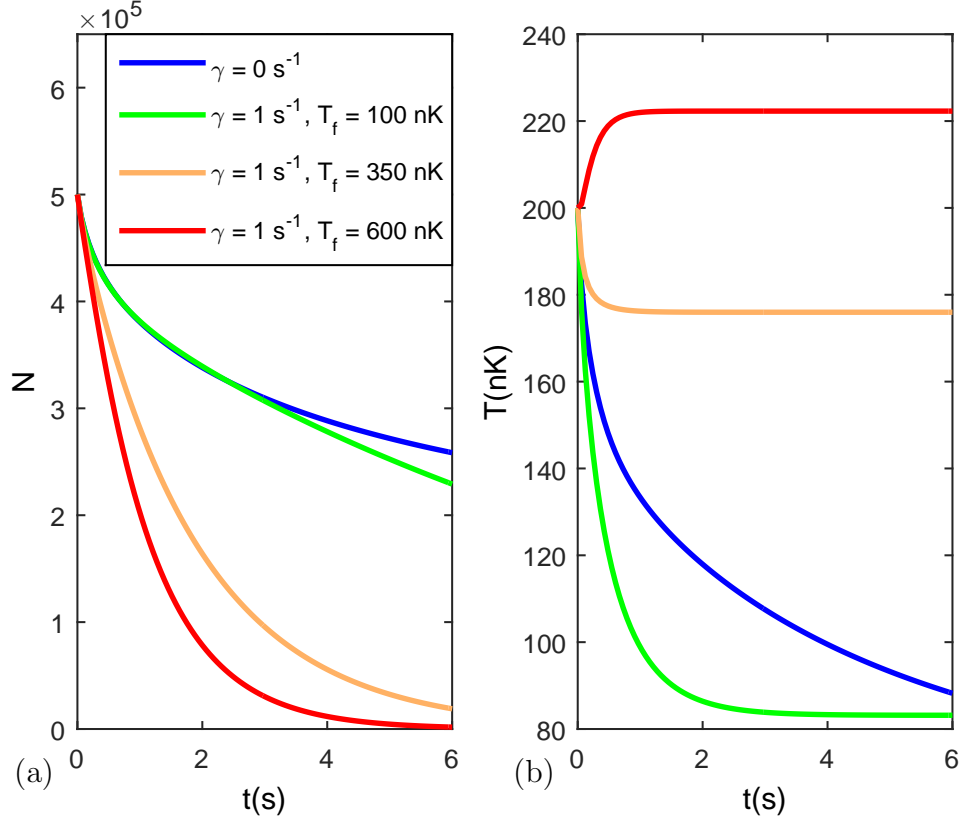


Figure 6.18: How the master equation model given by equation (6.50) is affected by a change in reservoir temperature, T_f . A Rabi frequency of $\Omega/2\pi = 8 \text{ kHz}$, a magnetic field gradient $B' = 1.1 \text{ T/m}$, a background decay rate $\Gamma_{bl} = 0.0087 \text{ s}^{-1}$ (set to match that given in chapter 8), an initial atom number $N(t_0) = 5 \times 10^5$ and an initial temperature $T(t_0) = 200 \text{ nK}$ were used for ^{87}Rb atoms. A Maxwell-Boltzmann initial distribution was also used with decay rates calculated by the full effect gravity model given by equation (5.136).

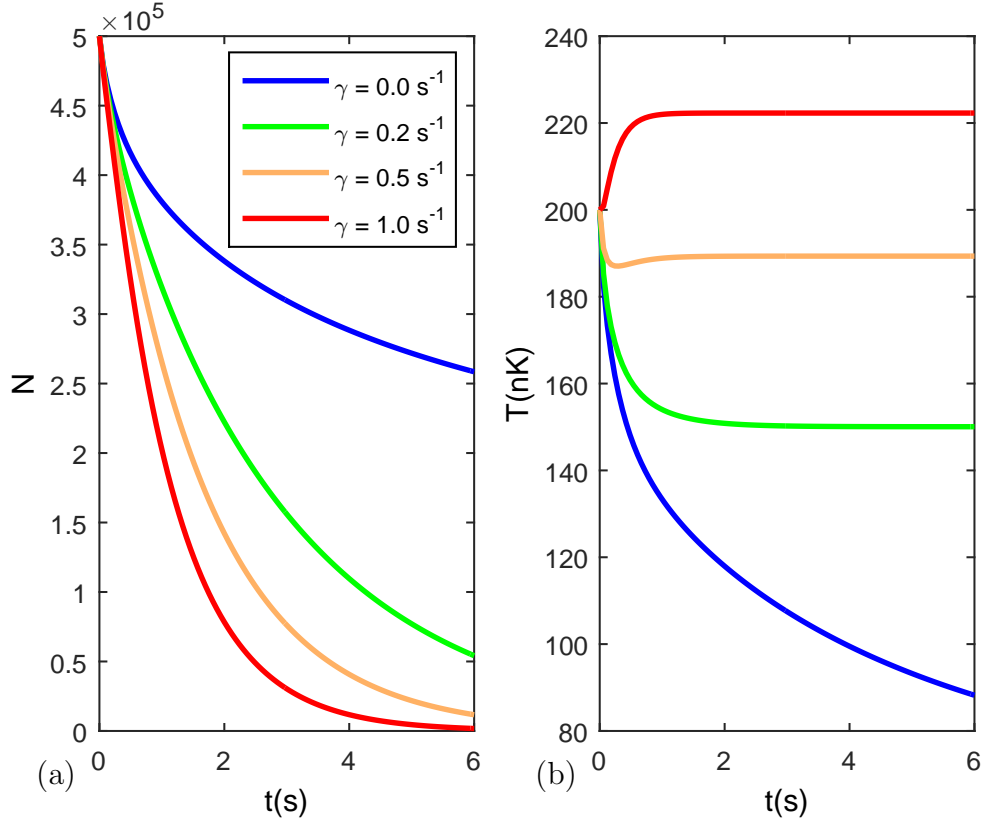


Figure 6.19: How the master equation model given by equation (6.50) is affected by a change in the relaxation parameter, γ . A Rabi frequency of $\Omega/2\pi = 8 \text{ kHz}$, a magnetic field gradient $B' = 1.1 \text{ T/m}$, a background decay rate $\Gamma_{bl} = 0.0087 \text{ s}^{-1}$ (set to match that given in chapter 8), an initial atom number $N(t_0) = 5 \times 10^5$ and an initial temperature $T(t_0) = 200 \text{ nK}$ were used for ^{87}Rb atoms. A Maxwell-Boltzmann initial distribution was also used with decay rates calculated by the full effect gravity model given by equation (5.136). The reservoir temperature was taken to be $T_f = 600 \text{ nK}$.

The changes in temperature of the cold atom cloud observed in figures 6.18 and 6.19 occur due to changes of energy of the trapped atoms. To understand the process described by equation (6.50) and the meaning of the parameters γ and \bar{n}_f , we now examine how the average energy per atom changes as a function of time.

If we define the average energy of a single trapped atom as:

$$\langle E(t) \rangle = \frac{1}{N(t)} \sum_{n=0}^{\infty} N_n(t) E_n, \quad (6.53)$$

then equation (6.50) can be used to calculate how the average energy of a single trapped atom varies in time. The average change in energy of a single trapped atom in time dt is given by:

$$\begin{aligned} \left\langle \frac{\partial E}{\partial t} \right\rangle &= \frac{1}{N(t)} \sum_{n=0}^{\infty} \frac{\partial N_n}{\partial t} E_n - \frac{1}{N(t)^2} \sum_{n=0}^{\infty} \frac{\partial N_n}{\partial t} \sum_{m=0}^{\infty} N_m E_m, \\ &= \frac{1}{N(t)} \sum_{n=0}^{\infty} \frac{\partial N_n}{\partial t} E_n - \frac{\langle E(t) \rangle}{N(t)} \sum_{n=0}^{\infty} \frac{\partial N_n}{\partial t}, \end{aligned} \quad (6.54)$$

$$= \left\langle \frac{\partial N}{\partial t} E(t) \right\rangle - \langle E(t) \rangle \left\langle \frac{\partial N}{\partial t} \right\rangle, \quad (6.55)$$

obtained by differentiation of equation (6.53). Using the rate of change of trapped atom number given by equation (6.50) we can obtain

$$\begin{aligned} \left\langle \frac{\partial E}{\partial t} \right\rangle &= \frac{1}{N(t)} \sum_{n=0}^{\infty} \left\{ \begin{aligned} &\gamma \bar{n}_f [n N_{n-1} E_n - (n+1) N_n E_n] \\ &+ \gamma (\bar{n}_f + 1) [(n+1) N_{n+1} E_n - n N_n E_n] \\ &- (\Gamma_n + \Gamma_{bl}) N_n E_n \end{aligned} \right\} \\ &- \frac{\langle E(t) \rangle}{N(t)} \sum_{n=0}^{\infty} \left\{ \begin{aligned} &\gamma \bar{n}_f [n N_{n-1} - (n+1) N_n] \\ &+ \gamma (\bar{n}_f + 1) [(n+1) N_{n+1} - n N_n] \\ &- (\Gamma_n + \Gamma_{bl}) N_n \end{aligned} \right\}. \end{aligned} \quad (6.56)$$

As the atomic energy levels E_n are harmonic oscillator energy levels, the energy spacings between levels is constant and given by $E_{n\pm 1} = E_n \pm \hbar\omega$. This can be used

to express equation (6.56) as:

$$\begin{aligned}
\left\langle \frac{\partial E}{\partial t} \right\rangle &= \frac{1}{N(t)} \sum_{n=0}^{\infty} \left\{ \begin{aligned} &\gamma \bar{n}_f [n N_{n-1} E_{n-1} + \hbar \omega n N_{n-1} - (n+1) N_n E_n] \\ &+ \gamma (\bar{n}_f + 1) [(n+1) N_{n+1} E_{n+1} - \hbar \omega (n+1) N_{n+1} - n N_n E_n] \\ &- (\Gamma_n + \Gamma_{bl}) N_n E_n \end{aligned} \right\} \\
&- \frac{\langle E(t) \rangle}{N(t)} \sum_{n=0}^{\infty} \left\{ \begin{aligned} &\gamma \bar{n}_f [n N_{n-1} - (n+1) N_n] \\ &+ \gamma (\bar{n}_f + 1) [(n+1) N_{n+1} - n N_n] \\ &- (\Gamma_n + \Gamma_{bl}) N_n \end{aligned} \right\}. \tag{6.57}
\end{aligned}$$

It can be seen by a simple substitution of variables that the following summations are equivalent:

$$\sum_{n=0}^{\infty} n N_{n-1} E_{n-1} = \sum_{m=0}^{\infty} (m+1) N_m E_m, \tag{6.58}$$

$$\sum_{n=0}^{\infty} (n+1) N_{n+1} E_{n+1} = \sum_{m=0}^{\infty} m N_m E_m, \tag{6.59}$$

as well as the related expressions with no energy term. There are then significant cancellations:

$$\begin{aligned}
\left\langle \frac{\partial E}{\partial t} \right\rangle &= \frac{\gamma \hbar \omega}{N(t)} \sum_{n=0}^{\infty} [\bar{n}_f n N_{n-1} - (\bar{n}_f + 1) (n+1) N_{n+1}] \\
&- \frac{1}{N(t)} \sum_{n=0}^{\infty} (\Gamma_n + \Gamma_{bl}) N_n E_n + \frac{\langle E(t) \rangle}{N(t)} \sum_{n=0}^{\infty} (\Gamma_n + \Gamma_{bl}) N_n. \tag{6.60}
\end{aligned}$$

By another change of variables,

$$\begin{aligned}
\left\langle \frac{\partial E}{\partial t} \right\rangle &= \frac{\gamma \hbar \omega}{N(t)} \sum_{n=0}^{\infty} [\bar{n}_f (n+1) N_n - (\bar{n}_f + 1) n N_n] \\
&- \frac{1}{N(t)} \sum_{n=0}^{\infty} (\Gamma_n + \Gamma_{bl}) N_n E_n + \frac{\langle E(t) \rangle}{N(t)} \sum_{n=0}^{\infty} (\Gamma_n + \Gamma_{bl}) N_n \tag{6.61}
\end{aligned}$$

we can interpret equation (6.61) such that the first line gives the relative heating rate of an atom in level n at time t . The second line takes into account how the loss of energy from the trap, through loss of atoms, affects the average energy of a trapped atom. Equation (6.61) can be written equivalently as

$$\begin{aligned}
\left\langle \frac{\partial E}{\partial t} \right\rangle &= \frac{\gamma \hbar \omega}{N(t)} \bar{n}_f \sum_{n=0}^{\infty} N_n - \frac{\gamma \hbar \omega}{N(t)} \sum_{n=0}^{\infty} n N_n \\
&+ \frac{\langle E(t) \rangle}{N(t)} \sum_{n=0}^{\infty} \Gamma_n N_n + \Gamma_{bl} \frac{\langle E(t) \rangle}{N(t)} \sum_{n=0}^{\infty} N_n \\
&- \frac{1}{N(t)} \sum_{n=0}^{\infty} \Gamma_n N_n E_n - \frac{\Gamma_{bl}}{N(t)} \sum_{n=0}^{\infty} N_n E_n. \tag{6.62}
\end{aligned}$$

As we know from previous definitions, given by equations (6.3), (6.31), and (6.53), the meanings associated with some of the terms in equation (6.62), we can use more appropriate notation to express the rate of change of the average energy of an atom as

$$\left\langle \frac{\partial E}{\partial t} \right\rangle = \gamma \hbar \omega (\bar{n}_f - \bar{n}) + \frac{\langle E(t) \rangle}{N(t)} \sum_{n=0}^{\infty} \Gamma_n N_n - \frac{1}{N(t)} \sum_{n=0}^{\infty} \Gamma_n N_n E_n. \quad (6.63)$$

Notice that the background loss rate does not contribute to the average change in energy of a single atom, as it leads to losses at an equal rate from all energy levels. Therefore although Γ_{bl} leads to a decrease in the total trap energy, the number of trapped atoms decreases due to background losses at the same rate, such that the average energy of a single trapped atom remains unaffected by the loss of atoms from all energy levels at the same rate. Using

$$\langle E \rangle = \frac{1}{N(t)} \sum_{n=0}^{\infty} N_n(t) \left[\hbar \omega \left(n + \frac{1}{2} \right) + V_0 \right] \quad (6.64)$$

$$= \hbar \omega \bar{n} + \frac{\hbar \omega}{2} + V_0 \quad (6.65)$$

we can express equation (6.63) alternatively in terms of the average energy of a trapped atom,

$$\left\langle \frac{\partial E}{\partial t} \right\rangle = \gamma (E_f - \langle E \rangle) + \frac{\langle E(t) \rangle}{N(t)} \sum_{n=0}^{\infty} \Gamma_n N_n - \frac{1}{N(t)} \sum_{n=0}^{\infty} \Gamma_n N_n E_n. \quad (6.66)$$

E_f is the final equilibrium energy that would be reached if there were no losses from the trap.

The formulae obtained for Γ_n are too complicated to solve equation (6.66) directly, however, it can still tell us information about the modelled trap setup. We can see that in the absence of any losses from the trap the average atomic energy will increase until it hits the equilibrium energy. In the limit in which non-adiabatic losses are negligible, such as the high Rabi frequency limit, equation (6.66) can be solved to give an expression for how the mean energy of a trapped atom varies in time;

$$\langle E(t) \rangle = (\langle E(t_0) \rangle - E_f) e^{-\gamma t} + E_f. \quad (6.67)$$

This agrees with our earlier assertions in regards to the meaning of γ and the behaviour of this master equation model. In the long time limit the system approaches a steady energy state determined by E_f , characterized by \bar{n}_f . The rate of this process is given by the relaxation parameter γ . The master equation model parameters γ and \bar{n}_f are not associated with any particular process and depend on whatever is acting as a coupling between the harmonic oscillator levels.

6.4.2 Parametric heating model

The master equation model is very general, in an attempt to cover a variety of different processes that may affect the trap. Alternatively, a more accurate model can be formed in the case in which we know that the dominant heating comes from noise in the trap parameters. Fluctuations in the trap frequency and equilibrium position can occur due to unavoidable fluctuations in the RF frequency, RF magnetic field amplitude and static magnetic field gradient [56]. The effects of this parametric heating are discussed in reference [69], which we shall review here.

Fluctuations in the trap centre

We first consider fluctuations in the trap centre, such that the Hamiltonian for the trap is given by

$$\hat{H} = \frac{\hat{p}_z^2}{2m_0} + \frac{m_0\omega^2}{2}[z - \delta Z(t)]^2, \quad (6.68)$$

where δZ is the fluctuating noise in the equilibrium position of the trap. The above Hamiltonian can be split up into the unperturbed Hamiltonian,

$$\hat{H}_0(z) = \frac{\hat{p}_z^2}{2m_0} + \frac{m_0\omega^2}{2}z^2, \quad (6.69)$$

we have assumed so far and the perturbation

$$\hat{V}(t, z) = \frac{m_0\omega^2}{2}(\delta Z^2 - 2z \cdot \delta Z). \quad (6.70)$$

As the noise is expected to have a small effect on the trap system we can use the techniques discussed in section 4 to use first order, time dependent perturbation theory to model the noise induced transitions. We can adapt equation (4.18) to

$$P_{n \rightarrow m}(t_f) = \frac{1}{\hbar^2} \left| \int_0^{t_f} e^{i\omega_{mn}t} V_{mn}(t) dt \right|^2, \quad (6.71)$$

where $P_{n \rightarrow m}(t_f)$ is the probability of finding an atom with energy E_m at time $t = t_f$ when it is known that the atom had energy E_n at $t = 0$. It can be seen from substituting equation (6.70) into equation (6.71) that

$$P_{n \rightarrow m}(t_f) = \frac{m_0^2\omega^4}{\hbar^2} |\langle m | \hat{z} | n \rangle|^2 \cdot \left| \int_0^{t_f} \delta Z(t') e^{i\omega_{mn}t'} dt' \right|^2. \quad (6.72)$$

It is now most convenient to express the position operator \hat{z} in terms of annihilation and creation operators, defined with equations (6.15) and (6.16), such that

$$P_{n \rightarrow m}(t_f) = \frac{m_0\omega^3}{2\hbar} |\langle m | \hat{a} + \hat{a}^\dagger | n \rangle|^2 \cdot \left| \int_0^{t_f} \delta Z(t') e^{i\omega_{mn}t'} dt' \right|^2. \quad (6.73)$$

We can thus use the relations

$$\hat{a}|n\rangle = \sqrt{n}|n-1\rangle, \quad (6.74)$$

$$\hat{a}^\dagger|n\rangle = \sqrt{n+1}|n+1\rangle, \quad (6.75)$$

to obtain

$$P_{n \rightarrow m}(t_f) \propto \left| \sqrt{n} \langle m|n-1\rangle + \sqrt{n+1} \langle m|n+1\rangle \right|^2. \quad (6.76)$$

The only non-zero transitions are those with $m = n \pm 1$, we therefore arrive at the transition rate given in reference [69],

$$\Gamma_{n \rightarrow n \pm 1} = \frac{P_{n \rightarrow n \pm 1}}{t_f} = \gamma_a \left(n + \frac{1}{2} \pm \frac{1}{2} \right). \quad (6.77)$$

Here γ_a determines the rate of transitions between neighbouring energy levels.

The heating rate γ_a is dependent on the atomic mass, trap frequency and the noise in the equilibrium position of the trap and we can return to equation (6.73) to derive a more convenient expression for it. From equation (6.73) we see that,

$$\gamma_a = \frac{m_0 \omega^3}{2\hbar} \frac{1}{t_f} \left| \int_0^{t_f} \delta Z(t') e^{\pm i \omega t'} dt' \right|^2. \quad (6.78)$$

If we assume the noise in the trap position is real, this is equivalent to

$$\gamma_a = \frac{m_0 \omega^3}{2\hbar} \frac{1}{t_f} \int_0^{t_f} \int_0^{t_f} \delta Z(t) \delta Z(t') e^{\pm i \omega (t' - t)} dt dt'. \quad (6.79)$$

If we assume that the noise is stationary and ergodic we are able to characterise the noise by its power spectrum [70]. Defining $\tau = t' - t$, as in reference [71],

$$\gamma_a = \frac{m_0 \omega^3}{2\hbar} \frac{1}{t_f} \int_{-t_f}^{t_f} \int_0^{t_f} \delta Z(t) \delta Z(t + \tau) e^{\pm i \omega \tau} dt d\tau. \quad (6.80)$$

The correlation function for fluctuations in the trap equilibrium position is described by

$$\langle \delta Z(t) \delta Z(t + \tau) \rangle = \frac{1}{t_f} \int_0^{t_f} \delta Z(t) \delta Z(t + \tau) dt, \quad (6.81)$$

such that we can write

$$\gamma_a = \frac{m_0 \omega^3}{2\hbar} \int_{-t_f}^{t_f} \langle \delta Z(t) \delta Z(t + \tau) \rangle e^{\pm i \omega \tau} d\tau. \quad (6.82)$$

This can be equivalently written as

$$\gamma_a = \frac{m_0 \omega^3}{2\hbar} \int_{-t_f}^{t_f} \langle \delta Z(t) \delta Z(t + \tau) \rangle \cos(\omega \tau) d\tau, \quad (6.83)$$

as the imaginary component of the exponential leads to an integral whose value is zero, which arises as the correlation function is an even function. The power

spectrum for the fluctuations in the trap equilibrium position is defined by the Fourier transform of the correlation function:

$$S_z(\omega) = \frac{1}{\pi} \int_{-\infty}^{\infty} \cos(\omega\tau) \langle \delta Z(t) \delta Z(t+\tau) \rangle d\tau. \quad (6.84)$$

Such that in the $t_f \rightarrow \infty$ limit we see that the heating can be expressed as

$$\gamma_a = \frac{\pi m_0 \omega^3}{2\hbar} S_z(\omega). \quad (6.85)$$

Which agrees with the results presented in reference [69].

It can be calculated from equation (6.85) that for a trap frequency of $\omega/2\pi = 1$ kHz and ^{87}Rb atoms a heating rate of one transition a second ($\gamma_a = 1 \text{ s}^{-1}$) occurs when the power spectral density for noise in the trap centre is $\sqrt{S_z(\omega)} = 4 \times 10^{-2} \text{ nm}/\sqrt{\text{Hz}}$.

Fluctuations in the trap frequency

We then repeat the procedure for noise associated with the trap frequency, described by the Hamiltonian

$$\hat{H} = \frac{\hat{p}_z^2}{2m_0} + \frac{m_0\omega^2}{2} \left[1 + \frac{\delta k_i}{k_i}(t) \right] z^2 \quad (6.86)$$

where $\delta k_i/k_i$ is the fractional fluctuation of $k_i = m_0\omega^2$, the spring constant of the trap harmonic oscillator. The unperturbed Hamiltonian is given as before by equation (6.69) and the perturbation is now given by

$$\hat{V}(t, z) = \frac{m_0\omega^2}{2} z^2 \cdot \frac{\delta k_i}{k_i}. \quad (6.87)$$

Use of equation (6.71) gives the expression for the probability for an atom to be found in the harmonic oscillator level m at time t_f when it was known to be in level n at $t = 0$, leading to the expression

$$P_{n \rightarrow m}(t_f) = \frac{m_0^2 \omega^4}{4\hbar^2} |\langle m | \hat{z}^2 | n \rangle|^2 \cdot \left| \int_0^{t_f} \frac{\delta k_i}{k_i}(t') e^{i\omega_{mn}t'} dt' \right|^2. \quad (6.88)$$

If we express the transition probability in terms of annihilation and creation operators:

$$P_{n \rightarrow m}(t_f) = \frac{\omega^2}{16} |\langle m | \hat{a}^2 + 1 + 2\hat{a}^\dagger \hat{a} + \hat{a}^{\dagger 2} | n \rangle|^2 \cdot \left| \int_0^{t_f} \frac{\delta k_i}{k_i}(t') e^{i\omega_{mn}t'} dt' \right|^2. \quad (6.89)$$

Relations (6.74) and (6.75) can be applied to see that

$$P_{n \rightarrow m}(t_f) \propto \left| \sqrt{n}\sqrt{n-1} \langle m | n-2 \rangle + (1+2n) \langle m | n \rangle + \sqrt{n+1}\sqrt{n+2} \langle m | n+2 \rangle \right|^2 \quad (6.90)$$

As we are only interested in $m \neq n$, the orthogonality of the harmonic oscillator wavefunctions thus ensures that the only non-zero transitions induced are those with $m = n \pm 2$. We therefore arrive at the transition rate given in reference [69] caused by fluctuations in the trap frequency,

$$\Gamma_{n \rightarrow n \pm 2} = \frac{P_{n \rightarrow n \pm 2}}{t_f} = \gamma_b (n + 1 \pm 1) (n \pm 1). \quad (6.91)$$

The heating rate γ_b determines the rate at which transitions with $|\Delta n| = 2$ occur. γ_b is dependent on the trap frequency and the noise associated with it, defined by

$$\gamma_b = \frac{\omega^2}{16} \frac{1}{t_f} \left| \int_0^{t_f} \frac{\delta k_i}{k_i}(t') e^{\pm 2i\omega t'} dt' \right|^2. \quad (6.92)$$

Following a similar procedure to before, we can define the power spectrum for the fluctuations in the spring constant [71] as

$$S_k(\omega) = \frac{1}{\pi} \int_{-\infty}^{\infty} \cos(\omega\tau) \left\langle \frac{\delta k_i}{k_i}(t) \frac{\delta k_i}{k_i}(t + \tau) \right\rangle d\tau \quad (6.93)$$

and express γ_b [69] as

$$\gamma_b = \frac{\pi\omega^2}{16} S_k(2\omega). \quad (6.94)$$

It can be calculated from equation (6.94) that for a trap frequency of $\omega/2\pi = 1$ kHz a heating rate of one transition a second ($\gamma_b = 1 \text{ s}^{-1}$) occurs when the power spectral density for noise in the trap frequency is $\sqrt{S_k(2\omega)} = 4 \times 10^{-4} \sqrt{\text{Hz}^{-1}}$.

We now have two processes that allow transitions between energy levels as shown in figure 6.20. Single level transitions that occur at a rate proportional to γ_a and double level transitions, that obey $\Delta n = \pm 2$, which occur at a rate proportional to γ_b . As in the master equation model the rate of transitions increases for higher energy states.

By considering the difference in rate between the transitions into and out of a given n state, we are thus able to use equations (6.77) and (6.91) to construct the parametric heating model:

$$\begin{aligned} \frac{\partial N_n}{\partial t} = & \gamma_a [nN_{n-1} - (n+1)N_n] + \gamma_a [(n+1)N_{n+1} - nN_n] \\ & + \gamma_b [n(n-1)N_{n-2} - (n+1)(n+2)N_n] \\ & + \gamma_b [(n+1)(n+2)N_{n+2} - n(n-1)N_n] - (\Gamma_n + \Gamma_{bl}) N_n. \end{aligned} \quad (6.95)$$

The parametric heating model provides a set of coupled differential equations which can be solved for a given initial condition to give the number of trapped atoms as a function of time. Matlab differential solver ‘ode45’ [61] was used here to find $N_n(t)$ from equation (6.95). Equation (6.3) was then used to determine the total

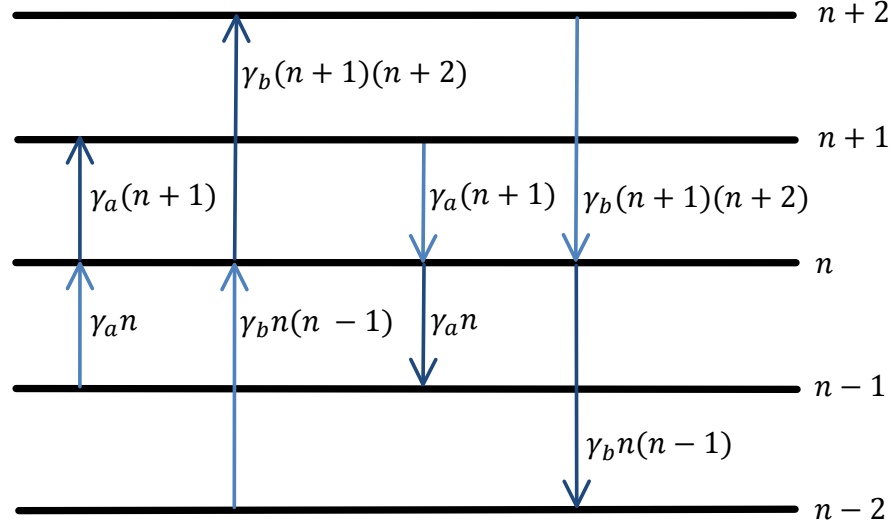


Figure 6.20: Transitions into and out of the n th energy level considered in the parametric heating model. γ_a and γ_b are heating rates with units s^{-1} .

number of trapped atoms, by summing the number of atoms with every possible energy.

Increasing the values of the heating rates γ_a and γ_b speeds up the loss of atoms from the trap and in general raises the atom cloud temperature, as shown in figure 6.21, with the γ_b heating rate having a greater effect than the heating rate γ_a .

Figure 6.22 shows the effect of changing the initial distribution for our parametric heating model. For an estimation of the temperature of the atom cloud a Maxwell-Boltzmann distribution has to be assumed, as equation (6.52) is a rearrangement of equation (6.34). However, a more accurate distribution of atomic energies may be given by an alternative distribution, for example, the Bose-Einstein or squeezed thermal initial distributions previously studied. Figure 6.22 (a) shows how this leads to a difference in the prediction for the number of trapped atoms.

Figure 6.22 (b) displays a measure of how much the distribution of atoms varies from a Maxwell-Boltzmann distribution. The variable N_{nt} is calculated from

$$N_{nt}(t) = \frac{1}{2} \sum_n |N_n(t) - N_n^{MB}[t, T(t)]| \quad (6.96)$$

where $N_n(t)$ is obtained from solution of equation (6.95) for the parametric heating model and N_n^{MB} is the number of atoms that would be predicted to be in the n th harmonic oscillator level for a Maxwell-Boltzmann distribution with temperature T . T is the temperature calculated from $N_n(t)$, using equation (6.52), assuming a

Maxwell-Boltzmann distribution. Therefore, if $N_n(t)$ can be modelled by a Maxwell-Boltzmann distribution the quantity N_{nt} should be zero.

Figure 6.22 (b) brings into question the validity of our temperature calculation. At short times, the distribution of atoms is strongly influenced by the model chosen for the initial distribution of atoms. At long times, the choice of initial distribution is not significant, however, the convergence of the atomic energy distribution is such that 15% of the atoms have an n value which differs from that predicted by the Maxwell-Boltzmann distribution associated with $T(t)$.

It should be noted that the measure N_{nt} applied to our prediction of the trapped atom number N_n does not measure the variance of displaced atom energies. N_{nt} given by equation (6.96) counts the number of atoms which are not found in locations predicted by the Maxwell-Boltzmann distribution N_n^{MB} . It achieves this by counting the number of atoms which transition out of their expected energy level and the number of phantom atoms, holes left behind where they should have been. The factor of a half then removes these phantom atoms, such that $N_{nt}(t)$ is the total number of displaced atoms. No information is retained in $N_{nt}(t)$ as to how great the energy difference associated with the transition is for each of the displaced atoms. For the minimal effect gravity model, a small change in atom energy would not affect the non-adiabatic decay rates dramatically. However, for the full effect gravity model even a small change in atom level can have a significant effect, as shown by figure 5.16.

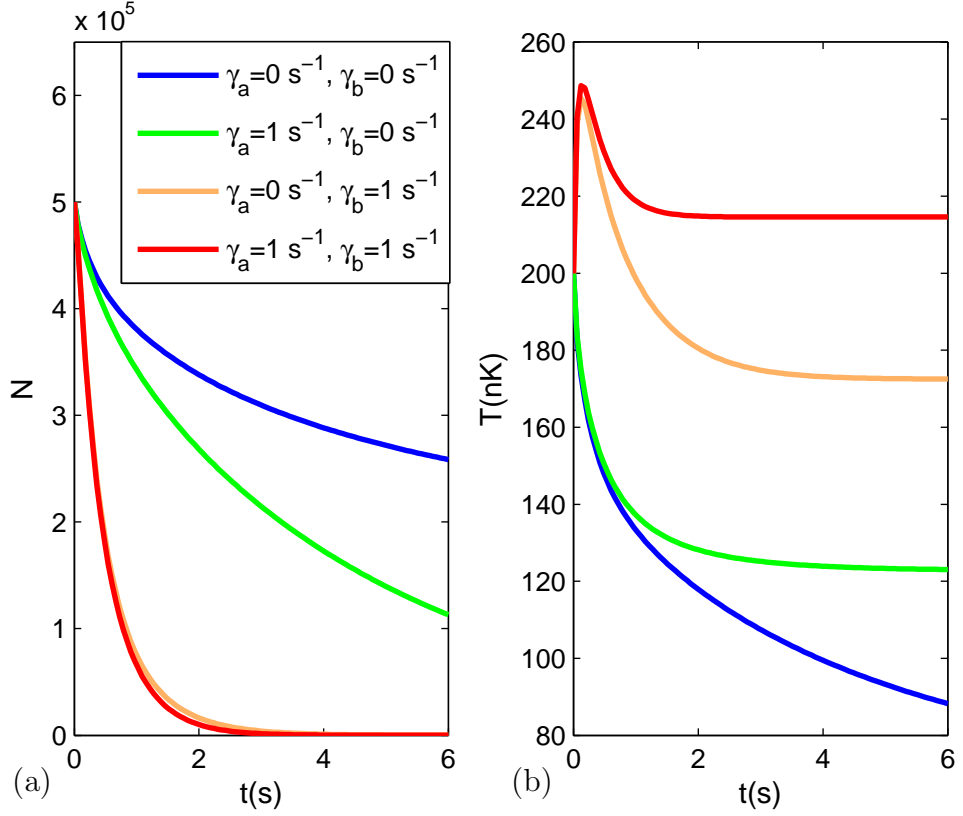


Figure 6.21: How the parametric heating model given by equation (6.95) is affected by changing γ_a and γ_b . A Rabi frequency of $\Omega/2\pi = 8$ kHz, magnetic field gradient $B' = 1.1$ T/m, background decay rate $\Gamma_{bl} = 0.0087 \text{ s}^{-1}$ (set to match that given in chapter 8), initial atom number $N(t_0) = 5 \times 10^5$ and initial temperature $T(t_0) = 200$ nK were used for ^{87}Rb atoms. A Maxwell-Boltzmann initial distribution of atoms with decay rates calculated by the full effect gravity model given by equation (5.136) was used.

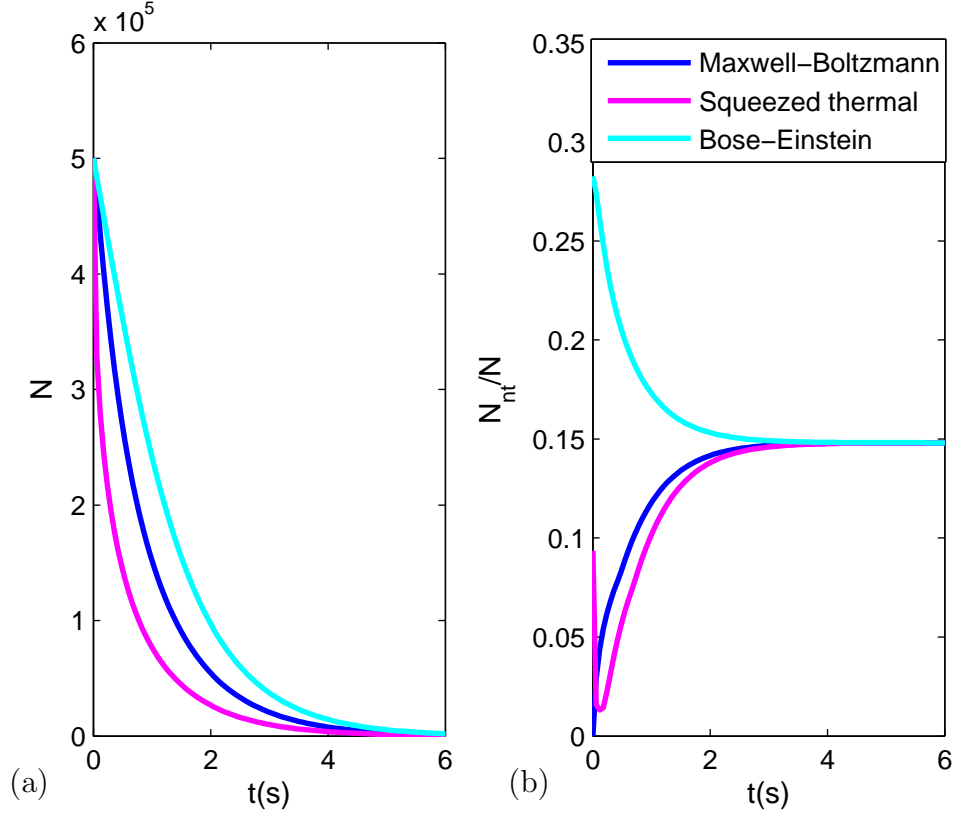


Figure 6.22: Affect of the initial distribution on the parametric heating model. (a) shows the trapped atom number evolution given by equation (6.95). (b) measures how well the time evolution of the distribution can be obtained by a Maxwell-Boltzmann distribution, by calculating equation (6.96). N_{nt} finds the number of atoms in the atom cloud that are not in n states predicted by a Maxwell-Boltzmann distribution, using the calculated temperature values obtained from equation (6.52). A Rabi frequency of $\Omega/2\pi = 8$ kHz, magnetic field gradient $B' = 1.1$ T/m, RF frequency $\omega_{\text{rf}}/2\pi = 1.2$ MHz, initial atom number $N(t_0) = 5 \times 10^5$ and initial temperature $T(t_0) = 200$ nK were used for ^{87}Rb atoms. Heating rates of $\gamma_a = \gamma_b = 0.5 \text{ s}^{-1}$ were used with decay rates calculated by the full effect gravity model given by equation (5.136).

As for the master equation model, we can use equation (6.54) to determine the rate of change of the mean energy of a trapped atom for the parametric heating model,

$$\begin{aligned}
\left\langle \frac{\partial E}{\partial t} \right\rangle &= \frac{1}{N(t)} \sum_{n=0}^{\infty} \left\{ \gamma_a [n N_{n-1} E_n - (n+1) N_n E_n] \right. \\
&\quad + \gamma_a [(n+1) N_{n+1} E_n - n N_n E_n] \\
&\quad + \gamma_b [n(n-1) N_{n-2} E_n - (n+1)(n+2) N_n E_n] \\
&\quad + \gamma_b [(n+1)(n+2) N_{n+2} E_n - n(n-1) N_n E_n] \\
&\quad \left. - (\Gamma_n + \Gamma_{bl}) N_n E_n \right\} \\
&\quad + \frac{\langle E(t) \rangle}{N(t)} \sum_{n=0}^{\infty} (\Gamma_n + \Gamma_{bl}) N_n. \tag{6.97}
\end{aligned}$$

Using the fact that the trap potential is given by a harmonic oscillator, we can write

$$\begin{aligned}
\left\langle \frac{\partial E}{\partial t} \right\rangle &= \frac{1}{N(t)} \sum_{n=0}^{\infty} \left\{ \gamma_a [n N_{n-1} (E_{n-1} + \hbar\omega) - (n+1) N_n E_n] \right. \\
&\quad + \gamma_a [(n+1) N_{n+1} (E_{n+1} - \hbar\omega) - n N_n E_n] \\
&\quad + \gamma_b [n(n-1) N_{n-2} (E_{n-2} + 2\hbar\omega) - (n+1)(n+2) N_n E_n] \\
&\quad + \gamma_b [(n+1)(n+2) N_{n+2} (E_{n+2} - 2\hbar\omega) - n(n-1) N_n E_n] \\
&\quad \left. - (\Gamma_n + \Gamma_{bl}) N_n E_n \right\} + \frac{\langle E(t) \rangle}{N(t)} \sum_{n=0}^{\infty} (\Gamma_n + \Gamma_{bl}) N_n. \tag{6.98}
\end{aligned}$$

Using equations (6.58) and (6.59), as well as

$$\sum_{n=0}^{\infty} n(n-1) N_{n-2} E_{n-2} = \sum_{m=0}^{\infty} (m+2)(m+1) N_m E_m, \tag{6.99}$$

$$\sum_{n=0}^{\infty} (n+1)(n+2) N_{n+2} E_{n+2} = \sum_{m=0}^{\infty} m(m-1) N_m E_m, \tag{6.100}$$

we can cancel many terms to obtain

$$\begin{aligned}
\left\langle \frac{\partial E}{\partial t} \right\rangle &= \frac{1}{N(t)} \sum_{n=0}^{\infty} \left\{ \hbar\omega \gamma_a [n N_{n-1} - (n+1) N_{n+1}] \right. \\
&\quad + 2\hbar\omega \gamma_b [n(n-1) N_{n-2} - (n+1)(n+2) N_{n+2}] \\
&\quad \left. - (\Gamma_n + \Gamma_{bl}) N_n E_n \right\} + \frac{\langle E(t) \rangle}{N(t)} \sum_{n=0}^{\infty} (\Gamma_n + \Gamma_{bl}) N_n. \tag{6.101}
\end{aligned}$$

Another change of variable gives us

$$\begin{aligned}
\left\langle \frac{\partial E}{\partial t} \right\rangle &= \frac{1}{N(t)} \sum_{n=0}^{\infty} \left\{ \hbar\omega \gamma_a [(n+1) N_n - n N_n] \right. \\
&\quad + 2\hbar\omega \gamma_b [(n+2)(n+1) N_n - n(n-1) N_n] \\
&\quad \left. - (\Gamma_n + \Gamma_{bl}) N_n E_n \right\} + \frac{\langle E(t) \rangle}{N(t)} \sum_{n=0}^{\infty} (\Gamma_n + \Gamma_{bl}) N_n, \tag{6.102}
\end{aligned}$$

which leads us to

$$\begin{aligned}
\left\langle \frac{\partial E}{\partial t} \right\rangle &= \frac{\hbar\omega\gamma_a}{N(t)} \sum_{n=0}^{\infty} N_n + \frac{8\hbar\omega\gamma_b}{N(t)} \sum_{n=0}^{\infty} \left(n + \frac{1}{2} \right) N_n \\
&+ \frac{\langle E(t) \rangle}{N(t)} \sum_{n=0}^{\infty} \Gamma_n N_n + \Gamma_{bl} \frac{\langle E(t) \rangle}{N(t)} \sum_{n=0}^{\infty} N_n \\
&- \frac{1}{N(t)} \sum_{n=0}^{\infty} \Gamma_n N_n E_n - \frac{\Gamma_{bl}}{N(t)} \sum_{n=0}^{\infty} N_n E_n.
\end{aligned} \tag{6.103}$$

Equations (6.3) and (6.53) allow us to express the time evolution of the change in the mean atomic energy as

$$\begin{aligned}
\left\langle \frac{\partial E}{\partial t} \right\rangle &= \hbar\omega\gamma_a - 8\gamma_b V_0 + 8\gamma_b \langle E(t) \rangle \\
&+ \frac{\langle E(t) \rangle}{N(t)} \sum_{n=0}^{\infty} \Gamma_n N_n - \frac{1}{N(t)} \sum_{n=0}^{\infty} \Gamma_n N_n E_n.
\end{aligned} \tag{6.104}$$

Note that for the same reasoning as for the master equation model, the background loss rate terms cancel. Equation (6.104) gives us the expression for how the average energy of a single atom varies with time in the parametric heating model.

Taking the limit in which $\Gamma_n \rightarrow 0$ we can solve equation (6.104) to find the mean energy of a trapped atom at any given time:

$$\langle E(t) \rangle = \left[\langle E(t_0) \rangle + \frac{(\hbar\omega\gamma_a - 8\gamma_b V_0)}{8\gamma_b} \right] e^{8\gamma_b t} - \frac{(\hbar\omega\gamma_a - 8\gamma_b V_0)}{8\gamma_b}. \tag{6.105}$$

This tells us more about the heating rates γ_a and γ_b . By setting $\gamma_a = 0$ we can see that fluctuations in the trap frequency lead to an exponential increase in the average trapped atom energy, given by

$$\langle E(t) \rangle = (\langle E(t_0) \rangle - V_0) e^{8\gamma_b t} + V_0. \tag{6.106}$$

By expanding out the exponential in equation (6.105) and then setting $\gamma_b = 0$, we can see that fluctuations in the trap centre lead to a linear increase in the average trapped atom energy, given by

$$\langle E(t) \rangle = \langle E(t_0) \rangle + \hbar\omega\gamma_a t. \tag{6.107}$$

The steady state of this model ($\frac{\partial N_n}{\partial t} = 0$) occurs when the occupation of all levels is equal. In this case \bar{n} is infinite. Using equation (6.52) to calculate the temperature as a function of time we would see that for non-zero γ_a and γ_b and no losses, the temperature will continue to rise forever. This model is therefore considered to describe a heating process and differs from the master equation dynamical model which instead tends to an equilibrium temperature.

By speeding up the loss of hot atoms figure 6.23 shows that, at the expense of a decrease in the number of trapped atoms, adding in heating effects can actually reduce the temperature of the atomic cloud further than if heating is negligible. Loss of any atoms from the trap removes energy from the system. If losses occur at the same rate for all possible atomic energies, due to Γ_{bl} , the average trapped atom energy does not change as has been seen mathematically. However, our non-adiabatic losses are dependent on the atomic energy. Hot atoms, those in high n states, in general decay much quicker than cold atoms in low n states. Hot atoms are therefore selectively lost from the trap and the atom cloud is effectively cooled by the removal of high energy atoms from within it.

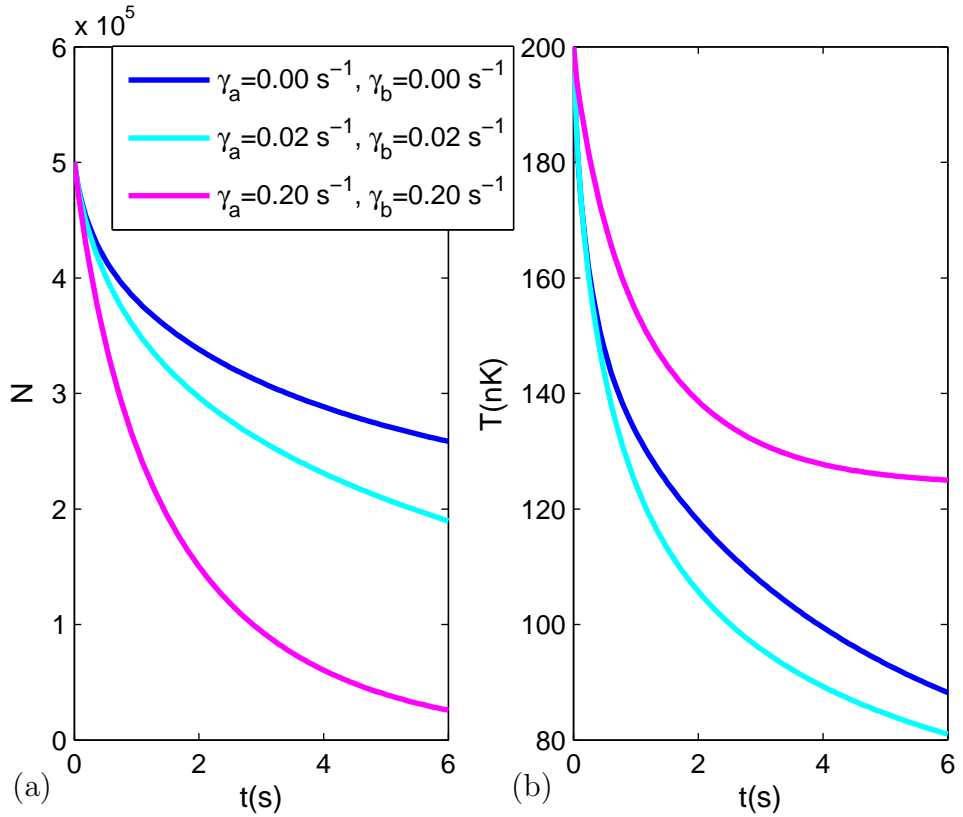


Figure 6.23: Affect of increasing heating rate on the parametric heating model given by equation (6.95). A Rabi frequency of $\Omega/2\pi = 8$ kHz, magnetic field gradient $B' = 1.1$ T/m, background decay rate $\Gamma_{bl} = 0.0087 \text{ s}^{-1}$ (set to match that given in chapter 8), initial atom number $N(t_0) = 5 \times 10^5$ and initial temperature $T(t_0) = 200$ nK were used for ^{87}Rb atoms. A Maxwell-Boltzmann initial distribution of atoms was assumed with decay rates calculated by the full effect gravity model given by equation (5.136).

Figure 6.24 details how the average atomic energy is affected by various heating and decay rates in the parametric heating model. When there are no energy dependent losses, the exponential behaviour of the γ_b decay rate can be seen; while the linear behaviour of the γ_a decay rate is very small for a rate of equivalent value. When energy dependent loss is present in the system, in this case provided by our non-adiabatic decay rates, the selective loss of hot atoms from the trap is significant enough such that the average energy of a single atom decreases counteracting the heating processes.

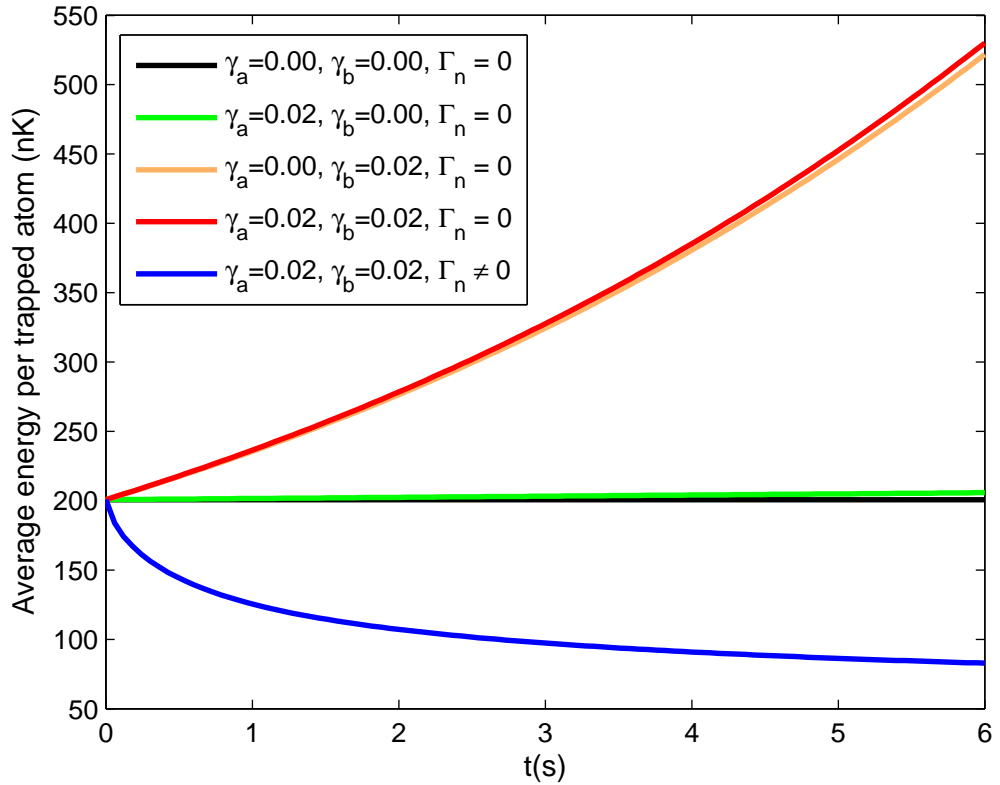


Figure 6.24: How the average energy per atom varies with heating rate and the presence or absence of non-adiabatic losses. Heating rate values are given in units of inverse seconds. A Rabi frequency of $\Omega/2\pi = 8$ kHz, magnetic field gradient $B' = 1.1$ T/m, initial atom number $N(t_0) = 5 \times 10^5$ and initial temperature $T(t_0) = 200$ nK were used for ^{87}Rb atoms. A Maxwell-Boltzmann initial distribution of atoms was assumed with decay rates calculated by the full effect gravity model given by equation (5.136).

6.5 Summary

In this section we studied the time evolution of the number of trapped atoms, using our decay rates derived from Fermi's Golden Rule and presuming every spin flip results in a loss of an atom from the trap. Found at the end of this summary, table 6.1 summarises the key models and table 6.2 summarises the key figures presented in this chapter.

Initially we did not take into consideration the possibility for transitions between atomic energy levels and used equation (6.4) to calculate the number of trapped atoms. We began our investigations by considering a thermal Maxwell-Boltzmann initial distribution of atomic energies. We saw for the first time in figure 6.5 how our different decay rates compare when predicting trapped atom number. This cannot be seen simply from comparing the decay rates alone, when more than one atom energy needs to be considered, as the appropriate weighted summation determined by equation (6.4) needs to be carried out. The pole approximation showed to be in very good agreement with the minimal effect gravity model, for the parameters considered in figure 6.5. The full effect gravity model predicted noticeably more atoms would remain trapped than in the minimal effect gravity model. This confirms, what was suspected from chapter 5, that gravity reduces the number of transitions and highlighting the importance of using the full effect gravity model for quantitative predictions.

We next examined the possibility for a squeezed thermal initial distribution in which atoms are more likely to be found at higher energies than is predicted by a Maxwell-Boltzmann distribution. This kind of initial distribution may occur if the trap is dropped too rapidly from a high Rabi frequency to a lower Rabi frequency value.

A Bose-Einstein initial distribution was also considered. This thermal distribution should provide the most accurate initial distribution for the low temperatures typical of ultracold atom traps. More information is required in using a Bose-Einstein distribution so we made some presumptions about the type of cold atom trap, modelling the case where the static magnetic field is given by a quadrupole distribution. Figure 6.13 indicated that for the Bose-Einstein initial distribution differences between the decay rates were smaller than those observed with the Maxwell-Boltzmann distribution, however, the general trends remained the same.

We next moved on to consider a more realistic scenario in which a trapped atoms energy was allowed to vary in time by considering the excitation and de-excitation of atoms. We first studied a master equation model, which treated the atom cloud as the system coupled to an unknown reservoir using an open quantum

system approach. We derived an infinite chain of differential equations, given by equation (6.50), which could be solved numerically to predict the number of trapped atoms as a function of time. This expression reduces to our previous equation (6.4) when we uncouple the system from the reservoir by setting the relaxation γ to be zero. This model works to bring the system and reservoir into equilibrium, as the system has a negligible effect on the reservoir, the system is effectively brought to the temperature of the reservoir.

We were able to improve upon this model for the case when the dominant cause of excitation and de-excitation is the result of fluctuations in the trap parameters. Following directly the work of reference [69], we saw that fluctuations in the trap centre lead to transitions one quantum apart which cause a linear heating effect. While fluctuations in the trap frequency lead to transitions two quantum apart and cause an exponential heating effect. This lead us to our parametric heating model given by the solution of the infinite chain of differential equations, given in equation (6.95). Adding a heating rate onto the trap speeds up the loss of trapped atoms. We saw that the time evolution of the temperature of the atom cloud can either increase or decrease depending on the value of the heating rates and the non-adiabatic decay rates.

$N_n(t_0)$	Reference	Temperature range	Ramp
Maxwell-Boltzmann	Eq. (6.12)	High T only	Slow
Squeezed thermal	Eq. (6.30)	High T only	Fast
Bose-Einstein	Eq. (6.47)	Any	Slow

Dynamical model	Reference	Transitions possible	Heating process
Standard	Eq. (6.4)	$\Delta n = 0$	None
Master equation	Eq. (6.50)	$\Delta n = 0, \pm 1$	Coupling to the unknown reservoir
Parametric heating	Eq. (6.95)	$\Delta n = 0, \pm 1, \pm 2$	Fluctuations in the trapping magnetic fields

Table 6.1: A table summarising how to form a prediction for the number of trapped atoms at any given time, $N(t)$. In this chapter we have considered three different initial distributions ($N_n(t_0)$) and three different dynamical methods for using $N_n(t_0)$ and our non-adiabatic decay rates Γ_n to calculate $N(t)$.

Transitions between n states	$N_n(t_0)$		
	Maxwell-Boltzmann	Squeezed thermal	Bose-Einstein
None	Fig. 6.5		
	Fig. 6.8	Fig. 6.8	
			Fig. 6.13
	Fig. 6.14	Fig. 6.14	Fig. 6.14
			Fig. 6.15
$\Delta n = 1$	Fig. 6.18		
	Fig. 6.19		
$\Delta n = 1$ and $\Delta n = 2$	Fig. 6.21		
	Fig. 6.22		
	Fig. 6.23		

Table 6.2: A table summarising the different results for trapped atom number presented in this chapter, for the three initial distributions introduced in sections 6.1, 6.2, and 6.3 and the three different methods for calculating the trapped atom number: Equation (6.4) which does not take any transitions between harmonic oscillator energy levels into consideration, the master equation model (6.4.1) which allows transitions between adjacent harmonic oscillator levels with $\Delta n = 1$ and the parametric heating model (6.4.2) which allows transitions between $\Delta n = 1$ and $\Delta n = 2$.

Chapter 7

Landau-Zener model for non-adiabatic losses

In this chapter we discuss using semiclassical Landau-Zener theory for modelling non-adiabatic losses from RF-dressed cold atom traps. A derivation of the Landau-Zener model is not given here but may be obtained by consulting references [72, 73] and [74]. We assess the validity of the Landau-Zener model by comparing with our quantum mechanical decay rates derived in chapter 5.

7.1 Landau-Zener model

The Landau-Zener model calculates the probability for an atom to make a transition between two energy levels at a crossing point. A crossing point occurs in RF-dressed traps at the resonance location, as indicated by figure 3.5. Losses due to non-adiabatic effects, that we have been studying, can be described in the hyperfine spin state basis as atoms crossing to untrapped hyperfine spin states. Examining the trap from the hyperfine basis, the Landau-Zener model is commonly used to judge the significance of non-adiabatic losses from RF-dressed cold atom traps [75, 24].

The Landau-Zener model treats the atom as travelling with a classical trajectory and finds the probability of transitions as a function of atomic speed, which it assumes is constant through the crossing. The Landau-Zener model has been studied extensively and is important to those investigating molecular dissociation and molecular spectroscopy [76].

The standard Landau-Zener model only considers crossings between two energy levels. The number of energy levels which cross at the resonance location, in RF-dressed cold atom traps, depends on the hyperfine structure of the atom. An atom with total angular momentum F , will have a crossing involving $2F + 1$ energy levels

at the resonance location. Fortunately, it has been shown by Suominen and Vitanov [77], that the transition probabilities for a crossing involving multiple hyperfine levels can be expressed in terms of the two level transition probabilities given by the original Landau-Zener theory.

For use of the Landau-Zener model we return to describing the RF-dressed atom trap in terms of the hyperfine spin states, rather than the RF-dressed spin states. We describe the trap after the rotating wave approximation has been performed but before we have dressed with the RF field, such that the trap potential is $\hat{V} \propto \Omega \hat{F}_x + \delta(z) \hat{F}_z$ given by equation (3.28).

To remain in the trap atoms are required to make transitions between hyperfine spin levels, as illustrated in figures 3.2 and 3.5. This is in contrast to transitions between dressed spin states which, as we have been studying, are undesirable and lead to losses from the trap.

RF-dressed cold atom traps keep atoms confined by continually causing atoms to transition between hyperfine spin levels. Atoms may be lost from the trap if, for instance, upon ‘entering’ the crossing region in state $m_{F'} = F$ they are not found in the state $m_{F'} = -F$ upon ‘leaving’ it. The work of Suominen and Vitanov tells us that the probability that an atom remains within the confines of an RF-dressed cold atom trap is given by

$$P_{LZ}(F, v) = \left[P_{LZ} \left(\frac{1}{2}, v \right) \right]^{2F} \quad (7.1)$$

[77], where $P_{LZ}(F, v)$ is the probability of transitions between the $m_{F'} = \pm F$ and $m_{F'} = \mp F$ hyperfine spin levels for an atom with speed v through the crossing region.

To calculate $P_{LZ}(\frac{1}{2}, v)$ we may turn to standard Landau-Zener theory. The potential for a spin-half RF-dressed cold atom trap, given by equation (3.28), is

$$V = \frac{\hbar}{2} \begin{pmatrix} \lambda z & \Omega \\ \Omega & -\lambda z \end{pmatrix}. \quad (7.2)$$

Following the Landau-Zener model, as given in reference [72], the probability for a transition between the two hyperfine spin levels on a single passage through the crossing point is given by

$$P_{LZ} \left(\frac{1}{2}, v \right) = 1 - \exp \left(-\frac{\pi \Omega^2}{2\lambda v} \right). \quad (7.3)$$

Every time the atom transverses the crossing indicated in figure 3.5, $1 - P_{LZ}$ gives the probability that it will be in an undesired state, such that it is likely to be lost from the trap. To turn this probability into a decay rate, we need only to

consider how many times the atom will ‘pass’ the crossing region per unit of time. We can obtain an expression of atomic frequency from the trap angular velocity using $\omega = 2\pi f$. We must also multiply by a factor of two, as the atom transverses the crossing region twice per period. We are thus able to obtain decay rates from the Landau-Zener model as a function of atomic speed, given by

$$\Gamma_v^{LZ} = \frac{\omega}{\pi} \left\{ 1 - \left[1 - \exp \left(-\frac{\pi\Omega^2}{2\lambda v} \right) \right]^{2F} \right\}. \quad (7.4)$$

Note that for atoms with $F > 1$ this will in fact lead to an underestimation of trapped atom number. This occurs as it is possible for atoms to transition to states other than $m_{F'} = \pm F$, from which they are not lost from the trap but instead lead to a heating of the trap. Such transitions are, however, still undesirable.

The concept of atomic speed relies on the idea of a classical trajectory. For a more direct comparison with our quantum mechanical decay rates, it is beneficial to describe the Landau-Zener decay rate in terms of the atomic energy level denoted by the quantum number n . By considering energy conservation of an atom at the resonance location, we can obtain the following expression

$$\hbar\omega \left(n + \frac{1}{2} \right) = \frac{1}{2}m_0v^2, \quad (7.5)$$

which leads to

$$v = \sigma\omega\sqrt{2n+1} \quad (7.6)$$

for the atomic speed through the resonance location. Therefore the Landau-Zener decay rate for an atom in the n th harmonic oscillator energy level is

$$\Gamma_n^{LZ} = \frac{\omega}{\pi} \left\{ 1 - \left[1 - \exp \left(-\frac{\pi\alpha\Omega}{2\omega\sqrt{2n+1}} \right) \right]^{2F} \right\}, \quad (7.7)$$

where the variable $\alpha = \frac{\Delta S}{\sigma}$ is defined as in equation (5.32).

We are now ready to compare the Landau-Zener predictions for non-adiabatic transitions with the obtained quantum mechanical results.

7.2 Comparison of the quantum mechanical and semiclassical models

Before preceding to a graphical comparison of our theory with the Landau-Zener model predicted decay rates and trapped atom number, we first compare our decay rates analytically in the low decay limit. We obtained a limiting expression for our

pole approximation decay rate in the limit $\alpha \rightarrow \infty$ in section 5.1.3 and we take the same limit for comparison with Landau-Zener here.

First a Taylor expansion is performed, with the knowledge that in the high α limit the quantity $1 - P_{LZ}(\frac{1}{2}, n)$ is small, giving us

$$\Gamma_n^{LZ} \approx \frac{2F\omega}{\pi} \exp\left(-\frac{\pi\alpha\Omega}{2\omega\sqrt{2n+1}}\right). \quad (7.8)$$

Use of our expression for the trap frequency in the high α limit, given by equation (5.84), leads to

$$\Gamma_n^{LZ} \approx \frac{2F^2\Omega}{\pi\alpha^2} \exp\left(-\frac{\pi\alpha^3}{2F\sqrt{2n+1}}\right) \quad (7.9)$$

where we have used that fact that we are considering $m_i = F$. Substitution of equation (5.81) for α gives us

$$\Gamma_n^{LZ} \approx \frac{2F}{\pi} \sqrt{\frac{\hbar F \lambda^2}{m_0 \Omega}} \exp\left[-\frac{\pi}{2F\sqrt{2n+1}} \left(\frac{m_0 F \Omega^3}{\hbar \lambda^2}\right)^{\frac{3}{4}}\right], \quad (7.10)$$

the expression for the Landau-Zener decay rate in the low decay ($\alpha \rightarrow \infty$) limit. The limiting behaviour for high Rabi frequency is given by

$$\Gamma_n^{LZ} \propto \frac{\exp\left(-d\Omega^{\frac{9}{4}}\right)}{\sqrt{\Omega}}, \quad (7.11)$$

where d is the appropriate constant when only Ω is allowed to vary. The limiting behaviour for low magnetic field gradient is given by

$$\Gamma_n^{LZ} \propto \lambda \exp\left(-\frac{d'}{\lambda^{\frac{3}{2}}}\right), \quad (7.12)$$

where d' is the appropriate constant when only λ is allowed to vary.

Comparison of the Landau-Zener model limiting behaviour, with that given in section 5.1.3 by equations (5.92), (5.93) and (5.94), shows clear differences between our model and the Landau-Zener model in the low decay regime. The dependence on both Rabi frequency and magnetic field gradient, the key trap parameters, is clearly different. Although as would be expected, both find decay minimised in the $\Omega \rightarrow \infty$ or $\lambda \rightarrow 0$ limits.

Figures 7.1 to 7.3 show how the decay predicted by the Landau-Zener model in general underestimates the rate of decay as predicted by our quantum mechanical models. It is possible for the Landau-Zener decay rate values to be greater than that predicted for the decay rate values obtained for the full effect gravity model. This can be seen in figure 7.1 and is due to the suppression of decay rates at specific values in the full effect gravity model. However, the Landau-Zener model is consistently

smaller than the minimal effect gravity decay rates which can be seen across figures 7.1, 7.2 and 7.3. The oscillations in the decay rates observed for the full effect gravity model with variation in Rabi frequency or magnetic field gradient are not observed and could not be obtained from the semiclassical Landau-Zener model.

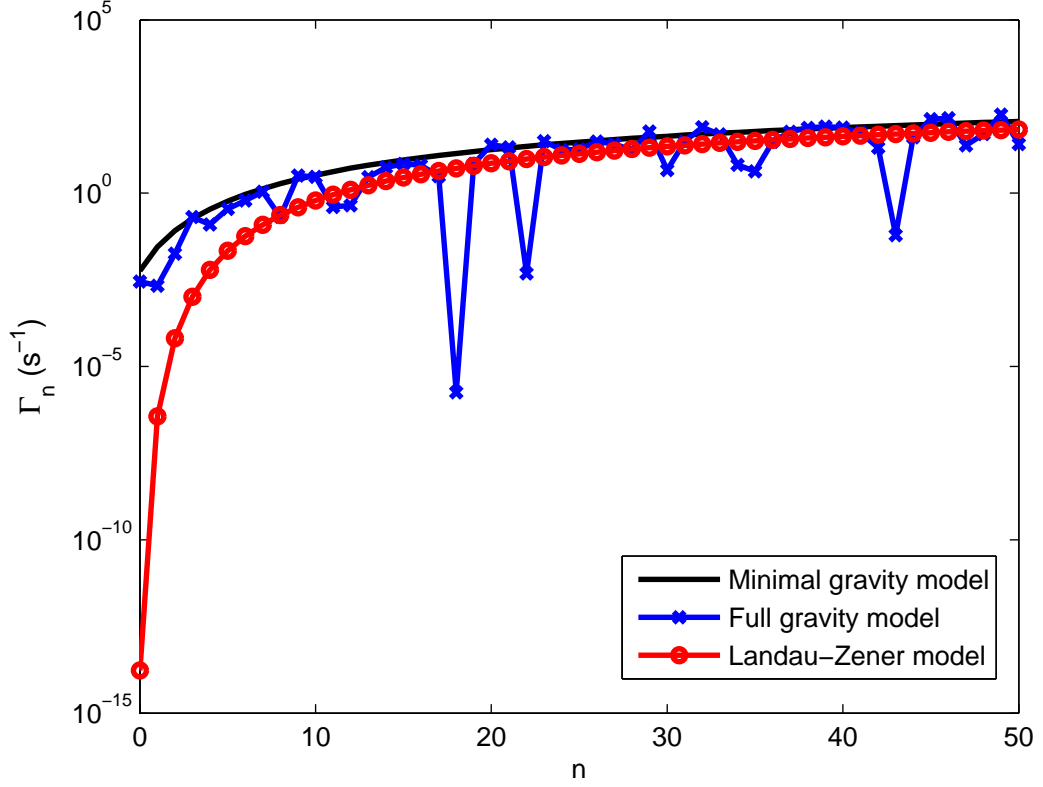


Figure 7.1: Comparing the Landau-Zener model with decay rates given by equation (7.7) with our quantum mechanical decay rates as a function of atomic energy E_n . The decay rates for the minimal effect gravity model are given by equation (5.35) with the decay rates for the full effect gravity model given by equation (5.136). Dotted lines are added to guide the eye. A magnetic field gradient of $B' = 1.1$ T/m and a Rabi frequency of $\Omega/2\pi = 8$ kHz were used. The trap frequency was calculated using equation (5.110) to be $\omega/(2\pi) = 0.87$ kHz(2sf) for the full effect gravity model and using equation (5.13) to be $\omega/(2\pi) = 0.92$ kHz(2sf) for the minimal effect gravity and Landau-Zener models. The atomic species is ^{87}Rb , with $F = 1$.

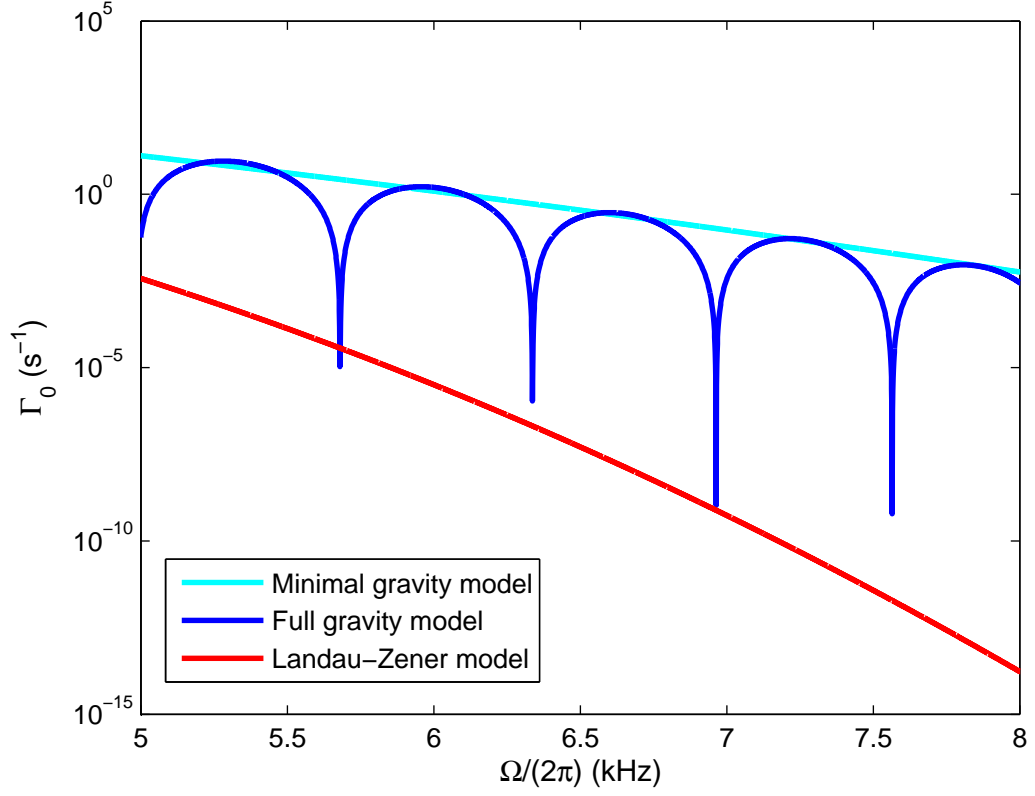


Figure 7.2: Comparing the Landau-Zener model with decay rates given by equation (7.7) with our quantum mechanical decay rates as a function of trap Rabi frequency. The decay rates for the minimal effect gravity model are given by equation (5.35) with the decay rates for the full effect gravity model given by equation (5.136). A magnetic field gradient of $B' = 1.1 \text{ T/m}$, ^{87}Rb atoms with $F = 1$ and $n = 0$ were used. The Landau-Zener model trap frequency was calculated using equation (5.13).

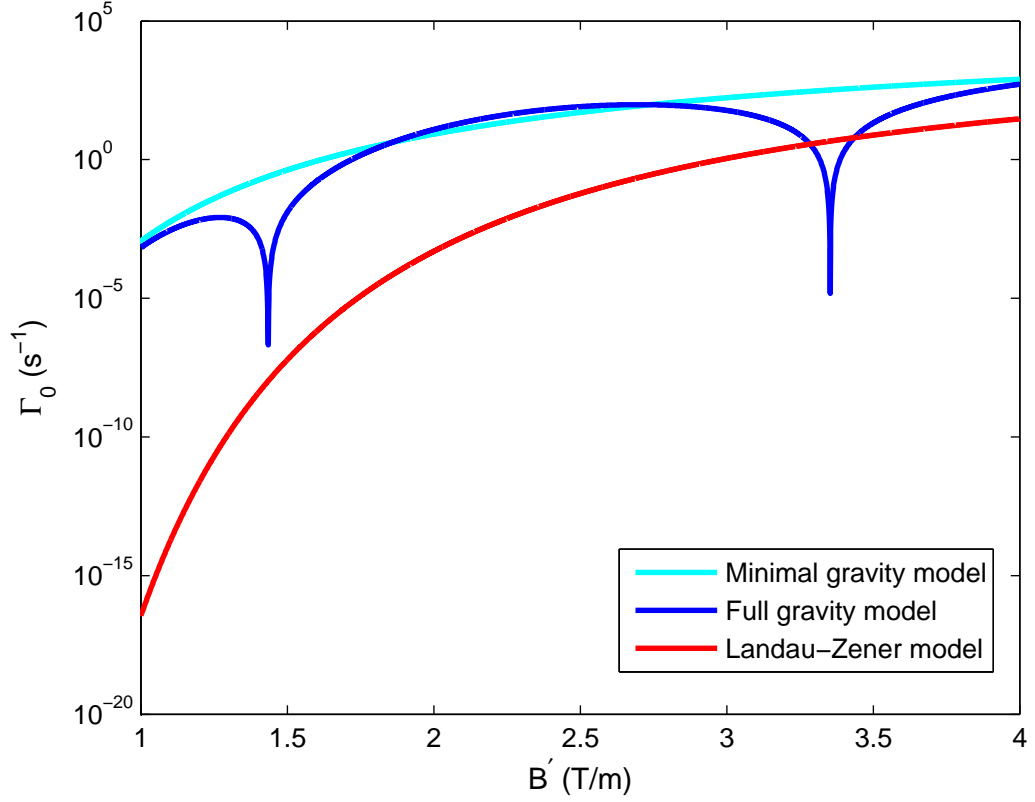


Figure 7.3: Comparing the Landau-Zener model with decay rates given by equation (7.7) with our quantum mechanical decay rates as a function of the trap magnetic field gradient. The decay rates for the minimal effect gravity model are given by equation (5.35) with the decay rates for the full effect gravity model given by equation (5.136). A Rabi frequency of $\Omega/2\pi = 8$ kHz, ^{87}Rb , with $F = 1$ and $n = 0$ were used. The Landau-Zener model trap frequency was calculated using equation (5.13).

Figures 7.4 and 7.5 show how the differences between the Landau-Zener decay rates and those given by our quantum mechanical models affect the prediction of trapped atom number. Both figures show that the Landau-Zener model overestimates the number of atoms remaining trapped. This overestimation of trapped atom number is clearest in figure 7.4, which is probably due to the large occupancy of the ground state in the Bose-Einstein distribution and the huge disparity in the ground state decay rates as shown in figure 7.1. Once a heating rate is included into the model, shown in figure 7.5 by the parametric heating model, the difference in the atom number prediction decreases. However, the difference between the Landau-Zener model and the minimal effect gravity is still much greater than the difference between the minimal effect gravity and full effect gravity models. The difference between the models is seen most clearly by examining the atom cloud temperature, the Landau-Zener model predicts significantly less cooling due to non-adiabatic effects.

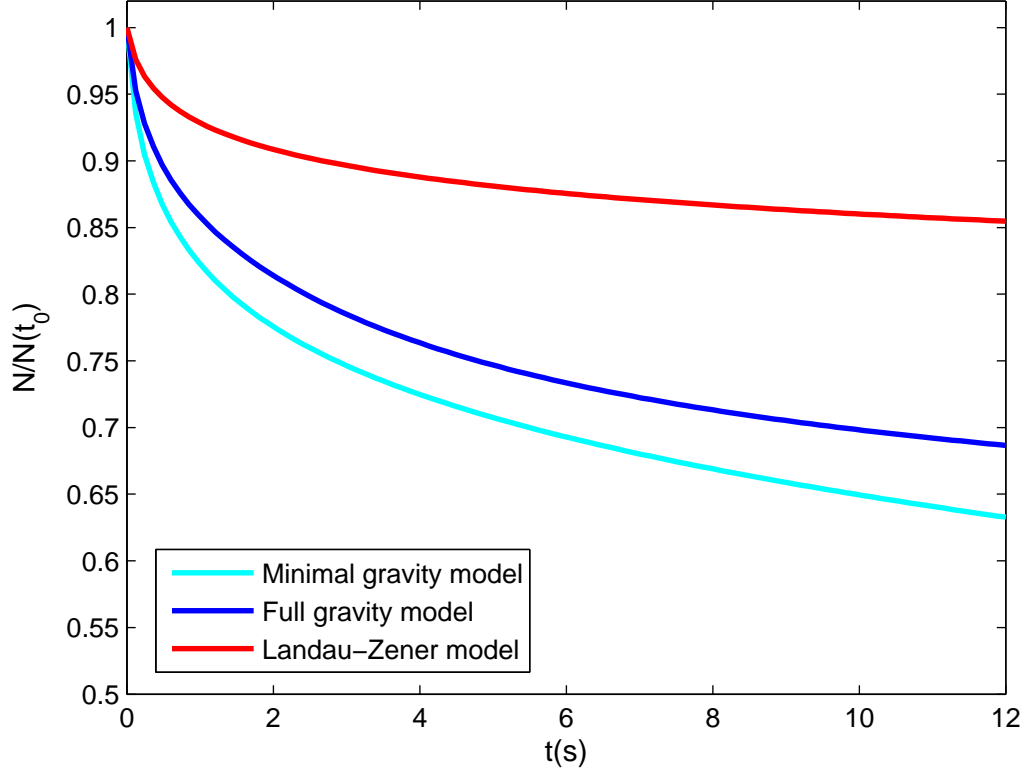


Figure 7.4: Comparing the Landau-Zener model trapped atom number prediction with our quantum mechanical models. A Bose-Einstein initial distribution was assumed with atom number calculated using equation (6.4). The Landau-Zener model decay rates were calculated from equation (7.7), the decay rates for the minimal effect gravity model are given by equation (5.35) and the decay rates for the full effect gravity model are given by equation (5.136). The atomic species is ^{87}Rb , with $F = 1$, $\Omega/2\pi = 8\text{ kHz}$, $B' = 1.1\text{ T/m}$, $\omega_{\text{rf}}/2\pi = 1.2\text{ MHz}$, $T(t_0) = 250\text{ nK}$ and $N(t_0) = 1 \times 10^6$ atoms.

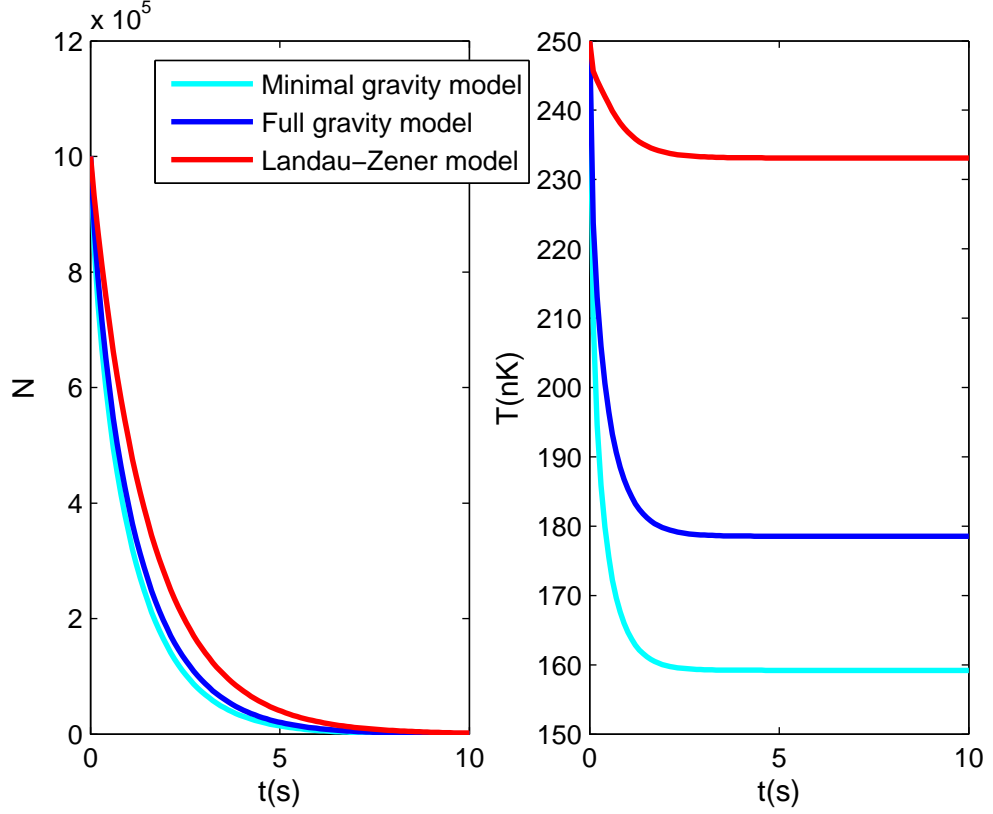


Figure 7.5: Comparing the Landau-Zener model trapped atom number prediction, for the parametric heating model, with our quantum mechanical models. A Maxwell-Boltzmann initial distribution was assumed. The parametric heating model (equation (6.95)) heating rates were given as $\gamma_a = 2.0 \text{ s}^{-1}$ and $\gamma_b = 0.2 \text{ s}^{-1}$. The Landau-Zener model decay rates were calculated from equation (7.7), the decay rates for the minimal effect gravity model are given by equation (5.35) and the decay rates for the full effect gravity model are given by equation (5.136). For ^{87}Rb , with $F = 1$, $\Omega/2\pi = 8 \text{ kHz}$, $B' = 1.1 \text{ T/m}$, $\omega_{\text{rf}}/2\pi = 1.2 \text{ MHz}$, $T(t_0) = 250 \text{ nK}$ and $N(t_0) = 1 \times 10^6$ atoms.

7.3 Summary

After discussing how the semiclassical Landau-Zener model can be used to obtain decay rates for losses from RF-dressed cold atom traps, we went on to compare the Landau-Zener decay rate, given by equation (7.7), with our decay rates for non-adiabatic transitions derived from Fermi's Golden Rule.

We found by considering the low decay limit, that the dependence on the trap Rabi frequency and magnetic field gradient is different between the Landau-Zener and quantum mechanical decay rates. We saw in figures 7.1 to 7.3 that the Landau-Zener decay rate is in general lower than the minimal effect gravity and full effect gravity models. This lead to an overestimation in trapped atom number seen in figures 7.4 and 7.5. It is also noteworthy that the oscillations observed in the full effect gravity decay rate, which arise due to a quantum mechanical effect, could not be replicated with semiclassical Landau-Zener theory.

We therefore conclude that caution should be applied if using Landau-Zener theory for estimating the rate of non-adiabatic transitions from RF-dressed cold atom traps. We have seen that, when a fully quantum mechanical model is considered, the obtained decay rates could be significantly higher than that predicted by Landau-Zener. Full quantum mechanical alternatives should be used for any quantitative analysis.

Part IV

Study of experimental data

Chapter 8

Explaining atomic losses in experimental data by non-adiabatic transitions

The group of H       Perrin in Paris have collected data on atom loss from an RF-dressed cold atom trap [78]. Investigations in the masters thesis of Matthieu Pierens could not find agreement between this experimental data, collected in the low Rabi frequency regime where non-adiabatic losses are believed to dominate, with semiclassical Landau-Zener theory [2]. In this section we shall compare our theory to the experimental data collected.

8.1 CNRS Paris 13 experiment

Key experimental details about the RF-dressed cold atom trap used to collect the data is now given. The trap setup is shown in figure 8.1 and discussed in greater depth in the thesis of Karina Merloti [78] and the 2013 New Journal of Physics paper [1].

The static magnetic field distribution is a quadrupole distribution, produced by two coils, of centimetre scale diameter, separated along the vertical axis. As mentioned in section 6.3 and given in equation (6.39), the iso-magnetic field lines for a quadrupole field are ellipsoids. The dressing RF field is provided by two further RF antenna coils, which in the case of the experimental data examined here, provide a circularly polarized RF field of the form,

$$\mathbf{B}_{\text{rf}} = B_{\text{rf}} \cdot \begin{pmatrix} \cos(\omega_{\text{rf}} t) \\ \sin(\omega_{\text{rf}} t) \\ 0 \end{pmatrix} \quad (8.1)$$

[1]. The atoms collect at the bottom of the resonant ellipsoid to form an atom cloud with the trap centre just below the resonant ellipsoid, as we have discussed in section 5.2.

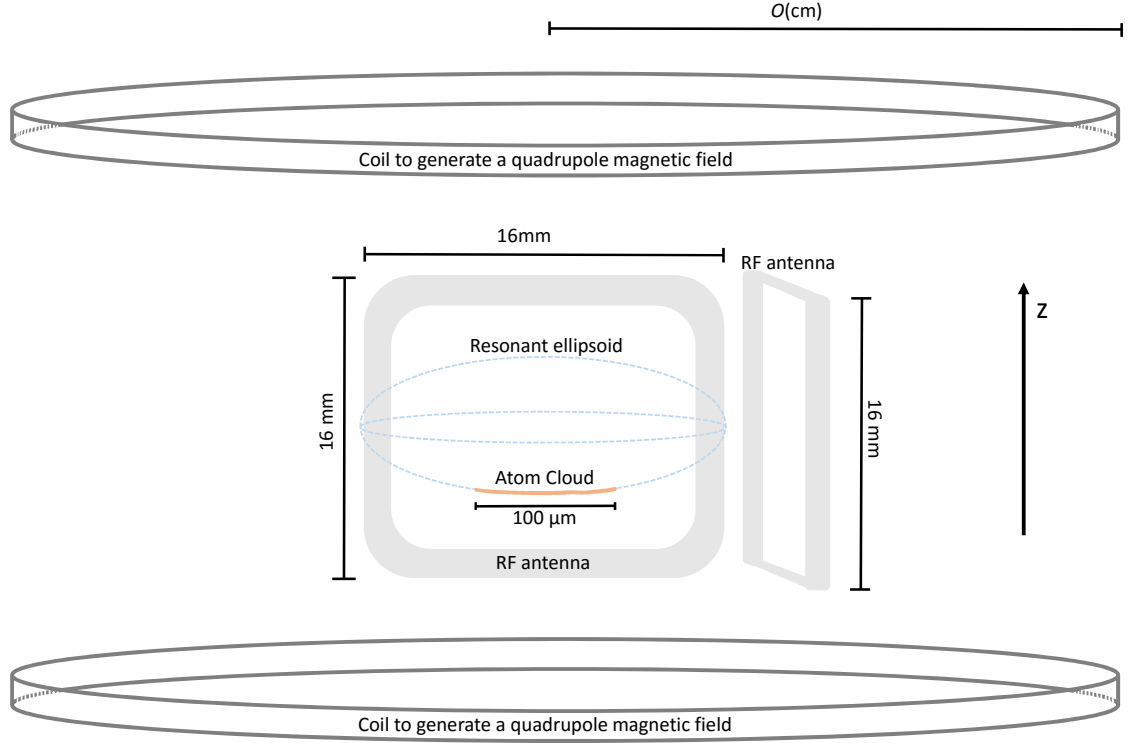


Figure 8.1: A schematic diagram showing the Paris experiment (not drawn to scale). The static magnetic field distribution is formed by current flowing through the two coils separated along the vertical axis. The RF field is generated by the RF antennas, located approximately 1 cm from the atoms, which are comprised of 10 loops of Copper wire [1]. The iso-B surface for the magnetic field distribution is an ellipsoid given by $x^2 + y^2 + 4\left(z - \frac{\omega_{\text{rf}}}{\lambda}\right)^2 = 4\frac{\omega_{\text{rf}}^2}{\lambda^2}$. The force of gravity causes the atoms to collect in an atom cloud at the bottom of the resonant ellipsoid.

Rubidium atoms (^{87}Rb) with dressed spin state $|F = 1, m_F = 1\rangle$ are trapped and experience a three dimensional adiabatic potential of the form [1]¹:

$$V(\rho, \tilde{z}) = \hbar m_F \sqrt{\frac{\Omega^2}{4} \left(1 - \frac{\tilde{z}}{\sqrt{\rho^2/4 + \tilde{z}^2}}\right)^2 + \left(\lambda \sqrt{\rho^2/4 + \tilde{z}^2} - \omega_{\text{rf}}\right)^2} + V_{na}(\rho, \tilde{z}) + m_0 g \left(\tilde{z} + \frac{\omega_{\text{rf}}}{\lambda}\right). \quad (8.2)$$

¹The zero of gravitational potential is chosen to be $z = 0$ rather than $\tilde{z} = 0$ used in [1].

This is in the form of equation (3.49) with the detuning and Rabi frequency now varying as functions of: $\rho = \sqrt{x^2 + y^2}$, a measure of the horizontal displacement from the centre of the resonant ellipsoid and \tilde{z} , the vertical displacement from the centre of the resonant ellipsoid. The non-adiabatic shift to the trapping potential is given by the term $V_{na}(\rho, \tilde{z})$. $V_{na}(0, z)$ is the term we have so far referred to as the ‘hump’, found in equation (3.49). The contribution $V_{na}(\rho, z)$ is significantly more complicated and can be derived by following the more general derivation for adiabatic potentials given in reference [42]².

Ignoring the V_{na} contribution, the potential landscape of the trap from equation (8.2) can be plotted to see the shape of the atom cloud as a function of temperature. Figure 8.2 shows that due to the gravitational force the centre of the trap is below the resonant ellipsoid and the atoms collect around the $\rho = 0$ location. The scale in figure 8.2 is not equal between the two directions, so in reality the cloud is very long and thin as shown in figure 8.3. The atom cloud is three dimensional and can be imagined by rotating figures 8.2 and 8.3 by an angle of π about the z axis, the symmetry axis at the centre of the atomic cloud. As the atom cloud is so small, on the micrometre scale, it is not possible to image directly in situ. Instead each measurement is a destructive process. The trapping potentials are switched off abruptly, the cloud then falls due to the gravitational force and expands until it is large enough to be imaged. Once the cloud has been imaged, it is lost from the trap and a new collection of Rubidium atoms have to be loaded to repeat the experiment.

The position dependent Rabi frequency is given by

$$\Omega(\rho, \tilde{z}) = \frac{\Omega}{2} \left(1 - \frac{\tilde{z}}{\sqrt{\frac{\rho^2}{4} + \tilde{z}^2}} \right) \quad (8.3)$$

and the detuning which takes into account the curvature of the resonant ellipse is given by

$$\delta(\rho, \tilde{z}) = \lambda \sqrt{\frac{\rho^2}{4} + \tilde{z}^2} - \omega_{\text{rf}}. \quad (8.4)$$

As the RF field is circularly polarized the Rabi frequency is now defined by [1]

$$\Omega = \left| g_F \frac{\mu_B}{\hbar} B_{\text{rf}} \right|. \quad (8.5)$$

The Paris trap is strongly anisotropic with $\omega_z \gg \omega_\rho$, as can be seen from figure 8.3. In the semiclassical interpretation, the higher the trap frequency, the

²Note that in equation 13 of reference [42] the unitary transformation should be defined $U(\mathbf{r}, t) = U_S(\mathbf{r})U_R(t)U_T(\mathbf{r}, t)$.

greater the change in the magnetic field orientation vector for each unit time of atom motion and therefore the ‘harder’ it is for an atom to adiabatically follow the local magnetic field direction. This is not necessarily the case when we consider the behaviour of our full effect gravity model decay rates, however, the general trend remains. Typical values for this trap for ω_z are of the order of magnitude of kHz compared to ω_ρ which is of the order of magnitude of Hz, such that we shall consider the vertical direction to be the dominant loss direction.

However, while our one dimensional model of atomic losses should be appropriate, three dimensional effects affect the trap frequency in the ρ direction. If a Taylor expansion is performed on equation (8.2) about the $\rho = 0$ location, we can achieve a harmonic approximation for the trap potential in the ρ direction with horizontal trapping frequency:

$$\omega_\rho = \left\{ \frac{\hbar m_F \lambda^2}{8m_0 (\omega_{\text{rf}} + \delta) \sqrt{\Omega^2 + \delta^2}} \left(2\delta - \frac{\Omega^2}{\omega_{\text{rf}} + \delta} \right) - \frac{\mathcal{H} \Omega^2 \lambda^4}{4m_0 (\omega_{\text{rf}} + \delta)^2 (\Omega^2 + \delta^2)^2} \left[\frac{3\omega_{\text{rf}} + 5\delta}{\omega_{\text{rf}} + \delta} + \frac{2[2\delta(\omega_{\text{rf}} + \delta) - \Omega^2]}{\Omega^2 + \delta^2} \right] \right\}^{\frac{1}{2}} \quad (8.6)$$

which reduces to equation (6.46) when $\rho = 0$.

We are now ready to begin the comparison of our theory with experimental data.

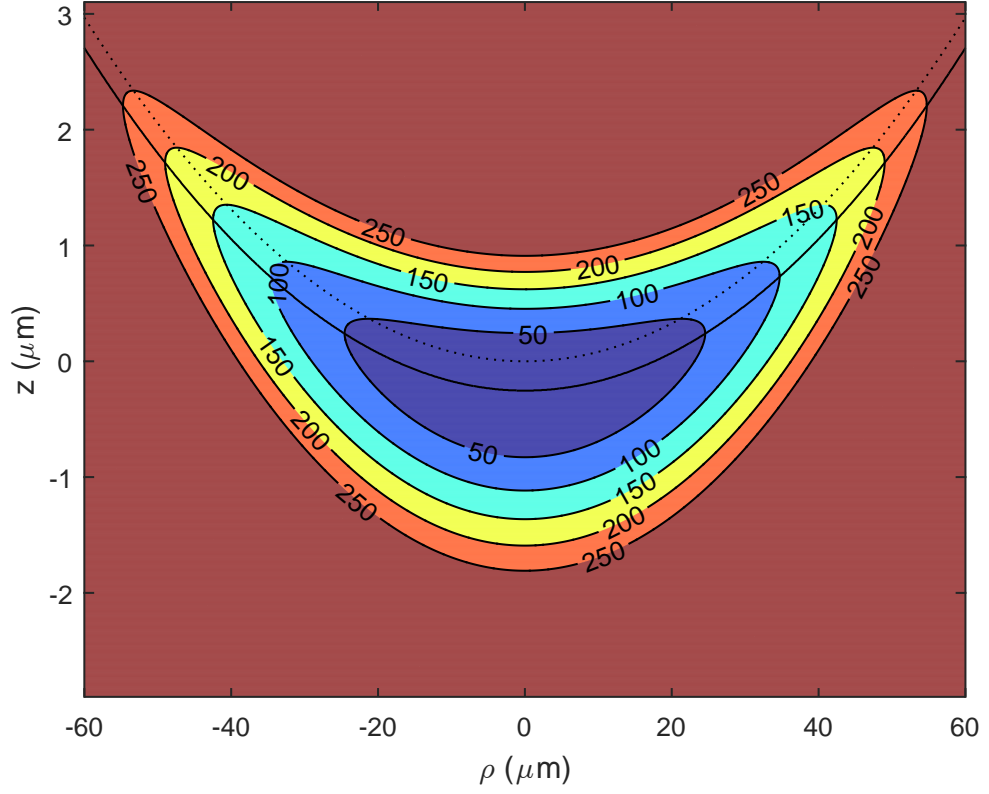


Figure 8.2: Atom cloud as theoretically predicted from the trap potentials given by equation (8.2). Contributions to the potential from non-adiabatic effects were not included. The contour lines are iso-potential lines given in units of nK. The solid black line is the minimum of the potential in the vertical direction and the dotted black line marks the location of the resonant ellipsoid. A magnetic field gradient $B' = 1.12 \text{ T/m}$, a Rabi frequency $\Omega/2\pi = 7 \text{ kHz}$ and an RF frequency $\omega_{\text{rf}}/2\pi = 1.2 \text{ MHz}$ were used to produce this graph. The minimum value of the trap potential is set to zero.

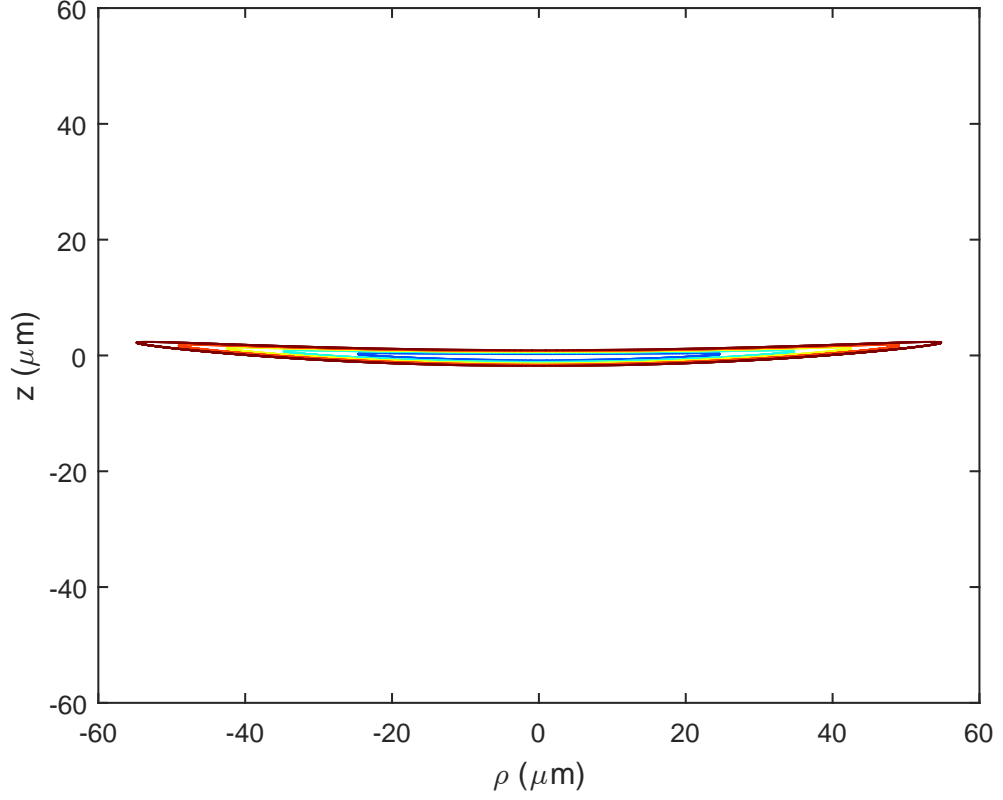


Figure 8.3: Atom cloud as theoretically predicted from the trap potentials given by equation (8.2), plotted with equal scales. Contributions to the potential from non-adiabatic effects were not included. The coloured lines are iso-potential lines given in units of temperature as: 250 nK dark red, 200 nK red, 150 nK yellow, 100 nK green and 50 nK blue. These indicate the size of the atom cloud based on its temperature. $B' = 1.12 \text{ T/m}$, $\Omega/2\pi = 7 \text{ kHz}$ and $\omega_{\text{rf}}/2\pi = 1.2 \text{ MHz}$ were used to produce this graph. The minimum value of the trap potential is set to zero.

8.2 Application of the presented models to experimental data

From the range of experimental data collected, four data sets shall be examined in detail. Each data set will be referred to by their experimentally determined Rabi frequency, $\Omega_{exp}/(2\pi) = 5, 7, 8$ and 9 kHz. Note that these Rabi frequencies are low compared to values typical of RF-dressed cold atom traps. Low Rabi frequency values are chosen specifically such that non-adiabatic transitions should be the dominant cause of loss from the trap. The experimental Rabi frequency values have an accuracy of 0.5 kHz. The RF synthesizer that generates the radio frequency magnetic field is not perfectly stable meaning that the Rabi frequency values fluctuate in time with $\Omega(t) = \Omega_{exp} \pm 2\pi \cdot 200$ Hz.

All four data sets were obtained with the same RF frequency and magnetic field gradient, as given in table 8.1.

Parameter	Value
B'	1.12 T/m
$\omega_{rf}/(2\pi)$	1.2 MHz
Γ_{bl}	0.0087 s^{-1}
$\Omega_i/(2\pi)$	52 kHz

Table 8.1: Trap parameter values for the experimental data studied.

The background loss rate (Γ_{bl}), which takes into account energy independent losses, is taken from reference [2]. The initial high loading Rabi frequency of the trap is given in table 8.1 by the parameter Ω_i and is used in calculations with a squeezed thermal initial distribution.

The experimental data was collected for an atom cloud that was largely comprised of thermal atoms but also had a BEC component. The percentage of the atom cloud that consisted of a BEC fluctuated in time and was in the following ranges for the four data sets considered:

- 5 kHz, $19\% \leq \text{BEC}/N(t) \leq 51\%$,
- 7 kHz, $15\% \leq \text{BEC}/N(t) \leq 25\%$,
- 8 kHz, $8\% \leq \text{BEC}/N(t) \leq 21\%$,

- 9 kHz, $0\% \leq \text{BEC}/N(t) \leq 15\%$.

Experimental data points in the following section are represented by black stars. It should be noted that each star represents a new run of the experimental setup. The trap is loaded and ramped to the desired Rabi frequency, the atoms are held in the trap for a certain time before the trap is switched off for the atom cloud to be imaged. The trap is then reloaded and the process repeated for the next time value. The experimental data is such that error bars cannot be displayed, as there was only one measurement per time value.

We will now compare our trapped atom number predictions with the experimental data. We will first compare the data to the simpler minimal effect gravity model, then to the more sophisticated full effect gravity model. Both models seem to underestimate the rate of non-adiabatic losses, with the full effect gravity model additionally predicting unrealistic sensitivity to the trap Rabi frequency. We shall see that reasonable agreement can only be obtained between theory and experiment when heating processes are taken into account. By using the parametric heating model, to account for heating processes that occur due to fluctuations in the trapping magnetic fields, the sensitivity of the trapped atom number prediction is reduced and the rate of non-adiabatic losses is increased to bring agreement between theoretical predictions and experiment results.

8.2.1 Minimal effect gravity model

To begin let us compare the experimental data with the minimal effect gravity model decay rates, using equation (6.4) to form a theoretical prediction for the time evolution of trapped atom number. We initially consider the theoretical prediction obtained with experimentally determined trap input parameters:

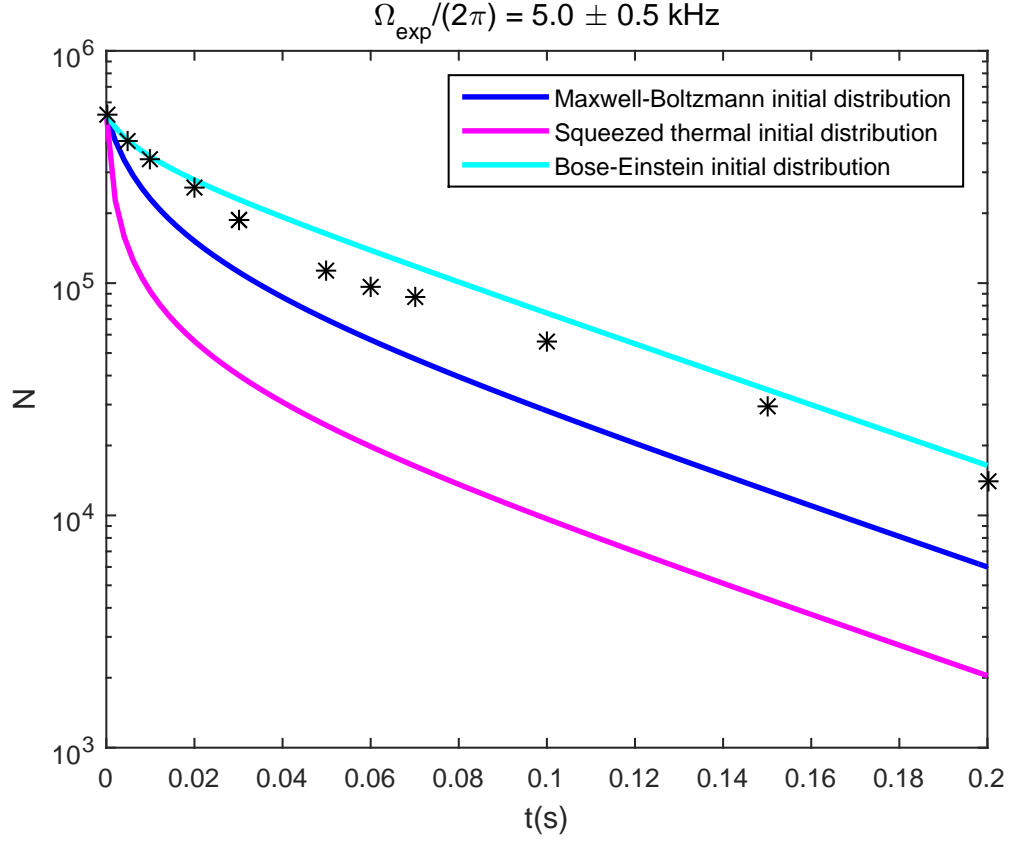


Figure 8.4: Trapped atom number (N) for the $\Omega_{\text{exp}}/2\pi = 5.0 \pm 0.5 \text{ kHz}$ experimental data as a function of time (t) given in seconds. Equation (5.35) was used to calculate the decay rates for a variety of initial distributions. Parameters given in table 8.1, an initial atom number of 5.33×10^5 atoms, a Rabi frequency $\Omega/2\pi = 5 \text{ kHz}$ and an initial temperature $T(t_0) = 218 \text{ nK}$ were used to produce this graph.

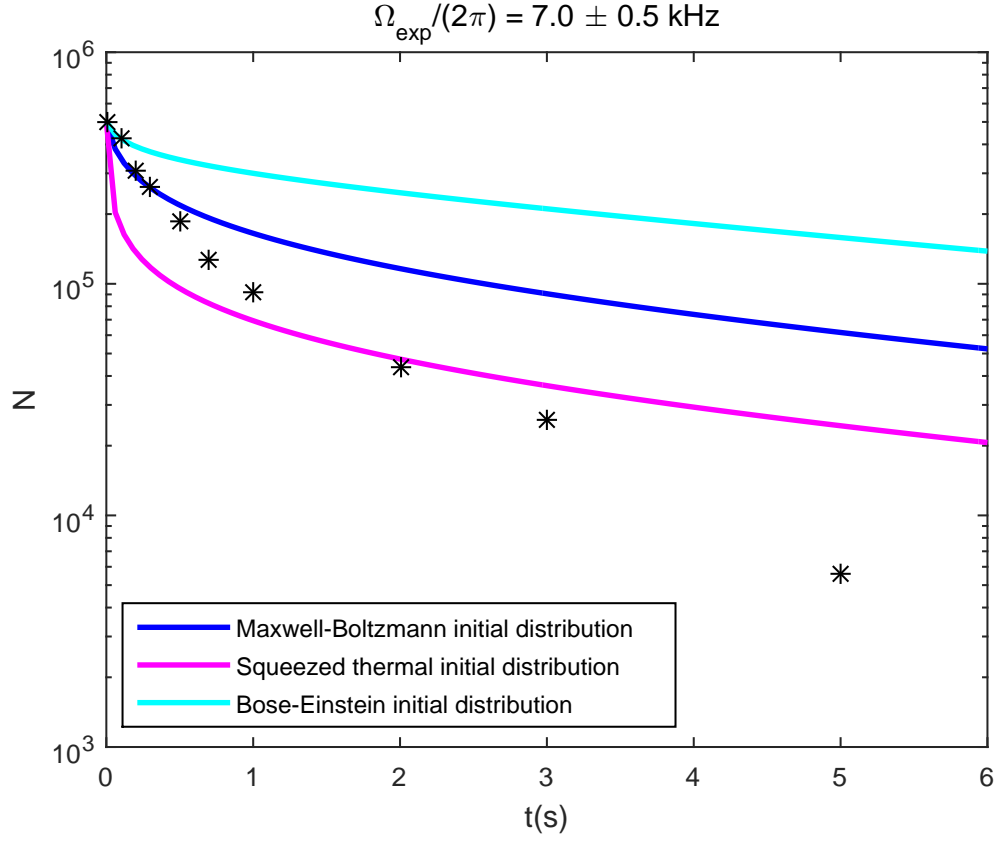


Figure 8.5: Trapped atom number (N) for the $\Omega_{\text{exp}}/2\pi = 7.0 \pm 0.5 \text{ kHz}$ experimental data as a function of time (t) given in seconds. Equation (5.35) was used to calculate the decay rates for a variety of initial distributions. Parameters given in table 8.1, an initial atom number of 5.02×10^5 atoms, a Rabi frequency $\Omega/2\pi = 7 \text{ kHz}$ and an initial temperature $T(t_0) = 209 \text{ nK}$ were used to produce this graph.

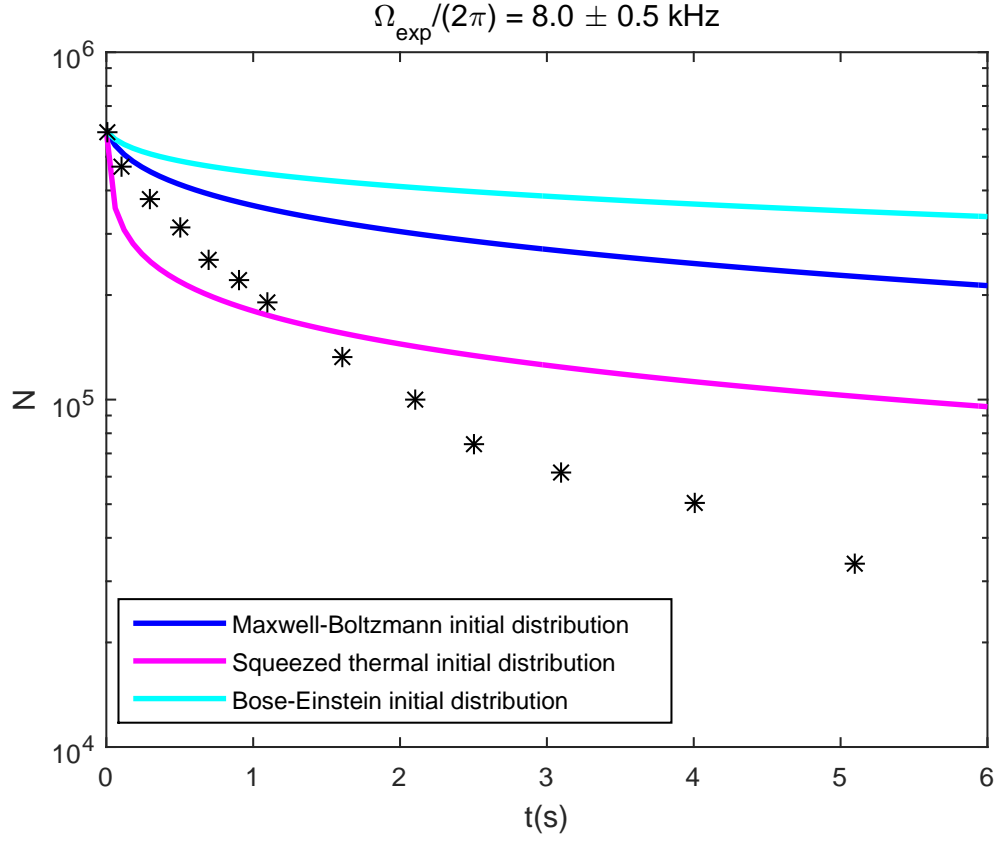


Figure 8.6: Trapped atom number (N) for the $\Omega_{\text{exp}}/2\pi = 8.0 \pm 0.5 \text{ kHz}$ experimental data as a function of time (t) given in seconds. Equation (5.35) was used to calculate the decay rates for a variety of initial distributions. Parameters given in table 8.1, an initial atom number of 5.92×10^5 atoms, a Rabi frequency $\Omega/2\pi = 8 \text{ kHz}$ and an initial temperature $T(t_0) = 232 \text{ nK}$ were used to produce this graph.

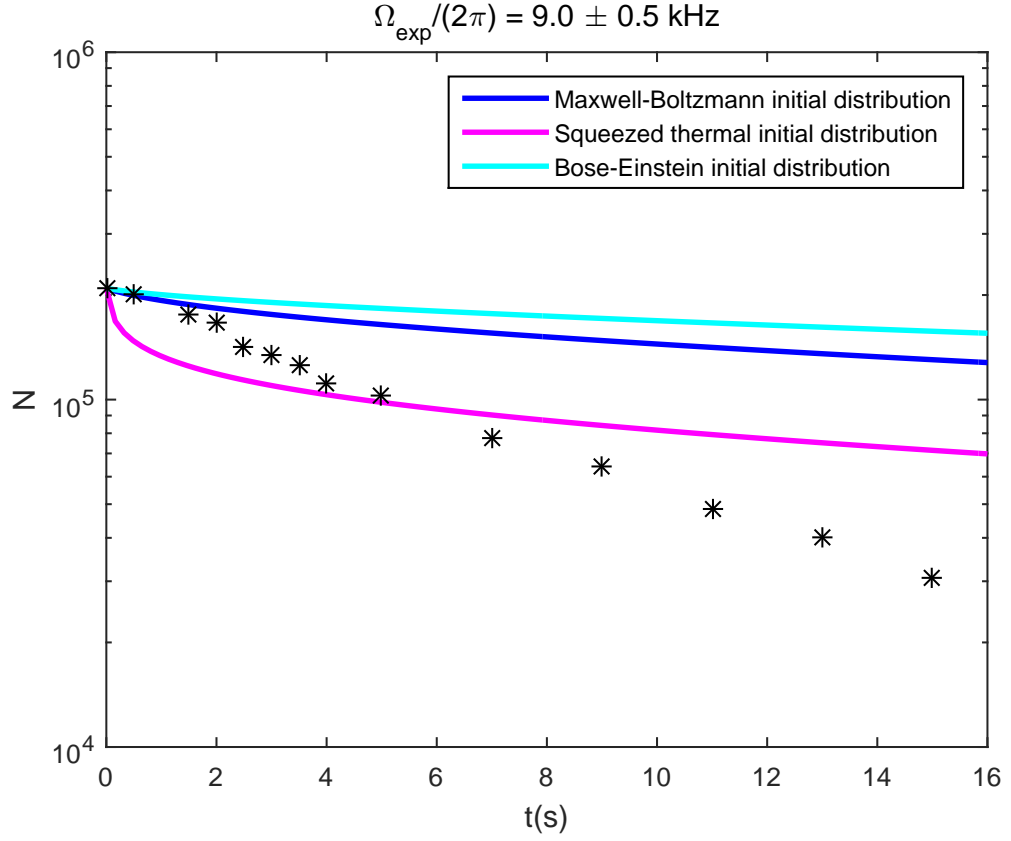


Figure 8.7: Trapped atom number (N) for the $\Omega_{\text{exp}}/2\pi = 9.0 \pm 0.5 \text{ kHz}$ experimental data as a function of time (t) given in seconds. Equation (5.35) was used to calculate the decay rates for a variety of initial distributions. Parameters given in table 8.1, an initial atom number of 2.09×10^5 atoms, a Rabi frequency $\Omega/2\pi = 9 \text{ kHz}$ and an initial temperature $T(t_0) = 148 \text{ nK}$ were used to produce this graph.

Figures 8.4 to 8.7 show that using the minimal effect gravity model, with the experimentally determined Rabi frequency and other trap parameters, does not provide a suitable match between predicted trapped atom number and the experimental data points. It is noteworthy that there is dramatic variation between the different initial distributions meaning that careful selection of the most appropriate distribution is required. Due to the low nano-Kelvin temperatures of the atom trap setup and the fact that the ramp between high loading Rabi frequency to the lower trap Rabi frequency was performed slowly, the Bose-Einstein distribution should give the most reliable initial energy distribution. It can be seen from figures 8.4 to 8.7 that the Bose-Einstein distribution consistently predicts more atoms should be in the trap than are experimentally observed. Further investigation is required to understand this overestimation in the theoretical prediction of the number of trapped atoms.

Regression fitting

There is unavoidable uncertainty in the values of the input parameters Ω , B' , $T(t_0)$, and $N(t_0)$ determined for the experimental data. To see if this can explain the differences between theory and experiment we perform non-linear least squares regression, by minimising

$$S = \sum_i \frac{\{N_i[\Omega, N(t_0)] - \mathcal{N}_i\}^2}{\mathcal{N}_i} \quad (8.7)$$

[79] where $N_i[\Omega, N(t_0)]$ is the number of trapped atoms at a given time t_i as calculated by theory and \mathcal{N}_i is the experimentally determined number of trapped atoms at time t_i . A weighting of $\sqrt{\mathcal{N}_i}$ is added as an approximation to the standard deviation of the data points and proved important in getting the fitting regime not to focus too heavily on the early time data points. Only Ω and $N(t_0)$ were varied due to interdependencies between the parameters which caused trouble for the fitting regime. Increasing the Rabi frequency and decreasing the magnetic field gradient have similar effects on the trapped atom number prediction, as seen in figure 6.3. While increasing the initial atom number or decreasing the initial temperature also have similar effects on the trapped atom number prediction, as seen in figure 6.4. For this reason only one parameter can be fit from each pair. Figures 8.8 to 8.11 show the results obtained from regression fitting Ω and $N(t_0)$ for our minimal effect gravity model.

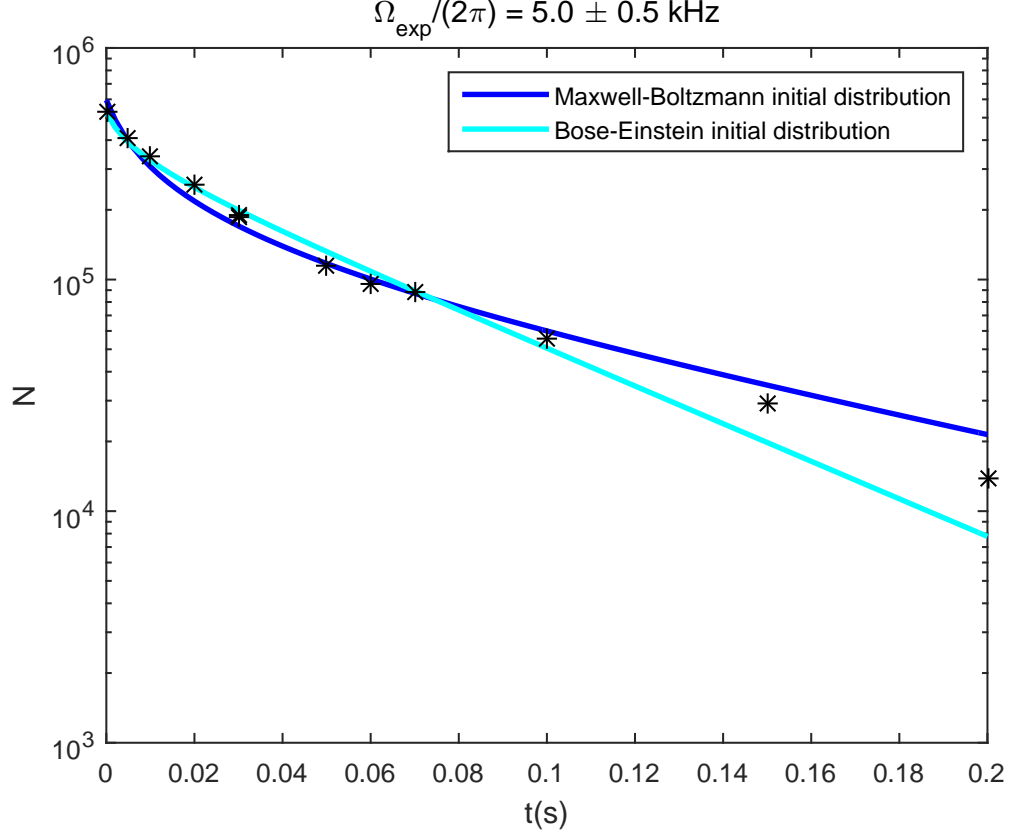


Figure 8.8: Trapped atom number (N) for the $\Omega_{\text{exp}}/2\pi = 5.0 \pm 0.5 \text{ kHz}$ experimental data as a function of time (t) given in seconds. Equation (5.35) was used to calculate the decay rates for a variety of initial distributions. The Rabi frequency and initial atom number were obtained using regression fitting given by equation (8.7). For the Maxwell-Boltzmann distribution the fitted values were $\Omega/2\pi = 5.22 \text{ kHz}$ and $N(t_0) = 5.96 \times 10^5$ with $S = 2.43 \times 10^4$, all given to three significant figures. For the Bose-Einstein distribution the fitted values were $\Omega/2\pi = 4.90 \text{ kHz}$ and $N(t_0) = 5.26 \times 10^5$ with $S = 1.34 \times 10^4$, all given to three significant figures. Parameters given in table 8.1 and an initial temperature $T(t_0) = 218 \text{ nK}$ were used to produce this graph.

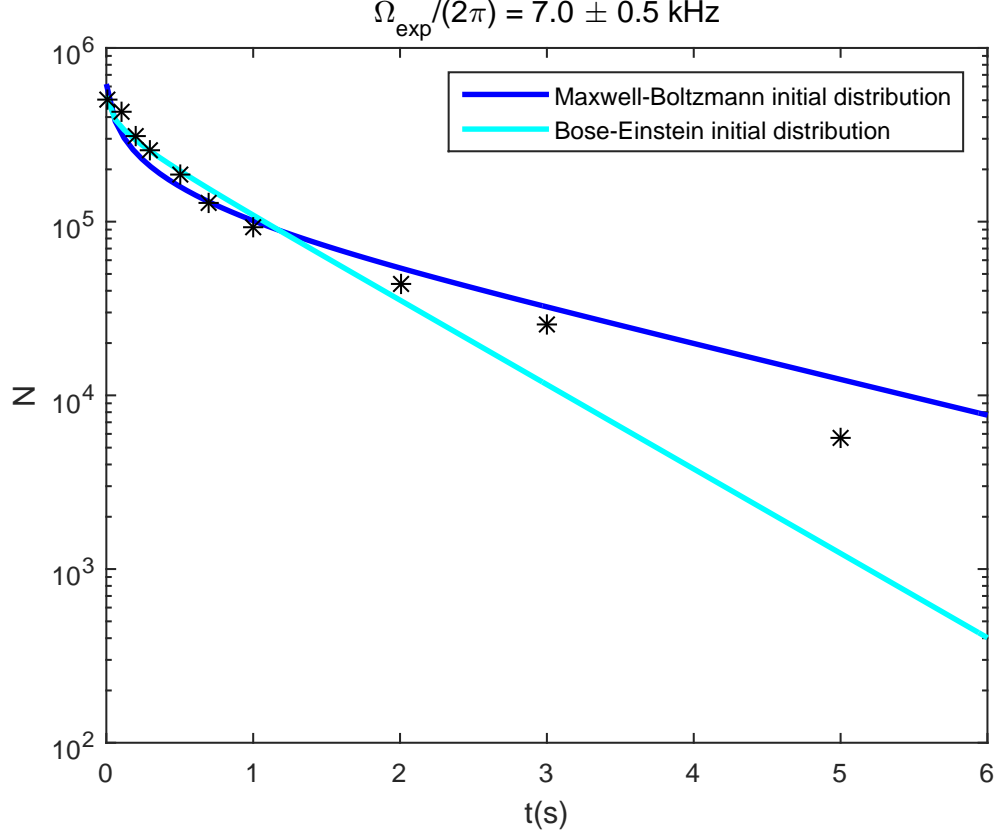


Figure 8.9: Trapped atom number (N) for the $\Omega_{\text{exp}}/2\pi = 7.0 \pm 0.5 \text{ kHz}$ experimental data as a function of time (t) given in seconds. Equation (5.35) was used to calculate the decay rates for a variety of initial distributions. The Rabi frequency and initial atom number were obtained using regression fitting given by equation (8.7). For the Maxwell-Boltzmann distribution the fitted values were $\Omega/2\pi = 6.47 \text{ kHz}$ and $N(t_0) = 6.20 \times 10^5$ with $S = 9.24 \times 10^4$, all given to three significant figures. For the Bose-Einstein distribution the fitted values were $\Omega/2\pi = 6.12 \text{ kHz}$ and $N(t_0) = 5.28 \times 10^5$ with $S = 3.78 \times 10^4$, all given to three significant figures. Parameters given in table 8.1 and an initial temperature $T(t_0) = 209 \text{ nK}$ were used to produce this graph.

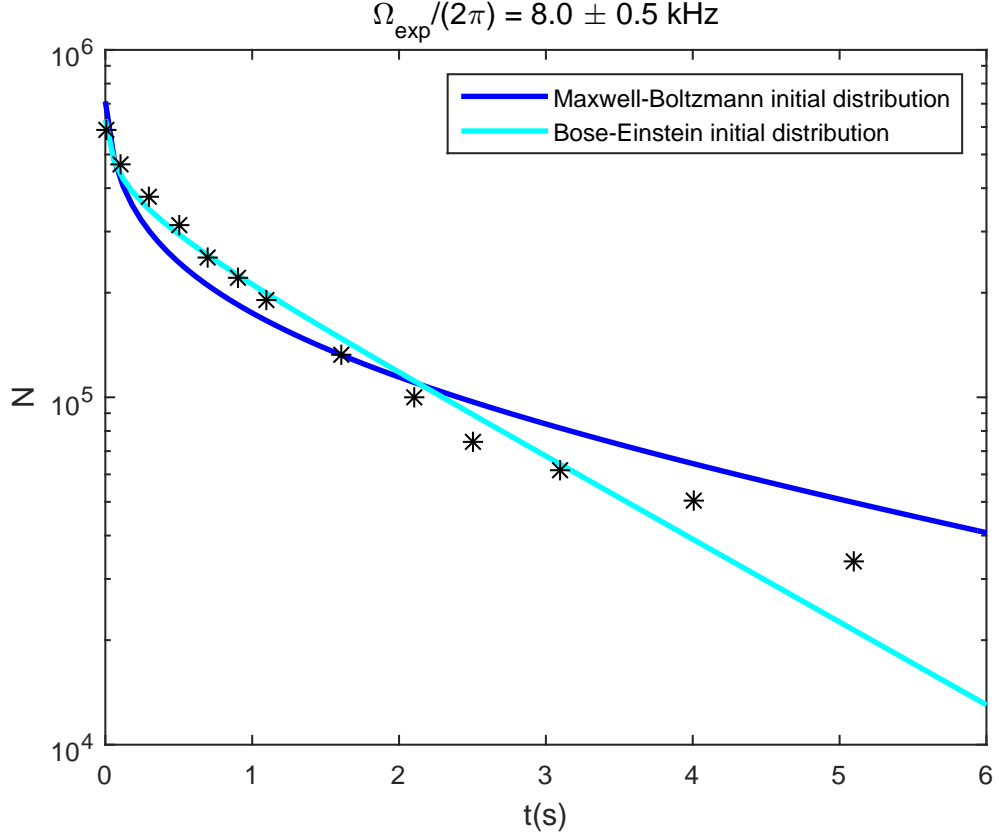


Figure 8.10: Trapped atom number (N) for the $\Omega_{\text{exp}}/2\pi = 8.0 \pm 0.5 \text{ kHz}$ experimental data as a function of time (t) given in seconds. Equation (5.35) was used to calculate the decay rates for a variety of initial distributions. The Rabi frequency and initial atom number were obtained using regression fitting given by equation (8.7). For the Maxwell-Boltzmann distribution the fitted values were $\Omega/2\pi = 6.81 \text{ kHz}$ and $N(t_0) = 7.11 \times 10^5$ with $S = 1.00 \times 10^5$, all given to three significant figures. For the Bose-Einstein distribution the fitted values were $\Omega/2\pi = 6.41 \text{ kHz}$ and $N(t_0) = 6.31 \times 10^5$ with $S = 2.16 \times 10^4$, all given to three significant figures. Parameters given in table 8.1 and an initial temperature $T(t_0) = 232 \text{ nK}$ were used to produce this graph.

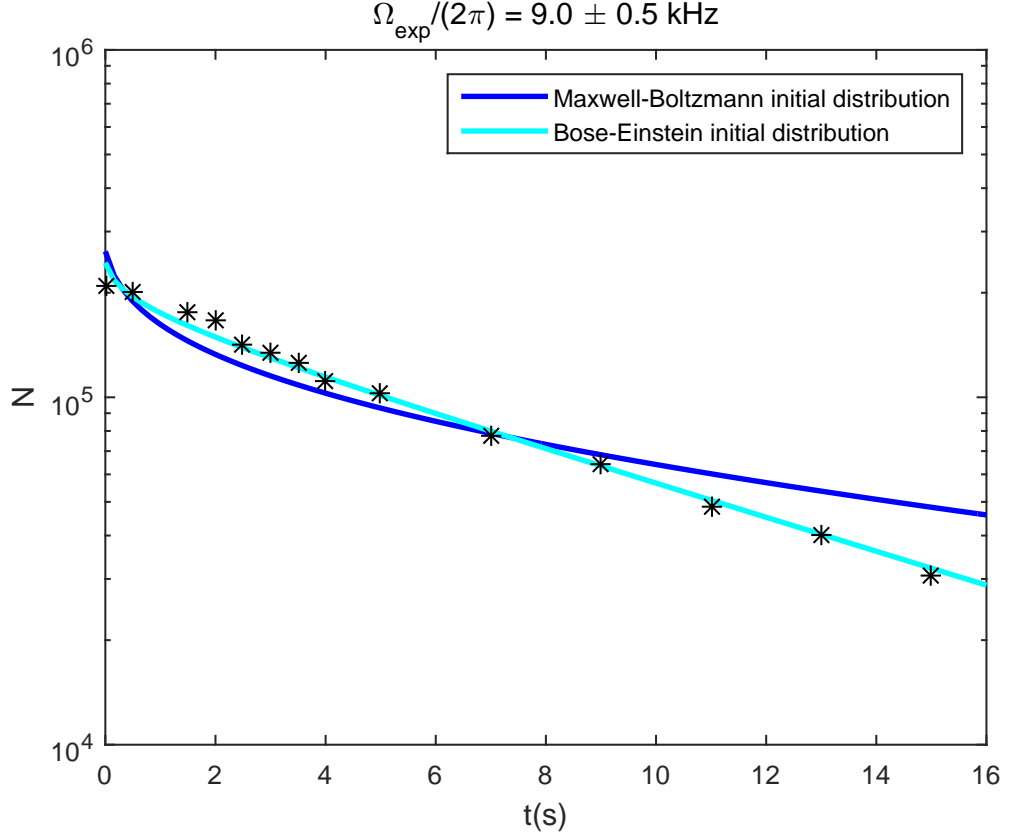


Figure 8.11: Trapped atom number (N) for the $\Omega_{\text{exp}}/2\pi = 9.0 \pm 0.5 \text{ kHz}$ experimental data as a function of time (t) given in seconds. Equation (5.35) was used to calculate the decay rates for a variety of initial distributions. The Rabi frequency and initial atom number were obtained using regression fitting given by equation (8.7). For the Maxwell-Boltzmann distribution the fitted values were $\Omega/2\pi = 7.54 \text{ kHz}$ and $N(t_0) = 2.63 \times 10^5$ with $S = 5.31 \times 10^4$, all given to three significant figures. For the Bose-Einstein distribution the fitted values were $\Omega/2\pi = 7.05 \text{ kHz}$ and $N(t_0) = 2.44 \times 10^5$ with $S = 9.64 \times 10^3$, all given to three significant figures. Parameters given in table 8.1 and an initial temperature $T(t_0) = 148 \text{ nK}$ were used to produce this graph.

The use of non-linear least squares regression fitting, for the input parameters of trap Rabi frequency and initial atom number, seems to greatly improve the apparent agreement between the theoretical prediction for the number of trapped atoms and the experimental data points. However, the absence of error bars on the data sets means extreme caution must be taken when comparing theory and experiment. Examination of the agreement between the fitted and experimentally determined Rabi frequencies, given in table 8.2, shows that there is significant discrepancy between theoretical and experimental Rabi frequency values.

We now see that there are at least two requirements necessary for agreement between theoretical predictions and experimental results. Firstly, we require that S values are low such that the predicted trapped atom number values do not differ greatly from the experimentally determined number of atoms. Additionally, we also require that the input variables of $\Omega, B', N(t_0), \Gamma_{bl}$ and, $T(t_0)$ (as well as Ω_i for the squeezed thermal initial distribution and ω_{rf} for the Bose-Einstein initial distribution) used to achieve these low S values agree with the experimentally determined values of these parameters. The results presented in figures 8.8 to 8.11 fulfil the requirement for low S values, however, they do not provide suitable agreement with experiment as most of the fitted Rabi frequencies are significantly below $\Omega_{exp}/(2\pi) - 0.5$ kHz.

	Maxwell-Boltzmann	Bose-Einstein
$\Omega_{exp}/(2\pi)$ (kHz)	$\Omega/(2\pi)$ (kHz)	$\Omega/(2\pi)$ (kHz)
5.0 ± 0.5	5.22 ± 0.09	4.90 ± 0.06
7.0 ± 0.5	6.47 ± 0.18	6.12 ± 0.12
8.0 ± 0.5	6.81 ± 0.17	6.41 ± 0.06
9.0 ± 0.5	7.54 ± 0.23	7.05 ± 0.06

Table 8.2: Fitted Rabi frequency values for the minimal effect gravity model associated with the results shown in figures 8.8 to 8.11. The uncertainties in the fitted values are calculated using the in-built Matlab function ‘nlparci’ that calculates the 95% confidence intervals [80].

The fact that the Rabi frequency values obtained from regression fitting do not fall within the experimentally expected region can be seen most clearly in figure 8.12. In particular, the values obtained for the Rabi frequency from regression fitting for the 7 kHz, 8 kHz and 9 kHz data sets are significantly lower than that expected

for the experimental data. This could have been predicted from figures 8.5 to 8.7 as the rate of non-adiabatic transitions increases with decreasing Rabi frequency, to reduce the predicted trapped atom number to match with the experimental data, a significant decrease in the Rabi frequency is needed. The fitting regime wants to group all data sets at lower Rabi frequencies, to compensate for the underestimated atom loss predicted by the model. This can be seen by the variation of the ‘goodness of fit’ S values with Rabi frequency shown in figure 8.13.

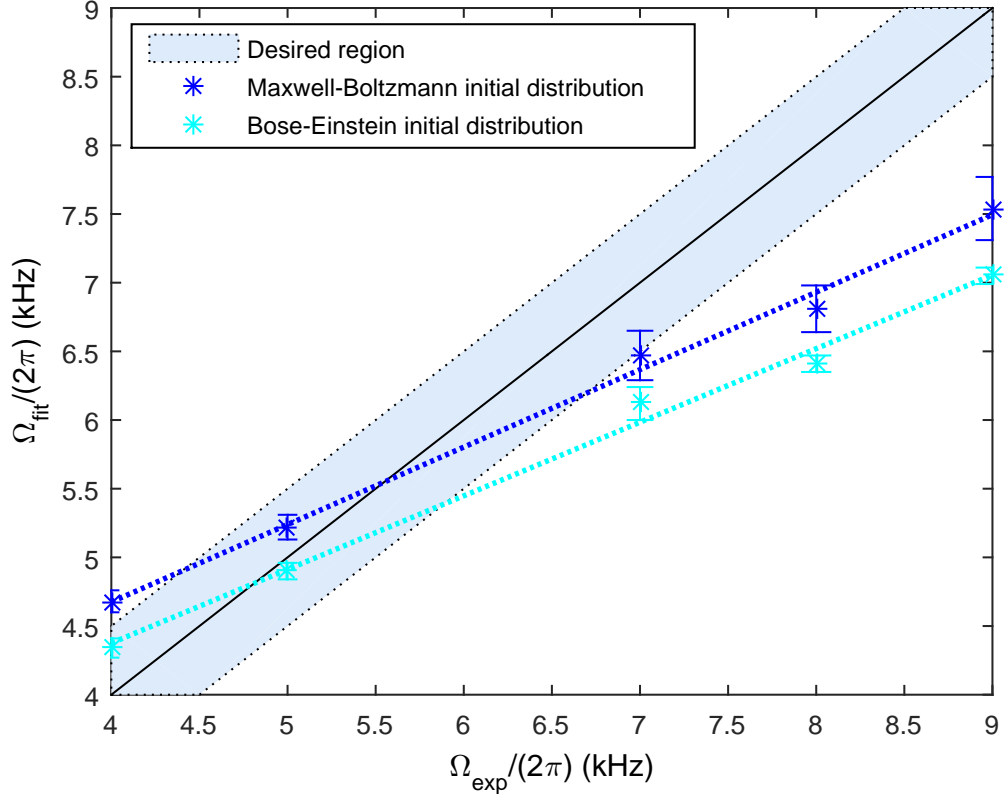


Figure 8.12: Comparison of fitted and experimentally determined Rabi frequencies for the minimal effect gravity model regression fitting. The values obtained by regression fitting, given in table 8.2, are represented by stars. Linear regression is applied, for the two initial distributions separately, to give the blue dotted lines. A black line is plotted to show the correlation which the fitted values would follow if they matched the experimental Rabi frequency values. The desired region is plotted, around the black line, taking into account an uncertainty of 0.5 kHz in the experimentally determined values for the trap Rabi frequency.

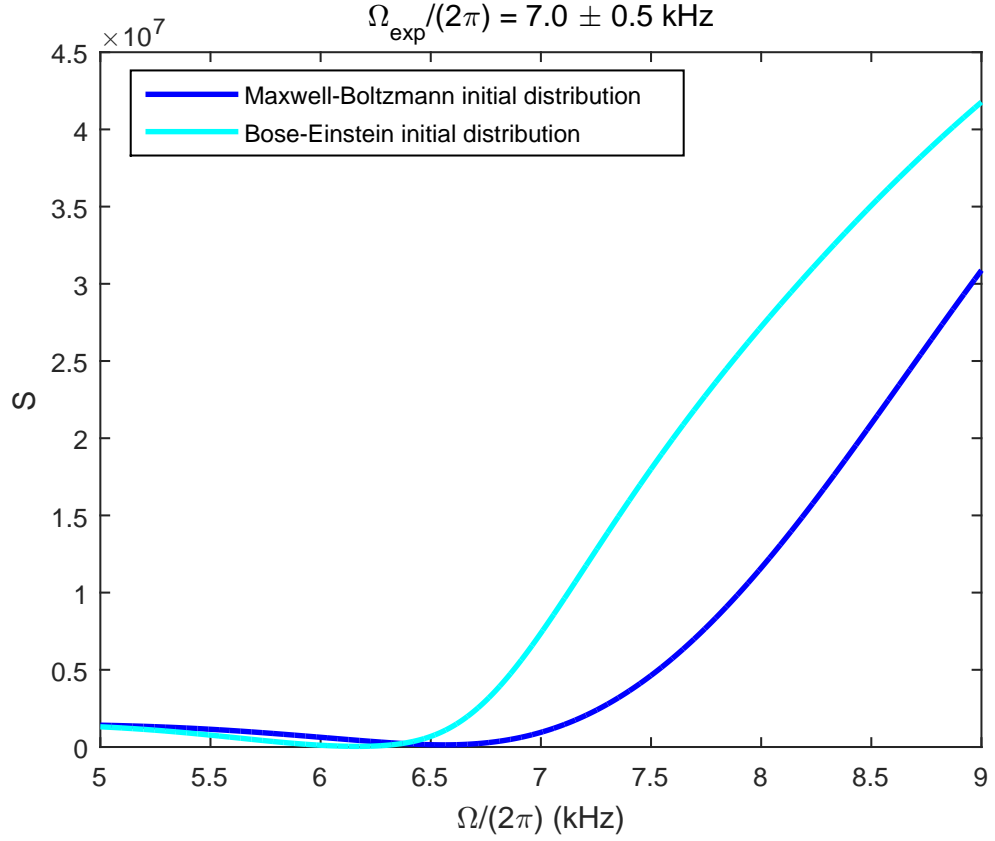


Figure 8.13: Values obtained for the least squares regression fitting variable (S) given by equation (8.7) for the $7.0 \pm 0.5 \text{ kHz}$ experimental data. Equation (5.35) was used to calculate the decay rates for the two initial distributions. Parameters given in table 8.1, an initial atom number of 5.02×10^5 atoms and an initial temperature $T(t_0) = 209 \text{ nK}$ were used to produce this graph.

It is important to consider that the fitting regime is only allowed to vary the initial atom number and Rabi frequency, with the initial temperature, magnetic field gradient and other input parameters kept fixed at their experimentally determined values. This was done purposefully due to interdependencies between the parameters and to reduce the risk of accidental fits. It should be noted that error in theory input parameters ($B', \Gamma_{bl}, \omega_{rf}, T(t_0)$) or use of a different weighting for the fitting (other than $\frac{1}{\sqrt{N_i}}$) will change the fitted Rabi frequencies obtained in table 8.2 and is not taken into consideration in the error bars for the fitted results. If there are any errors with the value of B' , this will affect the values of Ω given by the fitting regime. Similarly and perhaps more likely, if there are any inaccuracies in the values of $T(t_0)$ used this will affect the value of $N(t_0)$ obtained from regression fitting. As no variation in the magnetic field gradient has been considered, some of the shift in the value of the Rabi frequency could be reassigned to an increase in the magnetic field value. However, the discrepancy between the regression fitted Rabi frequency values and the experimentally determined Ω_{exp} values is so large that the discrepancy cannot be accounted for and we shall now try to improve agreement with experimental results by modelling the non-adiabatic decay rates using the more sophisticated full effect gravity model.

8.2.2 Full effect gravity model

We saw in chapters 5 and 6 that the full effect gravity model should be used, instead of the simpler minimal effect gravity model, to accurately determine the rate of non-adiabatic spin flips. Therefore we now continue our investigations using the non-adiabatic decay rates given by the full effect gravity model from this point onwards.

Figures 8.14 to 8.17 show the time evolution of the number of trapped atoms obtained using the experimentally determined Rabi frequency and other trap parameters, for the full effect gravity model decay rates.

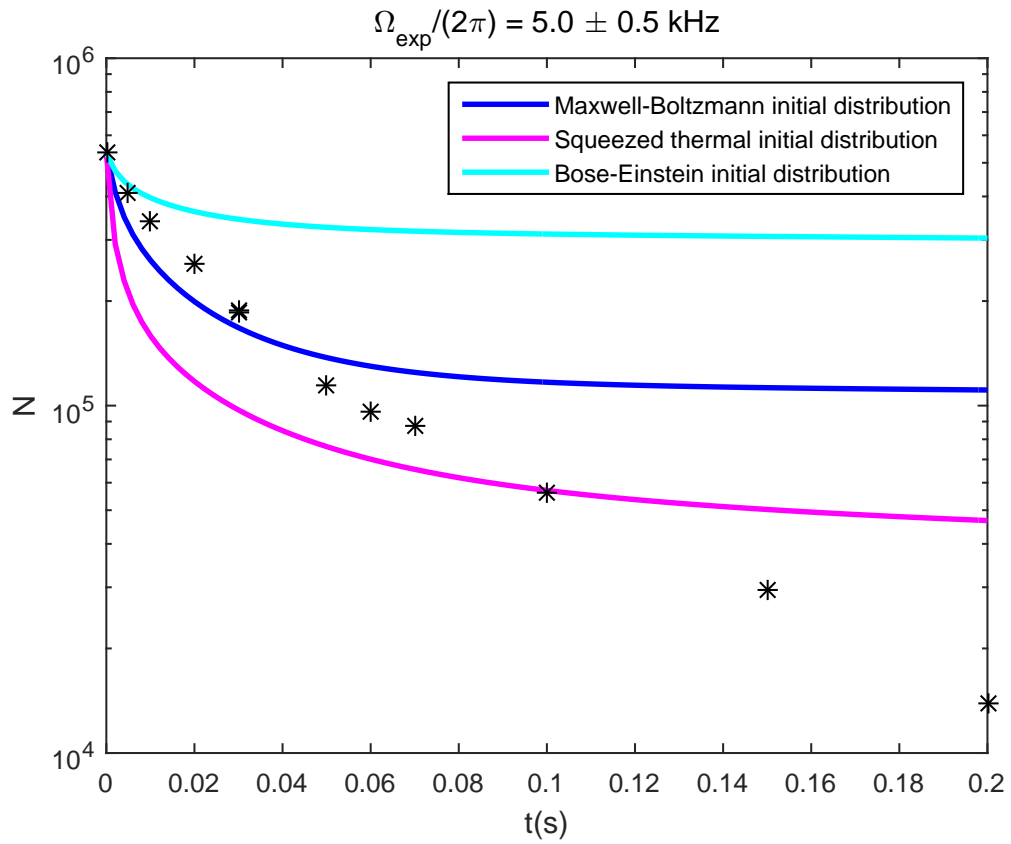


Figure 8.14: Trapped atom number for the $\Omega_{\text{exp}}/2\pi = 5.0 \pm 0.5 \text{ kHz}$ experimental data calculated using equation (5.136) for a variety of initial distributions. Parameters given in table 8.1, an initial atom number of 5.33×10^5 atoms, a Rabi frequency $\Omega/2\pi = 5 \text{ kHz}$ and an initial temperature $T(t_0) = 218 \text{ nK}$ were used to produce this graph.

There are clear differences between figures 8.4 to 8.7 for the minimal effect gravity model and figures 8.14 to 8.17 for the full effect gravity model. However, there are also similarities, most notably the large variation with different initial

distributions and the overestimation in the trapped atom number prediction of the Bose-Einstein distribution. Clearly there is still insufficient agreement at this stage between theoretical predictions and experimental results.

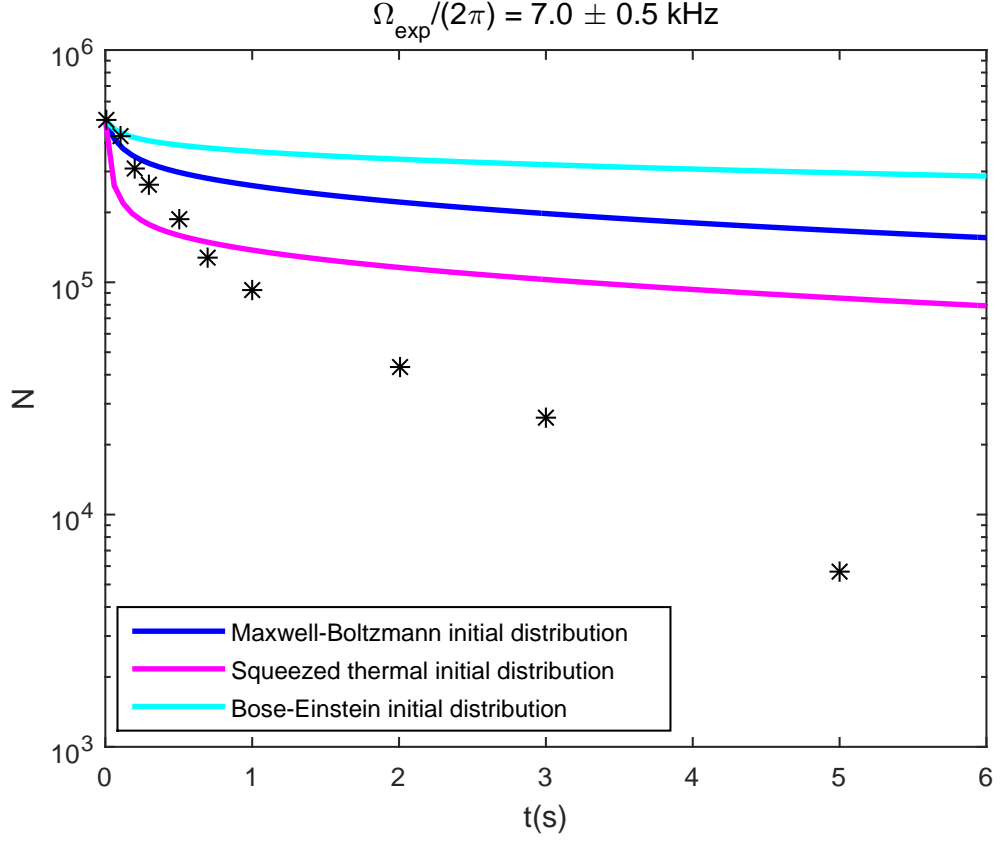


Figure 8.15: Trapped atom number for the $\Omega_{\text{exp}}/2\pi = 7.0 \pm 0.5 \text{ kHz}$ experimental data calculated using equation (5.136) for a variety of initial distributions. Parameters given in table 8.1, an initial atom number of 5.02×10^5 atoms, a Rabi frequency $\Omega/2\pi = 7 \text{ kHz}$ and an initial temperature $T(t_0) = 209 \text{ nK}$ were used to produce this graph.

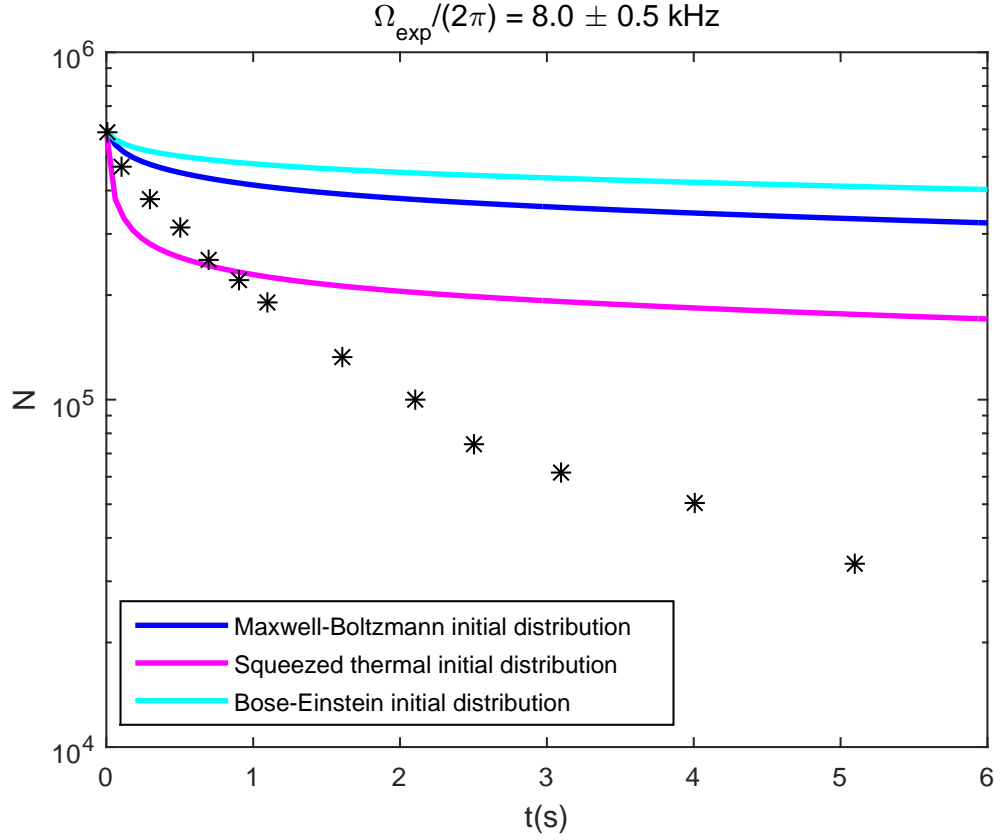


Figure 8.16: Trapped atom number for the $\Omega_{\text{exp}}/2\pi = 8.0 \pm 0.5 \text{ kHz}$ experimental data calculated using equation (5.136) for a variety of initial distributions. Parameters given in table 8.1, an initial atom number of 5.92×10^5 atoms, a Rabi frequency $\Omega/2\pi = 8 \text{ kHz}$ and an initial temperature $T(t_0) = 232 \text{ nK}$ were used to produce this graph.

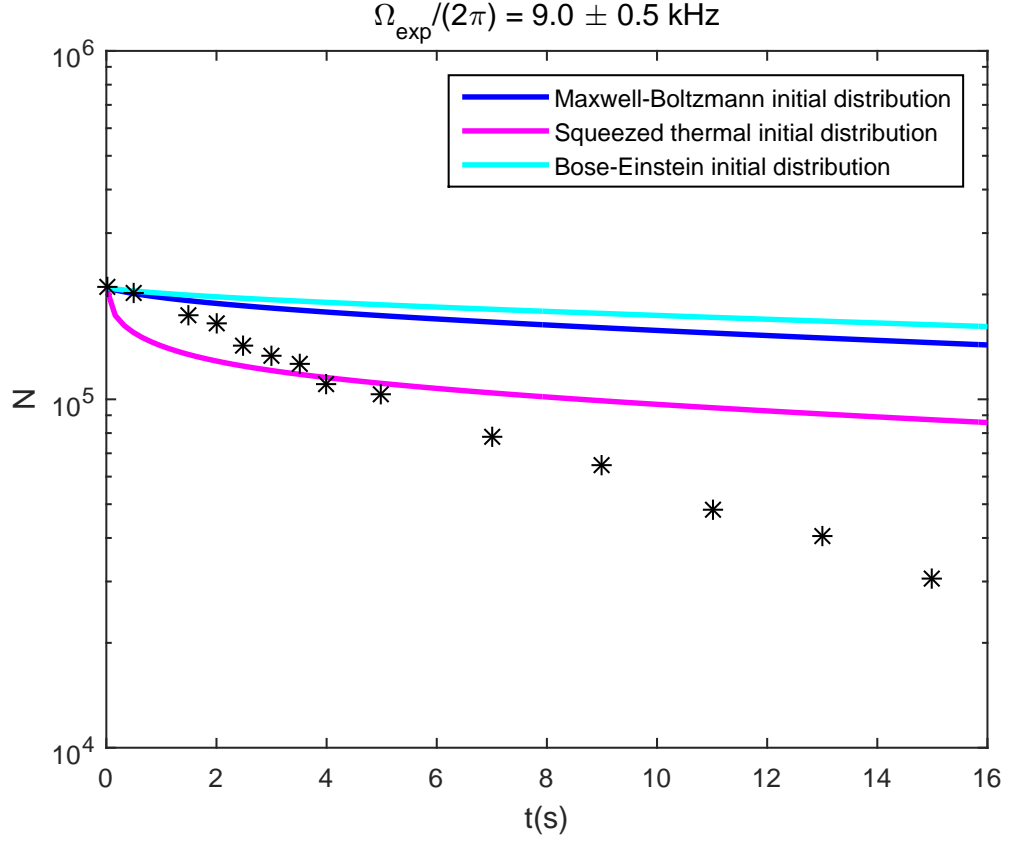


Figure 8.17: Trapped atom number for the $\Omega_{\text{exp}}/2\pi = 9.0 \pm 0.5 \text{ kHz}$ experimental data calculated using equation (5.136) for a variety of initial distributions. Parameters given in table 8.1, an initial atom number of 2.09×10^5 atoms, a Rabi frequency $\Omega/2\pi = 9 \text{ kHz}$ and an initial temperature $T(t_0) = 148 \text{ nK}$ were used to produce this graph.

Regression fitting

It would be desirable to use non-linear least squares regression fitting, as we did for our minimal effect gravity decay rates, to see if better agreement between theory and experiment can be obtained by allowing variation of Ω and $N(t_0)$. However, the oscillatory nature of the Airy function in equation (5.136), causes the theory curves of the predicted $N(t)$ to oscillate back and forth with Rabi frequency which causes tremendous trouble for the fitting regime. The consequences this has for regression fitting can be seen in figure 8.18 in which the goodness of fit (S), given as previously by equation (8.7), is plotted as a function of Rabi frequency.

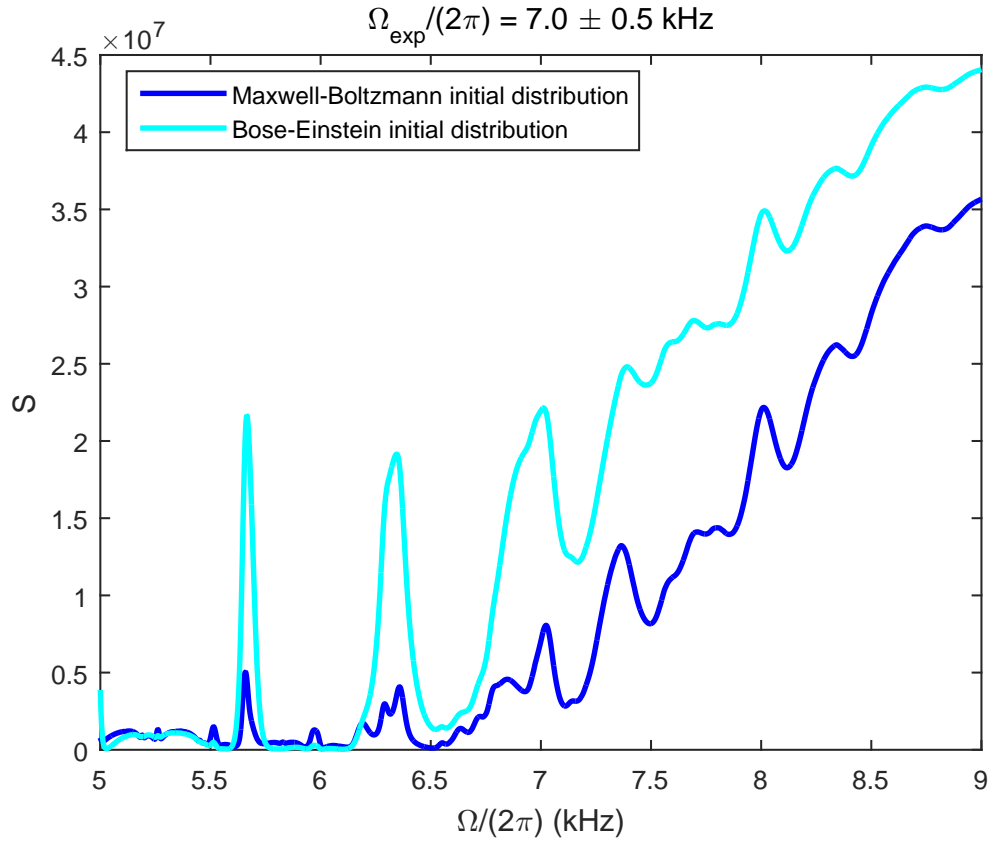


Figure 8.18: Values obtained for the least squares regression fitting given by equation (8.7) for the $\Omega_{\text{exp}}/2\pi = 7 \pm 0.5$ kHz experimental data. Equation (5.136) was used to calculate the decay rates for the two initial distributions. Parameters given in table 8.1, an initial atom number of 5.02×10^5 atoms and an initial temperature $T(t_0) = 209$ nK were used.

Desirably for use of regression fitting, and as is found in the minimal effect gravity model shown by figure 8.13, this plot would look like a giant valley and the

fitting regime would descend to the minima of that valley. However, figure 8.18 shows there are now many false minima present, which causes the fit obtained to be very sensitive to the starting values inputted. False minima pose a problem as fitting regimes tend to stop when they find the lowest point of whichever minima is closest to the inputted starting values, such that the regime never reaches the global lowest S value. The extent of the problem is seen in figure 8.19, which shows the fitting landscape when allowing the variation of both the Rabi frequency and the initial atom number for the purposes of regression fitting. Fitting becomes highly time consuming as plots similar to figure 8.19 have to be constructed to give guidance on a suitable set of starting values for the fitting regime, with many starting values needing to be tested.

Some of the valleys present in figure 8.19 lead to fits which by eye are clearly very poor and can be discounted. However, several of the valleys correlate to fits for which we do not have suitable information to discount. This means we have multiple potential fits for the experimental data, making it hard to determine which is the most appropriate fit. We shall see this later in figures 8.20 and 8.21. Additionally, simply minimising S does not necessarily give the best fit for the experimental data. This is partly due to the fact that we approximate the weighting suitable for the data set as we do not know the standard deviation of the experimental data points. Finding fits with low S allows us to find curves that match the experimental data well but the curve with the lowest S does not necessarily lead us to the most reliable prediction for the trap Rabi frequency. This means that we have to consider other information we have about the obtained fits (such as the discrepancy between the fitted Ω values and the experimental Ω_{exp} values) to determine the appropriateness of a regression fitted result.

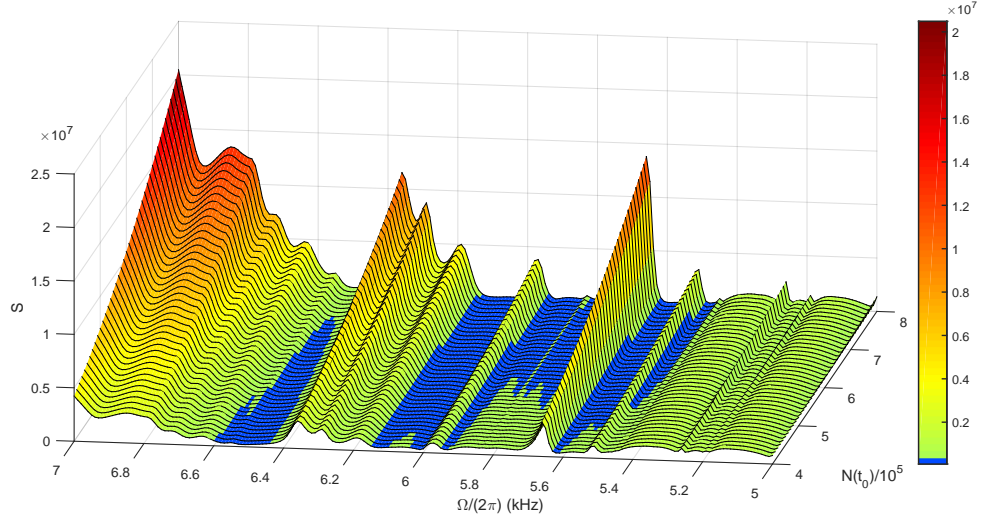


Figure 8.19: Fitting landscape for the $\Omega_{exp}/2\pi = 7 \pm 0.5$ kHz experimental data when both Rabi frequency and initial atom number are varied. The lines across the surface plot are slices in which only Ω is varied, equivalent to figure 8.18. The least squares regression values were calculated using equation (8.7). Equation (5.136) was used to calculate the decay rates for a Maxwell-Boltzmann initial distribution. Parameters given in table 8.1 and an initial temperature $T = 209$ nK were used to produce this graph.

Figure 8.20 shows two results obtained by using two different initial starting values of Ω and $N(t_0)$ for regression fitting of the 7 kHz experimental data set. The fits shown, by the blue and green lines, require lower Rabi frequencies than expected and higher initial atom number. Both values obtained for the fitted Rabi frequency are below 6.5 kHz, the lower bound of the experimental determination of the Rabi frequency. This mimics what was found in the minimal effect gravity case, although the disagreement between experimentally determined and fitted values has now increased. The sensitivity with Ω and the difficulty this causes for regression fitting in the full effect gravity model is illustrated in figure 8.20. Plotted in figure 8.20 are two theoretical predictions of trapped atom number, given by the blue and green curves, with fitted Rabi frequency and initial atom number values. The pink dashed line shows the theoretical trapped atom number prediction for the mean of their fitted Ω and $N(t_0)$ values. Even though the Rabi frequency used is only approximately 50 Hz away from two fitted Ω values, the pink curve is a poor match for the experimental data. This shows the extreme sensitivity of the theoretical atom number prediction to Rabi frequency. As the Rabi frequency has been increased,

the theoretical trapped atom number prediction has swung from the good fit along the blue curve, away from the data points to the pink dashed curve before returning to the data points along the green curve. This oscillatory behaviour also suggests why there are now multiple fits, as we effectively pass the same point twice for two different Ω values. It is a consequence of the fact that we no longer have a 1 – 1 mapping between Rabi frequency values and non-adiabatic decay rates in the full effect gravity model.

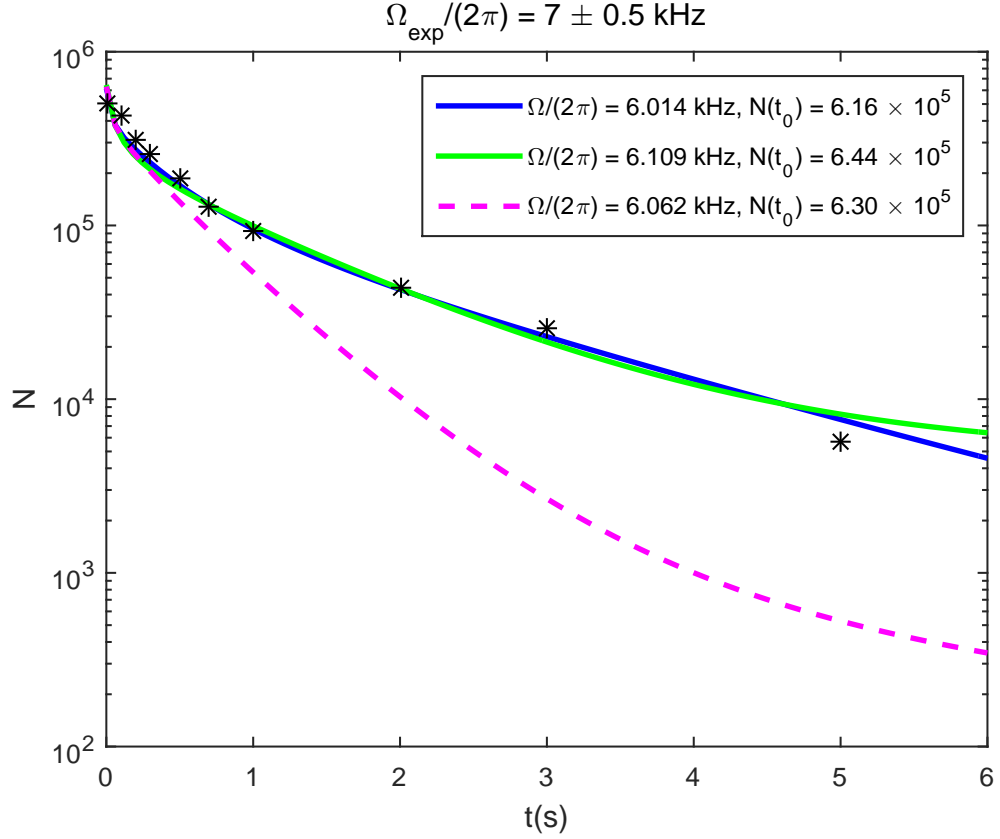


Figure 8.20: Two obtained results for the $\Omega_{\text{exp}}/2\pi = 7 \pm 0.5 \text{ kHz}$ experimental data, given by the solid blue and green curves, for a Maxwell-Boltzmann initial distribution. Also plotted is the predicted trapped atom number evolution for Rabi frequency and initial atom number values halfway in between the two sets of fits, given by the dashed pink curve. Equation (5.136) was used to calculate the decay rates and the fitting was performed by minimising equation (8.7). The two different fitted results were obtained by using different initial starting values in the fitting regime. The goodness of fit values are (given to three significant figures) $S = 5.65 \times 10^4$ for the blue curve, $S = 9.44 \times 10^4$ for the green curve and $S = 1.69 \times 10^5$ for the pink dashed curve. The Rabi frequency sensitivity is such that the fitted Rabi frequency values must be given to the nearest Hz. Parameters given in table 8.1 and an initial temperature $T(t_0) = 209 \text{ nK}$ were used.

Similar results are obtained using regression fitting with a Bose-Einstein initial distribution of atoms. The Bose-Einstein distribution results lead to lower S values with the curvature of the trapped atom number evolution matching the data points well at short times, as can be seen in figure 8.21. The fitted value for initial atom number is also closer to the experimentally recorded value of 5.02×10^5 atoms. However, the fitted Rabi frequency is once again too low to be within the experimentally determined value of 7 ± 0.5 kHz and is lower than that predicted for the Maxwell-Boltzmann initial distribution. The pink dashed line in figure 8.21, even though it has a Rabi frequency that is only 232 Hz away from two fitted Rabi frequency values provides poor agreement with the experimental data. Regardless of the initial distribution used, we cannot escape the high sensitivity of our full effect gravity model with respect to Rabi frequency.

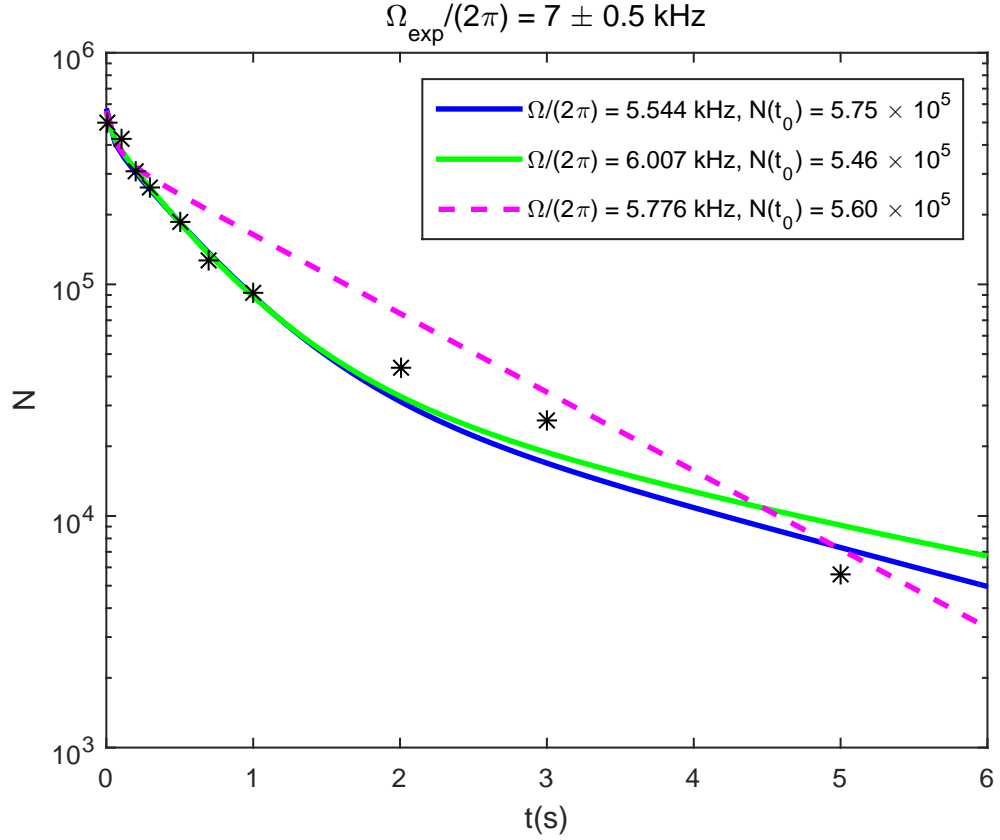


Figure 8.21: Two obtained results for the $\Omega_{\text{exp}}/2\pi = 7 \pm 0.5 \text{ kHz}$ experimental data, given by the solid blue and green curves, for a Bose-Einstein initial distribution. Also plotted is the predicted trapped atom number evolution for Rabi frequency and initial atom number with value halfway in between the two sets of fits, given by the dashed pink curve. Equation (5.136) was used to calculate the decay rates and the fitting was performed by minimising equation (8.7). The two different fitted results were obtained by using different initial starting values in the fitting regime. The goodness of fit values are (given to three significant figures) $S = 2.69 \times 10^4$ for the blue curve, $S = 1.65 \times 10^4$ for the green curve and $S = 1.67 \times 10^5$ for the pink dashed curve. The Rabi frequency sensitivity is such that the fitted Rabi frequency values must be given to the nearest Hz. Parameters given in table 8.1 and an initial temperature $T(t_0) = 209 \text{ nK}$ were used.

The extreme sensitivity with respect to Rabi frequency therefore makes regression fitting very difficult and draws the appropriateness of its use into question, however, it causes a much more significant problem. The predicted atom number at any given time varies greatly with Rabi frequency, as is shown in figure 8.22. A significant change is seen even for Rabi frequencies only a couple of Hertz apart, which is why theoretical Rabi frequency values are given in this section to the nearest 1 Hz. This is a consequence of the effects discussed in section 5.2 and is a purely quantum mechanical effect resulting from the oscillatory behaviour of the full effect gravity model decay rates with respect to Rabi frequency (see figure 5.17). However, this effect is not seen in the experimental data. The experimental data is not sampled at a high enough density of Rabi frequencies to form a plot which resembles figure 8.22 for comparison. Yet we can rule out such extreme Ω sensitivity as predicted. It is expected that the RF synthesizer that sets the Rabi frequency will fluctuate by around 200 Hz. If our predictions were correct, the experimental data points would not form a smooth curve but instead appear scattered, in a fashion that would almost appear random. This would imply that for a proper comparison with the experiment we require the sensitivity of the trapped atom number prediction to Rabi frequency to be reduced in some manner.

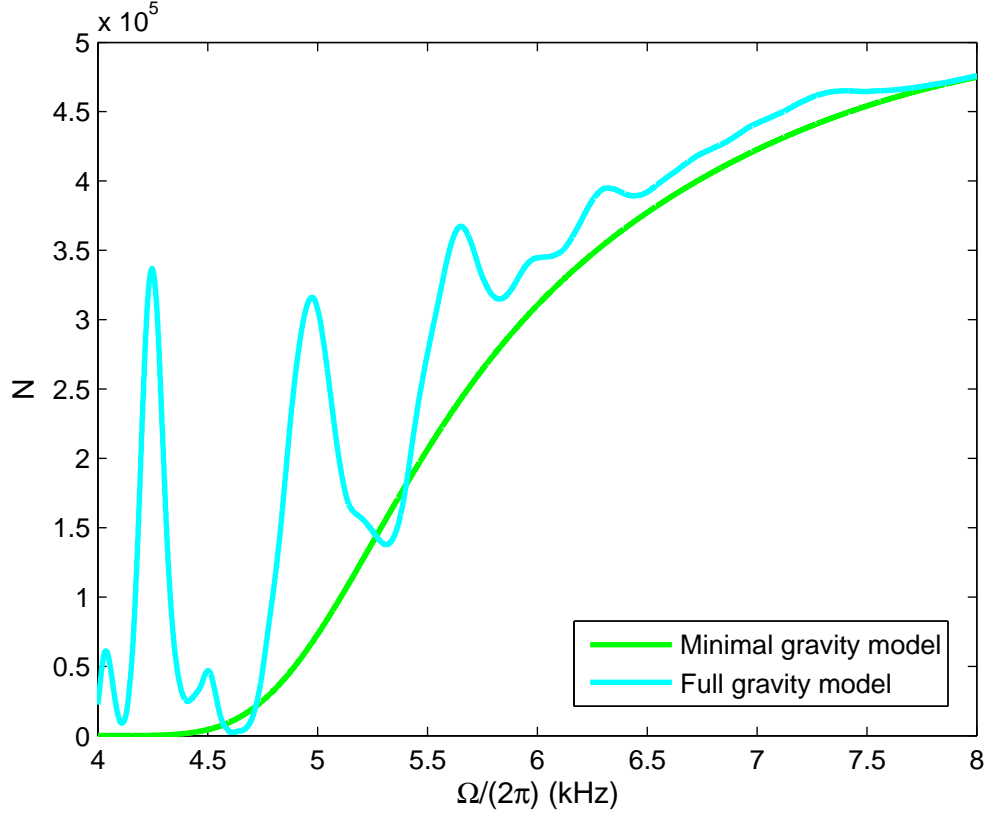


Figure 8.22: Predicted trapped atom number variation with Rabi frequency for the two models. The atom number is given $t = 0.1$ s after the trap was loaded and a Bose-Einstein initial distribution was used. Parameters given in table 8.1, an initial atom number $N(t_0) = 5.02 \times 10^5$ atoms and an initial temperature $T(t_0) = 209$ nK were used.

The sensitivity with Rabi frequency makes the results shown in figures 8.20 and 8.21 unsuitable for the experimental data. Figure 8.23 shows how the predicted atom number changes with a small change in Rabi frequency around the fitted value of $\Omega/2\pi = 6.014$ kHz taken from figure 8.20. As the Rabi frequency is increased, the predicted atom number curves move back and forth over each other. In the experiment the Rabi frequency experienced by the atoms at the location of maximum detuning will fluctuate due to unavoidable noise in the RF synthesizer that generates the RF frequency magnetic field. For the Paris experiment studied here, the stability is expected to be approximately 200 Hz. The theoretical prediction for the fitted value ± 0.2 kHz are given by the blue dashed and dotted curves in figure 8.23. However, the oscillatory behaviour means that data points would be found outside of the region in between these two curves, as demonstrated by the fit itself. If the fluctuation in the Rabi frequency was only 20 Hz, shown by the black dashed and

dotted lines, you see that this would still suggest a large variance for the trapped atom number which is not seen in the experimental data.

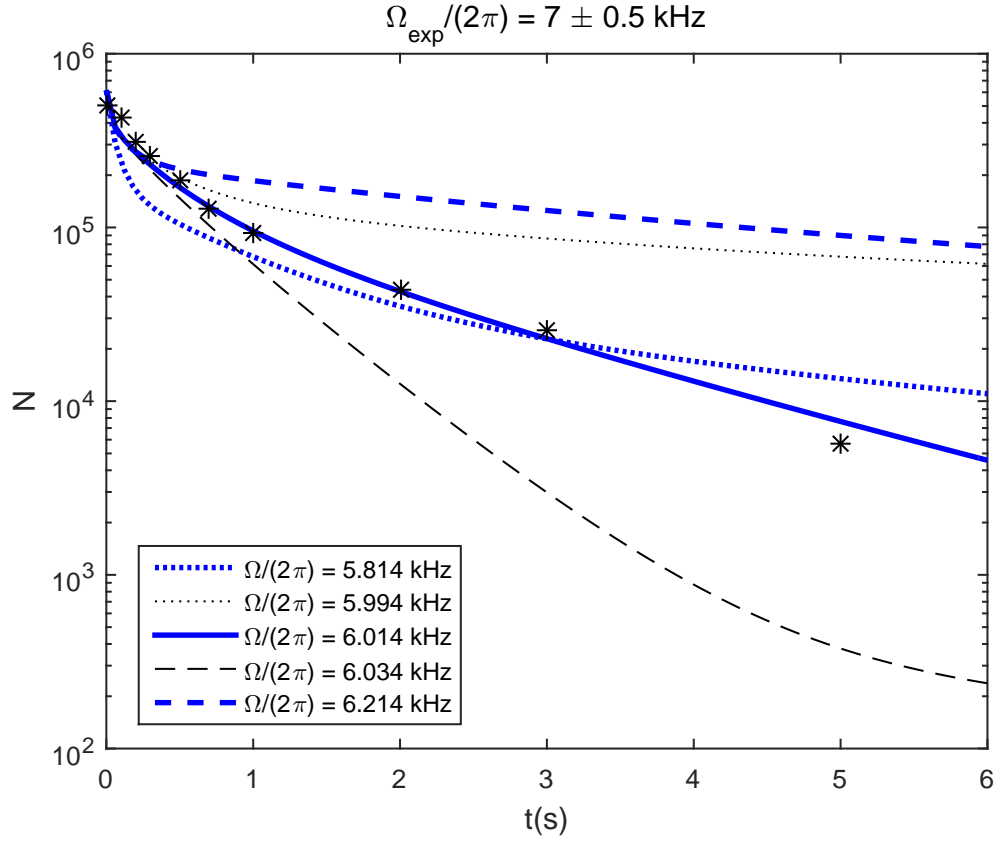


Figure 8.23: How the predicted trapped atom number (N) varies with time (t) given in seconds, for the fitted Rabi frequency of $\Omega/2\pi = 6.014$ kHz and values ± 0.02 kHz and ± 0.2 kHz of it. Equation (5.136) was used to calculate the decay rates and a Maxwell-Boltzmann initial distribution was used. The Rabi frequency sensitivity is such that the fitted Rabi frequency values must be given to the nearest Hz. Parameters given in table 8.1, an initial atom number of 6.16×10^5 atoms and an initial temperature $T(t_0) = 209$ nK were used to produce this graph.

The same problem occurs for a Bose-Einstein initial distribution, as demonstrated in figure 8.24 for the fitted Rabi frequency value $\Omega/2\pi = 6.007$ kHz taken from figure 8.21. Further investigation is required to understand why such extreme Rabi frequency sensitivity is not observed in the experimental data.

We conclude that we now have three requirements necessary to obtain successful agreement between experiment and theory:

- Good agreement between the theoretically predicted number of trapped atoms

and the experimentally determined number of trapped atoms, which corresponds to low S values.

- Input parameters for the theory ($\Omega, B', T(t_0), N(t_0), \Gamma_{bl}$, and ω_{rf}) must fall within the error bounds of the experimentally determined values of these parameters.
- The theoretical trapped atom number prediction should not vary significantly for a variation in the Rabi frequency of 200 Hz.

The fitted results presented in figures 8.20 and 8.21 fulfil only one of these requirements, having suitably low S values. We shall see in section 8.2.4 that, by including heating processes in our model, we are able to fulfil all three requirements and achieve suitable agreement between theory and experiment.

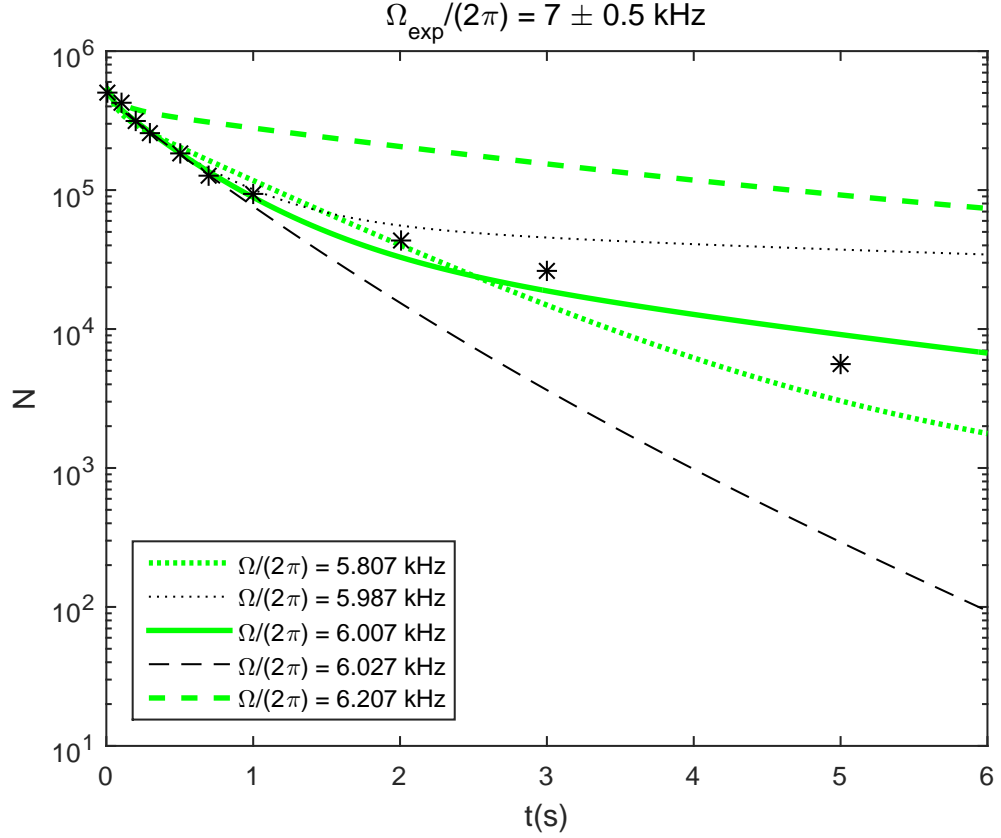


Figure 8.24: How the predicted trapped atom number (N) varies with time (t) given in seconds, for the fitted Rabi frequency of $\Omega/2\pi = 6.007 \text{ kHz}$ and values $\pm 0.02 \text{ kHz}$ and $\pm 0.2 \text{ kHz}$ of it. Equation (5.136) was used to calculate the decay rates and a Bose-Einstein initial distribution was used. The Rabi frequency sensitivity is such that the fitted Rabi frequency values must be given to the nearest Hz. Parameters given in table 8.1, an initial atom number of 5.46×10^5 atoms and an initial temperature $T(t_0) = 209 \text{ nK}$ were used.

8.2.3 Master equation model

We have seen in the preceding sections that use of equation (6.4) does not explain the experimental data recorded. The absorption imaging that allows experimental determination of the number of trapped atoms, can also be used to determine a temperature for the atom cloud [75]. This involves fitting a Gaussian to the image obtained and assumes a thermal distribution of atoms. Values of the temperatures obtained for a selection of different data sets are shown in figure 8.25. It is clear that at high Rabi frequencies the cloud temperature is increasing as a function of time. This is most evident for the 20 kHz data set, with the temperature more than doubling.

Increases in the trap temperature cannot be described in our $F = 1$ trap by non-adiabatic effects, which only lead to a decrease in energy of the system as atoms are removed, as we saw in discussions in section 6.4. Examining the effect of non-adiabatic losses alone a decrease in temperature would be expected, as shown in figure 8.25 for the 8 kHz data set. An increase in atom cloud temperature suggests there is a heating process affecting the trap. While heating is not directly observed in the lowest Rabi frequency data sets, it is likely that the same mechanism behind the heating observed in high Rabi frequency data sets is still present at low Rabi frequency. As non-adiabatic decay rates are highest at low Rabi frequency, in the balance between heating and losses, the trap temperature may continue to decrease. Alternatively the unknown heating process may have a Rabi frequency dependence which causes the heating to be negligible at low Rabi frequencies, further investigation would be required to determine whether this is the case.

To more accurately compare experiment and theory, we should therefore account for heating processes in our trap. Equation (6.4), which we have used so far in comparison with experiment, is unable to model heating processes. For an alternative we first turn to the master equation model, discussed in section 6.4.1. We attempt to fit to experimental data using non-linear least squares regression, by minimising

$$S = \sum_i \left(1 - \frac{N_i}{\mathcal{N}_i}\right)^2 + \sum_i \left(1 - \frac{T_i}{\mathcal{T}_i}\right)^2. \quad (8.8)$$

$N_i(\Omega, N(t_0))$ and $T_i(\Omega, N(t_0))$ are the number of trapped atoms and temperature of the atom cloud respectively, at a given time t_i as calculated for our theoretical full effect gravity model. \mathcal{N}_i and \mathcal{T}_i are the experimentally determined number of trapped atoms and atom cloud temperature at time t_i . We choose to fit to both trapped atom number and temperature for a given data set, to help improve the reliability of our fit. This is desirable as there are now an increased number of

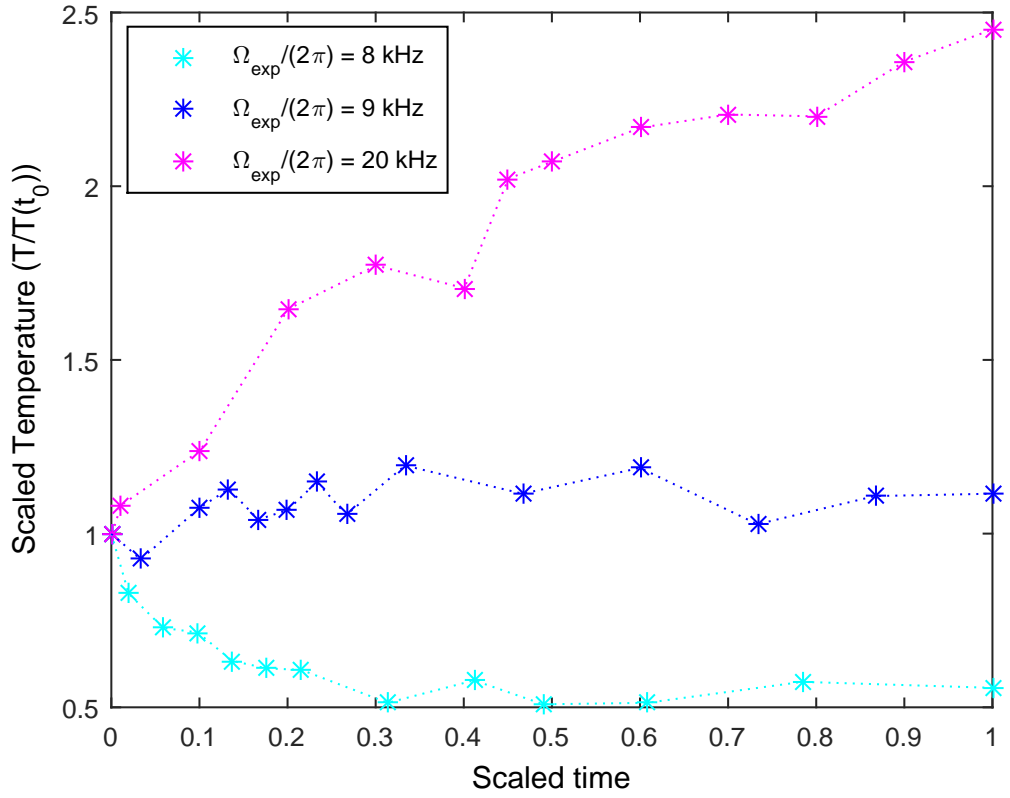


Figure 8.25: Variation in time of the recorded trap temperatures for three different Rabi frequency data sets. The temperatures plotted have been scaled by the initial trap temperature, which is 232 nK for the 8 kHz data set, 148 nK for the 9 kHz data set and 184 nK for the 20 kHz data set. The times plotted have been scaled by the time value of the final data point, which is 5.1 s for the 8 kHz data set, 15 s for the 9 kHz data set and 100.1 s for the 20 kHz data set. Experimental data points are represented by stars with dotted lines to guide the eye.

parameters to fit due to the unknown heating process. By fitting to both trapped atom number and temperature experimental data points, this should minimise the risk of accidental fits (see appendix B.1).

It should be noted that using equation (8.8), instead of equation (8.7), has meant removing the weighting from our data sets. Additionally, the determination of temperature and the number of trapped atoms are treated as equally reliable, which is a reasonable assumption but not necessarily the case. We discussed in section 6.4, with figure 6.22 the possible unreliability of our temperature prediction, meaning that the determined values of the trap temperature are likely to be less reliable than the theoretical prediction for the number of trapped atoms.

To allow agreement with experimental procedure, from this point onwards a Maxwell-Boltzmann initial distribution will be assumed. This is necessary for use of equation (6.52) to determine temperature, as discussed in section 6.4.1. The hope would be that any systematic error in the temperature determination, due to incorrect modelling of the distribution of atomic energies, should be equivalent in both our prediction and the experimental temperature values.

For the master equation model it was found that apparent interdependencies between γ and \bar{n}_f make fitting very difficult. The fitting regime which tries to minimise S , as defined in equation (8.8), seems to want ever higher \bar{n}_f and ever lower γ . The issue is indicated by figure 8.26 which shows that there is a channel for which several pairings of (γ, \bar{n}_f) lead to similar values of S .

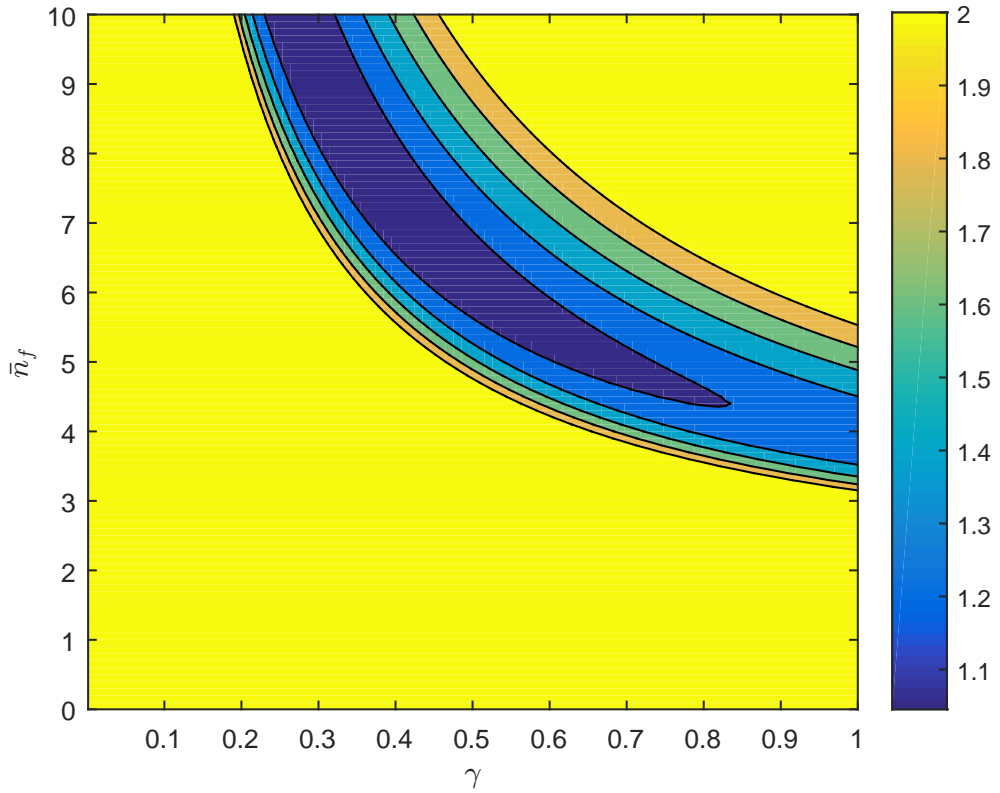


Figure 8.26: Contour plot to illustrate the problem with fitting using the master equation model. The goodness of fit as given by equation (8.8) was calculated for a selection of relaxation parameter, γ and mean bath occupation numbers \bar{n}_f values and plotted with contours spaced apart by a value of 0.2.

Without a way to determine γ and \bar{n}_f , associated with the unknown heating process, other than fitting and without the knowledge of any relationship between

then any fitted values obtained using the master equation model are not reliable. As fluctuations in the trap input parameters should count for the majority of the experimentally observed heating, we progress to using the parametric heating model, discussed in section 6.4.2, to predict the number of trapped atoms and the temperature of the atomic cloud.

8.2.4 Parametric heating model

Fluctuations in the trap parameters can lead to a heating process, which we describe using the parametric heating model. In section 6.4.2 we determined expressions for the heating rates γ_a and γ_b given by equations (6.85) and (6.94) respectively. These expressions give γ_a in terms of the power spectrum for the fluctuations in the trap centre and γ_b in terms of the power spectrum of fractional fluctuations in the spring constant associated with a harmonic oscillator approximation of the trapping potential. Fluctuations in the location of the trap centre and the value of the trap spring constant arise due to fluctuations in the currents that generate the static and RF frequency magnetic fields used to form the RF-dressed trap. We now wish to express the heating rates in terms of fractional fluctuations in the trap horizontal static magnetic field gradient ($B'/2$), RF magnetic field amplitude (B_{rf}) and RF frequency (ω_{rf}). To convert between power spectrum we can use the following formulae:

$$S_z(\omega) = \left(X \frac{\partial Z}{\partial X} \right)^2 S_X(\omega) \quad (8.9)$$

[56] for fluctuations in the trap centre, where Z gives the position of the trap centre and where X is the fractional fluctuation in the new parameter of interest, or

$$S_k(\omega) = \left(\frac{X}{k} \frac{\partial k}{\partial X} \right)^2 S_X(\omega) \quad (8.10)$$

for fractional fluctuations in the trap spring constant k_i . By assuming that the trap centre is situated at the lowest height of the resonant ellipsoid³ we can approximate the location of the trap centre (Z) by

$$Z \approx -\frac{\omega_{\text{rf}}}{\lambda} = -\frac{\hbar\omega_{\text{rf}}}{2|g_F|\mu_B b'} \quad (8.11)$$

where $b' = \frac{B'}{2}$ is the magnetic field gradient in the horizontal direction. Therefore,

$$\gamma_a = \frac{m_0\omega^3\omega_{\text{rf}}^2}{4\hbar\lambda^2} [S_B(\nu) + S_{\text{rf}}(\nu)] \quad (8.12)$$

where $\omega = 2\pi\nu$. This assumes there are no cross correlations between the noise in the magnetic field gradient and RF frequency, which is reasonable as the currents which produce them are generated by different sources. The power spectrum for the fractional fluctuation in the magnetic field gradient is given by

$$S_B(\omega) = \frac{1}{\pi} \int_{-\infty}^{\infty} \cos(\omega\tau) \left\langle \frac{\delta b'(t)}{b'} \frac{\delta b'(t+\tau)}{b'} \right\rangle d\tau \quad (8.13)$$

³This neglects the fact that the trap centre is slightly below resonance (see equation 5.104).

while the power spectrum for the fractional fluctuation in the RF frequency is

$$S_{\text{rf}}(\omega) = \frac{1}{\pi} \int_{-\infty}^{\infty} \cos(\omega\tau) \left\langle \frac{\delta\omega_{\text{rf}}(t)}{\omega_{\text{rf}}} \frac{\delta\omega_{\text{rf}}(t+\tau)}{\omega_{\text{rf}}} \right\rangle d\tau. \quad (8.14)$$

Ignoring any contribution from the hump or gravitational effects, the spring constant for the trap harmonic oscillator can be approximated as

$$k_i \approx \frac{\hbar m_i \lambda^2}{\Omega} = \frac{4m_i |g_F| \mu_B b'^2}{B_{\text{rf}}}. \quad (8.15)$$

Use of equation (8.10) then expresses the heating rate as

$$\gamma_b = \frac{\omega^2}{32} [4S_B(\nu) + S_{\text{Brf}}(\nu)], \quad (8.16)$$

where S_B is defined as in equation (8.13) and

$$S_{\text{Brf}}(\omega) = \frac{1}{\pi} \int_{-\infty}^{\infty} \cos(\omega\tau) \left\langle \frac{\delta B_{\text{rf}}(t)}{B_{\text{rf}}} \frac{\delta B_{\text{rf}}(t+\tau)}{B_{\text{rf}}} \right\rangle d\tau \quad (8.17)$$

is the power spectrum for fractional fluctuations in the RF magnetic field amplitude. Once again we have dismissed the possibility for cross correlations, as the static magnetic field gradient and RF magnitude are produced by different sets of coils with different current generators.

For the RF-dressed trap studied here $\gamma_a \gg \gamma_b$ provided the various noises in the system do not differ by several orders of magnitude. If we consider the case where fluctuations in the magnetic field gradient are the dominant cause of noise in the trap, we can derive the expression

$$\gamma_b = \frac{\Omega^2}{2\alpha^2 \omega_{\text{rf}}^2} \gamma_a, \quad (8.18)$$

such that the unknown heating rate γ_b can now be calculated from the heating rate γ_a . The variable α is as defined in equation (5.32).

Using equation (8.18) to calculate the heating rate γ_b , regression fitting was performed by minimising equation (8.8) to find fitted values for the heating rate γ_a and the trap Rabi frequency. Ω was allowed to vary in the fitting regime to take into account any errors in the experimental determination of the Rabi frequency, which the predicted trapped atom number remains sensitive to. The other trap parameters were assumed to be as experimentally predicted. The predicted trapped atom number and atom cloud temperature time evolutions obtained as a result of the regression fitting, are shown for each of the experimental data sets by solid lines in figures 8.27 to 8.30. Also plotted in figures 8.27 to 8.30 are the predicted trapped atom number and temperature time evolution for Rabi frequencies ± 200 Hz away from the experimentally determined value.

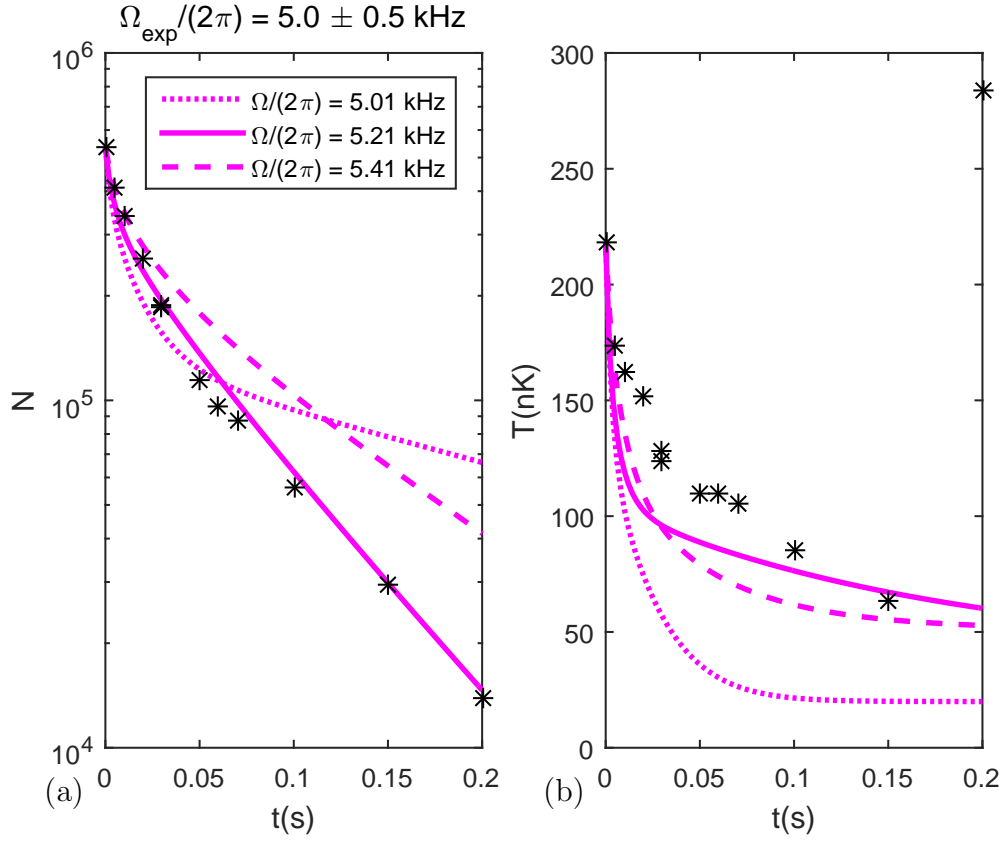


Figure 8.27: Trapped atom number (N) and atom cloud temperature (T) of the $\Omega_{\text{exp}}/2\pi = 5.0 \pm 0.5$ kHz experimental data for the parametric heating model. The decay rates are those obtained for the full effect gravity model given by equation (5.136). Parameters given in table 8.1, an initial atom number of 5.33×10^5 atoms and an initial temperature $T(t_0) = 218$ nK were used to produce this graph. The fitted parameters were $\gamma_a = 3.18 \text{ s}^{-1}$ and $\Omega/2\pi = 5.21$ kHz with $S = 0.554$, all given to three significant figures. Calculated from equation (8.18), $\gamma_b = 7.26 \times 10^{-6} \text{ s}^{-1}$ (3sf). For this data set only, the last data point at $t = 0.2$ s was not included in the fitting as its high temperature was believed to be anomalous data point. Notice the evidence of Rabi frequency sensitivity in the large predicted variance in the trapped atom number for $t > 0.03$ s.

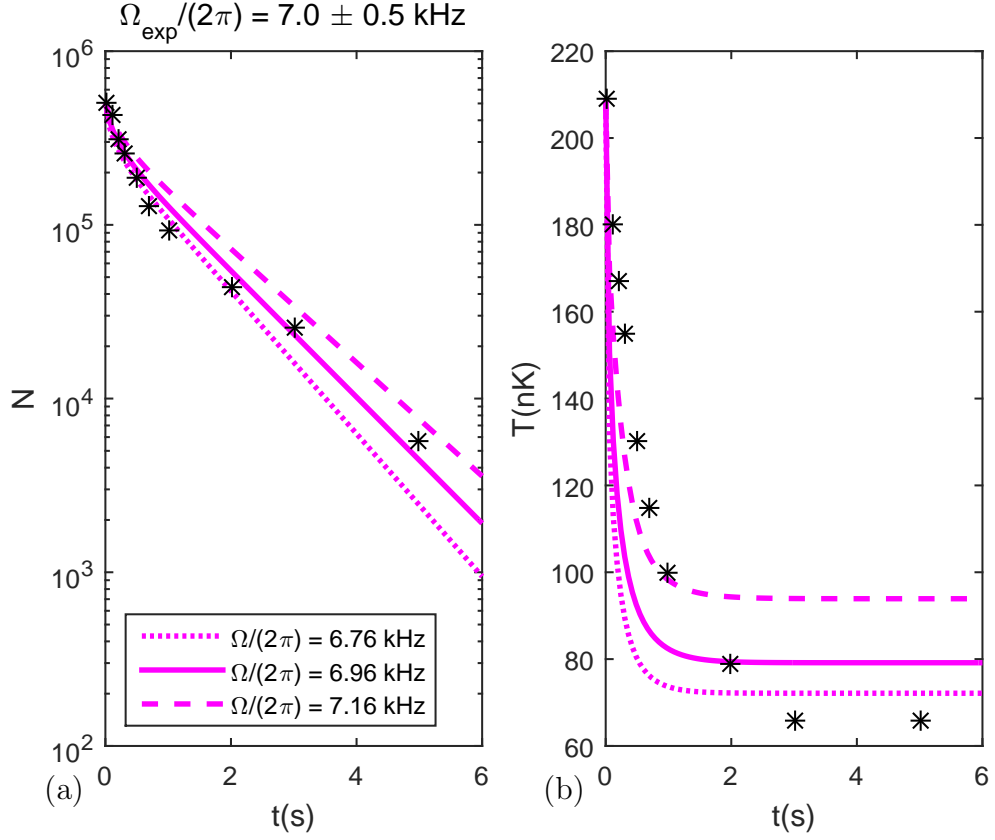


Figure 8.28: Trapped atom number (N) and atom cloud temperature (T) of the $\Omega_{\text{exp}}/2\pi = 7.0 \pm 0.5$ kHz experimental data for the parametric heating model. The decay rates are those obtained for the full effect gravity model given by equation (5.136). Parameters given in table 8.1, an initial atom number of 5.02×10^5 atoms and an initial temperature $T(t_0) = 209$ nK were used to produce this graph. The fitted parameters were $\gamma_a = 2.18 \text{ s}^{-1}$ and $\Omega/2\pi = 6.96$ kHz with $S = 0.929$, all given to three significant figures. Calculated from equation (8.18), $\gamma_b = 5.69 \times 10^{-6} \text{ s}^{-1}$ (3sf).

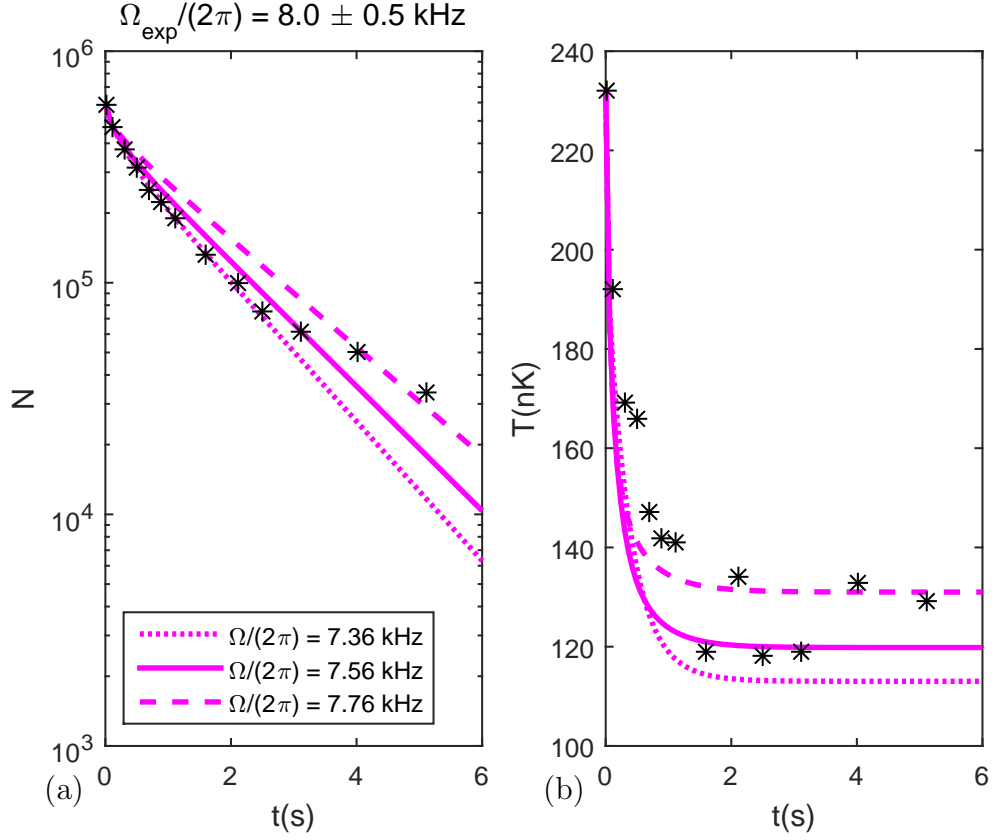


Figure 8.29: Trapped atom number (N) and atom cloud temperature (T) of the $\Omega_{\text{exp}}/2\pi = 8.0 \pm 0.5$ kHz experimental data for the parametric heating model. The decay rates are those obtained for the full effect gravity model given by equation (5.136). Parameters given in table 8.1, an initial atom number of 5.92×10^5 atoms and an initial temperature $T(t_0) = 232$ nK were used to produce this graph. The fitted parameters were $\gamma_a = 2.69 \text{ s}^{-1}$ and $\Omega/2\pi = 7.56$ kHz with $S = 0.615$, all given to three significant figures. Calculated from equation (8.18), $\gamma_b = 7.31 \times 10^{-6} \text{ s}^{-1}$ (3sf).

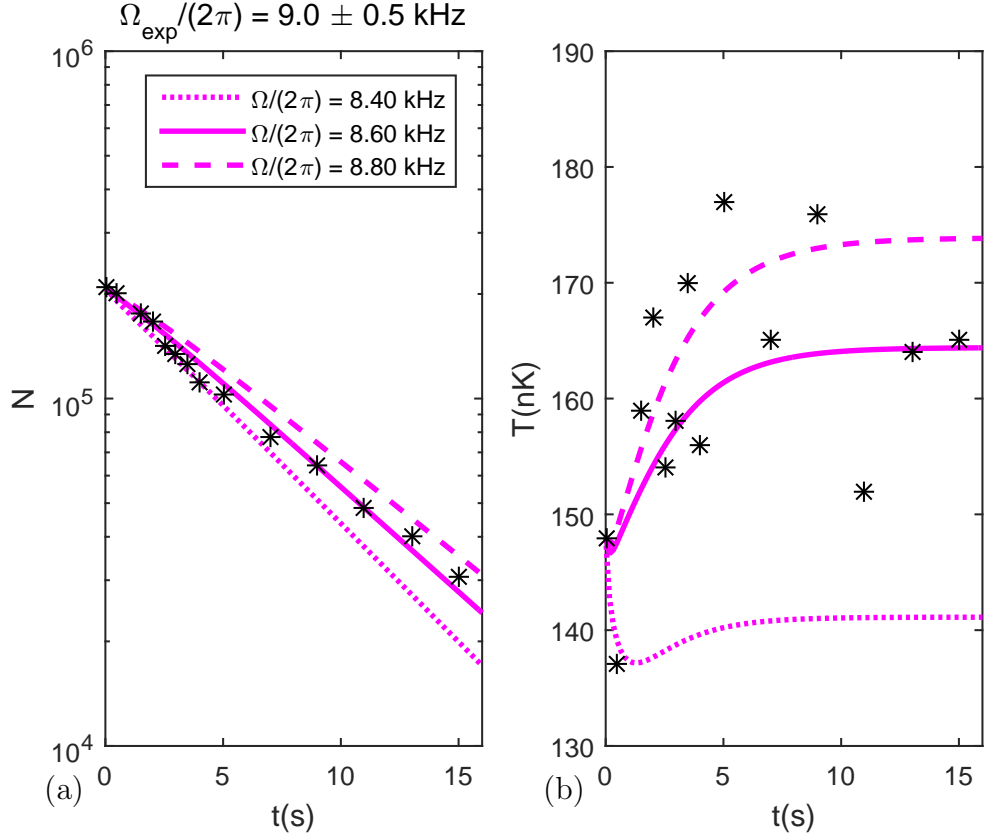


Figure 8.30: Trapped atom number (N) and atom cloud temperature (T) of the $\Omega_{\text{exp}}/2\pi = 9.0 \pm 0.5 \text{ kHz}$ experimental data for the parametric heating model. The decay rates are those obtained for the full effect gravity model given by equation (5.136). Parameters given in table 8.1, an initial atom number of 2.09×10^5 atoms and an initial temperature $T(t_0) = 148 \text{ nK}$ were used to produce this graph. The fitted parameters were $\gamma_a = 0.849 \text{ s}^{-1}$ and $\Omega/2\pi = 8.60 \text{ kHz}$ with $S = 0.105$, all given to three significant figures. Calculated from equation (8.18), $\gamma_b = 2.46 \times 10^{-6} \text{ s}^{-1}$ (3sf).

The results obtained for the parametric heating model are a significant improvement compared to the previous results obtained using equation (6.4) to calculate $N(t)$. Inclusion of a heating process increases the predicted rate of loss of atoms from the trap, as seen in section 6.4.2. This counteracts the problem experienced previously in sections 8.2.1 and 8.2.2 with the overestimation of the trapped atom number.

Additionally, including a heating process in our model has reduced the sensitivity of the trapped atom number prediction to Rabi frequency. The difference between $\Omega + 0.2\text{ kHz}$ and $\Omega - 0.2\text{ kHz}$ is now relatively tight and suitable for the experimental data. This removes the issue that prevented previous attempts at fitting with the full effect gravity model, discussed in section 8.2.2. It is interesting to see that the Rabi frequency sensitivity, a purely quantum mechanical effect which arises from the overlap of two wavefunctions, has been reduced significantly by inclusion of a suitably strong heating process in the trap.

However there are still issues with the fitting, for the 5 kHz data set the result obtained, shown in figure 8.27, is unreliable due to the large atom number variance it predicts for $t > 0.03\text{ s}$ which is not seen in the experimental data points. In this case the fitted heating rate values are not sufficient to appropriately reduce the sensitivity to Ω . This could potentially indicate a problem arising with our theory at very low Rabi frequencies, perhaps due to the fact that we are not accounting correctly for the three dimensional nature of non-adiabatic effects in the trap potentials or perhaps an issue with Fermi's Golden Rule. At such extremely low Rabi frequencies the non-adiabatic couplings are high and this makes our weak coupling assumption necessary for Fermi's Golden Rule questionable. As mentioned when the experimental data was introduced, the atom cloud studied does contain a BEC component, with the 5 kHz data set having the largest BEC fraction compared to the total number of trapped atoms. This could explain the lack of agreement between theory and experiment for the 5 kHz data set as our model is not appropriate for use with BECs as it does not consider interactions between atoms. All of this indicates areas of potential future research.

The agreement between theoretically calculated and experimentally determined temperatures displayed in figures 8.27 to 8.30 is obviously not as good as the agreement observed with trapped atom number. As discussed in sections 6.4.2 and 8.2.3, our determination of trap temperature is not as reliable as our determination of trapped atom number. Taking this into consideration the obtained agreement with the experimental temperature values is reasonable. The observed large variance of the temperature values recorded for the 9 kHz data set (in comparison to

the lower Rabi frequency data sets) could indeed be explained by our model as theoretically we predict a similar increase in temperature variance with increasing Rabi frequency. This would imply the scattering of temperature data points observed in the 9 kHz data set is the result of the 200 kHz fluctuations in the RF synthesizer.

The tabulated values for the fitted γ_a and Ω values, as well as the calculated γ_b values and an estimate of the power spectrum obtained from

$$S_B(\nu) = \frac{4\hbar\lambda^2}{m_0\omega^3\omega_{\text{rf}}^2}\gamma_a \quad (8.19)$$

are given in table 8.3.

It should be noted that even if fluctuations in the magnetic field were not dominant, the formula given by equation (8.18) is still the most convenient for fitting. If the power spectrums were all of equivalent magnitude, $S_B(\omega) \approx S_{\text{rf}}(\omega) \approx S_{\text{Brf}}(\omega)$, then equation (8.18) would be scaled by a factor of $\frac{5}{8}$. As γ_b is so small, it is currently having a negligible effect on the trapped atom prediction and the results obtained would be as given in figures 8.27 to 8.30. The only way for γ_b to have a non-negligible contribution to the heating process in the trap would be for $S_{\text{Brf}}(\omega)$ to be several orders of magnitude larger than $S_B(\omega)$.

There remains uncertainty with the fitting results as error in theory input parameters (B' , $T(t_0)$, Γ_{bl} and $N(t_0)$) or use of a different formula for S (other than equation (8.8)) will change the fitted Rabi frequencies, and is not taken into consideration in the error bars presented for the fitted results given in table 8.3. However, it is promising that the values obtained for the power spectrum, for fractional fluctuations in the magnetic field gradient, are relatively consistent and of appropriate value. This implies that our methodology is appropriate and any deviation from the fitted results presented is small. The value of the power spectrum calculated from our fits would ideally be the same across all Rabi frequencies. This occurs as all data sets have the same magnetic field gradient and so it is expected that the current fluctuations in the coils, which generate the static trapping magnetic fields, are of a similar magnitude for each data set. This is assumed in derivation of the relation connecting γ_a and γ_b given in equation (8.18). Therefore, there should be consistency in the power spectrum values calculated from our regression fits. While the values of S_B in table 8.3 do vary with Rabi frequency, it is encouraging to see relatively consistent values for the power spectrum values determined.

$\Omega_{exp}/2\pi(\text{kHz})$	$\gamma_a(s^{-1})$	$\gamma_b/10^{-6}(s^{-1})$	$\Omega/2\pi(\text{kHz})$	$S_B \text{ (dB/Hz)}$
5.0 ± 0.5	3 ± 3	7 ± 7	5.21 ± 0.11	-
7.0 ± 0.5	2.2 ± 0.4	5.8 ± 1.1	6.96 ± 0.14	-118.9 ± 1.0
8.0 ± 0.5	2.7 ± 0.6	7.3 ± 1.7	7.56 ± 0.15	-117.5 ± 1.2
9.0 ± 0.5	0.85 ± 0.05	2.46 ± 0.15	8.60 ± 0.04	-121.7 ± 0.3

Table 8.3: Parametric heating model results associated with figures 8.27 to 8.30.

The heating rate γ_a and Rabi frequency values are obtained from regression fitting using equation (8.8). The heating rate γ_b is calculated from equation (8.18). The power spectrum associated with the fractional fluctuations in the magnetic field gradient, calculated from equation (8.19), is expressed in units of decibel Hertz where $S_B = -119 \text{ dB/Hz} = 10^{-11.9} \text{ s}$. The uncertainties in the fitted values are calculated using the in-built Matlab function ‘nlparci’ that calculates the 95% confidence intervals [80]. The power spectrum for the 5 kHz data set is not given as the fitted values are unreliable, due to the high sensitivity of the trapped atom number with respect to Rabi frequency which still exists for this data set.

Figure 8.31 shows how, in contrast to figure 8.12 for the minimal effect gravity model, the fitted Rabi frequencies agree well with the experimentally determined Ω_{exp} values. As mentioned previously, we have not allowed the fitting regime to vary the values of the trap parameters of B' , $T(t_0)$ and $N(t_0)$ using instead the experimentally determined values for these parameters. This has been done purposely to reduce the probability of accidental fits by limiting the number of fitted parameters and to avoid issues with interdependencies between fitted parameters as discussed in section 8.2.1. However, not accounting for any error in some of the key trap parameters will affect the exact value of γ_a and Ω obtained through fitting. Therefore, the good agreement with experimental Rabi frequency values gives us confidence in the model used but it cannot give us certainty in the quantitative values of the Rabi frequency and heating rate γ_a obtained. However, it is encouraging to see that for the parametric heating model the fitted Rabi frequency values are within the experimental uncertainty of 0.5 kHz, as is shown in figure 8.31. This is particularly promising when considering the complications associated with dynami-

cally modelling the occupancy and decay rates for several harmonic oscillator states⁴ and allowing for error in only two of the model input parameters.

The results presented in figures 8.28 to 8.30 fulfil all three requirements necessary to provide successful agreement between theory and experiment; low S values, agreement between theoretically used and experimentally determined Rabi frequency values, and suitable sensitivity to fluctuations in the Rabi frequency of 200 Hz. While there is clearly room for further investigation, if the complicated nature of the experimental setup is considered, we can conclude that the loss of atoms recorded in the experimental data studied is the result of non-adiabatic losses, which we can model using quantum mechanical decay rates by incorporating a heating process into the prediction of trapped atom number.

⁴Typically $0 \leq n \leq 100$ harmonic oscillator levels were required for solving equation (6.95) for the parametric heating model. However, it varies significantly based on trap parameters and heating rates used, so thorough testing is recommended.

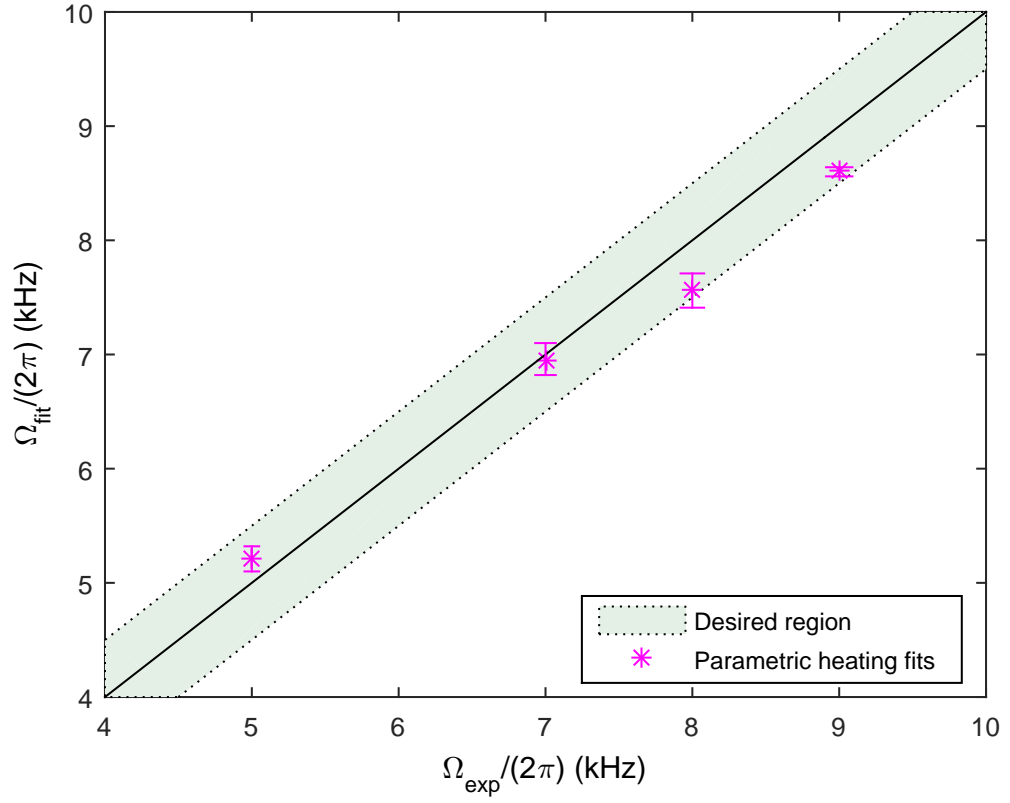


Figure 8.31: Comparison of fitted and experimentally determined Rabi frequencies for the parametric heating model regression fitting using equation (8.8). The fitted values from table 8.3 are represented as stars. A black line is plotted to show the correlation which the fitted values would follow if they matched the experimental Rabi frequency values. The desired region is plotted, around the black line, taking into account an uncertainty of 0.5 kHz in the experimentally determined values for the trap Rabi frequency.

8.3 Summary

In this chapter we have compared the theoretical predictions for trapped atom number with experimental data recorded by the Villetaneuse group of H       Perrin. Their trap consists of a quadrupole field generated by two macroscopic coils separated along the vertical axis, with two further coils to generate the RF magnetic fields. The trap is highly anisotropic so that we consider non-adiabatic losses in the vertical direction alone, assuming all losses in the other directions are negligible. The three dimensional nature of the atom trap was considered to improve the accuracy of the formula for ω_p , required for Bose-Einstein initial distributions.

Initially, the minimal effect gravity model was compared to the experimental data, using equation (6.4) to calculate the number of trapped atoms. When experimentally determined input parameters are used theoretical predictions generally overestimate the number of trapped atoms, as seen in figures 8.4 to 8.7. Non-linear least squares regression fitting was performed, however, the values of Rabi frequency obtained from regression fitting varied significantly from the experimentally predicted Ω values, as shown in figure 8.12, such that the underestimation of the rate of losses from the trap was still unaccounted for.

Comparison with the experimental data continued using the more sophisticated full effect gravity model, with non-adiabatic decay rates given by equation (5.136). Using experimentally determined input parameters the overestimation of the number of trapped atoms was still observed and had increased in comparison to the overestimation of the minimal effect gravity model. Regression fitting for the full effect gravity model is difficult and unreliable due to a large number of false minima caused by high sensitivity to the value of Rabi frequency inputted. The large variation in predicted trapped atom number which results from this Rabi frequency sensitivity prevented agreement with experiment. The RF synthesizer that produces the RF field in the experiment is expected to cause the Rabi frequency to fluctuate by up to 200 Hz. For this amount of Ω variation, the full effect gravity model predictions calculated using equation (6.4) indicate that the trapped atom number variance should be significantly more than was observed in the experimental data. Further investigation was required to find out why the sensitivity of the trapped atom number to Rabi frequency predicted by the theory had not been observed.

Examination of the time evolution of the atom cloud temperature indicated that there was a heating process present in the trap. Equation (6.4), which had previously been used to predict the number of trapped atoms, was replaced by dynamically updating the atomic energy distribution as discussed in section 6.4. Modelling the heating in a general manner, using the master equation model, expe-

experienced difficulties due to the unreliability of regression fitting caused by apparent interdependencies between the relaxation parameter (γ) and the final temperature of the system (T_f) which together characterise the heating process.

It is known that fluctuations in the currents used to generate the trapping magnetic fields, can lead to fluctuations in the trap centre and frequency which cause a heating process in the trap. Using the parametric heating model, discussed in section 6.4.2, we were able to express the predicted heating rates in terms of power spectrum for fractional fluctuations in: the static magnetic field gradient (B'), RF frequency (ω_{rf}) and RF magnetic field amplitude (B_{rf}). For the case in which the magnetic field gradient is the dominant cause of noise in the trap, we were able to calculate the heating rate γ_b based on its relation to the heating rate γ_a . Good agreement was found with experimental data when regression fitting the values of γ_a and Ω , as is shown in figures 8.28 to 8.30. A significant finding was that the incorporation of a suitably strong heating rate reduces the Rabi frequency sensitivity, so that the variation in trapped atom number is appropriate for the experimental data. Further investigation is required to understand why the fit obtained for the 5 kHz data set still displays dramatic Ω sensitivity. However, for all of the data sets: heating increases the loss of atoms from the trap which explains our previous overestimation of trapped atom number; values obtained from regression fitting, given in table 8.3, give a reasonable prediction for the noise in the magnetic field gradient and there is good agreement between fitted and experimentally determined Rabi frequency values, as presented in figure 8.31.

While there cannot be complete confidence in the values fitted, due to the complicated nature of the problem and the increasing number of unknowns, we can have confidence in the model used. The suitability of the values obtained for the power spectrum of fractional fluctuations in the static magnetic field gradient implies that the experimentally recorded decline in atoms at these relatively low Rabi frequencies was the result dominantly of non-adiabatic losses from the trap. We are able to model how the number of trapped atoms declines due to non-adiabatic transitions, using the full effect gravity model decay rates and accounting for heating processes with the parametric heating model.

Table 8.4 summarises the key figures presented in this chapter in the process of comparing theoretical atom number predictions with experimental data. While table 8.5 summarises the theoretical results presented in the experimental comparison process.

Decay rate	Heating	$N_n(t_0)$		Regression fitting used	Agreement with experiment
Γ_{MG}	X	Maxwell-Boltzmann	Squeezed thermal	Bose-Einstein	
		Figs. 8.4 - 8.7 Figs. 8.8 - 8.11	Figs. 8.4 - 8.7 Figs. 8.8 - 8.11	X ✓	X X
Γ_{FG}	X	Figs. 8.14 - 8.17 Fig. 8.20	Figs. 8.14 - 8.17	X	X
				✓	X
				✓	X
		Fig. 8.23		✓	X
Γ_{FG}	✓			✓	X
		Figs. 8.27 - 8.30		✓	✓

Table 8.4: A table summarising the experimental comparison process. The different methods for calculating the trapped atom number are formed by varying the decay rate model used, the presence or absence of heating processes and the initial distribution considered. The three initial distributions are introduced in sections 6.1, 6.2 and 6.3. When heating is present the parametric heating model, given by equation (6.4.2), is used; otherwise equation (6.4) is used. The different decay rates are denoted by Γ_{MG} for the minimal effect gravity model (equation (5.35)) and Γ_{FG} for the full effect gravity model (equation (5.136)). When regression fitting is used input parameters are selected such that S , given in equations (8.7) and (8.8), is minimised. The final column shows that it is only by combining the non-adiabatic decay rate with the parametric heating model that successful agreement between experiment and theory is obtained. Successful agreement with experiment means that: S values are suitably low, the theoretical Rabi frequency used is suitably close to the experimentally determined value of the Rabi frequency, and the value of the trapped atom number prediction does not vary significantly for a fluctuation of the Rabi frequency of 200 Hz (see table 8.5).

Decay rate	Heating	Regression fitting used	Low S value	$\Omega/(2\pi) \geq \Omega_{exp}/(2\pi) - 0.5 \text{ kHz}$ $\cap \Omega/(2\pi) \leq \Omega_{exp}/(2\pi) + 0.5 \text{ kHz}$	Appropriate $\Delta N(\Omega/(2\pi) \pm 200 \text{ Hz})$
Γ_{MG}	X	X	X	✓	✓
		✓	✓	X	✓
Γ_{FG}	X	X	X	✓	X
		✓	✓	X	X
Γ_{FG}	✓	✓	✓	✓	✓ $\Omega/2\pi \geq 7 \text{ kHz}$

Table 8.5: A table summarising the results of the experimental comparison process. The first three columns specify the defining attributes of a given result (see table 8.4), the final three columns assess the suitability of the result presented. A ✓ in the ‘Low S value’ column indicates suitable agreement between the theoretically predicted number of trapped atoms and the experimentally determined number of trapped atoms. The next column, expresses which results used suitable theoretical Rabi frequency values, taking into account the error bound on the experimental determination of the Rabi frequency. The final column contains a ✓ when the results obtained are such that the trapped atom number prediction behaves appropriately with a fluctuation in Rabi frequency value of 200 Hz. A ✓ in all three final columns indicates successful agreement between theoretical results and experimental data.

Part V

Conclusions

Chapter 9

Summary, conclusion and outlook

In this thesis an alternative to the semiclassical Landau-Zener theory, for modelling non-adiabatic transitions from RF-dressed cold atom traps has been developed. Several formulae for the rate of non-adiabatic transitions, obtained using Fermi's Golden Rule, have been presented in this thesis.

We first developed our minimal effect gravity model, a simple model which gives the general trend of the quantum mechanical decay rates. Within this model we are able to calculate the rate of non-adiabatic transitions, using numerical integration for equation (5.35) or from our analytical expression for atoms with the lowest allowed trap energy given by equation (5.27). In this model we were able to confirm that to reduce losses due to non-adiabatic transitions large Rabi frequencies or small magnetic field gradients are desirable. By approximating the integrals within equation (5.35) by the residue of the pole located within them, we obtained an analytic approximation to the decay rate from any allowed trapped atom energy, given by equation (5.74). This pole approximation holds reasonably well, improving with increasing atomic energy or in the low decay limit.

The full effect gravity model was next developed, taking into account the tilt of the adiabatic potentials caused directly by gravity. For this model we obtained a decay rate for non-adiabatic transitions, given by equation (5.136), which displays some interesting quantum mechanical effects. For example, figure 5.16 shows how atoms with higher energy can have a lower decay rate than their less energetic companions. This is a purely quantum mechanical effect from the overlap of the initial trapped state and final untrapped state wavefunctions and is only seen when gravity is incorporated into the model. The full effect gravity decay rate also displays oscillations with regards to Rabi frequency and magnetic field gradient. Such results could not be obtained from the semiclassical Landau-Zener theory. This work suggests that it may be possible to choose specific Rabi frequencies that are particularly

long lived, to maximise trap lifetimes. Further investigation on this matter would be interesting and required to understand whether this could be experimentally achievable.

The process by which our Fermi's Golden Rule decay rates can be transformed into the more experimentally useful value of trapped atom number was next discussed. Predicted time evolution for Maxwell-Boltzmann, squeezed thermal and Bose-Einstein initial distributions were considered. We used our atom number predictions to investigate how losses were affected by the non-adiabatic contribution to the trapping potential, referred to as the 'hump'. We found the contribution of the hump to be noticeable but very small, indicating that the usual negligence of it is reasonable. We subsequently developed more realistic models in which the atom number was calculated from an infinite chain of differential equations, such that it could dynamically update and include a heating rate if necessary.

With this information of non-adiabatic decay rates and predicted trapped atom number, we were ready to compare the quantum mechanical theories developed with the semiclassical Landau-Zener model. We found clear differences between our quantum mechanical decay rates and the Landau-Zener decay rate. Most significantly Landau-Zener theory led to an underestimation of losses due to non-adiabatic effects.

This thesis was concluded by exploring unaccounted for experimental results, where atom loss was believed to be due to non-adiabatic transitions. Initially we encountered several issues. When comparing with experimentally determined input parameters, we found a consistent overestimation in atom number as predicted by theory in comparison to the experimental data points. This translated to a very low fitted Rabi frequency when using non-linear, least squares, regression fitting. When using the full effect gravity model, regression fitting became highly time consuming and unreliable. This was due to the high Rabi frequency sensitivity in the full effect gravity decay rates. The atom number prediction was extremely sensitive to Rabi frequency but no sign of this was found in the experimental data.

An explanation is offered by examining how the number of trapped atoms is affected by sufficiently strong heating rates. It can be seen in experimental temperature data, for high Rabi frequencies, that there appears to be a heating process in the trap. By assuming that this heating is caused by fluctuations in the currents that produce the trapping magnetic fields, we are able to model the heating effects with the parametric heating model. It was found that sufficiently strong heating rates reduce the Rabi frequency sensitivity of our trapped atom number prediction and offer an explanation for the previous overestimation in atom number.

Applying our theory to experimental results has been an inspiring conclusion

to this study, improving the quality and diversity of the presented results. The added complexity of a full experimental setup and the inherent uncertainty and inability to truly isolate a system, are important for any theorist to understand and remember. Interestingly, the results obtained imply that undesirable noise in the trapping potential is vital for reducing the quantum mechanical sensitivity with Rabi frequency, that would otherwise cause dramatic fluctuations in the trapped atom number. This highlights the complexity of forming quantitative predictions for non-adiabatic losses from RF-dressed cold atom traps.

This complexity ensures this thesis is far from the last word on non-adiabatic transitions within RF-dressed traps. While our investigations have increased our understanding of the important aspects to consider when comparing with experiment and increased our theoretical capabilities by contributing a quantum mechanical model to the theorists toolbox, there is still much that could be done to extend both of these aims. From the theory point of view, it would be desirable to have an analytic formula for the full effect gravity decay rate given by equation (5.136), to understand more about these quantum mechanical effects and for ease of use as a possible replacement to Landau-Zener. Our models are only one dimensional, which is suitable for the anisotropic trap studied here. However, a full three dimensional treatment would provide generality and allow use in a wider range of traps. In this treatment, the contribution of the hump becomes highly complex and has not been considered in any currently published work. Another route to generality would be to consider the affect of interactions between atoms and to investigate how the situation would change considering a case in which the atom cloud is dominated by a Bose-Einstein condensate. Additionally, it would be highly interesting to see if any quantum interference effects can be observed by considering the V_B decay process or multistage decays for traps with $F \geq 2$. This would undoubtedly involve setting up more complicated models describing the atom's wavefunctions for the trapped and untrapped states.

From an experimental point of view, while the agreement between experiment and predicted atom losses are reasonable, it would be desirable to understand better the origin of the heating process in the trap. There seems to be some mechanism hindering agreement with experimental results at low Rabi frequencies, below 7 kHz, that could warrant further investigation. Comparison with a wider range of experimental observations would be desirable. An investigation to see if we could tailor experiments to try to detect the predicted Ω sensitivity, would be highly interesting and clear proof of quantum mechanical effects. This thesis is a step towards greater understanding of non-adiabatic losses from RF-dressed cold atom traps,

which should hopefully grow as a topic and develop as RF-dressed traps themselves gain greater importance and interest.

Bibliography

- [1] K. Merloti, R. Dubessy, L. Longchambon, A. Perrin, P-E. Pottie, V. Lorent, and H. Perrin. A two-dimensional quantum gas in a magnetic trap. *New Journal of Physics*, 15:033007, 2013.
- [2] Matthieu Pierens. Mesure de α pour l'imagerie et pertes Landau-Zener. Master's thesis, Laboratoire de physique des lasers, Paris, France, 2013.
- [3] A. Migdall, J. V. Prodan, W. D. Phillips, T. H. Bergeman, and H. J. Metcalf. First observation of magnetically trapped neutral atoms. *Physical Review Letters*, 54(24):2596–2599, 1985.
- [4] Jakob Reichel and Vladen Vuletic. *Atom Chips*. Wiley-VCH, 2011.
- [5] M. H. Anderson, J. R. Ensher, M. R. Matthews, C. E. Wieman, and E. A. Cornell. Observation of Bose-Einstein condensation in a dilute atomic vapor. *Science*, 269:198–201, 1995.
- [6] K. B. Davis, M.-O. Mewes, M. R. Andrews, N. J. van Druten, D. S. Durfee, D. M. Kurn, and W. Ketterle. Bose-Einstein condensate in a gas of sodium atoms. *Physical Review Letters*, 75(22):3969–3974, 1995.
- [7] W. Ketterle. Nobel lecture: When atoms behave as waves: Bose-Einstein condensation and the atom laser. *Reviews of Modern Physics*, 74(4):1131–1151, 2002.
- [8] H. Perrin. Ultra cold atoms and Bose-Einstein condensation for quantum metrology. *The European Physical Journal, Special Topics*, 172:37–55, 2009.
- [9] M. R. Matthews, B. P. Anderson, P. C. Haljan, D. S. Hall, C. E. Wieman, and E. A. Cornell. Vortices in a Bose-Einstein condensate. *Physical Review Letters*, 83(13):2498–2501, 1999.

- [10] K. W. Madison, F. Chevy, W. Wohlleben, and J. Dalibard. Vortex formation in a stirred Bose-Einstein condensate. *Physical Review Letters*, 84(5):806–809, 2000.
- [11] K. E. Wilson, Z. L. Newman, J. D. Lowney, and B. P. Anderson. In situ imaging of vortices in Bose-Einstein condensates. *Physical Review A*, 91:023621, 2015.
- [12] V. Giovannetti, S. Lloyd, and L. Maccone. Quantum-enhanced measurements: Beating the standard quantum limit. *Science*, 306:1330–1336, 2004.
- [13] M. F. Riedel, P. Böhi, Y. Li, T. W. Hänsch, A. Sinatra, and P. Treutlein. Atom-chip-based generation of entanglement for quantum metrology. *Nature*, 464:1170–1173, 2010.
- [14] A. Peters, K. Y. Chung, and S. Chu. Measurement of gravitational acceleration by dropping atoms. *Nature*, 400:849–852, 1999.
- [15] F. Sorrentino *et al.* A compact atom interferometer for future space missions. *Microgravity Science and Technology*, 22(4):551–561, 2010.
- [16] I. Bloch, T. W. Hänsch, and T. Esslinger. Atom laser with a cw output coupler. *Physical Review Letters*, 82(15):3008–3011, 1999.
- [17] F. Gerbier, P. Bouyer, and A. Aspect. Quasicontinuous atom laser in the presence of gravity. *Physical Review Letters*, 86(21):4729–4732, 2001.
- [18] J. J. Brehm and W. J. Mullin. *Introduction to the structure of matter*. John Wiley and Sons, 1989.
- [19] D. A. Smith, S. Aigner, S. Hofferberth, M. Gring, M. Andersson, S. Wildermuth, P. Krüger, S. Schneider, T. Schumm, and J. Schmiedmayer. Absorption imaging of ultracold atoms on atom chips. *Optics Express*, 19(9):8471–8485, 2011.
- [20] C. V. Sukumar and D. M. Brink. Spin-flip transitions in a magnetic trap. *Physical Review A*, 56(3):2451–2454, 1997.
- [21] D. M. Brink and C. V. Sukumar. Majorana spin-flip transitions in a magnetic trap. *Physical Review A*, 74:035401, 2006.
- [22] W. Ketterle and D. E. Pritchard. Trapping and focusing ground state atoms with static fields. *Applied Physics B*, 54:403–406, 1992.

- [23] T. Esslinger, I. Bloch, and T. W. Hänsch. Bose-Einstein condensation in a quadrupole-ioffe-configuration trap. *Physical Review A*, 58(4):R2664–R2667, 1998.
- [24] M. Gildemeister, E. Nugent, B. E. Sherlock, M. Kubasik, B. T. Sheard, and C. J. Foot. Trapping ultracold atoms in a time-averaged adiabatic potential. *Physical Review A*, 81:031402, 2010.
- [25] E. L. Raab, M. Prentiss, A. Cable, S. Chu, and D. E. Pritchard. Trapping of neutral sodium atoms with radiation pressure. *Physical Review Letters*, 59(23):2631–2634, 1987.
- [26] J. Reichel. Microchip traps and Bose-Einstein condensation. *Applied Physics B, Lasers and Optics*, 75:469–487, 2002.
- [27] J. Fortágh and C. Zimmermann. Magnetic microtraps for ultracold atoms. *Reviews of Modern Physics*, 79:235–289, 2007.
- [28] S. Groth, P. Krüger, S. Wildermuth, R. Folman, T. Fernholz, J. Schmiedmayer, D. Mahalu, and I. Bar-Joseph. Atom chips: Fabrication and thermal properties. *Applied Physics Letters*, 85(14):2980–2982, 2004.
- [29] G. A. Kazakov and T. Schumm. Magic radio-frequency dressing for trapped atomic microwave clocks. *Physical Review A*, 91:023404, 2015.
- [30] R. Szmuk, V. Dugrain, W. Maineult, J. Reichel, and P. Rosenbusch. Stability of a trapped-atom clock on a chip. *Physical Review A*, 92:012106, 2015.
- [31] T. Calarco, E. A. Hinds, D. Jaksch, J. Schmiedmayer, J. I. Cirac, and P. Zoller. Quantum gates with neutral atoms: Controlling collisional interactions in time-dependent traps. *Physical Review A*, 61:022304, 2000.
- [32] A. Negretti, P. Treutlein, and T. Calarco. Quantum computing implementations with neutral particles. *Quantum Information Processing*, 10(6):721–753, 2011.
- [33] R. A. Pepino, J. Cooper, D. Z. Anderson, and M. J. Holland. Atomtronic circuits of diodes and transistors. *Physical Review Letters*, 103:140405, 2009.
- [34] J. R. Anglin and W. Ketterle. Bose-Einstein condensation of atomic gases. *Nature*, 416:211–218, 2002.

- [35] M.C. Beeler, R. A. Williams, K. Jiménez-García, L. J. LeBlanc, A. R. Perry, and I. B. Spielman. The spin hall effect in a quantum gas. *Nature*, 498:201–204, 2013.
- [36] T. Esslinger. Fermi-Hubbard physics with atoms in an optical lattice. *Annual Review of Condensed Matter Physics*, 1:129–152, 2010.
- [37] O. Zobay and B. M. Garraway. Two-dimensional atom trapping in field-induced adiabatic potentials. *Physical Review Letters*, 86(7):1195–1198, 2001.
- [38] Y. Colome, E. Knyazchyan, O. Morizot, B. Mercier, V. Lorent, and H. Perrin. Ultracold atoms confined in rf-induced two-dimensional trapping potentials. *Europhysics Letters*, 67(4):593–599, 2004.
- [39] David J. Griffiths. *Introduction to Quantum Mechanics*. Pearson Education International, 2nd edition, 2005.
- [40] Daniel V. Schroeder. *An introduction to Thermal Physics*. Addison Wesley Longman, international edition, 2000.
- [41] Christopher J. Foot. *Atomic Physics*. Oxford University Press, 2005.
- [42] I. Lesanovsky, S. Hofferberth, J. Schmiedmayer, and P. Schmelcher. Manipulation of ultracold atoms in dressed adiabatic radio-frequency potentials. *Physical Review A*, 74:033619, 2006.
- [43] O. Morizot, Y. Colombe, V. Lorent, H. Perrin, and B. M. Garraway. Ring trap for ultracold atoms. *Physical Review A*, 74:023617, 2006.
- [44] W. H. Heathcote, E. Nugent, B. T. Sheard, and C. J. Foot. A ring trap for ultracold atoms in an rf-dressed state. *New Journal of Physics*, 10:043012, 2008.
- [45] T. Schumm, S. Hofferberth, L. M. Andersson, S. Wildermuth, S. Groth, I. Bar-Joseph, J. Schmiedmayer, and P. Krüger. Matter-wave interferometry in a double well on an atom chip. *Nature*, 1:57–62, 2005.
- [46] A. D. Cronin, J. Schmiedmayer, and D. E. Pritchard. Optics and interferometry with atoms and molecules. *Reviews of Modern Physics*, 81(3):1051–1129, 2009.
- [47] M. A. Cirone, A. Negretti, T. Calarco, P. Krüger, and J. Schmiedmayer. A simple quantum gate with atom chips. *The European Physical Journal D*, 35:165–171, 2005.

- [48] Claude Cohen-Tannoudji, Bernard Diu, and Franck Laloë. *Quantum Mechanics*. Wiley-Interscience, 2005.
- [49] Stephen M. Barnett and Paul M. Radmore. *Methods in Theoretical Quantum Optics*. Oxford University Press, 1997.
- [50] J. J. Sakurai and Jim Napolitano. *Modern Quantum Mechanics*. Pearson Education International, 2nd edition, 2011.
- [51] D. T. Pegg and G. W. Series. On the reduction of a problem in magnetic resonance. *Proceedings of the Royal Society of London, Series A*, 332:281–289, 1973.
- [52] I. S. Gradshteyn and I. M. Ryzhik. *Table of Integrals, Series and Products*. Academic Press, 6th edition, 2000.
- [53] A. F. J. Levi. *Applied Quantum Mechanics*. Cambridge University Press, 2003.
- [54] Guillermo Verlarde. *Mecánica Cuántica*. McGraw-Hill/Interamericana de España, 2002.
- [55] Christopher C. Gerry and Peter L. Knight. *Introductory Quantum Optics*. Cambridge University Press, 2005.
- [56] O. Morizot, L. Longchambon, R. Kollengode Easwaran, R. Dubessy, E. Knyazchyan, P-E. Pottie, V. Lorent, and H. Perrin. Influence of the Radio-Frequency source properties on RF-based atom traps. *The European Physical Journal D*, 47:209–214, 2008.
- [57] O. Zobay and B. M. Garraway. Atom trapping and two-dimensional Bose-Einstein condensates in field-induced adiabatic potentials. *Physical Review A*, 69:023605, 2004.
- [58] Mary L. Boas. *Mathematical Methods in the Physical Sciences*. John Wiley & Sons, 3rd edition, 2006.
- [59] Graham Woan. *The Cambridge handbook of Physics formulas*. Cambridge University Press, 2003.
- [60] Milton Abramowitz and Irene A. Stegun. *Handbook of Mathematical Functions*. US Government Printing Office, Washington, USA, 1972.
- [61] MATLAB release 2009b, The MathWorks Inc., Natick, Massachusetts, United States.

- [62] Jerrold E. Marsden and Michael J. Hoffman. *Basic Complex Analysis*. W. H. Freeman Publishers (New York), 3rd edition, 1999.
- [63] M. S. Kim, F. A. M. de Oliveira, and P. L. Knight. Properties of squeezed number states and squeezed thermal states. *Physical Review A*, 40:2494–2503, 1989.
- [64] R. K. Pathria. *Statistical Mechanics*. Elsevier, 2nd edition, 2006.
- [65] C. Cohen-Tannoudji, J. Dupont-Roc, and G. Grynberg. *Atom-Photon Interactions*. John Wiley and Sons, 1992.
- [66] Howard Carmichael. *An Open Systems approach to Quantum Optics*. Springer-Verlag, 1993.
- [67] Rodney Loudon. *The quantum theory of light*. Oxford University Press, 2nd edition, 1983.
- [68] P. Lambropoulos and D. Petrosyan. *Fundamentals of Quantum Optics and Quantum Information*. Springer, 2007.
- [69] M. E. Gehm, K. M. O’Hara, T. A. Savard, and J. E. Thomas. Dynamics of noise-induced heating in atom traps. *Physical Review A*, 58(5):3914–3921, 1998.
- [70] F. Reif. *Fundamentals of statistical and thermal physics*. McGraw-Hill, 1965.
- [71] Kerson Huang. *Introduction to Statistical Physics*. CRC Press, 2nd edition, 2010.
- [72] M. S. Child. *Molecular collision theory*. Academic Press, 1974.
- [73] C. Zener. Non-adiabatic crossing of energy levels. *Proceedings of the Royal Society of London, Series A*, 137(833):696–702, 1932.
- [74] C. Wittig. The Landau-Zener formula. *The Journal of Physical Chemistry B*, 109:8428–8430, 2005.
- [75] O. Morizot, C. L. Garrido Alzar, P.-E. Pottie, V. Lorent, and H. Perrin. Trapping and cooling of rf-dressed atoms in a quadrupole magnetic field. *Journal of Physics B: Atomic, molecular and optical physics*, 40:4013–4022, 2007.
- [76] Hélène Lefebvre-Brion and Robert W. Field. *Perturbations in the spectra of diatomic molecules*. Academic Press, 1986.

- [77] N. V. Vitanov and K.-A. Suominen. Time-dependent control of ultracold atoms in magnetic traps. *Physical Review A*, 56(6):R4377, 1997.
- [78] Karina Merloti. *Condensat de Bose-Einstein dans un piège habillé: modes collectifs d'un superfluide en dimension deux*. PhD thesis, Université Paris-Nord - Paris XIII, 2013.
- [79] Louis Lyons. *Statistics for nuclear and particle physicists*. Cambridge University Press, 1992.
- [80] MATLAB release 2015a, The MathWorks Inc., Natick, Massachusetts, United States.
- [81] P. M. Morse and H. Feshbach. *Methods of Theoretical Physics*. McGraw-Hill, 1953.
- [82] George Arfken. *Mathematical Methods for Physicists*. Academic Press, 2nd edition, 1970.

Part VI

Supporting material

Appendix A

Saddle point method

To attain an analytic approximation for the minimal effect gravity model decay rate, given by equation (5.35), we turn to the method of steepest descents (also commonly known as the saddle point method). The saddle point method involves deforming our path of integration from the real axis to a path in the complex plane that crosses the most significant saddle point across its steepest path. Such a deformation is possible due to Cauchy's integral theorem [81] and can be surprisingly accurate. To simplify our integrals the Hermite generator function,

$$e^{-t^2+2tx} = \sum_{q=0}^{\infty} \frac{t^q}{q!} H_q(x) \quad (\text{A.1})$$

taken from Gradshteyn and Ryzhik [52], was used to remove the Hermite polynomials from our integrals, so that the integrals we are trying to find are;

$$\int_{-\frac{L}{2\sigma}}^{\frac{L}{2\sigma}} \frac{e^{-\frac{x^2}{2}}}{x^2 + \frac{\Delta S^2}{\sigma^2}} e^{(2t \pm ik_n \sigma)x} dx \quad (\text{A.2})$$

and

$$\int_{-\frac{L}{2\sigma}}^{\frac{L}{2\sigma}} \frac{x e^{-\frac{x^2}{2}}}{\left(x^2 + \frac{\Delta S^2}{\sigma^2}\right)^2} e^{(2t \pm ik_n \sigma)x} dx. \quad (\text{A.3})$$

Please note that for this appendix section alone, the symbol t does not indicate the passage of time and is instead defined from equation (A.1).

The saddle point method [82, 81] was applied to the integral given in equation (A.2), such that

$$\int_{-\frac{L}{2\sigma}}^{\frac{L}{2\sigma}} \frac{e^{-\frac{x^2}{2}}}{x^2 + \alpha^2} e^{(2t + iw\alpha)x} dx \approx \sqrt{\frac{-2\pi}{F''(y_0)}} e^{F(y_0)}, \quad (\text{A.4})$$

where

$$\alpha = \frac{\Delta S}{\sigma} \quad (\text{A.5})$$

and scaling

$$k_n \sigma = w \alpha. \quad (\text{A.6})$$

For this integral,

$$F(y) = -\frac{y^2}{2} + 2ty + iw\alpha y - \ln(y^2 + \alpha^2), \quad (\text{A.7})$$

$$F'(y) = -y + 2t + iw\alpha - \frac{2y}{y^2 + \alpha^2}, \quad (\text{A.8})$$

$$F''(y) = -1 - \frac{2}{y^2 + \alpha^2} + \frac{4y^2}{(y^2 + \alpha^2)^2}. \quad (\text{A.9})$$

The value of y_0 is given by $F'(y_0) = 0$, which leads to the polynomial,

$$y_0^3 - (2t + iw\alpha)y_0^2 + (2 + \alpha^2)y_0 - \alpha^2(2t + iw\alpha) = 0 \quad (\text{A.10})$$

and the expression that

$$\int_{\frac{-L}{2\sigma}}^{\frac{L}{2\sigma}} \frac{e^{-\frac{x^2}{2}}}{x^2 + \alpha^2} e^{(2t+iw\alpha)x} dx \approx -\sqrt{\frac{2\pi}{(\alpha^2 + y_0^2)^2 + 2(\alpha^2 - y_0^2)}} e^{-\frac{y_0^2}{2} + (2t+iw\alpha)y_0}. \quad (\text{A.11})$$

This is the expression for the saddle point approximation, all that is required is the determination of the location of the saddle point given by y_0 . As the assumption $z \ll \Delta S$ has already been made in modelling our atomic wavefunctions, it makes sense to assume α is large and look for solutions of the form

$$y_0 = \sum_{p=-1}^{\infty} \frac{\lambda_p}{\alpha^p}, \quad (\text{A.12})$$

for the case $\alpha \gg 1$ and

$$y_0 = \sum_{p=-1}^{\infty} \sum_{q=-1}^{\infty} \frac{\mu_{pq}}{\alpha^{p+q}}, \quad (\text{A.13})$$

for the high t limit, $t \gg \alpha \gg 1$. Here λ is a constant that is not dependent on α (but may be dependent on t) and μ is a constant that is not dependent on t or α ¹.

Let us first examine the $\alpha \gg 1$ case, substitution of equation (A.12) into equation (A.10) gives

$$\begin{aligned} & \sum_{p=-1}^{\infty} \sum_{q=-1}^{\infty} \sum_{r=-1}^{\infty} \frac{\lambda_p \lambda_q \lambda_r}{\alpha^{p+q+r}} - 2t \sum_{a=-1}^{\infty} \sum_{b=-1}^{\infty} \frac{\lambda_a \lambda_b}{\alpha^{a+b}} - iw \sum_{d=-1}^{\infty} \sum_{e=-1}^{\infty} \frac{\lambda_d \lambda_e}{\alpha^{d+e-1}} \\ & + 2 \sum_{f=-1}^{\infty} \frac{\lambda_f}{\alpha^f} + \sum_{s=-1}^{\infty} \frac{\lambda_s}{\alpha^{s-2}} - 2t\alpha^2 - iw\alpha^3 = 0, \end{aligned} \quad (\text{A.14})$$

¹This notation is used for this appendix section only and should not be confused with the magnetic field gradient in frequency units or chemical potential represented by λ and μ respectively in the majority of this thesis.

by selecting out the co-efficients for the α^N case (where $N = 3, 2, 1, 0, -1, \dots$) we see that

$$\begin{aligned} & \sum_{p=-1}^{2-N} \sum_{q=-1}^{1-N-p} \lambda_p \lambda_q \lambda_{(-N-p-q)} - 2t \sum_{a=-1}^{1-N} \lambda_a \lambda_{(-N-a)} - iw \sum_{d=-1}^{2-N} \lambda_d \lambda_{(1-N-d)} \\ & + 2\lambda_{(-N)} + \lambda_{(2-N)} - 2t\delta_N^2 - iw\delta_N^3 = 0. \end{aligned} \quad (\text{A.15})$$

By substituting each value of N from highest to lowest, the values of the λ co-efficients can be discovered. There are three roots given to order of α^{-2} as

$$y_{iw} = iw\alpha + 2t - \frac{2iw}{\alpha(1-w^2)} - \frac{4t(1+w^2)}{\alpha^2(1-w^2)^2}, \quad (\text{A.16})$$

$$y_i = i\alpha + \frac{i}{\alpha(1-w)} + \frac{2t}{\alpha^2(1-w)^2}, \quad (\text{A.17})$$

$$y_{-i} = -i\alpha - \frac{i}{\alpha(1+w)} + \frac{2t}{\alpha^2(1+w)^2}. \quad (\text{A.18})$$

Equation (A.16) is chosen for use as the other two roots are always situated very close to the poles at $\pm i\alpha$ and are therefore inappropriate for performing the saddle point approximation.

Let us now examine the case $t \gg \alpha \gg 1$, substitution of equation (A.13) into equation (A.10) gives the more complicated expression of

$$\begin{aligned} & \sum_{p=-1}^{\infty} \sum_{q=-1}^{\infty} \sum_{a=-1}^{\infty} \sum_{b=-1}^{\infty} \sum_{d=-1}^{\infty} \sum_{e=-1}^{\infty} \frac{\mu_{pq}\mu_{ab}\mu_{de}}{\alpha^{p+a+d}t^{q+b+e}} - 2 \sum_{h=-1}^{\infty} \sum_{j=-1}^{\infty} \sum_{f=-1}^{\infty} \sum_{l=-1}^{\infty} \frac{\mu_{hj}\mu_{fl}}{\alpha^{h+f}t^{j+l-1}} \\ & - iw \sum_{r=-1}^{\infty} \sum_{s=-1}^{\infty} \sum_{m=-1}^{\infty} \sum_{z=-1}^{\infty} \frac{\mu_{rs}\mu_{mz}}{\alpha^{r+m-1}t^{s+z}} + 2 \sum_{u=-1}^{\infty} \sum_{v=-1}^{\infty} \frac{\mu_{uv}}{\alpha^u t^v} + \sum_{y=-1}^{\infty} \sum_{x=-1}^{\infty} \frac{\mu_{yx}}{\alpha^{y-2}t^x} \\ & - 2t\alpha^2 - iw\alpha^3 = 0. \end{aligned} \quad (\text{A.19})$$

Selecting out the co-efficients for the $\alpha^N t^M$ case (where N and M are integers ≤ 3) gives

$$\begin{aligned} & \sum_{p=-1}^{2-N} \sum_{q=-1}^{2-M} \sum_{a=-1}^{1-N-p} \sum_{b=-1}^{1-M-q} \mu_{pq}\mu_{ab}\mu_{(-N-p-a)(-M-q-b)} - 2 \sum_{h=-1}^{1-N} \sum_{j=-1}^{2-M} \mu_{hj}\mu_{(-N-h)(1-M-j)} \\ & - iw \sum_{r=-1}^{2-N} \sum_{s=-1}^{1-M} \mu_{rs}\mu_{(1-N-r)(-M-s)} + 2\mu_{(-N)(-M)} + \mu_{(2-N)(-M)} \\ & - 2\delta_N^2 \delta_M^1 - iw\delta_N^3 \delta_M^0 = 0. \end{aligned} \quad (\text{A.20})$$

In a similar process to finding the λ co-efficients for the $\alpha \gg 1$ case, the μ co-efficients can be discovered by specifying values for N and M to give the desired root, that is the root that is not too near a pole, to order $\frac{1}{t^2}$ as

$$y_0 = 2t + iw\alpha - \frac{1}{t} + \frac{iw\alpha}{2t^2}. \quad (\text{A.21})$$

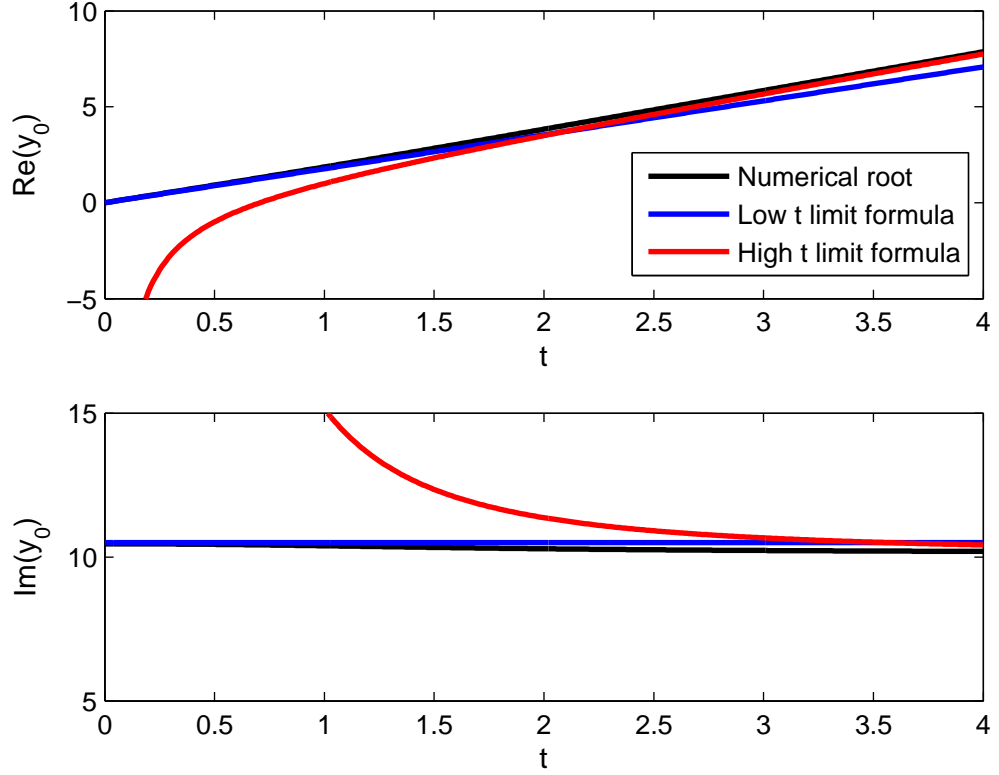


Figure A.1: How the low t limit formula for y_0 given by equation (A.16) and the high t limit formula given by equation (A.21) match the location of the saddle point as calculated numerically. The numerical determination of y_0 was undertaken by solving the polynomial (A.10) using the in-built function ‘roots’ using Mathworks software, Matlab [61]. A magnetic field gradient of $B' = 1.1 \text{ T/m}$ and a Rabi frequency of $\Omega/2\pi = 26 \text{ kHz}$ were used for the atomic ground state of ^{87}Rb atoms.

Figure A.1 is a graph showing how equation (A.16) for low t and equation (A.21) for high t match the location of the chosen saddle point.

Substitution of equation (A.16) for low t and equation (A.21) for high t into equation (A.11) gives the contribution to the integral for the deformed path through the saddle point given at y_0 .

However, the presence of the pole at $+i\alpha$ needs to be taken into consideration. If the location of the saddle point is above the pole, than the pole contributes to the saddle point method approximation as it is within the closed contour of the integral in the complex plane. Figure A.2 shows a diagram of the case for which the pole is between the saddle point and the real axis.

Path \mathcal{A} is the path we would like to integrate over the real axis, the saddle point method instead deforms the integration path to path \mathcal{C} which passes through the saddle point across its steepest slope. Paths \mathcal{B} and \mathcal{D} are necessary to close the loop but as the integral goes to zero at $\pm\infty$ these contributions are negligible. Therefore, in the absence of poles the Cauchy integral theorem leads to $\mathcal{A} + \mathcal{B} + \mathcal{C} + \mathcal{D} = 0$. Once \mathcal{B} and \mathcal{D} are neglected $\mathcal{A} = -\mathcal{C}$, the expression given in equation (A.11).

However, when $\text{Im}(y_0) > \alpha$ the pole is within the region enclosed by the integration loop. This is depicted in figure A.2. The Cauchy integral theorem then tells us that $\mathcal{A} + \mathcal{B} + \mathcal{C} + \mathcal{D} = \mathcal{P}$ where \mathcal{P} is the residue of the pole [62]. In this case neglecting \mathcal{B} and \mathcal{D} leads to $\mathcal{A} = \mathcal{P} - \mathcal{C}$. This expression we shall use later on in equation (A.26).

As we discussed in section 5.1.2, the residue of the pole is found by multiplying the Laurent series co-efficient for the term $\frac{1}{z}$ by the product $2\pi i$. It is calculated as follows for the pole at $i\alpha$. The integrand is

$$f(y) = \frac{e^{-\frac{y^2}{2} + (2t + i\omega\alpha)y}}{(y + i\alpha)(y - i\alpha)}, \quad (\text{A.22})$$

where a change of variable $z = y - i\alpha$ gives

$$f(z) = e^{\frac{\alpha^2}{2} + 2it\alpha - \omega\alpha^2} \frac{e^{-\frac{z^2}{2} + (2t - i\alpha + i\omega\alpha)z}}{2i\alpha z \left(1 - \frac{iz}{2\alpha}\right)}. \quad (\text{A.23})$$

Further expansion, in direct similarity to the steps taken in section 5.1.2, gives

$$f(z) = \frac{e^{\frac{\alpha^2}{2} + 2it\alpha - \omega\alpha^2}}{2i\alpha} \sum_{p=0}^{\infty} \sum_{q=0}^{\infty} \sum_{r=0}^{\infty} \frac{\left(-\frac{1}{2}\right)^p}{p!} \frac{(2t - i\alpha + i\omega\alpha)^q}{q!} \left(\frac{i}{2\alpha}\right)^r z^{2p+q+r-1}. \quad (\text{A.24})$$

For the co-efficient of $\frac{1}{z}$, $p = q = r = 0$ giving the pole contribution to the integral as

$$\mathcal{P} = \frac{\pi}{\alpha} e^{\frac{\alpha^2}{2} + 2it\alpha - \omega\alpha^2}. \quad (\text{A.25})$$

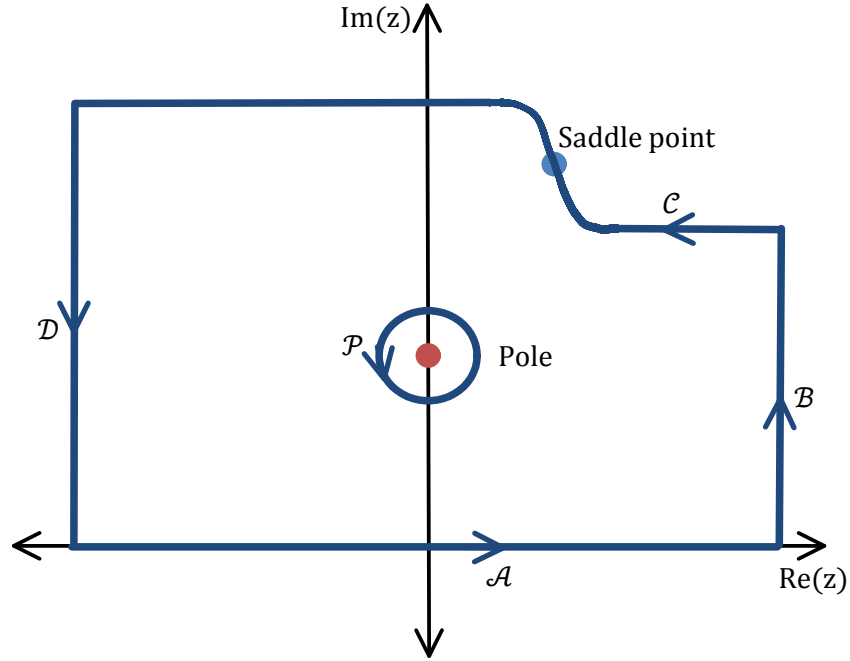


Figure A.2: Deformation of the integration path for the saddle point method including pole contribution.

This gives the saddle point approximation to the integral, when the pole contributes, as

$$\int_{\frac{-L}{2\sigma}}^{\frac{L}{2\sigma}} \frac{e^{-\frac{x^2}{2}}}{x^2 + \alpha^2} e^{(2t+iw\alpha)x} dx = \frac{\pi}{\alpha} e^{\frac{\alpha^2}{2} + 2it\alpha - w\alpha^2} - \sqrt{\frac{2\pi}{(\alpha^2 + y_0^2)^2 + 2(\alpha^2 - y_0^2)}} e^{-\frac{y_0^2}{2} + (2t+iw\alpha)y_0}, \quad (\text{A.26})$$

where y_0 is the location of the saddle point as given by the polynomial (A.10) and approximated by equations (A.16) and (A.13).

Multiplication of both sides of equation (A.33) by e^{-t^2} and reapplication of the generator function (A.1) gives

$$\sum_{r=0}^{\infty} \frac{t^r}{r!} \int_{-\frac{L}{2\sigma}}^{\frac{L}{2\sigma}} \frac{H_r(x) e^{-\frac{x^2}{2}}}{x^2 + \alpha^2} e^{i w \alpha x} dx = \frac{\pi}{\alpha} e^{\frac{\alpha^2}{2} - w \alpha^2} \sum_{q=0}^{\infty} \frac{t^q}{q!} H_q(i \alpha) - \sqrt{\frac{2\pi}{(\alpha^2 + y_0^2)^2 + 2(\alpha^2 - y_0^2)}} e^{-\frac{y_0^2}{2} + (2t + i w \alpha) y_0 - t^2} \quad (\text{A.27})$$

It is now necessary to extract the desired t^n co-efficient from equation (A.27), how to achieve this is not immediately obvious, especially as the location of the saddle point y_0 is dependent on t . Fortunately there is a region of interest in which we can neglect the contribution to the integral from path \mathcal{C} , the path that crosses the saddle

point, and use the residue of the pole as the dominant contribution to the integral. This simplifies equation (A.27) and allows us to continue our analysis as detailed in the pole approximation section starting from equation (A.33). The following figures demonstrate the region in which the residue of the pole dominates the saddle point approximation.

To approximate the saddle point method by the residue from the pole, we must first ensure that the pole is within the loop, that goes through the real axis and the saddle point, as depicted in figure A.2. Figures A.3 and A.4 show that this appears to be a suitable assumption. The location of y_0 in the imaginary plane is consistently found to be higher than the location of the pole. The saddle point location moves further away from the pole for higher n states, indicating that the most limiting case would be the ground state. The saddle point also moves further from the pole as the Rabi frequency is increased.

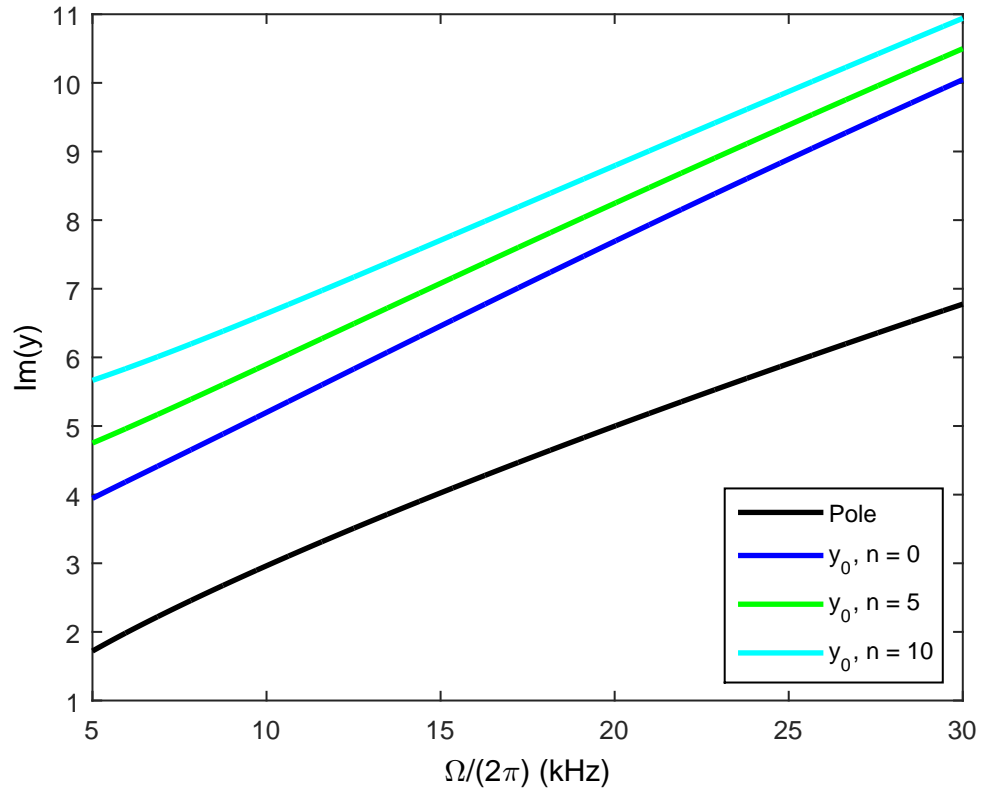


Figure A.3: Demonstrating that the pole residue should be taken into account in the saddle point method approximation. The location of the pole was calculated from equation (A.16) and the pole at $y = i\alpha$ was chosen. In producing this graph a magnetic field gradient $B' = 1.5 \text{ T/m}$ and $t = 0.1$ were used.

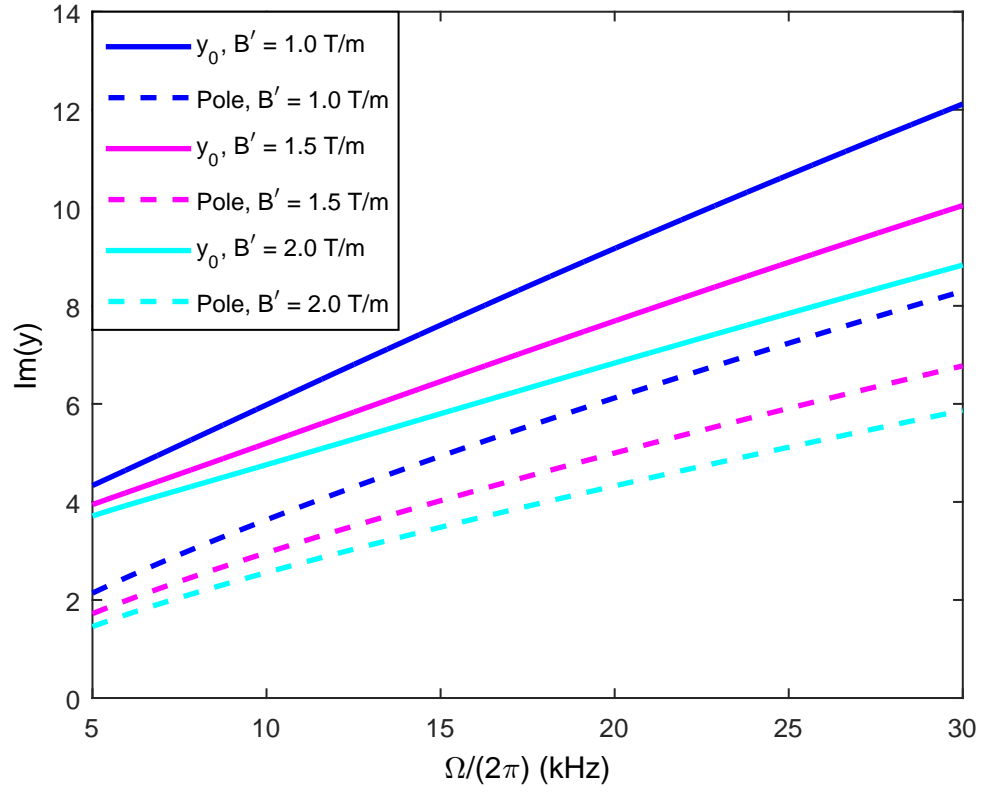


Figure A.4: Demonstrating how the location of the pole and the saddle point vary in the imaginary plane for a variety of different magnetic field gradients. The harmonic oscillator ground state $n = 0$ (which figure A.3 indicates to be the most restrictive) is used to produce this graph, as well as a value of $t = 0.1$.

Figures A.3 and A.4 indicate that we should take account of the pole in our saddle point approximation. However, they do not indicate how significant the pole contribution is to the saddle point approximation. Figures A.5 and A.6 show this domination of the pole in the region of interest. Figure A.5 shows how the different methods for integrating equation (A.2) are in agreement, although the pole approximation is deviating at low Rabi frequency. The saddle point approximation is seen in figure A.6 to be a very good approximation for the integral varying by less than 1% of the value obtained by numerical integration. The pole approximation differs by just below 10% for the parameters plotted, indicating that it is the main contribution to the saddle point approximation and that it provides a reasonable approximation to integral A.2.

Figure A.7 compares the pole approximation with the numerical quadrature method when varying the atomic energy labelled by the quantum number n and the

magnetic field gradient B' . For the values plotted the maximum fractional difference between the pole approximation for integral (A.2) and that obtained by numerical integration is still about 10%, with the pole approximation preferring low magnetic field gradients and high n values.

The pole approximation improves significantly with greater initial atomic energy. This is not favourable for modelling non-adiabatic losses as the low energy states are the most highly populated, with the majority of atoms being found in the harmonic oscillator ground state. However, we may still obtain a suitable approximation to the decay rate using the residue of the pole to calculate equation (A.2). Additionally, we do already have an exact expression for the ground state decay rate, as detailed in section 5, so that the pole approximation does not need to be used for Γ_0 . To continue with an analytic treatment of the decay rate from any initial n state, we select the region in which the residue of the pole is a good approximation for the integral and continue our derivation using the pole approximation.

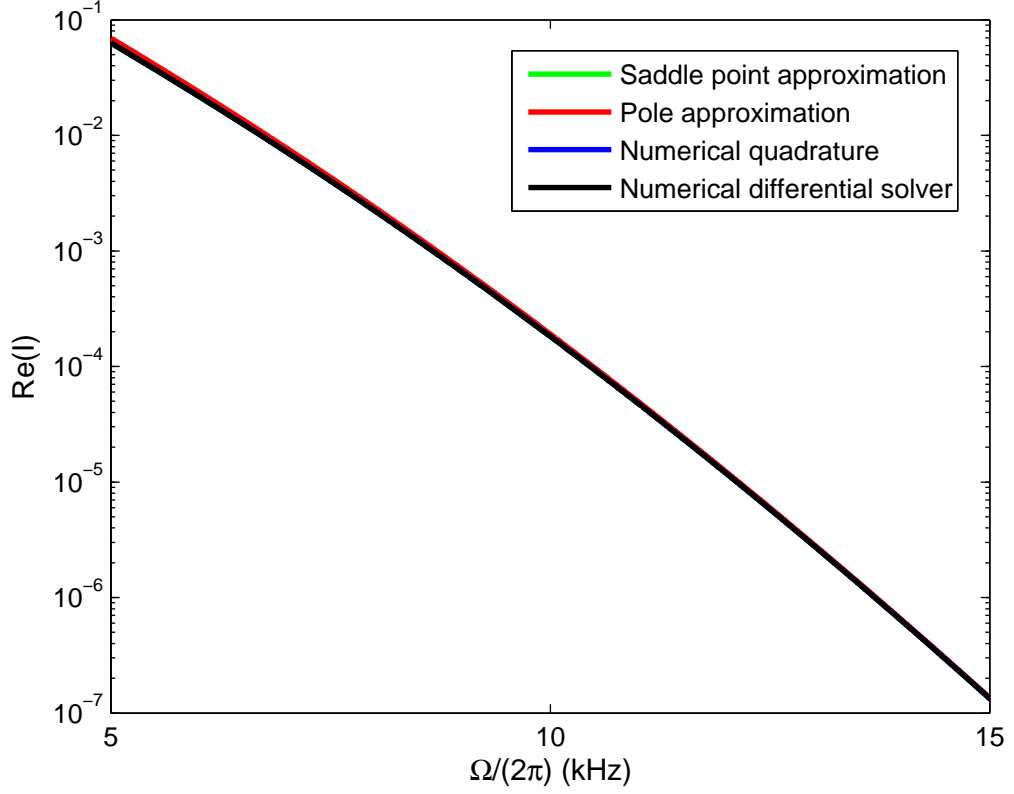


Figure A.5: The integral given by equation (A.2), for a magnetic field gradient of $B' = 1.5 \text{ T/m}$, $t = 0.1$ and with the trapping state being the harmonic oscillator ground state. The green line (under the black line) is the saddle point approximation as given by equation (A.26) taking into account the contribution from the pole and using equation (A.16) as the location of the saddle point. The red line is the pole approximation given by equation (A.33), assuming that the saddle point approximation is dominated by the contribution from the pole. The blue line (under the black line) is a numerical integration of equation (A.2) using Matlab solver ‘quadgk’ and the black line is a numerical integration using Matlab’s in-built differential solver ‘ode45’ [61].

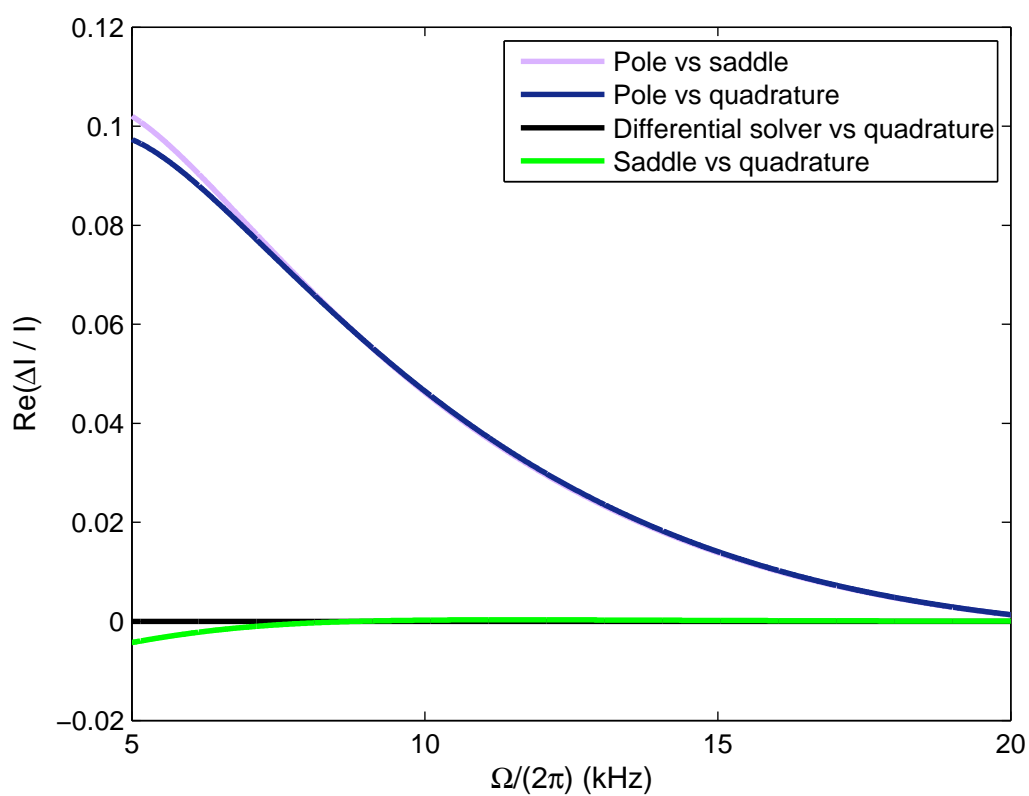


Figure A.6: Fractional difference between the different methods for calculating the integral, where the fractional difference of A vs B is given by $\text{real}(A - B)/\text{real}(B)$. As in figure A.5 $n = 0$, $t = 0.1$ and $B' = 1.5 \text{ T/m}$ were used.

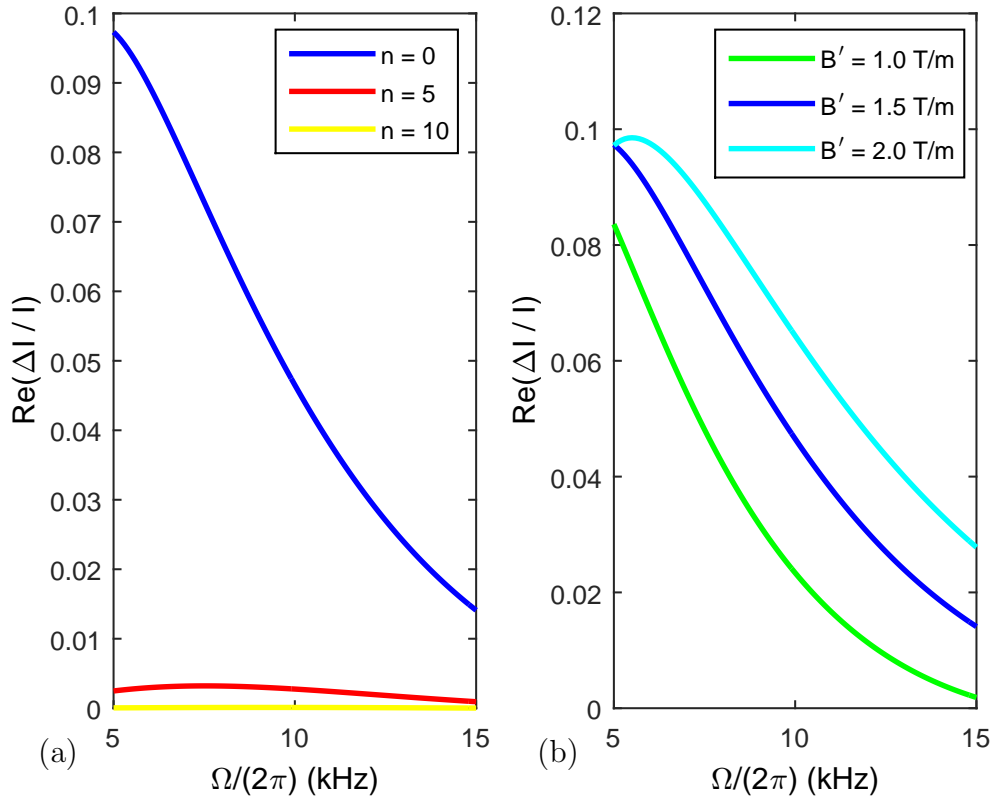


Figure A.7: Fractional difference between the pole approximation and the numerical quadrature method. (a) uses a value of $B' = 1.5$ T/m, $t = 0.1$ and varies the initial harmonic oscillator state n , while (b) uses a value of $n = 0$, $t = 0.1$ and varies the magnetic field gradient.

To use the pole approximation to find an analytic formula for Γ_n , we now need to approximate the integral given in equation (A.3). We calculate the residue of the $+i\alpha$ pole for the integral (A.3), following a very similar process to that found in section 5.1.2. The integrand of equation (A.3) is

$$f_2(y) = \frac{ye^{-\frac{y^2}{2} + (2t+iw\alpha)y}}{(y+i\alpha)^2(y-i\alpha)^2}. \quad (\text{A.28})$$

A change of variable $z = y - i\alpha$ gives

$$f_2(z) = -e^{\frac{\alpha^2}{2} + 2it\alpha - w\alpha^2} \frac{(z+i\alpha)e^{-\frac{z^2}{2} + (2t-i\alpha+iw\alpha)z}}{4\alpha^2 z^2 \left(1 - \frac{iz}{2\alpha}\right)^2}, \quad (\text{A.29})$$

before further expansion leads to

$$\begin{aligned} f_2(z) = & -\frac{e^{\frac{\alpha^2}{2} + 2it\alpha - w\alpha^2}}{4\alpha^2} \sum_{p=0}^{\infty} \sum_{q=0}^{\infty} \sum_{r=0}^{\infty} \left[\frac{\left(-\frac{1}{2}\right)^p (2t-i\alpha+iw\alpha)^q}{p! q!} \right. \\ & \left. \times (r+1) \left(\frac{i}{2\alpha}\right)^r (z+i\alpha) z^{2p+q+r-2} \right]. \end{aligned} \quad (\text{A.30})$$

For the co-efficient of $\frac{1}{z}$, there are three configurations of p, q and r which have $\frac{1}{z}$ terms: $p = q = r = 0$, $p = q = 0 \cap r = 1$, and $p = r = 0 \cap q = 1$. This gives the pole contribution to the integral as

$$\mathcal{P}_2 = \frac{\pi}{2\alpha} (2t - i\alpha + iw\alpha) e^{\frac{\alpha^2}{2} + 2it\alpha - w\alpha^2}. \quad (\text{A.31})$$

Meaning that we can approximate integral (A.3) as:

$$\int_{\frac{-L}{2\sigma}}^{\frac{L}{2\sigma}} \frac{xe^{-\frac{x^2}{2}}}{(x^2 + \alpha^2)^2} e^{(2t+ik_n\sigma)x} dx \approx \frac{\pi}{2\alpha} (2t + ik_n\sigma - i\alpha) e^{\frac{\alpha^2}{2} + 2it\alpha - k_n\Delta S}. \quad (\text{A.32})$$

In direct similarity to figure A.7, figure A.8 shows the fractional difference between the pole approximation and numerical quadrature methods for integral (A.3). The pole approximation is worse for integral (A.3) than it is for integral (A.2), placing more stringent requirements on selecting a high enough Rabi frequency, magnetic field gradient and initial atomic energy. This could pose a problem as our study focuses on the low Rabi frequency limit in which non-adiabatic transitions occur with suitably high frequency for observation. However, it is also an advantage that the pole approximation accuracy increases in the high Rabi frequency limit, as this is the limit in which RF-dressed cold atom traps favourably operate.

If we take the approximation that our integrals are given by the contribution to the saddle point method from the residue of the pole,

$$\int_{\frac{-L}{2\sigma}}^{\frac{L}{2\sigma}} \frac{e^{-\frac{x^2}{2}}}{x^2 + \alpha^2} e^{(2t \pm ik_n\sigma)x} dx \approx \frac{\pi}{\alpha} e^{\frac{\alpha^2}{2} \pm 2it\alpha - k_n\Delta S} \quad (\text{A.33})$$

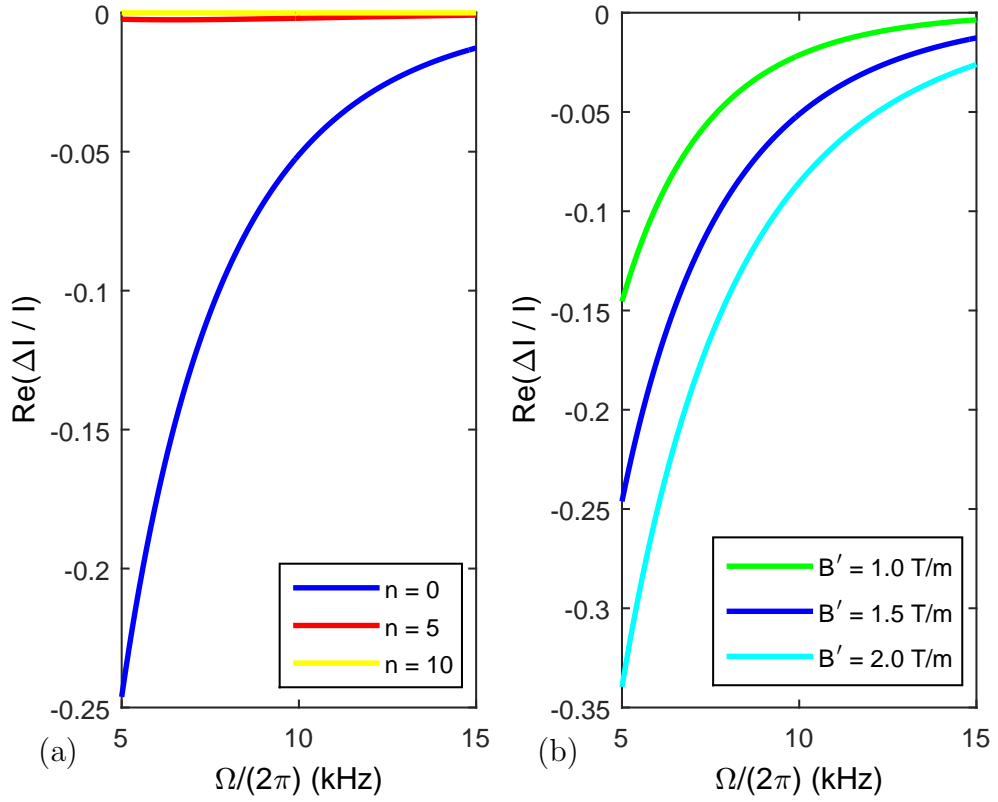


Figure A.8: Fractional difference between the pole approximation and the numerical quadrature method for (A.3). (a) uses a value of $B' = 1.5$ T/m, $t = 0.1$ and varies the initial harmonic oscillator state n , while (b) uses a value of $n = 0$, $t = 0.1$ and varies the magnetic field gradient.

and

$$\int_{-\frac{L}{2\sigma}}^{\frac{L}{2\sigma}} \frac{x e^{-\frac{x^2}{2}}}{(x^2 + \alpha^2)^2} e^{(2t \pm i k_n \sigma)x} dx \approx \frac{\pi}{2\alpha} (2t \pm i k_n \sigma \mp i\alpha) e^{\frac{\alpha^2}{2} \pm 2it\alpha - k_n \Delta S}. \quad (\text{A.34})$$

The generator function can now be used for the second time to aid us in selecting out the integral we require. Multiplication of both sides of equation (A.33) by e^{-t^2} and reapplication of the generator function (A.1) gives

$$\sum_{r=0}^{\infty} \frac{t^r}{r!} \int_{-\frac{L}{2\sigma}}^{\frac{L}{2\sigma}} \frac{H_r(x) e^{-\frac{x^2}{2}}}{x^2 + \alpha^2} e^{\pm i k_n \sigma x} dx = \frac{\pi}{\alpha} e^{\frac{\alpha^2}{2} - k_n \Delta S} \sum_{q=0}^{\infty} \frac{t^q}{q!} H_q(\pm i\alpha), \quad (\text{A.35})$$

which selecting out the t^n co-efficient gives

$$\int_{-\frac{L}{2\sigma}}^{\frac{L}{2\sigma}} \frac{H_n(x) e^{-\frac{x^2}{2}}}{x^2 + \alpha^2} e^{\pm i k_n \sigma x} dx = \frac{\pi}{\alpha} e^{\frac{\alpha^2}{2} - k_n \Delta S} H_n(\pm i\alpha). \quad (\text{A.36})$$

For equation (A.34),

$$\begin{aligned} & \sum_{r=0}^{\infty} \frac{t^r}{r!} \int_{-\frac{L}{2\sigma}}^{\frac{L}{2\sigma}} \frac{H_r(x) x e^{-\frac{x^2}{2}}}{(x^2 + \alpha^2)^2} e^{\pm i k_n \sigma x} dx \\ &= \frac{\pi}{2\alpha} e^{\frac{\alpha^2}{2} - k_n \Delta S} \left[2 \sum_{q=0}^{\infty} \frac{t^{q+1}}{q!} H_q(\pm i\alpha) \pm i(k_n \sigma - \alpha) \sum_{p=0}^{\infty} \frac{t^p}{p!} H_p(\pm i\alpha) \right] \quad (\text{A.37}) \end{aligned}$$

which selecting out the t^n co-efficient gives

$$\begin{aligned} & \int_{-\frac{L}{2\sigma}}^{\frac{L}{2\sigma}} \frac{H_n(x) x e^{-\frac{x^2}{2}}}{(x^2 + \alpha^2)^2} e^{\pm i k_n \sigma x} dx \\ &= \frac{\pi}{2\alpha} e^{\frac{\alpha^2}{2} - k_n \Delta S} [2n H_{n-1}(\pm i\alpha) \pm i(k_n \sigma - \alpha) H_n(\pm i\alpha)]. \quad (\text{A.38}) \end{aligned}$$

Equations (A.36) and (A.38) are equivalent to equations (5.51) and (5.71) given in section 5.1.2 respectively. The discussion and conclusions of the suitability of the pole approximation are continued there.

Appendix B

Double exponential fit

It is noteworthy that a double exponential,

$$N(t) = Ae^{-at} + Be^{-bt} \quad (\text{B.1})$$

where A, B have units {Number of atoms remaining trapped} and a, b have units s^{-1} , fits the experimental data well, as can be seen in figures [B.1](#) to [B.4](#).

The reason for this is not known. Equation [\(6.4\)](#) only approximates as a double exponential when the majority of the atomic population is contained within the ground state and first excited state. This, however, does not explain the double exponential fit. Any relationship between the parameters describing the physics of the experiment; the Rabi frequency Ω , magnetic field gradient B' , initial atom number $N(t_0)$ and initial temperature $T(t_0)$, and the parameters for the experimental fit A, B, a, b is unknown. There are three possibilities to explain the double exponential fit:

- (a) the double exponential is not related to the physics describing the atomic losses from the trap and the fitted co-efficients A, B, a, b do not relate to any physical parameters,
- (b) the theory is incorrectly modelling the losses caused by the RF coupling and should instead give a double exponential formula for the atomic losses relating A, B, a, b to the physical parameters,
- (c) there is(are) some other loss mechanism(s) which is(are) dominant in the system and provides a double exponential formula for the atomic losses relating A, B, a, b to the physical parameters which describe this(these) other dominant loss mechanism(s).

In favour of point (a), the least squares fitting regime implemented has the characteristic that it is much easier to fit a curve the more parameters the fitting

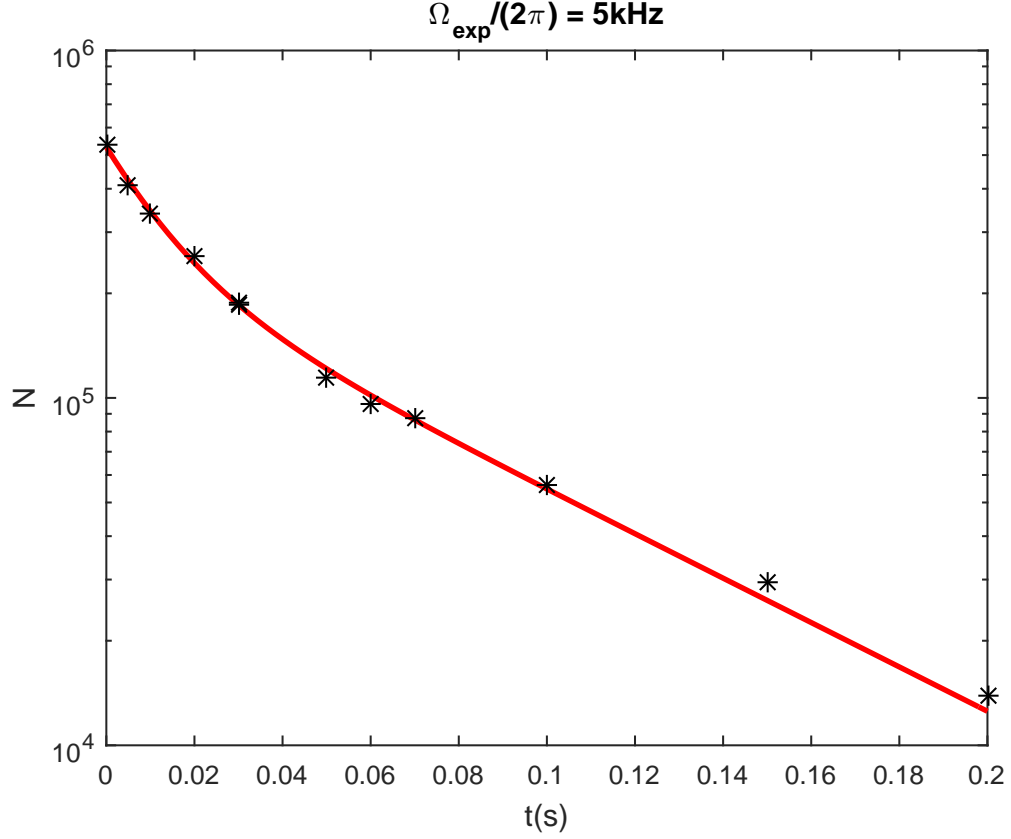


Figure B.1: Double exponential fit for the $\Omega_{exp}/2\pi = 5$ kHz experimental data using equation (B.1). The fit was calculated using Mathworks, Matlab function ‘nlinfit’ [61] and given to three significant figures is $\{A, a, B, b\} = \{29.0, 72.6, 23.7, 14.7\}$.

regime is allowed to vary. The double exponential has a four parameter fit, meaning it is relatively easy for the least squares fitting regime to produce a suitable fit with the experimental data.

Additionally in favour of discounting point (b), looking at table B.1 it can be seen that there is no clear correlation between the Rabi frequency and the fitted A, B, a, b parameters. Each experiment is a new trap setup with, for example, the atoms having different initial temperatures which could mask the Rabi frequency dependence. However, in the theoretical results presented here and in the semiclassical Landau-Zener model, it is predicted that the non-adiabatic losses have a strong dependence on the Rabi frequency, so we would expect to see some correlation.

As points (b) and (c) cannot be ruled out, the double exponential is noteworthy. However, there is no current physical interpretation for why a double exponential should match the experimental data and the ease of a multiple parameter regression fit indicate point (a) is the most likely explanation.

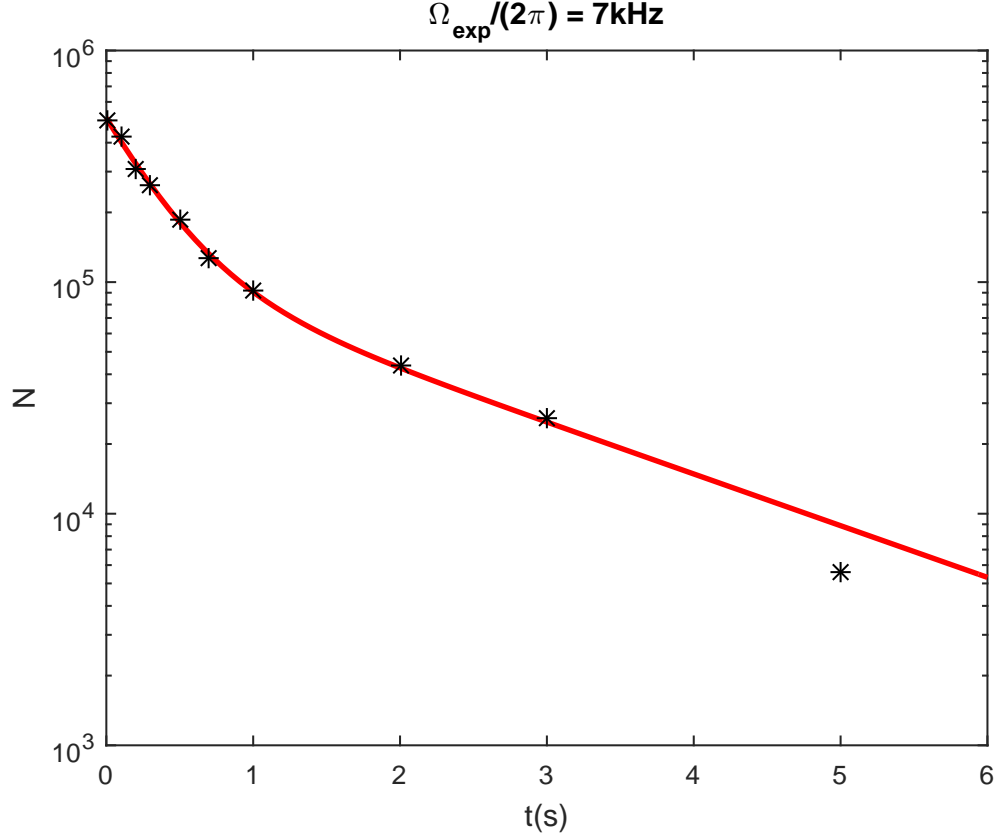


Figure B.2: Double exponential fit for the $\Omega_{exp}/2\pi = 7\text{ kHz}$ experimental data using equation (B.1). The fit was calculated using Mathworks, Matlab function ‘nlinfit’ [61] and given to three significant figures is $\{A, a, B, b\} = \{39.5, 2.92, 11.6, 0.514\}$.

$\Omega_{exp}(1/2\pi \text{ kHz})$	$A/N(t_0)$	a	$B/N(t_0)$	b
5	0.544	72.6	0.445	14.7
7	0.787	2.92	0.231	0.514
8	0.389	3.66	0.593	0.570
9	0.861	0.179	0.166	0.0361

Table B.1: Fitted values for the double exponential given to three significant figures.

Taking point (a) as a suitable explanation, the figures B.1 to B.4 are a reminder to show how reasonable matching with the experimental data points can be obtained by regression fitting with too many degrees of freedom without any

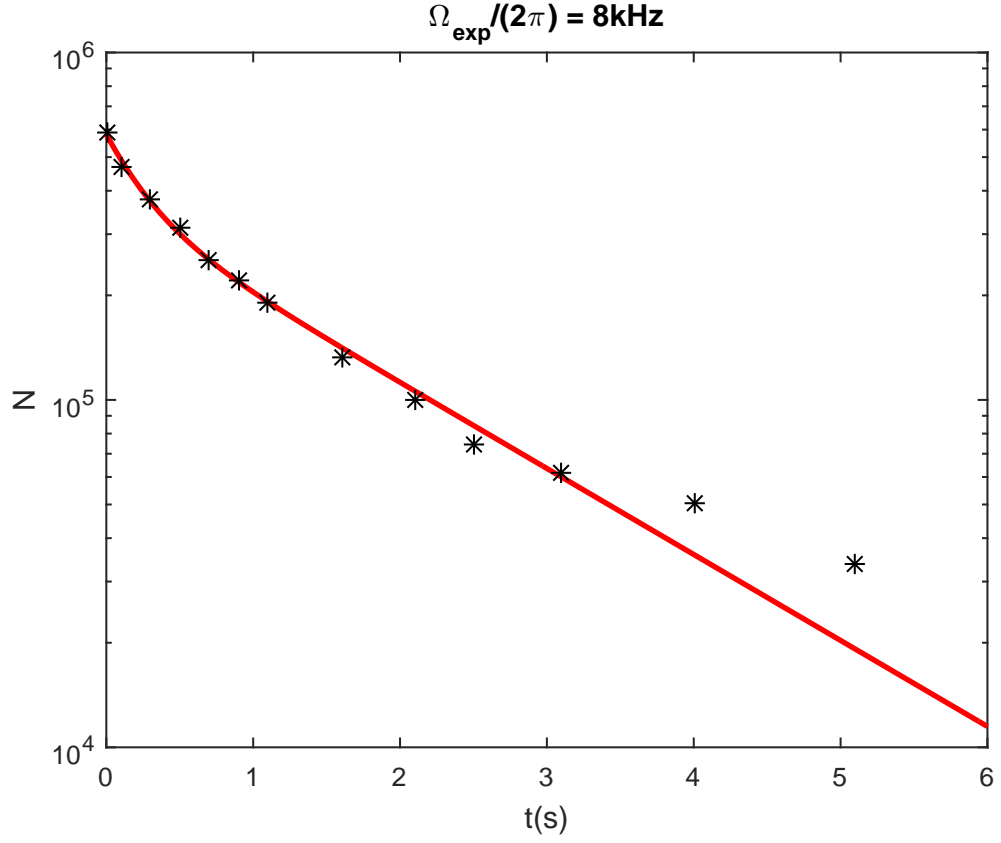


Figure B.3: Double exponential fit for the $\Omega_{\text{exp}}/2\pi = 8\text{ kHz}$ experimental data using equation (B.1). The fit was calculated using Mathworks, Matlab function ‘nlinfit’ [61] and given to three significant figures is $\{A, a, B, b\} = \{23.0, 3.66, 35.1, 0.570\}$.

physical significance to the results.

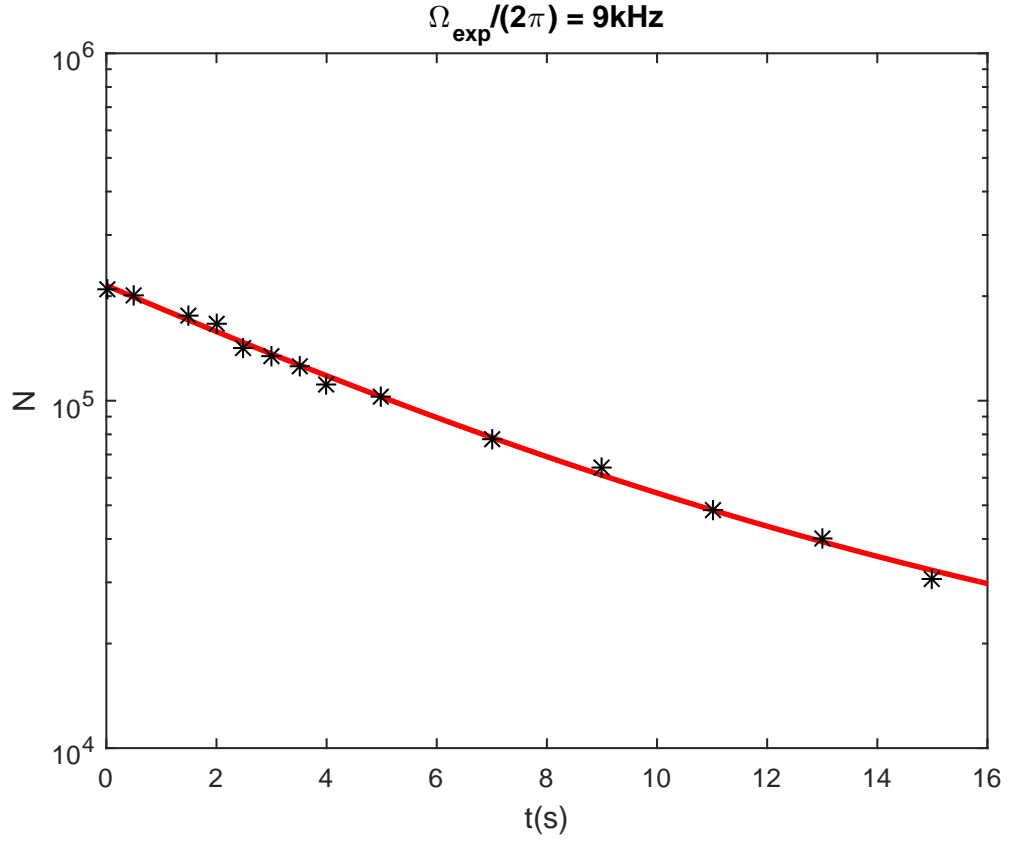


Figure B.4: Double exponential fit for the $\Omega_{\text{exp}}/2\pi = 9\text{kHz}$ experimental data using equation (B.1). The fit was calculated using Mathworks, Matlab function ‘nlinfit’ [61] and given to three significant figures is $\{A, a, B, b\} = \{18.0, 0.179, 3.47, 0.0361\}$.

Appendix C

Asymmetric box example

In the minimal effect gravity model of the system described in chapter 5 we take a box symmetrically centred at the origin, whose walls are later extended to infinity in the approximation that once the atom is in the $m_f = 0$ state it acts as a free particle. The wavefunction of the system is thus given by equation 5.14. This appendix section briefly looks at the consequences of taking an asymmetric box about the origin. This is a more general situation than that discussed in chapter 5 and is shown by the schematic diagram in figure C.1.

The potential experienced by an atom in the $m_f = 0$ state is now given in its more general form,

$$V_f(z) = \begin{cases} \infty, & z \leq L_1, \\ \hbar m_f \Omega + \frac{\mathcal{H}(m_f)}{\Delta S^2}, & L_1 \ll z \ll L_2, \\ \infty, & z \geq L_2. \end{cases}$$

This can be made equivalent to our symmetric box, used in section 5.1 for the minimal effect gravity model, by setting $L_1 = -\frac{L}{2}$ and $L_2 = \frac{L}{2}$. However, in this section

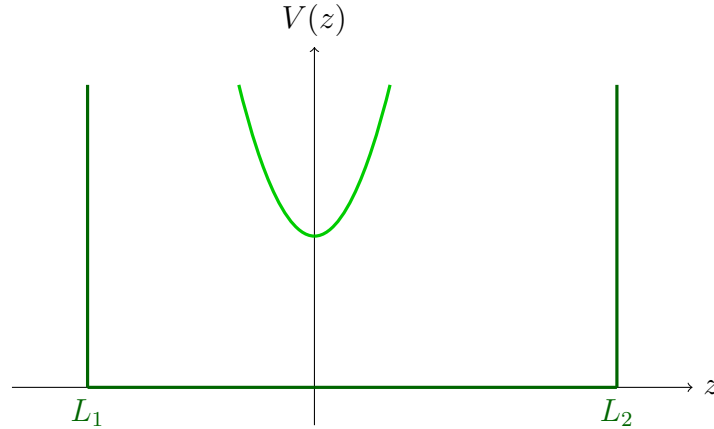


Figure C.1: Asymmetric box model

we shall continue with L_1 and L_2 unconstrained. Substitution into the Schrödinger equation gives us a second order differential equation for the wavefunction of the system,

$$\frac{\partial^2 \Psi}{\partial z^2} = -k^2 \Psi \quad (\text{C.1})$$

where

$$k = \sqrt{\frac{2m_0}{\hbar^2} \left[E_{n_f} - \hbar m_f \Omega - \frac{\mathcal{H}(m_f)}{\Delta S^2} \right]}. \quad (\text{C.2})$$

The solution to the Schrödinger equation (C.1) is

$$\Psi(z) = Ae^{ikz} + Be^{-ikz}, \quad (\text{C.3})$$

where A and B are constants to be determined. The system has two boundary conditions,

$$0 = Ae^{ikL_1} + Be^{-ikL_1}, \quad (\text{C.4})$$

$$0 = Ae^{ikL_2} + Be^{-ikL_2}. \quad (\text{C.5})$$

Rearrangement of equation (C.4) gives $B = -Ae^{2ikL_1}$, which can be substituted into equation (C.5) giving the relation $e^{2ik(L_2-L_1)} = 1$. This leads to the quantization condition,

$$k(L_2 - L_1) = n_f \pi. \quad (\text{C.6})$$

The quantization condition can be used to write the constant B in a more convenient form in terms of the co-efficient A as

$$B = (-1)^{n_f+1} Ae^{ik(L_1+L_2)}, \quad (\text{C.7})$$

we can see that the sign of B differs between even and odd n_f states and the phase of B is dependent on the asymmetry of the box ($L_1 + L_2$).

The wavefunction, with the boundary conditions incorporated, is now given by

$$\Psi(z) = A [e^{ikz} + (-1)^{n_f+1} e^{ik(L_1+L_2)} e^{-ikz}]. \quad (\text{C.8})$$

The remaining constant, A , can be determined from the normalization condition:

$$\begin{aligned} 1 &= |A|^2 \int_{L_1}^{L_2} [e^{-ikz} + (-1)^{n_f+1} e^{-ik(L_1+L_2)} e^{ikz}] [e^{ikz} + (-1)^{n_f+1} e^{ik(L_1+L_2)} e^{-ikz}] dz, \\ 1 &= 2|A|^2 \int_{L_1}^{L_2} 1 + (-1)^{n_f+1} \cos[k(L_1 + L_2) - 2kz] dz, \\ 1 &= 2|A|^2 \left[z - \frac{(-1)^{n_f+1}}{2k} \sin[k(L_1 + L_2) - 2kz] \right]_{L_1}^{L_2}, \\ 1 &= 2|A|^2 (L_2 - L_1), \end{aligned}$$

where the sine terms disappear due to the application of the quantization condition. If we take A to be real, ignoring any global phase factor, we find

$$A = \frac{1}{\sqrt{2(L_2 - L_1)}} \quad (\text{C.9})$$

so that the amplitude of the wavefunction is inversely proportional to the width of the box.

The wavefunction for the system can now be written in terms of recognizable variables,

$$\Psi(z) = \frac{1}{\sqrt{2(L_2 - L_1)}} \left[e^{ikz} + (-1)^{n_f+1} e^{ik(L_1+L_2)} e^{-ikz} \right]. \quad (\text{C.10})$$

Equation (5.14) is a special case of equation (C.10) with no asymmetry, $L_1 + L_2 = 0$, and box width L .

The wavefunction can be considered to be describing a stationary wave probability solution formed from two travelling waves, one travelling in the positive z direction and the other travelling in the negative z direction. The two travelling waves have equal amplitude and the same modulus of momenta k . The two travelling waves must always destructively interfere at L_1 and L_2 , as the wavefunction must be zero at the box boundary due to the infinite potential beyond. This ensures that L_1 and L_2 are always nodes of the stationary wave solution and leads to the normalization condition. To ensure the location of nodes at L_1 and L_2 there is a phase difference between the two travelling waves at the origin, defined by $\Delta\phi(z=0) = k(L_1 + L_2) + (n_f + 1)\pi$, dependent on the asymmetry of the box.

To investigate further this asymmetric box model we shall now derive a decay rate using Fermi's Golden Rule. For simplicity, we consider a case with constant coupling κ , rather than our position dependent non-adiabatic coupling. For a constant coupling situation the interaction matrix element is given by,

$$V_{ikf} = \frac{\kappa}{\sqrt{n!2^{n+1}(L_2 - L_1)\sigma\sqrt{\pi}}} \int_{L_1}^{L_2} H_n\left(\frac{z}{\sigma}\right) e^{-\frac{z^2}{2\sigma^2}} \left[e^{ikz} + (-1)^{n_f+1} e^{ik(L_1+L_2)} e^{-ikz} \right] dz \quad (\text{C.11})$$

This integral can be approximated using 7.376.1 from Gradshteyn and Ryzhik [52]. To make this approximation it is not necessary for L_1 and L_2 to be equal in magnitude but separately they both need to be large enough so that the integrand is approximately zero beyond their locations.

This approximates the interaction matrix element as

$$V_{ikf} \approx \frac{2\pi^{\frac{1}{4}}\kappa\sqrt{\sigma}i^{n-1}}{\sqrt{n!2^n(L_2 - L_1)}} H_n(k\sigma) e^{-\frac{k^2\sigma^2}{2}} e^{i\left[\frac{k}{2}(L_1+L_2) + \frac{\pi}{2}(n+n_f)\right]} \times \sin\left[\frac{k}{2}(L_1 + L_2) + \frac{\pi}{2}(n + n_f)\right]. \quad (\text{C.12})$$

The amplitude of the interaction element is thus given by

$$|V_{i\kappa f}|^2 = \frac{2^2 \sqrt{\pi} |\kappa|^2 \sigma}{n! 2^n (L_2 - L_1)} |H_n(k\sigma)|^2 e^{-k^2 \sigma^2} \sin^2 \left[\frac{k}{2} (L_1 + L_2) + \frac{\pi}{2} (n + n_f) \right]. \quad (\text{C.13})$$

This can be written in terms of the quantum number n_f , using the quantization condition (C.6),

$$\begin{aligned} |V_{i\kappa f}|^2 &= \frac{2^2 \sqrt{\pi} |\kappa|^2 \sigma}{n! 2^n (L_2 - L_1)} \left| H_n \left(\frac{n_f \pi \sigma}{L_2 - L_1} \right) \right|^2 e^{-\frac{n_f^2 \pi^2 \sigma^2}{(L_2 - L_1)^2}} \\ &\quad \times \sin^2 \left[\frac{\pi}{2} n_f \left(\frac{L_1 + L_2}{L_2 - L_1} \right) + \frac{\pi}{2} (n + n_f) \right] \end{aligned} \quad (\text{C.14})$$

after which we can use of the double angle formula for sine to simplify the last term leading us to the expression:

$$\begin{aligned} |V_{i\kappa f}|^2 &= \frac{2^2 \sqrt{\pi} |\kappa|^2 \sigma}{n! 2^n (L_2 - L_1)} \left| H_n \left(\frac{n_f \pi \sigma}{L_2 - L_1} \right) \right|^2 e^{-\frac{n_f^2 \pi^2 \sigma^2}{(L_2 - L_1)^2}} \\ &\quad \times \left\{ \sin \left[\frac{\pi}{2} n_f \left(\frac{L_1 + L_2}{L_2 - L_1} \right) \right] \times \cos \left[\frac{\pi}{2} (n + n_f) \right] \right. \\ &\quad \left. + \cos \left[\frac{\pi}{2} n_f \left(\frac{L_1 + L_2}{L_2 - L_1} \right) \right] \times \sin \left[\frac{\pi}{2} (n + n_f) \right] \right\}^2. \end{aligned} \quad (\text{C.15})$$

It can be seen that there are two distinct behaviours emerging depending on whether $n_f + n$ is odd or even. If $n_f + n \in \text{even}$:

$$|V_{i\kappa f}|^2 = \frac{2^2 \sqrt{\pi} |\kappa|^2 \sigma}{n! 2^n (L_2 - L_1)} \left| H_n \left(\frac{n_f \pi \sigma}{L_2 - L_1} \right) \right|^2 e^{-\frac{n_f^2 \pi^2 \sigma^2}{(L_2 - L_1)^2}} \sin^2 \left[\frac{\pi}{2} n_f \left(\frac{L_1 + L_2}{L_2 - L_1} \right) \right]. \quad (\text{C.16})$$

If $n_f + n \in \text{odd}$:

$$|V_{i\kappa f}|^2 = \frac{2^2 \sqrt{\pi} |\kappa|^2 \sigma}{n! 2^n (L_2 - L_1)} \left| H_n \left(\frac{n_f \pi \sigma}{L_2 - L_1} \right) \right|^2 e^{-\frac{n_f^2 \pi^2 \sigma^2}{(L_2 - L_1)^2}} \cos^2 \left[\frac{\pi}{2} n_f \left(\frac{L_1 + L_2}{L_2 - L_1} \right) \right]. \quad (\text{C.17})$$

Instead of looking at the combined system, the system can instead be viewed as if there are two possible reservoirs available for any particular harmonic oscillator n state to decay into. For a given harmonic oscillator energy E_n it can decay into the reservoir $n_f + n \in \text{even}$ with interaction matrix element given by equation (C.16), or the reservoir $n_f + n \in \text{odd}$ with interaction matrix element given by equation (C.17). For a finite box the system will most likely decay into whichever bath has an energy E_{n_f} closest to E_n . However, when the limit $L \rightarrow \infty$ is taken the difference between n_f and $n_f \pm 1$ becomes infinitesimally small and the system is equally likely to decay into either of the two baths, so that

$$\langle \Gamma \rangle = \Gamma_1 \cup \Gamma_2, \quad (\text{C.18})$$

$$\langle \Gamma \rangle = \Gamma_1 + \Gamma_2. \quad (\text{C.19})$$

If Fermi's Golden Rule is now used to obtain the rate of transitions into either of the two reservoirs this leads to the expression

$$\langle \Gamma_n \rangle = \frac{2\pi}{\hbar} [|V_1|^2 D_1(E) + |V_2|^2 D_2(E)]. \quad (\text{C.20})$$

For the total system equations (C.2) and (C.6) can be combined to give an expression for the energy in terms of n_f which can be differentiated to give the density of all states,

$$\frac{\partial n_f}{\partial E} = \frac{m_0(L_2 - L_1)^2}{\hbar^2 \pi^2 n_f}. \quad (\text{C.21})$$

When observing the system from the viewpoint of consisting of two independent reservoirs, for each of the reservoirs there are half as many states as there would be in the total system. Such that the density of states for each of the reservoirs is halved,

$$D_1(E) = D_2(E) = \frac{1}{2} \frac{\partial n_f}{\partial E} = \frac{m_0(L_2 - L_1)^2}{2\hbar^2 \pi^2 n_f}. \quad (\text{C.22})$$

Therefore the decay rate is given by

$$\langle \Gamma_n \rangle = \frac{m_0(L_2 - L_1)^2}{\hbar^3 \pi n_f} (|V_1|^2 + |V_2|^2) \quad (\text{C.23})$$

where

$$\begin{aligned} |V_1|^2 + |V_2|^2 &= \frac{2^2 \sqrt{\pi} |\kappa|^2 \sigma}{n! 2^n (L_2 - L_1)} \left| \text{H}_n \left(\frac{n_f \pi \sigma}{L_2 - L_1} \right) \right|^2 e^{-\frac{n_f^2 \pi^2 \sigma^2}{(L_2 - L_1)^2}} \\ &\quad \times \left\{ \sin^2 \left[\frac{\pi}{2} n_f \left(\frac{L_1 + L_2}{L_2 - L_1} \right) \right] + \cos^2 \left[\frac{\pi}{2} n_f \left(\frac{L_1 + L_2}{L_2 - L_1} \right) \right] \right\}, \\ |V_1|^2 + |V_2|^2 &= \frac{2^2 \sqrt{\pi} |\kappa|^2 \sigma}{n! 2^n (L_2 - L_1)} \left| \text{H}_n \left(\frac{n_f \pi \sigma}{L_2 - L_1} \right) \right|^2 e^{-\frac{n_f^2 \pi^2 \sigma^2}{(L_2 - L_1)^2}}. \end{aligned}$$

This leads to the expression

$$\langle \Gamma_n \rangle = \frac{m_0 (L_2 - L_1) |\kappa|^2 \sigma}{n! 2^{n-2} \hbar^3 \sqrt{\pi} n_f} \left| \text{H}_n \left(\frac{n_f \pi \sigma}{L_2 - L_1} \right) \right|^2 e^{-\frac{n_f^2 \pi^2 \sigma^2}{(L_2 - L_1)^2}}. \quad (\text{C.24})$$

Now the decay no longer depends on the box asymmetry, only the box width. This indicates that we can safely take the special case of a symmetric box, as we did in section 5. Note, however, this is only valid as we are taking the $L \rightarrow \infty$ limit.

By rewriting equation (C.24) using the quantization condition,

$$\langle \Gamma_n \rangle = \frac{m_0 \sqrt{\pi} |\kappa|^2 \sigma}{n! 2^{n-2} \hbar^3 k} |\text{H}_n(k\sigma)|^2 e^{-k^2 \sigma^2} \quad (\text{C.25})$$

where k selects out the resonant energy $E_n = E_{n_f}$, we see that, in fact, the box width and position become irrelevant for the decay rate in the $L \rightarrow \infty$ limit. This

is as we desire as the use of the box is a mathematical construct which should not affect the obtained decay rate. The only box parameter of interest is the momenta of the particle in the box k for the resonant energy $E_n = E_{n_f}$.

By considering this constant coupling case, we have therefore seen the origin of the factor of a half in our density of states in equation (5.26) and that the symmetric box model is appropriate.